

**Quantifying Fluid Overload with Portable Magnetic Resonance  
Sensors**

by

Lina Avancini Colucci

B.S., Mechanical Engineering  
Duke University, 2012

Submitted to the Harvard-MIT Health Sciences and Technology Program  
in partial fulfillment of the requirements for the degree of

Doctor of Philosophy in Medical Engineering and Medical Physics

at the

Massachusetts Institute of Technology

June 2018

© Massachusetts Institute of Technology 2018. All rights reserved.

**Signature redacted**

Author .....  
Harvard-MIT Health Sciences and Technology Program  
April 13, 2018

**Signature redacted**

Certified by .....  
Michael J. Cima, PhD  
David H. Koch Professor of Engineering  
Thesis Supervisor

**Signature redacted**

Accepted by .....  
Emery N. Brown, MD, PhD  
Director, Harvard-MIT Program in Health Sciences and Technology  
Professor of Computational Neuroscience and Health Sciences and Technology





# Quantifying Fluid Overload with Portable Magnetic Resonance Sensors

by

Lina Avancini Colucci

Submitted to the Harvard-MIT Health Sciences and Technology Program  
on April 13, 2018, in partial fulfillment of the  
requirements for the degree of  
Doctor of Philosophy in Medical Engineering and Medical Physics

## Abstract

The objective of this work was to translate the diagnostic capabilities of magnetic resonance imaging (MRI) to the patient bedside, specifically for the purpose of quantifying fluid overload.

MRI is used extensively in clinical medicine, but it is still not used for routine diagnostics due to high cost, limited availability, and long scan times. Many of these impracticalities come from the hardware requirements associated with generating images. Images, however, are not necessary to harness some of magnetic resonance's (MR's) diagnostic potential. This thesis demonstrates that a single-voxel MR sensor can obtain the same results as a traditional MRI in both phantoms and humans.

A clinical study with hemodialysis patients and age-matched healthy controls was performed at MGH. The  $T_2$  relaxation times of study participants' legs were quantified at multiple time points with both a 1.5T clinical MRI scanner and a custom 0.27T single-voxel MR sensor.

The results showed that the first sign of fluid overload is an increase in the relative fraction of extracellular fluid in the muscle. The relaxation time of the extracellular fluid in the muscle eventually increases after more fluid accumulates. Importantly, these MR findings occur before signs of lower-extremity edema are detectable on physical exam.

Two healthy control subjects became dehydrated over the course of the study and the relative fraction of their extracellular fluid decreased. This incidental finding suggests MR can measure the full spectrum of hydration states.

Furthermore, a single MRI measurement at a single time point can distinguish fluid overloaded patients from healthy controls. The amplitude associated with extracellular fluid most closely correlates to fluid loss, and these amplitude decreases are detectable with both the MRI and MR sensor.

The results of this work point towards a promising future of using cheaper, faster MR sensors for bedside diagnostics.

Thesis Supervisor: Michael J. Cima, PhD

Title: David H. Koch Professor of Engineering



## Acknowledgments

It takes a village to complete any type of clinical study and my doctoral work was no exception. I am deeply grateful to many people for their help and support in this journey.

First and foremost, thank you to my PhD adviser, **Prof. Michael J. Cima**, for taking me on as a graduate student. Thank you for advising me through a project with so much breadth - from magnetic resonance (MR) physics, to the mechanical and electrical engineering involved in sensor development, to running a clinical trial, and, finally, to the intensive data science and algorithm development necessary to make sense of our data. This project has provided me with immense intellectual growth and stimulation throughout the years. I had no idea what magnetic resonance was when I first joined your lab and have, in the years since, fallen in love with its beauty, elegance, and power.

Thank you to my thesis committee chair, **Prof. Elfar Adalsteinsson**, for the incredible support. I met Elfar early in my graduate career and he shaped it for the better. Elfar introduced me to various people in the MRI world, encouraged me to submit to ISMRM for the first time, and generally taught me a lot about MRI.

Thank you to my thesis committee member, **Prof. Matt Rosen**, for the great ideas and advice. Matt has the rare ability to give advice across logarithms of scale: from the granular “let’s sit down and program this pulse sequence together”, to broad advice about career and life. I get excited and energized about the future of MR every time I talk to Matt.

Thank you to my committee member and clinical collaborator, **Dr. Kristin Corapi**. None of this clinical work would have happened without her. Thank you for believing in this project from the beginning, for teaching me how to do patient work in an academic hospital, and how to navigate the world of paperwork involved in IRB approvals and human-research.

Thank you to the **MGH Clinical Research Center (CRC)** as well my **MGH Nephrology** collaborators: Ravi Thadhani, Andrew Allegretti, Rayhnuma Ahmed, Dorrie Sullivan. A special thank you to Xavier Vela Parada for making our 5am start times much less painful than they would have otherwise been and for infecting everyone around him with his passion for medicine. Also, a special thank you to Denny Ausiello and Herb Lin for their support of this project throughout the years.

Thank you to Mary Sylvia-Reardon and the **MGH Dialysis Clinic** for opening your doors to our research and accommodating us into your busy space. Thank you to all of the MGH dialysis

nurses, especially the ones who came in on their off days to help us dialyze our study participants.

Thank you to my **radiology collaborators** across multiple institutions. Each of you taught me something (or many things) about MR and I am very grateful: Larry Wald, Jason Stockman, Clarissa Zimmerman Cooley,  $B_0$  Zhao, Pablo Garcia-Polo, Thomas Witzel, Andre van der Kouwe, John Kirsch, Larry White, Mary O'Hara,  $B_0$  Zhu, Neha Koonjoo, Jeff Stout, Patrick McDaniel, Kawin Setsompop, Atsushi Takahashi, Steve Shannon, Sheeba Arnold Anteraper, Mary Hochman, Deb Burnstein, Melissa Haskell, Giorgia Grisot, Cris LaPierre, and Martin Torriani.

Thank you especially to everyone from the **Martinos Center**. The Martinos Center is one of the largest MRI centers in the world and a very special place in the universe. It has the highest concentration of intelligence and helpfulness in one place that I have encountered to date.

Thank you to the **Cima Lab** and its collaborators on this project: Chris Vassiliou, Matt Li, Ashvin Bashyam, Chris Frangieh, Joanne Lee, Andrew Hall, Yasmin Siraj. Thank you to Lenny Rigione, Barbara Layne, and Wendy Brown for their hard work in keeping the lab running smoothly. Thank you to Dan Vong for his help with administration of our grants.

Thank you to the **statisticians** that I consulted over the course of my doctoral work from the Harvard IQSS (especially Simo Goshev and Steve Worthington), Harvard Catalyst, and the Koch Institute Core.

Thank you to my **funding** sources: Institute of Soldier Nanotechnologies, MIT-MGH Grand Challenges Grant (thank you to Charlie Sodini and David Louis for their continued support of this project), and the National Science Foundation's GRFP.

Of course, thank you to the many **patients** who volunteered for our studies throughout the years. We literally could not have done this without you. The desire to not let any of you down kept me going through the difficult times of this project.

Thank you to my **friends** for all of the great memories: my HST MEMP class, my Elm Street roommates (Isha Jain, Evi Van Itallie, Abbie Groff, Judith Lieberum - all soon-to-be doctors), Katerina Mantzavinou, Monica Stanciu, Adrian Dalca, Raj Banerjee, Angelica Ahrens, Lauren Friedman, Braveen Ragunathan, Nina Woolley Ragunathan, Priya Garg, and many others from both near and far.

Thank you to the **Harvard Ballet Company** and **MIT Chamber Music Society** for helping me do the things that keep me balanced. A giant thank you to **MIT Hacking Medicine** and all of its incredible members for some of the most memorable moments of my life and for bringing me into the epicenter of healthcare innovation.

Thank you to my mom – **Rita Avancini** – and my dad – **Jose Colucci** – for infecting me with their passions for discovery and invention. My mom is a biologist and my dad is an engineer and by showing me the beauty of their respective fields, they unknowingly set me down this path of biomedical engineering and hopefully changing healthcare for the better.

And finally, thank you to **Sidney R. Primas**. From our late-night conversations discussing my data to your encouragement when things were tough, you have supported me from across the country and from across the living room. You are brilliant and kind and hardworking and I could not be more grateful to have you in my life.

Thank you. <sup>1</sup>

---

<sup>1</sup> **A Final Note** Throughout my PhD, I would find myself sporadically looking up people's theses and reading through their acknowledgments page. In case there are others who do the same: to you, whoever you are, thank you for taking a look and I'll leave you with one of my favorite quotes:

“Some people see things as they are, and ask why. I dream of things that never were, and ask why not.”  
– Robert Kennedy / George Bernard Shaw

I hope you keep dreaming and asking, “Why not?”

# Contents

<b>1</b>	<b>Introduction</b>	<b>11</b>
<b>2</b>	<b>Background</b>	<b>13</b>
2.1	Applications of Relaxometry and Existing Quantitative MRI Studies . . . . .	14
2.2	Deconvolution Methods: Making Sense of Single-Voxel Measurements . . . . .	14
2.3	Portable Single-Voxel MR Sensors . . . . .	15
2.4	The Economic and Clinical Need for Fluid Monitoring . . . . .	16
2.5	MRI Relaxometry to Quantify Fluid Overload . . . . .	17
2.6	Future Vision for MR Sensors in Medicine . . . . .	17
<b>3</b>	<b>Dialysis Study: Overview</b>	<b>19</b>
3.1	Hemodialysis Patients: Expectation versus Reality . . . . .	20
3.2	Pilot Study: Overview and Conclusions . . . . .	20
3.3	Methodology . . . . .	21
3.4	Demographics . . . . .	23
<b>4</b>	<b>Dialysis Study: MRI</b>	<b>26</b>
4.1	MRI Methodology: Overall . . . . .	27
4.1.1	T2 MRI Scan of Upper Calf . . . . .	27
4.1.2	Analysis Workflow . . . . .	27
4.1.3	Regions of Interest . . . . .	27
4.2	Pixel-by-Pixel Analysis . . . . .	29
4.2.1	Methods: Fits and Model Selection . . . . .	30
4.2.2	Methods: Criteria for Discarding Fitting Results . . . . .	34
4.2.3	Methods: Calculating Pixel SNR . . . . .	49

4.2.4	Physiologic Meaning of Bi-exponential Fits . . . . .	56
4.2.5	Results . . . . .	58
4.3	ROI Bi-Exponential Analysis . . . . .	74
4.3.1	Methods . . . . .	74
4.3.2	Results and Discussion . . . . .	74
4.3.3	Conclusions . . . . .	84
4.4	ROI ILT Analysis . . . . .	88
4.4.1	Methods: The Inverse Laplace Transform (ILT) . . . . .	88
4.4.2	Methods: L-Curve Criterion . . . . .	89
4.4.3	Methods: Applying the ILT and Post-Processing . . . . .	94
4.4.4	Results and Discussion . . . . .	96
<b>5</b>	<b>Phantom Studies</b>	<b>109</b>
5.1	Methods . . . . .	110
5.1.1	Phantoms and Ex-Vivo Tissues Experiment . . . . .	110
5.1.2	Agar Phantoms Experiment . . . . .	110
5.1.3	Results and Discussion . . . . .	110
5.2	Agar Experiment . . . . .	117
5.3	Contamination of T2 Measurement . . . . .	117
5.4	Conclusions . . . . .	121
<b>6</b>	<b>Dialysis Study: MR Sensor</b>	<b>123</b>
6.1	MR Sensor Methodology . . . . .	124
6.1.1	MR Sensor Hardware . . . . .	124
6.1.2	MR Sensor Pulse Sequence . . . . .	124
6.1.3	MR Sensor Set-up in the Hospital . . . . .	127
6.1.4	MR Sensor Data Analysis . . . . .	127
6.2	Results and Discussion . . . . .	129
6.2.1	3-Exponential Analysis . . . . .	129
6.3	Necessary ROI Size to Separate Fluid Overload Patients from Healthy Controls . . . . .	131
6.4	ILT Analysis . . . . .	139
6.4.1	Individual Subjects . . . . .	139
6.4.2	Group Averages . . . . .	144

<b>7</b>	<b>Conclusions</b>	<b>149</b>
<b>8</b>	<b>Recommended Next Steps</b>	<b>154</b>
8.1	Analyze Additional Dialysis Study Data . . . . .	154
8.2	Low Field Scanner Measurements . . . . .	155
8.3	Healthy Human Study . . . . .	156
8.4	2-D Relaxometry Measurements . . . . .	156
8.5	Apply EPG-correction Methods to CPMG data . . . . .	157
<b>A</b>	<b>Analysis Workflow</b>	<b>162</b>

# Chapter 1

## Introduction

Magnetic resonance imaging (MRI) has transformed the way medicine is practiced since its development in the 1970s<sup>1,2</sup>. MRI enables physicians to take detailed images of the inside of the human body without any ionizing radiation or known harmful effects. While the majority of MRI scans are qualitative, the root of its unparalleled soft-tissue contrast is actually quantitative.

Quantitative biomarkers –  $T_2$  and  $T_1$  relaxation times, diffusion, and proton density, among others – give origin to the different shades of grey in a standard MRI image. Quantifying these metrics (called relaxometry parameters) provides information about the molecular environment being measured.

The birth of MRI began in the quantitative realm. From the first measurement of nuclear induction in 1945 through the next three decades, the magnetic resonance (MR) research community discovered various types of relaxometry parameters and techniques with which to measure them<sup>1,3-5</sup>.

When computing power advanced such that Fourier transforms could be done in a time-effective manner, however, imaging – in other words, MRI – became the new focus of the MR community<sup>1,2</sup>. Research into quantitative MR biomarkers became less popular and generations of radiologists learned to interpret MRI images qualitatively.

Recently, however, the development of a novel imaging technique called MR Fingerprinting (MRF) that enables rapid quantification of multiple relaxometry parameters has sparked renewed interest in the quantitative biomarker space<sup>6</sup>. Hundreds of MRF papers have been published in the 5 years since the original paper<sup>1</sup>. Quantitative biomarkers already have many diagnostic uses, such as monitoring progression of multiple sclerosis, assessing iron overload in the liver, and identifying

---

<sup>1</sup>At the time of writing, there are over 350 citations of Dan Ma's original 2013 paper.

brain tumors<sup>7-9</sup>. More clinical applications for relaxometry continue to be discovered, especially with the increased attention on relaxometry due to the invention of MRF.

We became interested in using relaxometry to measure fluid levels in the body. There are many conditions like congestive heart failure and chronic kidney disease where the body's normal fluid homeostasis mechanisms are not functioning properly<sup>10-12</sup>. These patients accumulate liters of excess fluid and their organs begin to shut down after a certain point. Surprisingly, in the diagnostic toolkit of the 21st century physician, there are no good tools for assessing a patient's volume status.

Physicians estimate fluid levels through a variety of methods that are either invasive, non-specific, or insensitive. Thousands of medical errors and billions of dollars of unnecessary expenditure occur annually due to improper fluid management<sup>10,13-18</sup>.

Most of MR signal in body comes from water molecules so we hypothesized that MRI was a good modality for assessing fluid status<sup>19</sup>. There have been a few one-off studies with MRI to assess fluid overload<sup>20-23</sup>, but no researcher to our knowledge has seriously explored the potential of MR to monitor hypervolemia. We understand the reasons for this - an MRI scan is expensive and time-consuming. It does not make sense to use multi-million-dollar MRI scanners for routine volume measurements. We, however, believed that we had a way around this.

We hypothesized that we could get the same diagnostic information about fluid levels in the body using a single-voxel (i.e. non-imaging) MR sensor as with an MRI. We developed an MR sensor that measured quantitative relaxometry parameters in the body but did not generate images. Removing the need to generate images made the hardware smaller, faster, and cheaper<sup>24,25</sup>.

There are fields that already use single-voxel relaxometry techniques. The oil industry uses single-voxel relaxometry to determine where to drill for oil<sup>26-28,28-30</sup>. The food quality control industry uses it to determine oil and moisture content of foods<sup>31-33</sup>. Airport security uses it to determine if a fluid is explosive or not<sup>34,35</sup>. These industries have harnessed the power of single-voxel MR sensors as a rapid, quantitative, and non-invasive measurement. We believe medicine could benefit from MR sensors as well.

First, we used MRI to discover how fluid physiology manifests in MR measurements. Second, we performed phantom studies to understand how to translate results from MRI to a single-voxel MR sensor. Finally, we collected data with our custom MR sensor on hypervolemic patients.

Our goal is for this doctoral work to be the beginning a future where the diagnostic potential of MR is brought out of multi-million MRI suites to the patient bedside, and, eventually, to the patient's home.

## **Chapter 2**

# **Background**

This chapter introduces background on the various building blocks of this doctoral work. First, we discuss the current diagnostic applications of relaxometry and single-voxel relaxometry techniques. Next, we reveal the economic and clinical need for fluid monitoring. And, finally, we introduce the vision of how MR sensors will be used in clinical medicine in the future.

## 2.1 Applications of Relaxometry and Existing Quantitative MRI Studies

Relaxometry refers to the quantitative measurement of  $T_2$ ,  $T_2^*$ , and  $T_1$  relaxation times, all of which reflect different information about the proton environment. Quantitative magnetic resonance imaging (qMRI) measurements have long been a goal of the field of MR but there are many challenges in taking these measurements including long measurement times, radiofrequency (RF) coil imperfections, differing analysis techniques, and more.

Despite these challenges there is ample relaxometry research and this research was further fueled by the recent development of a novel acquisition technique called magnetic resonance fingerprinting (MRF), which enables qMRI measurements to be taken much faster than ever before<sup>6</sup>.

Relaxometry measurements have important diagnostic applications to a wide variety of diseases. In multiple sclerosis, brain tumors, stroke, and epilepsy, relaxometry measurements are used to monitor disease progression and help differentiate between healthy and pathological tissue that might otherwise be missed visually<sup>7</sup>. Relaxometry is used to measure iron overload in the body (i.e. hemochromatosis, sickle cell disease, etc.) and this approach has replaced gold-standard biopsy procedures in many hospitals<sup>7</sup>. Cartilage diseases (osteoarthritis and other degenerative diseases) can be detected earlier and non-invasively monitored through relaxometry<sup>7</sup>. Additional relaxometry applications include monitoring tumor, inflammation, heart attacks, and more. Relaxometry measurements reveal information about the physical properties of water molecules, which, in turn, reveal information about the in vivo tissue and its possible pathologies, such as fluid overload.

## 2.2 Deconvolution Methods: Making Sense of Single-Voxel Measurements

Images are not necessary to obtain quantitative relaxometry measurements. Single-voxel measurements can be taken and interpreted through deconvolution algorithms. Relaxation times are modeled as exponentials and in vivo systems are often multi-exponential in nature. Multi-exponentially originates from water compartmentation within a single tissue (i.e. intracellular vs. extracellular water in muscle) or from multiple tissues with distinct fluid environments (i.e. fat and muscle measured together) within a single voxel. Distinct water compartments are created when water molecules do not move between two spaces during the time frame of the measurement. If molecular exchange of water is slow compared to the measured relaxation time, then distinct relaxation times are measured. On the other hand, if molecular exchange of water is fast and water molecules are moving between the two spaces during the measurement, a single relaxation time is measured.

In vivo systems can be modeled as sums of individual exponentials where each amplitude relates to the relative volume fraction of that water compartment and each relaxation time relays information about the type of fluid environment (tissue type). There are many ways to “deconvolve” this multi-exponential data to obtain the constituent exponentials. Two of the most common methods are non-linear least squares fitting (NLLS) and an inverse Laplace transform (ILT). NLLS fitting requires fitting the data to a pre-determined number of exponentials. It is fast and provides a stable fit, but choosing the appropriate number of exponentials can be difficult in biological systems<sup>36</sup>.

ILT is a robust technique that can be used to resolve the number, time constants, and volume fractions of individual components in multi-exponential data without pre-defined models or a priori assumptions. The ILT generates a relaxogram – a probability distribution function of relaxation values present in the data - where the area under a peak is proportional to the number of protons (volume) in the sample with a specific relaxation value. Comparing the different peak locations and areas under the curve over time allows one to assess complex water distribution changes within the system<sup>37</sup>. The drawbacks of the ILT algorithm are long computing times and challenges in determining an appropriate smoothing factor for the computation.

A smoothing factor is a required input to the ILT algorithm that compromises accuracy and stability. The ILT inversion is an ill-defined problem with multiple possible solutions, especially in the presence of noise<sup>38,39</sup>. Repeating the inversion multiple times may yield multiple different results. The smoothing factor aims to stabilize the fit to make it repeatable, but it will do so at the expense of accuracy. The L-curve criterion, cross validation, and the chi-squared criterion test are just some of the regularization methodologies to find the optimal smoothing factor for any given dataset<sup>25,40,41</sup>. Various algorithmic techniques exist for deconvolving multi-exponential data, which make it possible to monitor individual fluid compartments from single-voxel quantitative relaxometry measurements.

### **2.3 Portable Single-Voxel MR Sensors**

Portable magnetic resonance sensors that take single-voxel measurements have been used for decades in fields like oil logging and food quality control. The oil industry has developed “inside out” magnets that can be dropped in oil wells to determine the rock composition and oil/water quantity and quality<sup>28,28,30</sup>. The first pulsed-MR magnets for oil applications were deployed in the early 1990s by the NUMAR and Schlumberger Corporations<sup>29</sup>.

The NMR MOUSE (MOBILE Universal Surface Explorer) was developed in 1996 for noninvasive investigation of arbitrarily shaped objects that do not fit within the bore of a traditional cylindrical NMR scanner<sup>42</sup>. Eidmann et al. built this small 2.5kg surface scanner to illustrate that MR signals could be measured by an inhomogeneous  $B_1$  field perpendicular to an inhomogeneous  $B_0$  field<sup>42</sup>. Variations on this initial NMR MOUSE have been built including the NMR MOLE (Mobile Lateral Explorer) and other single-sided probes<sup>43</sup>. Benchtop MR sensors like the Bruker Minispec or SpinSolve series exist for animal testing and/or food quality control<sup>44</sup>. The Magritek Terranova uses Earth's magnetic field for measurements<sup>45</sup>. Because of inhomogeneities in the  $B_0$  and  $B_1$  fields in these sensors, single- and multi-echo techniques such as Hahn echoes and spin echoes are typically employed for measurements<sup>46</sup>. These single-voxel MR sensors provide similar information as quantitative MRI scans for a fraction of the cost and size. We have built portable MR sensors for human measurements.

## 2.4 The Economic and Clinical Need for Fluid Monitoring

Maintenance of fluid balance in the body is critical to physical and cognitive function yet no accurate and practical assessment method currently exists. Proper fluid management is compromised in patients with kidney disease, heart failure, and sepsis; it is also critical for competitive athletes, soldiers, and the elderly. Current approaches rely on indirect measures that are subjective or invasive measures that cannot be routinely performed<sup>47</sup>. These methods include blood and urine chemistry, bioimpedance, and radioisotope dilution. All are either invasive, require a lab, or are not clinically reliable<sup>47,48</sup>. Thousands of medical errors and billions of dollars of unnecessary expenditure occur annually due to improper fluid management in the US<sup>13-15,49</sup>.

This project specifically works on monitoring fluid overload, a symptom commonly encountered in patients with heart or kidney failure. Fluid overload is a physiological state in which the body's water and sodium homeostasis mechanisms are not functioning and the body accumulates fluid through various vicious downward spiraling mechanisms.

Heart failure (HF), for example, is a chronic condition in which the heart is unable to pump sufficient blood to meet the body's metabolic demands<sup>50-54</sup>. HF leads to over \$39 billion in health costs – equivalent to 1-2% of the total US healthcare spending – of which 60% is attributable to hospitalizations<sup>55,56</sup>. Hospitalization is generally precipitated by dyspnea, which is an advanced symptom of fluid overload (congestion)<sup>53,57</sup>. Catheterization to assess filling pressures of the heart

is the clinical gold standard for determining fluid status of HF patients, but the procedure is invasive and carries risks so it is not performed on every patient<sup>57-59</sup>. Hospitalized patients are generally discharged when their symptoms improve, which does not necessarily mean their underlying volume overload has been fully treated. It is thought that untreated fluid overload is the reason for frequent hospital readmissions<sup>57</sup>. The Affordable Care Act's mandate for reducing hospital readmissions of HF patients underscores the need for an accurate, noninvasive way to assess volume overload in HF patients<sup>58-60</sup>. MR measurements are a direct, noninvasive method to quantify water in tissue. In addition, portable MR sensors make this measurement possible in the clinic, home, or field.

## **2.5 MRI Relaxometry to Quantify Fluid Overload**

MR relaxometry provides a direct measure of water volumes and environment. MR directly measures hydrogen in water molecules, which improves the sensitivity of MR to fluid measurements compared to other methods, like bioimpedance, where water is not directly measured. In fact, in a head-to-head comparison of MRI versus bioimpedance spectroscopy for muscle hydration measurements, MRI was found to have greater reliability<sup>61</sup>. Studies using MRI have quantified fluid status using relaxometry measurements, including that: relaxation times were correlated with peripheral edema in rats<sup>21,62,63</sup>,  $T_1$  and  $T_2$  relaxation times of the calf subcutaneous tissue was higher in fluid overloaded patients than in healthy volunteers<sup>20,23,64</sup>, and  $T_1$  and  $T_2$  changes in the calf tracked with fluid changes for single individuals over time<sup>20,22,65,66</sup>. Our goal was to translate these MRI findings correlating relaxometry measurements to fluid levels into affordable and convenient bedside MR sensors.

## **2.6 Future Vision for MR Sensors in Medicine**

Physiological sensors will play a critical role in bringing about a new paradigm of distributed, continuous, and preventative care as healthcare becomes less centralized and dependent on episodic and reactionary care<sup>67</sup>.

Medicine has long considered quantitative MR relaxometry to be a holy grail but the imaging scans to obtain these measurements are prohibitively time consuming to be used in regular clinical practice<sup>6</sup>. Non-medical fields, on the other hand, such as oil logging and food quality control have used portable MR systems to take quantitative measurements for many years<sup>25,26,31,34,35</sup>. By

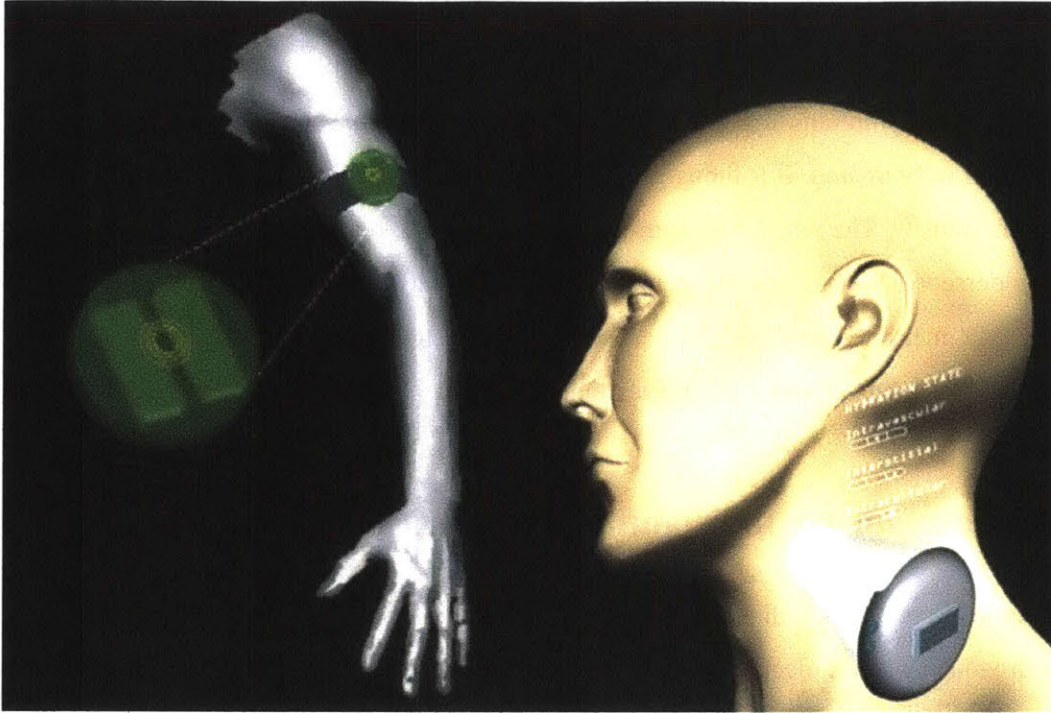


Figure 2-1: The future of MR sensors. These drawings imagine a future in which NMR sensors are fixtures in the doctor's office for assessing the full spectrum of hydration states, from dehydration to congestive heart failure.

bringing these areas together, portable, quantitative MR sensors will have applications to many clinical diagnostic areas including malignancies (breast/skin cancer), musculoskeletal diseases (lymphedema, muscular inflammatory diseases), and physiological measurements (fluid monitoring)<sup>20,63,68,69</sup>. MR is well suited for quantifying fluid since MR signal in the body comes largely from water molecules.

The ability to robustly quantify fluid accumulation in the body will have tremendous cost and care improvement implications for CHF, CKD, sepsis, hospital critical care situations, and more. Early identification of congestion can prompt medication interventions that prevent hospitalization, improve patient outcomes and decrease healthcare expenditures. Furthermore, this project represents a step towards a future in which the diagnostic power of MR can be harnessed through portable sensors in the doctor's office or patient home instead of being solely available through expensive and time-consuming MRI scanners (Figure 2-1). We envision a future where the measurement of fluid status is as ubiquitous as that of the other vital signs.

## Chapter 3

# Dialysis Study: Overview

This chapter introduces the Dialysis Study – a four year-long endeavor – which constituted the bulk of my doctoral work.

The Dialysis Study consisted of two portions. The first, which came to be called the “pilot study,” was an 8-month period of data collection on 26 dialysis inpatients. In the pilot study, we measured patients’ upper calves with the commercially-available NMR MOUSE<sup>46</sup> and their fingers with the Cima Lab’s custom finger MR sensor<sup>1</sup>. The data on this cohort did not include MRI scans and was collected exclusively at the Massachusetts General Hospital (MGH) Dialysis Clinic on inpatients who had been admitted to MGH for reasons unrelated to our study. There is a short section in this chapter that summarizes our learnings from this pilot study.

The second portion of the Dialysis Study was conducted over the span of 2.5 years on 7 dialysis outpatients and 7 healthy controls. This second portion included measurements with both an MRI and the Cima Lab’s custom single-sided sensor (the NMR MOUSE was no longer used). From here on, except when stated otherwise, the term “Dialysis Study” will refer to this second portion of our work. This second portion was the more fruitful of the two portions because it incorporated our learnings from the pilot and had side-by-side MR sensor and MRI data, which proved invaluable in helping us make sense of the MR sensor data.

The motivation, methodology, and demographics of the Dialysis Study will be introduced in this chapter.

---

<sup>1</sup>The Cima Lab bought one of the first NMR MOUSE sensors that Magritek ever produced.

### **3.1 Hemodialysis Patients: Expectation versus Reality**

We chose to work with end-stage renal disease (ESRD) patients who are treated with hemodialysis (HD) (herein referred to as dialysis or HD patients for brevity) in order to test our hypothesis that MR relaxometry could be used to assess fluid levels. HD patients experience large fluid losses (1-4L) in a short period of time (3-4 hours). This would enable us to do pre- and post-measurements on the same person at very different fluid states within a single day.

In hindsight, HD patients had much more complex physiology, particularly during dialysis, than we had anticipated. For example, when patients are initially connected to the machine they experience hemodilution as approximately 300cc's of saline are delivered intravenously over a few seconds. Over the course of dialysis, patients lose fluid at varying rates, depending on their clinical status. At the end of dialysis, patients experience an increase in fluid volume (but not hemoconcentration or dilution) as the blood that is present in the dialysis machine tubing is returned to their body.

Additional complexities we encountered in working with an HD patient population included a discrepancy between weight loss and the machine-reported ultrafiltration volume, the fact that we did not know (and, in fact, the nephrology community does not know) the location where fluid was being pulled from in patients' bodies, and that we did not know what sorts of vascular adaptations occur over time to dialysis patients.

Despite being more challenging than we had anticipated, working with ESRD patients treated with dialysis did fit our goal of working with a population that experienced large and rapid fluid losses. We made several interesting discoveries about how fluid physiology shows up in MR data.

### **3.2 Pilot Study: Overview and Conclusions**

A pilot study was conducted with 26 hemodialysis inpatients at MGH across an 8-month period during 2015. Our conclusions from this pilot study were as follows:

1. We can detect the initial saline fluid bolus in the finger data in certain patients. This finding suggests that the finger sensor might be capable of measuring signal from the vascular fluid space.
2. We need a better leg sensor with a larger measurement voxel. The slice thickness of the NMR MOUSE was approximately 200um, which made it difficult to measure the same location

across different time points.

3. There was not a lot of lower-leg edema in the cohort: only one patient had lower-extremity edema detectable on physical exam.
4. Weight change and the ultrafiltration volume reported on the dialysis machine do not always match. Occasionally, the two values were very different.
5. There are potential gender differences between males and females, particularly in the finger sensor measurements

### **3.3 Methodology**

This section contains a description of the overall Dialysis Study methodology. Details about the specific measurement and analysis techniques are included in the following chapters.

#### **Recruitment and Consent**

Maintenance hemodialysis (HD) outpatients and age-matched healthy controls were recruited for the study. HD patients were recruited from both the pilot study as well as area clinicians. Healthy controls were recruited through email advertisement. Enrollment was limited to males over the age of 25 years, with a BMI between 18.5-40, without a pacemaker or metal implants, without severe anemia (Hgb < 7.5mg/dL), and without amputations (other than finger or toe amputations). In earlier pilot studies, potential gender differences were observed with the portable MR sensors therefore participation in this trial was limited to males. Furthermore, healthy control subjects could not have renal, cardiac, or other chronic diseases and were age-matched (to the decade) to HD subjects. The study was approved by the Partners Healthcare's Institutional Review Board (IRB) and written, informed consent was obtained from each participant by a member of the study staff. A translator was used when necessary.

#### **Arrival and AM MRI Scan**

Volunteers arrived at the Martinos Center (Charlestown, MA) either by their own transportation or by a taxi arranged by the study staff. Subjects underwent MRI scans of their upper calf and index finger on the side of their body that was contralateral to their dialysis access (or right side for healthy controls) for 0.75-1 hour.

The study team and the participant then commuted to MGH's main campus to either the MGH Dialysis Unit (Bigelow 10) or the MGH Clinical Research Center (CRC, White 12) depending on space availability on that day.

## **MGH Main Campus**

HD patients received their usual hemodialysis treatment (3-4 hours) with an ultrafiltration volume prescribed by the nephrologist on staff to attain their set dry weight. Healthy controls (HCs) sat (in a reclined supine position) on a hospital stretcher for 4 hours. All subjects were given the option of a to-go snack before returning to the Martinos Center for the second MRI. All intake and output was recorded for each participant during the 4 hour study interval.

## **Pre- and Post- Measurements**

The following set of measurements were taken on every study participant at both arrival and discharge:

- A standing weight (average of 3 measurements)
- Baseline vital signs (pulse, blood oxygenation, blood pressure) taken by a nurse
- Baseline  $T_2$  measurements of the right upper calf with the Cima Lab's custom single-sided MR sensor (the same anatomical location that was measured with the MRI). Details of the sensor are described in section 6.1.1.
- Baseline  $T_2$  measurements of the right index finger with the Cima Lab's custom bore MR sensor (again, same anatomical location that was scanned in the MRI)
- Bioimpedance measurements of the whole body (wrist-to-ankle electrode placement) and leg (upper calf-to-lower calf electrode placement)
- Length and circumference measurements of the lower leg and finger
- (When possible for dialysis patients) Crit-line measurements were downloaded at the end of the treatment

## **Blood Work**

All subjects had blood drawn at the beginning of the 4 hour study interval to measure: serum sodium, blood urea nitrogen (BUN), creatinine, complete blood count (specifically, hemoglobin and hematocrit), serum osmolality, and brain natriuretic peptide (BNP). This was the only blood work

done on healthy controls. ESRD patients had additional labs collected before and after dialysis for routine labs need by dialysis staff and blood to save in a bio-repository.

### **Hourly Measurements**

The following measurements were taken hourly during the subjects' prescribed dialysis treatment or for the duration of the 4hr period of bedrest: (1) upper calf  $T_2$  measurements with the single-sided MR sensor, (2) index finger  $T_2$  measurements with the bore MR sensor, and (3) whole body and leg bioimpedance measurements, and (4) vital signs (pulse, blood pressure, blood oxygenation).

### **PM MRI**

After completion of dialysis or designated 4 hour period of bed rest was complete at MGH, the study team and participant returned to the Martinos Center for a second set of identical MRI scans as was done upon arrival.

### **Deviations of Study Protocol**

Two dialysis subjects did not finish the second PM MRI scan. For one patient this was due to him feeling unwell, which is normal for him after dialysis. For the other patient, there were timing delays earlier in the day and the MRI scanner was reserved after us, which meant we could not finish the full set of scans.

### **Notes**

Only the leg MRI and leg MR sensor data were analyzed in this thesis. We recommend that future researchers analyze the additional data that was collected in this study.

## **3.4 Demographics**

The demographics of the study cohort is summarized in Table 3-1. Healthy controls (n=7, n=6 unique individuals, mean age  $54.2 \pm 4.9$ ) were well age-matched to dialysis patients (n=7, n=5 unique individuals, mean age  $55.1 \pm 10.3$ ). Dialysis patients had elevated BUN, creatinine, and BNP levels, as is expected due to their end-stage renal disease.

Healthy control 2 (HC02) was dehydrated at the start of the study based on his serum osmolality and serum sodium levels. We expect that HC02 got progressively more dehydrated since healthy controls were not permitted to eat or drink anything during the 4 hours of the study.

Healthy control 6 (HC06) was tending towards dehydration at the start of the study based on his serum osmolality and sodium levels. HC06 was remarkable because, unlike the other subjects, he did not have a “to-go snack” after the 4 hour study interval, before returning for the second MRI. We therefore believe he was dehydrated during the second MRI scan, having not replenished the fluids he lost during the 4 hours of no eating or drinking.

Subject	Age (yrs)	Race	BMI (kg/m <sup>2</sup> )	Fluid Loss (kg)	Fluid Loss (%)	Sodium (mmol/L)	BUN (mg/dL)	Creatinine (mg/dL)	WBC (x10e3/uL)	Platelets (x10e3/uL)	Osmolality (mOsm/kg)	BNP (pg/mL)
<i>Ref Range</i>			<i>18.5-24.9</i>			<i>134-144</i>	<i>6-24</i>	<i>0.76-1.27</i>	<i>3.4-10.8</i>	<i>150-379</i>	<i>275-295</i>	<i>0-100</i>
HC01	52.3	White	21.38	0.5	0.7	141	7	0.62	5.9	321	286	
HC01b	53.7	White	21.02	0.3	0.4	141	12	0.73	4.9	275	286	16
HC02	47.4	Asian	25.71	0.9	1.3	144	18	0.8	2.3	240	302	12.1
HC03	63	White	32.36	0.8	0.8	137	18	1.13	8	374	287	11.8
HC04	55.1	White	20.14	0.4	0.7	140	20	0.88	4.9	264	297	25.8
HC05	58.3	White	30.05	0.6	0.7	139	20	0.62	4.8	118	289	21.6
HC06	49.8	White	24.84	0.4	0.5	142	17	0.81	3.9	195	294	23
<b>Mean</b>	<b>54.2</b>		<b>25.1</b>	<b>0.6</b>	<b>0.7</b>	<b>140.6</b>	<b>16.0</b>	<b>0.8</b>	<b>5.0</b>	<b>255.3</b>	<b>291.6</b>	<b>18.4</b>
(Std)	(4.9)		(4.4)	(0.2)	(0.3)	(2.1)	(4.4)	(0.2)	(1.6)	(77.1)	(5.8)	(5.4)
HDMRI01	62.9	White	30.23	0.8	1	142	61	7.05	7.19	127	312	4120
HDMRI01b	63.6	White	26.6	0.5	0.7	139	54	7.19	8.17	120	303	8815
HDMRI02	57.5	Multiple	24.96	1.8	2.3	137	53	7.93	6.97	140	308	3449
HDMRI02b	58	Multiple	27.62	2.1	2.7	139	48	9.02	5.55	109	307	15095
HDMRI03	64.5	Asian	22.78	3.7	5.3	138	92	11.44	9.26	189	312	7569
HDMRI04b	42.6	Multiple	38.56	3.6	3	141	52	9.66	8.37	230	311	2947
HDMRI05	36.2	White	23.6	2.5	3.1	138	47	5.71	7.93	375	301	608
<b>Mean</b>	<b>55.1</b>		<b>27.8</b>	<b>2.2</b>	<b>2.6</b>	<b>139.1</b>	<b>58.1</b>	<b>8.3</b>	<b>7.6</b>	<b>184.3</b>	<b>307.7</b>	<b>6086.1</b>
(Std)	(10.3)		(5.0)	(1.2)	(1.4)	(1.6)	(14.5)	(1.8)	(1.1)	(87.4)	(4.1)	(4495.9)

Figure 3-1: Summary of demographics for the dialysis study cohort. Values for healthy controls (HC) at the top of the table and dialysis patients (HDMRI) at the bottom. Blood values were from draws done at the start of the study. Healthy controls were well age-matched to dialysis patients. Dialysis patients had larger BMIs and experienced larger fluid losses than healthy controls.

## Chapter 4

# Dialysis Study: MRI

This chapter presents the specific methodology and data of the MRI portion of the dialysis study. Two types of analysis were performed on the MRI data:

1. **Pixel-by-Pixel Analyses:** bi-exponential fits were performed on *each pixel* of the MRI image.
2. **ROI Analyses:** data from pixels of a single tissue type were averaged together into a single  $T_2$  decay curve. The average decay curves were then processed with bi-exponential or inverse Laplace transform (ILT) fits.

This chapter first presents details of the overall MRI methodology and then discusses the two types of analysis separately. The algorithms and statistical techniques used to analyze the MRI data and later the MR sensor data are introduced and described in this chapter.

## 4.1 MRI Methodology: Overall

### 4.1.1 T2 MRI Scan of Upper Calf

Quantitative  $T_2$  MRI scans of the upper calf were obtained on a 1.5T Siemens Avanto Scanner (software version Syngo MR  $B_17$ ) and CP extremity coil at Bay 2 of the Martinos Center's (Charlestown, MA). The scan (se2d32) had parameters TR 3300ms, TE 8ms, 32 echoes, 1 average, 4 slices of 5mm thickness with 60% spacing (3mm) between slices, 192x144 matrix (75% phase FOV), 1x1mm in-plane pixel resolution, and a total acquisition time of 7 minutes 53 seconds.

The right upper calf was positioned at the center of the extremity coil using padding when necessary. A localizing capsule was placed on the lateral side of the calf at the same location that the MR sensor would measure. The sagittal scans were taken such that the capsule appeared in every slice. Phantoms were placed on top of the calf and padding was placed around everything to limit both phantom and leg movement. The scans were exported as magnitude Dicom images (Siemen's IMA format). The same scan was performed both before (AM) and after (PM) the 4-hour study interval, approximately 5-6 hours apart. The AM scans started between 7-9am.

### 4.1.2 Analysis Workflow

The raw Dicom images from the scanner were converted to Nifti format with FreeSurfer (Martinis Center, Charlestown, MA), regions of interest (ROIs) were hand-drawn on each slice of each scan using FSLEyes (and the older version, FSLview) (Paul McCarthy, University of Oxford, Oxford, UK), and all further analysis was performed in Matlab 2017b (The Mathworks, Inc.). All processing scripts are available on this project's Github repository and the analysis workflow is detailed in Appendix A.

### 4.1.3 Regions of Interest

The following regions of interest (ROIs) were hand-drawn on each slice of each scan using FSLEyes (Figure 1.1):

- **Muscular Tissue** - includes muscle, fascia, nerves, and blood vessels. ROIs of the following sub-regions of the muscle were drawn on slice 1 of each scan:
  - **Gastrocnemius** (both medial and lateral heads)
  - **Soleus**

- **Deep Posterior** (included flexor hallucis longus, tibialis posterior, flexor digitorum longus)
- **Anterior** (included tibialis anterior, extensor hallucis longus, extensor digitorum longus)
- **Lateral** (included peroneus brevis and peroneus longus)
- **Subcutaneous Tissue** - includes skin, fat and blood vessels in the fat
- **Bone** - the bone in both tibia and fibula
- **Marrow** - the marrow in both tibia and fibula

A drawing of the anatomical structure of the lower leg is shown in Figure 4-2. An example of the hand-drawn ROIs are shown in Figure 4-1. These anatomical ROIs were drawn by Lina while referencing anatomy atlases, but would likely benefit (especially the sub-muscle ROIs) from a check by a radiologist.

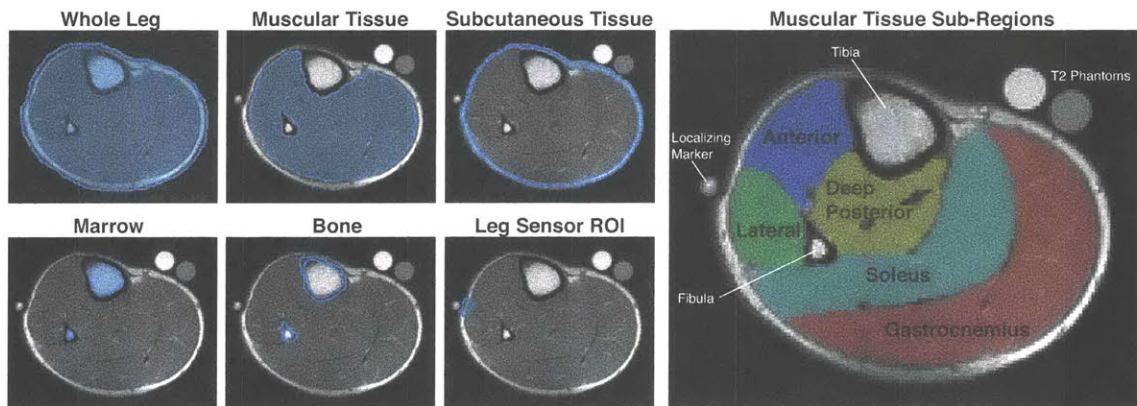


Figure 4-1: Visual depiction of the ROIs that were drawn on each of the MRI scans.

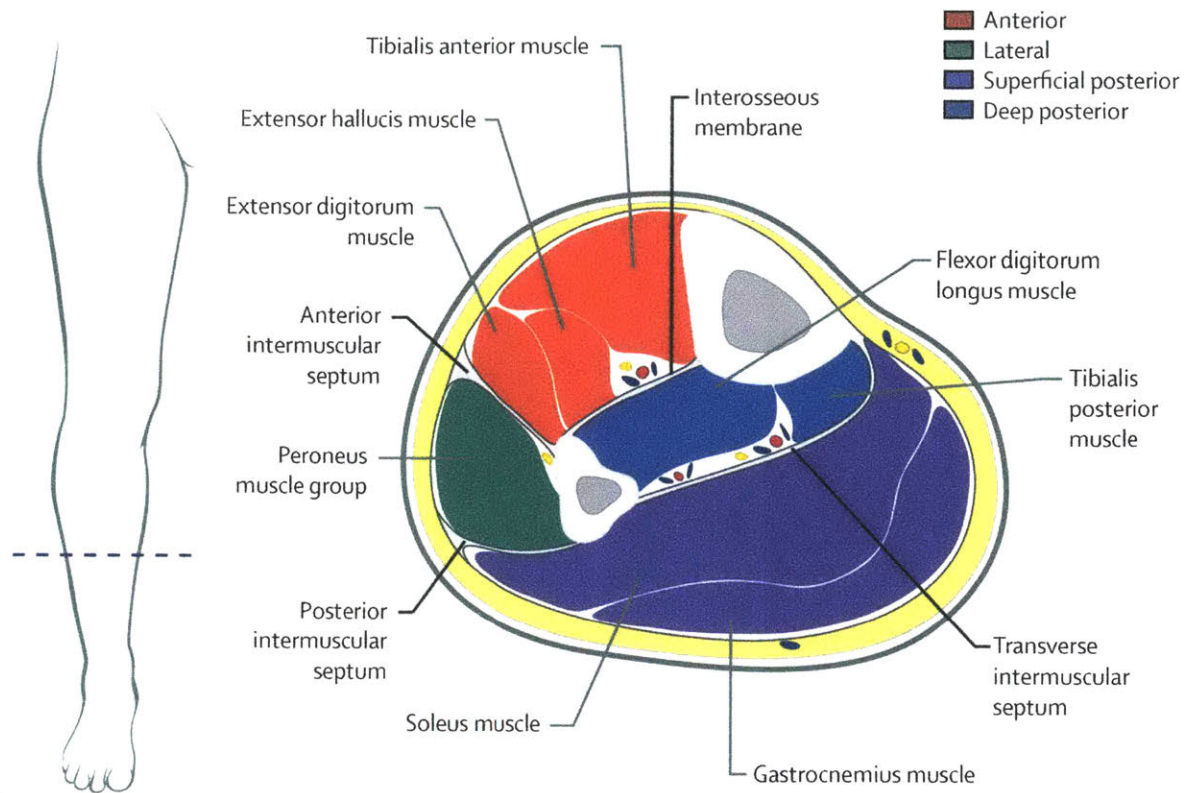


Figure 4-2: Transverse anatomy of the lower leg. [Source: The Lancet].

## 4.2 Pixel-by-Pixel Analysis

The following section discusses the methodology for analyzing the MRI data in a pixel-by-pixel manner. It contains the following sub-sections:

- Methodology: Fits and Model Selection
- Criteria for Discarding Fit Results
- Methods for Calculating Pixel SNR
- Results
  - Relaxation Times
  - Relative Amplitudes
- Discussion and Conclusions

## 4.2.1 Methods: Fits and Model Selection

### Bi-Exponential Fits

The  $T_2$  MRI images were analyzed by fitting each pixel on each slice with a bi-exponential decay:

$$\text{Bi-Exponential Fit} = \text{Amp}_1 * e^{-\frac{\text{time}}{T_2\text{RelaxationTime}_1}} + \text{Amp}_2 * e^{-\frac{\text{time}}{T_2\text{RelaxationTime}_2}} \quad (4.1)$$

The starting values used for the 2-exponential fit were [1500, 50, 1500, 210] for the amplitude 1,  $T_2$  relaxation time 1, amplitude 2, and  $T_2$  relaxation time 2, respectively. The upper and lower limits for the fittings were set to 10,000 and 0, respectively. We used a non-linear least squares fitting method with a Trust-Region algorithm to perform the fits.

The first amplitude and relaxation time are referred to as the *short component*, and the second amplitude and relaxation time are referred to as the *long component*. Relaxation time 1 is always lower than relaxation time 2. The physiological meaning of the components is discussed in section 4.2.4.

After the fits were completed, fit results were discarded if certain criteria were met (see section 4.2.2). Various histograms and cumulative distribution functions (CDFs) of the remaining fit values were generated and statistics were calculated.

### Verifying Model Section

We utilized the extra sum-of-squares F-test, or simply F-test, to determine the optimal number of exponentials that should be used to model the data<sup>70</sup>. The test compares two nested models where one model is a simpler version (i.e. certain parameters are set to zero) of the other. The F-test determines whether the additional parameters, which yield a decrease in degrees of freedom, of the more complex model is worth the reduction in residuals (sum of squares) that it achieves. The relationship between the relative increase in sum-of-squares and relative increase in degrees of freedom is expressed as an F ratio:

$$\text{Sum of Squares} = SS = \sum_{i=1}^n (y - y_i)^2 \quad (4.2)$$

$$F \text{ ratio} = \frac{\frac{SS1-SS2}{SS2}}{\frac{DF1-DF2}{DF2}} = \frac{\frac{SS1-SS2}{DF1-DF2}}{\frac{SS2}{DF2}} \quad (4.3)$$

where  $y$  is the true value of the data,  $y_i$  is the value predicted by the model, and  $DF$ , or degrees of freedom, is defined as  $n - m$  where  $n$  is the number of data points and  $m$  is the number of parameters in the model.

We expect the F ratio to be close to 1 if the simpler model is correct. If the ratio is greater than 1, either (1) the more complicated model is correct, or (2) the simpler model is correct but random chance led the complex model to have a better fit. The p-value tells us the chance of that second situation occurring by chance.

The p-value is obtained from an F distribution look-up table, which requires knowing the degrees of freedom of the numerator ( $DF1-DF2$ ) and denominator ( $DF2$ ) of the F ratio. The null hypothesis is that the simpler model is correct. If the p-value is large, we accept that the simpler model is correct. If the p-value is small, however, then we reject the null hypothesis and accept the more complex model. We set our p-value threshold to the traditional 0.05. Table 4.1 shows the F-test results for pixels in the muscular tissue, subcutaneous tissue, bone, and marrow.

The optimal model for fitting the MRI data is a bi-exponential decay across all tissue types, except for bone. Three-exponential fits are able to converge on certain pixels and occasionally they are deemed a better model by the F-test than a bi-exponential fit. However, all of the three-exponential fit results were deleted by one of the pixel discarding criterion discussed in section 4.2.2.

### **Rician Distribution Corrections**

In this section, we will briefly discuss our rationale for not performing Rician-distribution correction in our multi-exponential fits.

Noise in MRI data follows a Rician distribution due to the rectified nature of the signal (this is discussed in greater detail in section 4.2.3). For noisy MRI data, the image intensity in the pixels of interest is also governed by a Rician distribution<sup>71</sup>. In these situations, it is good practice to correct for the non-Gaussian distribution in order to reduce bias in one's results<sup>71,72</sup>. A Rician distribution is biased towards higher values and artificially decreased signal variance<sup>72</sup>. There is not a universally agreed upon definition of noisy MRI data, but the cutoff is defined as  $SNR < 2$  by some researchers and as  $SNR < 40$  by others<sup>72</sup>. Since 90% of our pixels had an  $SNR > 40$ , we would not gain much

<b>F-test Comparison of Multi-Exponential Fits for MRI Data</b>					
	SNR	Mono- vs Bi-exponential		Bi- vs 3-Exponential	
		F ratio	p-value	F ratio	p-value
Muscular Tissue	70.74	45.16	2.44E-09*	1.46	0.25
Subcutaneous Tissue	140.10	86.76	1.76E-12*	1.77	0.19
$B_{0ne}$	5.41	0.092	0.91	-7.45E-05	1
Marrow	130.11	60.88	9.87E-11*	7.50E-08	0.99

Table 4.1: F-test comparison of mono- versus bi-exponential and bi- versus 3-exponential fit for sample MRI data across multiple tissue types. A p-value  $< 0.05$  indicates that the more complex of the two models is correct. A bi-exponential fit was the correct model to use across all tissue types, except for bone.  $B_{0ne}$  had a very low SNR, which may have been the reason for a mono-exponential fit being better. The data shown in this table are from randomly chosen pixels in slice 1 of Healthy Control 1's AM scan. The results were verified across other patients and scans as well. A bi-exponential fit was the best model choice across all pixels that were tested, except for those located in the bone.

by performing a Rician distribution correction and therefore chose not to do so.

### Vertical Offset Term

In this section, we will discuss our choice to not include a vertical offset term in our multi-exponential fits.

A vertical offset is not usually included in multi-exponential analysis of biological data (none of these MRI method papers include nor mention an offset<sup>73-80</sup>), but it rarely *does* make an appearance in MRI literature<sup>81-84</sup>. Furthermore, many of our  $T_2$  curves do not fully decay due to the 32-echo limit of the Siemens scanners. Since it is impossible to know what our curve's behaviors would be at full relaxation, the question - will these curves decay to zero or do they, indeed, have a vertical offset? - is valid.

The fact that a vertical offset is sporadically seen in MRI literature combined with the fact that we do not truly know what our decay curves look like at full relaxation, makes it worthwhile to address our decision for not including a vertical offset term.

First, let us discuss reasons why a  $T_2$  curve might not decay all the way to zero:

1. MRI data may not decay all the way to zero because the noise floor is centered around a value greater than 0 due to the rectified nature of a magnitude MRI signal. It is appropriate to include an offset to account for this non-zero noise baseline<sup>9,85</sup>. We expect the fitted offset term to be equal between neighboring pixels (certainly within a few millimeters of each other

but perhaps not across multiple centimeters if the noise levels vary across the image). If the MRI  $T_2$  data does *not* decay fully, however, then it is not appropriate to include an offset term because high SNR data follows a Gaussian distribution and non-linear least squares fitting is well suited to dealing with Gaussian noise.

2. If a very long  $T_2$  signal is present in the voxel, then it might appear like a vertical offset exists in the data. Certain groups utilize an offset to account for long  $T_2$  signal, like CSF, but this is not technically correct<sup>84,86</sup>. Instead, it would be most accurate to fit the  $T_2$  data with an additional exponential in order to account for the long  $T_2$  signal. The  $T_2$  relaxation time of deionized water is the upper bound of anything that could reasonably be measured in the human body and can be used as an upper limit benchmark.
3. The MRI signal might not decay to zero if a “steady-state” signal has been formed by the particular pulsing sequence used. The refocusing train of a CPMG sequence causes stimulated echoes, which, under certain conditions, may lead to the signal being continuously recalled instead of being permitted to decay fully. It is known that imperfect refocusing pulses (i.e. a pulse not equal to  $180^\circ$ ) can lead to an accumulation of stimulated signal later in the echo train. Dielectric effects and imperfect slice excitation profiles contribute to imperfect  $B_1$  pulses<sup>83</sup>. It would be appropriate to include an offset term in this scenario.

We have discussed the scenarios that might cause a  $T_2$  curve to not decay fully to zero. The proper reasons for including a vertical offset term in the exponential fit are (1) fully decaying  $T_2$  relaxation data with a non-zero noise floor and (2) a “steady-state” signal due to stimulated echoes.

The majority of our data does not decay fully due to the 32-echo limit of the Siemens’s scanners, therefore the first valid reason for including an offset term does not apply. Only  $T_2$  relaxation times below 35ms decay fully with our acquisition parameters. Greater than 98% of our pixels have relaxation times above 35ms (with a mono-exponential fit since bi-exponential fits have one short and one long relaxation time). We did not want to have different fits for different pixels. Furthermore, we attempted to fit our data with mono- and bi-exponential fits with offsets expecting that neighboring pixels would have nearly identical offset terms in our data. We found, however, that neighboring pixels had significantly different offset terms. The offset was therefore not reflecting true baseline noise levels, which should hold constant in a 2-millimeter span, and, rather, pointed to an offset caused by stimulated echo effects. By not including an offset term to account for a non-zero noise floor we realize that we may be biasing the results of certain pixels to longer  $T_2$

relaxation times. Nevertheless, our  $T_2$  values have good correspondence with values reported in literature.

With regards to the steady state signal, researchers have shown that both  $B_1$  inhomogeneities and imperfect refocusing pulses contribute to the offset<sup>83,87</sup>. It is very likely that we have imperfect refocusing pulses given the CPMG-type sequence that we are using<sup>88</sup>. There are extended phase graph (EPG) methods for modeling and correcting for the imperfect pulses, which were beyond the scope of this thesis work<sup>89-91</sup>. A simpler fix is to ignore the initial point of the  $T_2$  decay and include an offset term<sup>83</sup>. A large amount of the benefit is derived from just excluding the initial point without the offset term<sup>83</sup>, and this is what we opted to do.

In conclusion, we chose to not include offsets in any of our MRI data analysis, which is consistent with the methodology of much of the MRI literature and gave us  $T_2$  relaxation values that corresponded to what has been described in literature. Future work should implement the EPG correction methods to better account for stimulated echo contributions in the data.

### **Implementation Notes**

Scripts to apply the F-test are found on Github: `analysis_optimal_multiexp_model.m`. F-test results are summarized in the Excel file called `Ftest.xlsx`

### **4.2.2 Methods: Criteria for Discarding Fitting Results**

We developed 4 criteria for determining when a particular bi-exponential fit result was not reliable and should be discarded:

#### **1. Criteria 1: Minimum and Maximum Measurable $T_2$ Relaxation Times for a Given TE and SNR**

##### **Motivation**

There is both a minimum and maximum rate of decay ( $T_2$  relaxation time) that can be detected for a given curve based on the curve's point spacing and signal-to-noise ratio (SNR). For example, if the first time point of a decay curve is at 8ms, naturally, it will not be possible to measure signal with a 50us decay rate because all of the signal will have decayed away by the time the first time point is collected. On the flipside, if the last time point of a curve occurs at 256ms (as it does for our MRI data), it will not be possible to accurately measure

a 2,000ms decay rate since scarcely any signal will have decayed by 256ms. The minimum measurable  $T_2$  is limited by the sampling rate, whereas the maximum measurable  $T_2$  is limited by the curve's SNR. If the curve had infinite SNR, there would *not* be an upper limit to the measurable  $T_2$ . Since there is always noise present in our MRI data, there is an upper  $T_2$  limit.

We sought to understand these minimum and maximum values and the factors that impacted them through simulated decay curves that mimicked our MRI data. The lower- and upper-bounds determined from these simulations were included in the criteria for throwing away pixel-by-pixel fit results.

## Methods

The pixel-by-pixel SNR of our human MRI data ranged from 35-175 (section 4.2.3 discusses how noise and SNR were calculated). We generated single exponential decay curves with SNRs ranging from 20-250 and parameters that modeled our human MRI data: 32 points with a point spacing (echo time, TE) of 8ms and an amplitude of 3000.

$$\text{time} = TE : TE : 32 * TE \quad (4.4)$$

$$\text{Synthetic Decay Curve} = \text{Amplitude} * e^{-\frac{\text{time}}{T_2 \text{ Relaxation Time}}} \quad (4.5)$$

$$\text{SNR} = \frac{\text{max}(\text{Synthetic Decay Curve})}{\text{stdev}(\text{Synthetic Decay Noise Floor})} \quad (4.6)$$

The decay rates ranged from  $0.25 - 200 * TE$ , which, for TE=8ms, represented 2-1600ms. The decay curves generated at each SNR are seen in figure 4-3.

Each decay curve was fit with a single exponential fit of the same formula. The error between the measured relaxation time and the actual relaxation time was calculated in both absolute and relative terms.

$$\text{Absolute Error} = T_2 \text{ Relaxation Time}_{\text{actual}} - T_2 \text{ Relaxation Time}_{\text{measured}} \quad (4.7)$$

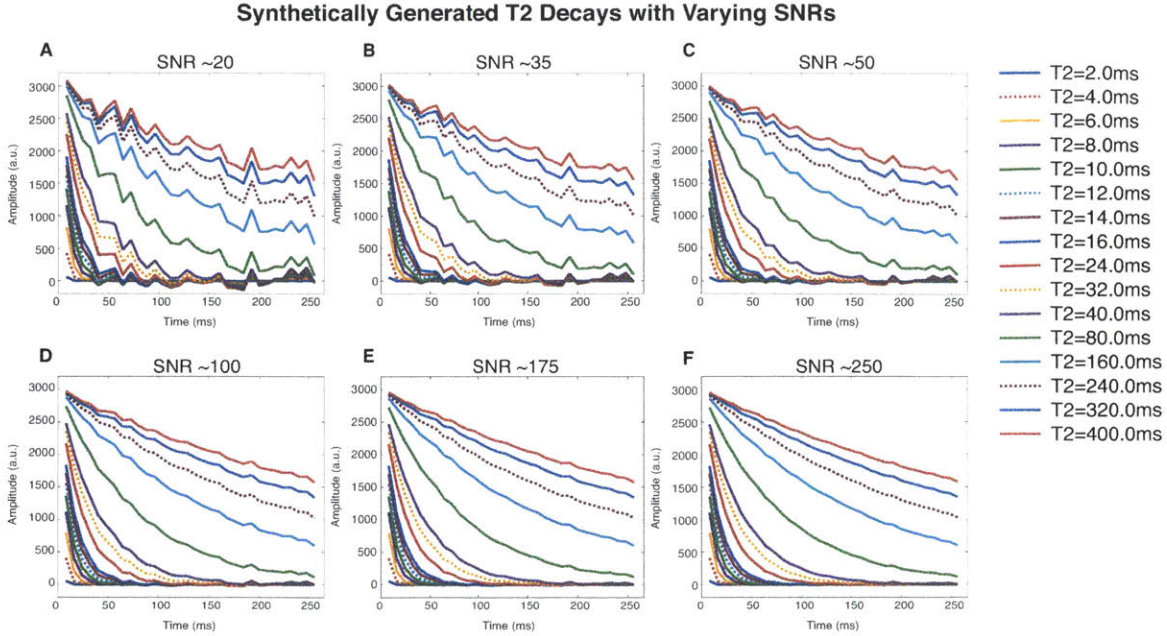


Figure 4-3: Synthetically generated mono-exponential decay curves with SNRs of 20, 35, 50, 100, 175, 250 (A-F), and  $T_2$  relaxation times from 2-400ms at each SNR level. For another analysis, curves with relaxation times up to 1600ms were generated but are not shown here.

$$\text{Relative Error} = \frac{\text{Absolute Error}}{\text{Actual } T_2 \text{ Relaxation Time}} * 100\% \quad (4.8)$$

These errors were plotted across multiple  $T_2$  relaxation times and SNRs as seen in Figure 4-4. Section 4.2.3 explains how SNR was calculated.

## Results and Discussion

### Minimum $T_2$

The higher the SNR of the curve, the lower the error of the measured  $T_2$  relaxation time for a given  $T_2$  value. The minimum error across all SNRs occurred at 0.5TE. The relative error increased from 0.5TE to 3TE and then decreased. We chose 5% relative error as an acceptable error threshold. All of the relative errors were below 5% from 0.5TE onwards with the exception of those from curves with an SNR of 20. The minimum SNR required for the results above 0.5TE to stay below a 5% error was 35.

It is important to note that for the conditions of this simulation, although the relative errors sometimes increase above 5%, the absolute errors were actually small. For example, the

## Accuracy of T<sub>2</sub> Measurements for TE=8.0ms based on SNR

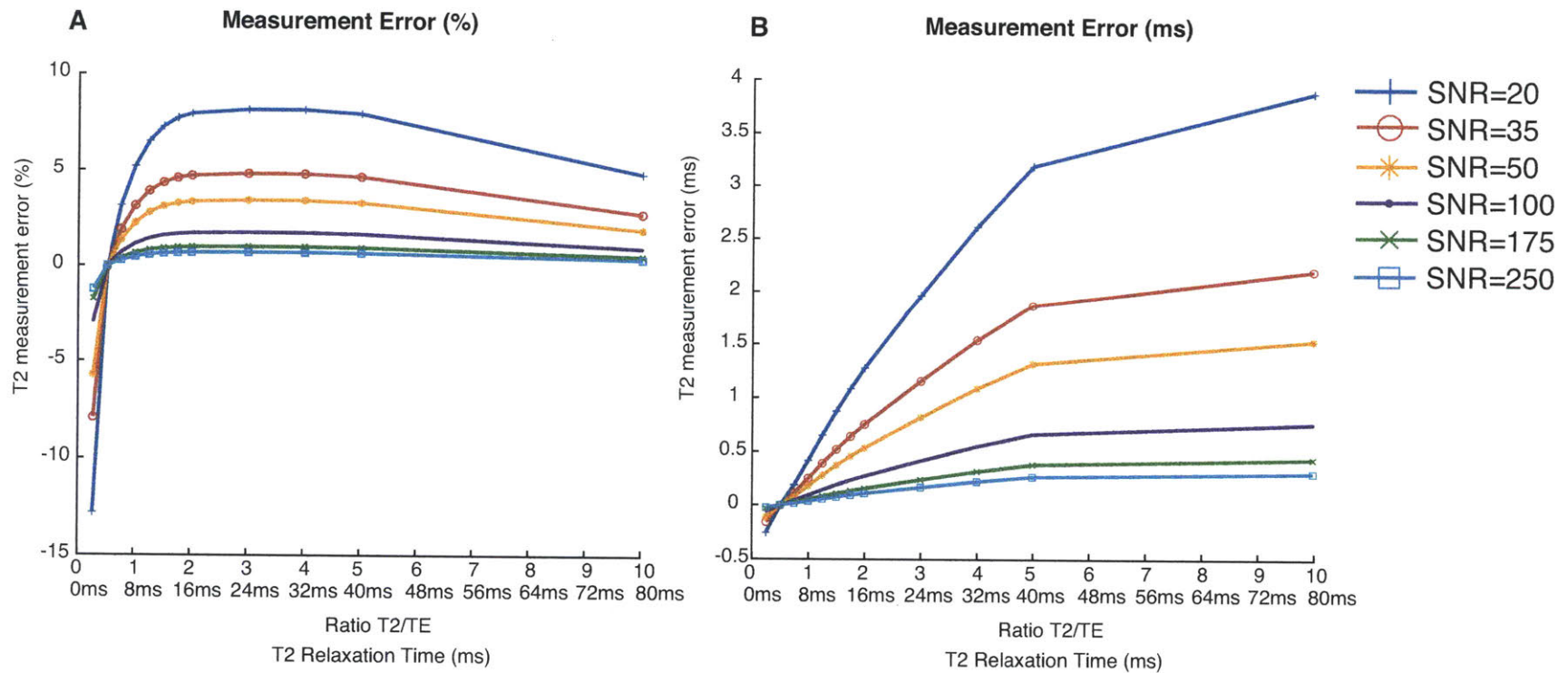


Figure 4-4: The error of the measured relaxation time versus the actual  $T_2$  Relaxation Time (also specified as the ratio of  $T_2/TE$ ) of various synthetically generated decays with different SNRs (represented by different lines). The left subplot (A) shows the relative error as a percentage of the true  $T_2$  value, whereas (B) shows the absolute error between the measured and true  $T_2$  value in milliseconds. The minimum  $T_2$  that can be measured with less than 5% error is  $0.5TE$ , which for our MRI data of  $TE=8ms$  is  $4ms$ .

relative errors below  $0.5TE$  were  $\sim 10\%$  for certain curves yet that  $10\%$  relative error represented less than  $0.5\text{ms}$  in absolute error. The absolute error never rose above  $4\text{ms}$  - and was usually below  $2\text{ms}$  - in our simulations (see Figure 4-4B). These absolute errors represented an acceptable level of error to us, but we wanted to develop a criterion that could be applied consistently across all decay curve analyses and if the  $TE$  were larger, then a  $10\%$  relative error would correspond to a larger absolute error that would not be acceptable.

We **concluded** that a decay curve with a point spacing of  $TE$  can reliably measure decay rates of  $0.5TE$  ( $4\text{ms}$  for our MRI data) and higher. Any rates below  $0.5TE$  may not be accurate, especially for data with SNR below 50. These findings are independent of  $TE$ . Pixels that were deleted by this criterion are shown in Figure 4-7.

### **Minimum $T_2$ with Skipping the First Point**

In our MRI data, the first data point ( $TE=8\text{ms}$ ) is almost always lower than the second data point ( $TE=16\text{ms}$ ), resulting in a  $T_2$  decay that looks like the one in Figure 4-5.

The lowered first point is due to the fact that it does not have stimulated echo contributions. Data coming from a CPMG pulse sequence has stimulated echo contributions which give a signal boost to all points except the first one. The first point is a pure spin-echo signal and is therefore lower than the other points. It is standard practice to discard the initial point of a  $T_2$  decay resulting from a CPMG sequence.

We repeated the analysis above with a decay curve that had the first point removed, such that the time array was now:

$$\text{time} = 2 * TE : TE : 32 * TE \quad (4.9)$$

The time array was now only 31 points in length.

The errors follow the same pattern as seen previously except that the errors below  $0.5TE$  are slightly larger, especially for the decays with larger SNRs (see Figure 4-6). The *conclusion that fits below  $0.5TE$  should be discarded is maintained.*

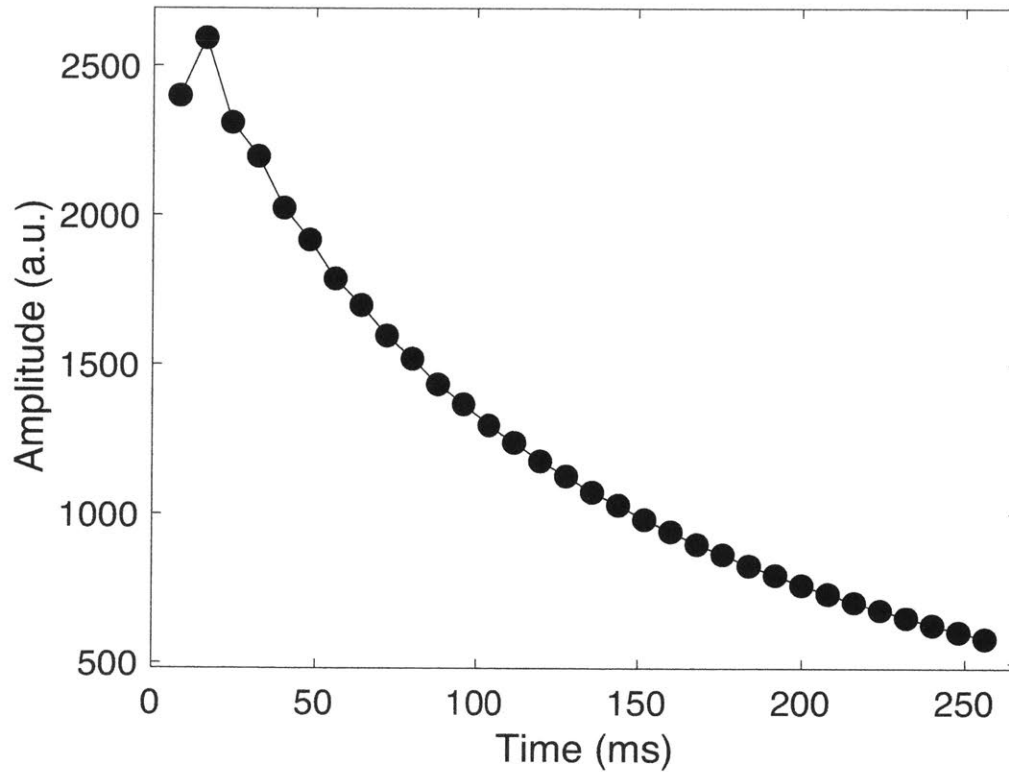


Figure 4-5: This  $T_2$  decay has its first point lower than the second point. The first point is lower because it does not have the additional signal boost from stimulated echo effects, which all of the other points have.

### Accuracy of T2 Measurements for TE=8.0ms based on SNR (with skipping the 1st point)

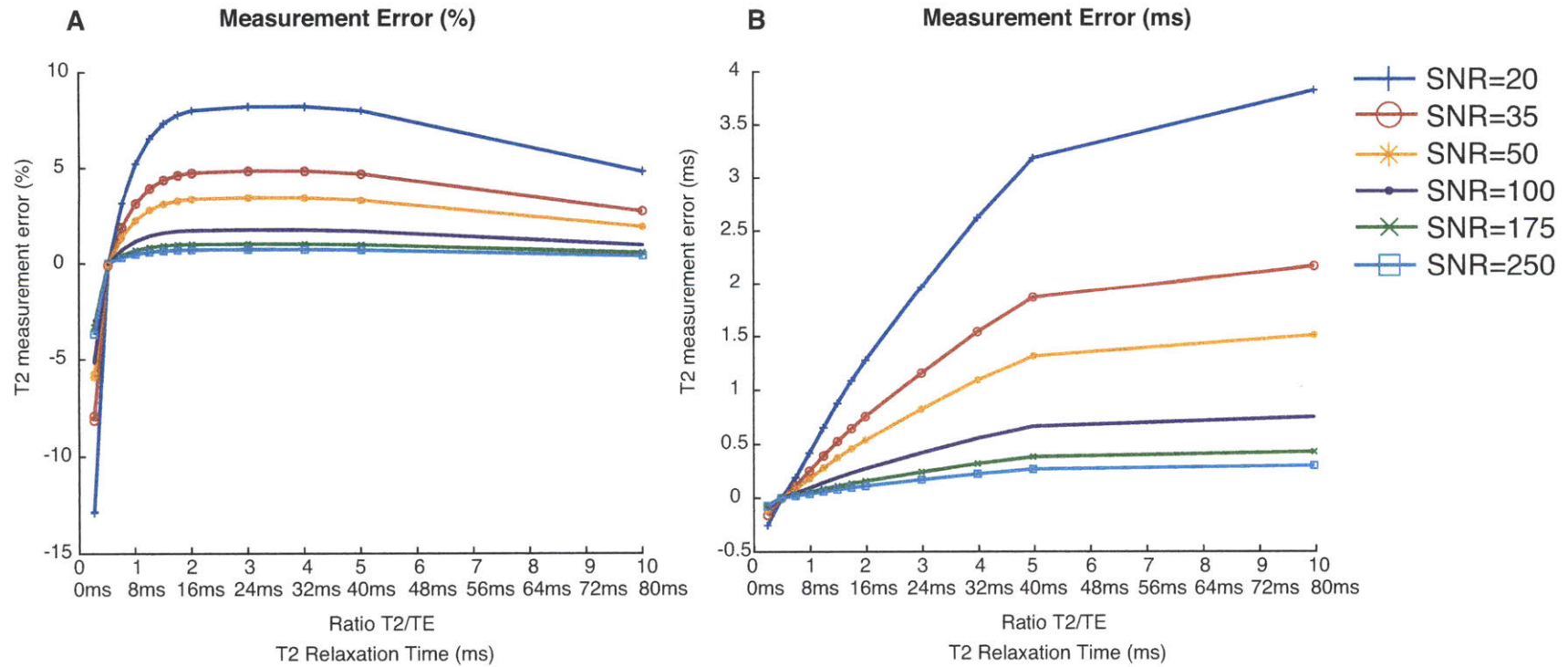


Figure 4-6: The same analysis as in Figure 4-4 repeated on decay curves that were missing the first point. Subplot (A) shows the relative error as a percentage of the true  $T_2$  value, whereas (B) shows the absolute error between the measured and true  $T_2$  value in milliseconds. The errors are slightly larger for these curves without an initial point, but the conclusion that minimum  $T_2$  that can be measured with less than 5% error is 0.5TE is unchanged.

### Pixels Deleted by Minimum T<sub>2</sub> Criteria

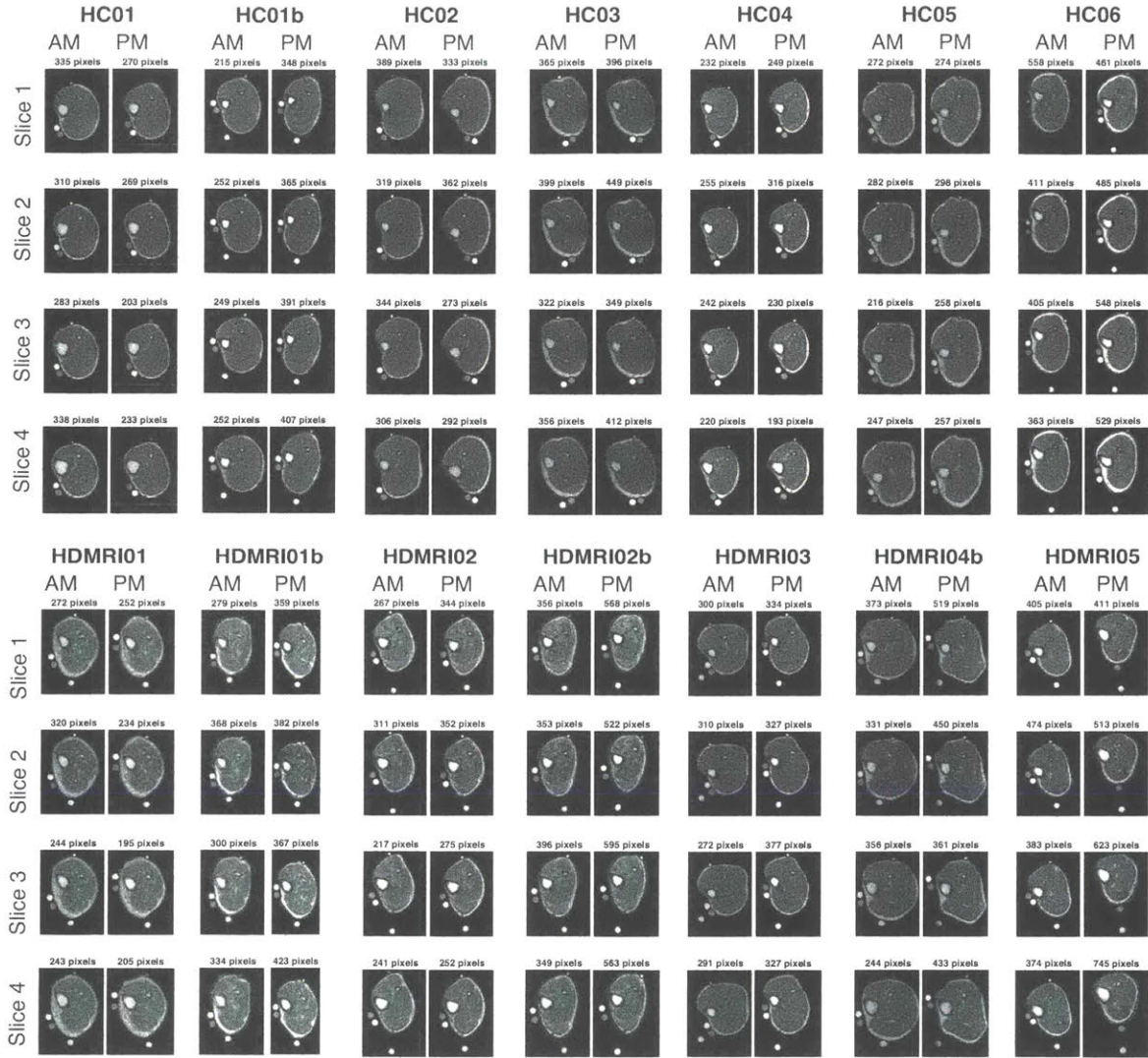


Figure 4-7: Bi-Exponential Fittings: Pixels (highlighted in blue) on each scan that were deleted by the minimum  $T_2$  criteria. The deleted pixels tended to be located in the bone and background, areas with little or no signal. The minimum  $T_2$  that can be measured with less than 5% error is  $0.5TE$ , which for our MRI scans is equal to 4ms.

<b>Maximum <math>T_2</math> Relaxation Time that can be Measured with Allowable Error</b>		
<b>SNR</b>	<b>5% Error</b>	<b>10ms Error</b>
20	640ms	408ms
35	1020ms	504ms
50	1408ms	584ms
100	2696ms	800ms
175	4672ms	1015ms
250	6640ms	1222ms
Best Fit Line for Max. Measurable $T_2$		
	$25.63 * SNR + 197.6$	$3.459 * SNR + 392.3$

Table 4.2: Summary of the maximum  $T_2$  relaxation time that can be measured at each SNR level with either (A) 5% error, or (B) 10ms error. These results were taken from the simulations of Figure 4-8 and are shown visually in Figure 4-9.

### Maximum $T_2$

The next minimum in error (after 0.5TE) occurred around 30TE (240ms for our MRI data) as seen in Figure 4-8. After 30TE, the measurement error increased monotonically. The error was lower for higher SNR curves. For example, a curve with an SNR of 250 could measure a relaxation time of 1280ms with <10ms error. A curve with SNR of 20, however, could only measure a relaxation time of 400ms with <10ms error.

The 10ms error criteria was more conservative than the 5% error criteria. We decided to use the 5% error criteria. Since the 5% cutoff varied drastically based on SNR, the criteria need to be applied dynamically based on each pixel's SNR.

For each pixel, its SNR was looked up and its maximum measurable  $T_2$  was be calculated based on the empirically-derived equation from the results of Figure 4-8. The best-fit line describing the empirical results is show in Figure 4-9, summarized in Table 4.2 and described by the following equations:

$$\text{Maximum Measurable } T_2 \text{ with 10ms Error} = 3.45 * SNR + 392.3 \quad (4.10)$$

$$\text{Maximum Measurable } T_2 \text{ with 5% Error} = 25.63 * SNR + 197.6 \quad (4.11)$$

If the calculated  $T_2$  was larger than the maximum  $T_2$  cutoff, then that pixel was deleted from the dataset. Pixels that were deleted by this criterion are shown in Figure 4-10.

## Maximum Measurable T2 Relaxation Time

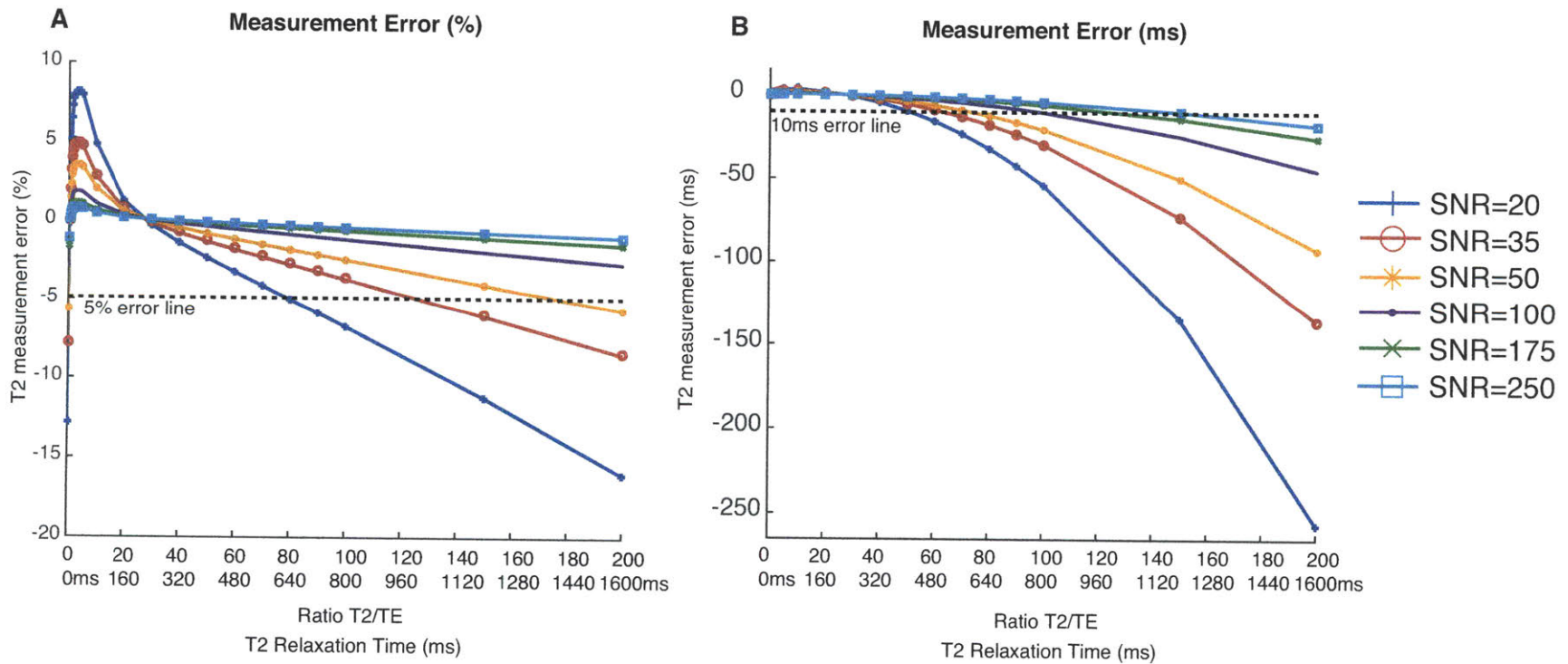


Figure 4-8: The error of the measured relaxation time versus the actual  $T_2$  Relaxation Time (also specified as the ratio of  $T_2/TE$ ) of various synthetically generated decays with different SNRs (represented by different lines) extended out to larger  $T_2/TE$  ratios. The horizontal line on subplot (A) shows the maximum  $T_2$  that can be measured with less than 5% error for each SNR, and subplot (B) shows the maximum  $T_2$  that can be measured with less than a 10ms error at each SNR level.

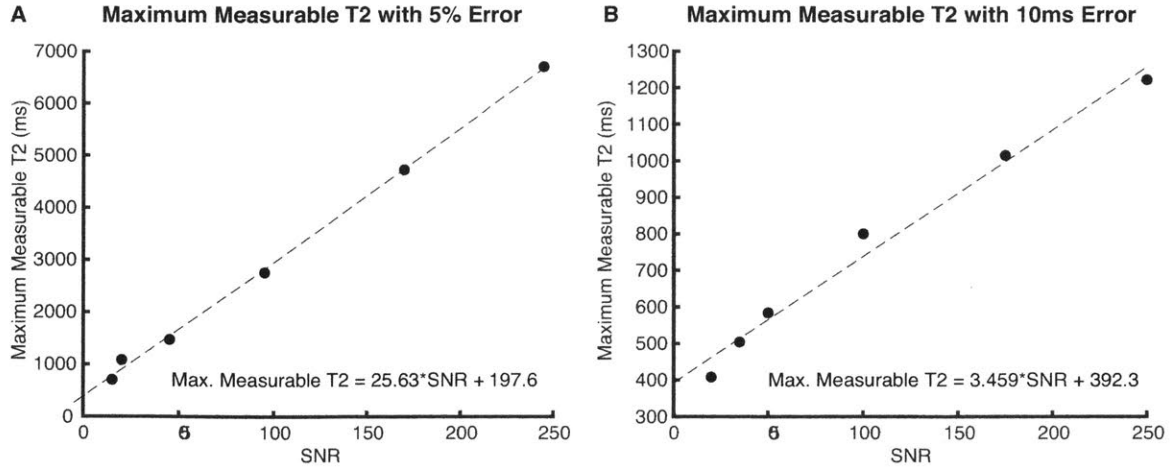


Figure 4-9: The maximum measurable  $T_2$  relaxation time at each SNR level in order to stay within (A) 5% relative error, or (B) 10ms absolute error. The points on each curve are empirically derived from the simulations of Figure 4-8 and described by a best-fit line that allows calculation of maximum  $T_2$  based on SNR.

### Limitations of Minimum and Maximum $T_2$ Criteria

The modeling work that yielded the minimum and maximum  $T_2$  criteria was done for a single exponential decay with a single exponential fit. Our human MRI data is multi-exponential and is fit with up to two exponential decays. Nevertheless, the results from the simplified simulations offer valuable insights for how to place bounds around our fits. Future work could involve extending these simulations to bi-exponential data based on the relaxation times and relative amplitudes found in the leg. We expect that bounds from simulated bi-exponential data will be more restrictive than the ones placed at the moment.

Furthermore, this simulation work was done with a single 'seed' of white Gaussian noise values (which is why all of the simulated  $T_2$  decays rise and fall in the same places). A more robust way to do this simulation would involve running the simulation many times with different seeds and then averaging together the results of each run. Future work may involve doing these simulations to determine the more robust upper and lower  $T_2$  bounds.

## 2. Criteria 2: RMSE Cutoff

The root mean squared error (RMSE) is a generalized metric of goodness of fit. If the RMSE is too large, then the fit was a poor one. RMSE is defined as

$$\text{Root Mean Square Error} = \text{RMSE} = \sqrt{\frac{\sum_{i=1}^n (y - y_i)^2}{v}} \quad (4.12)$$

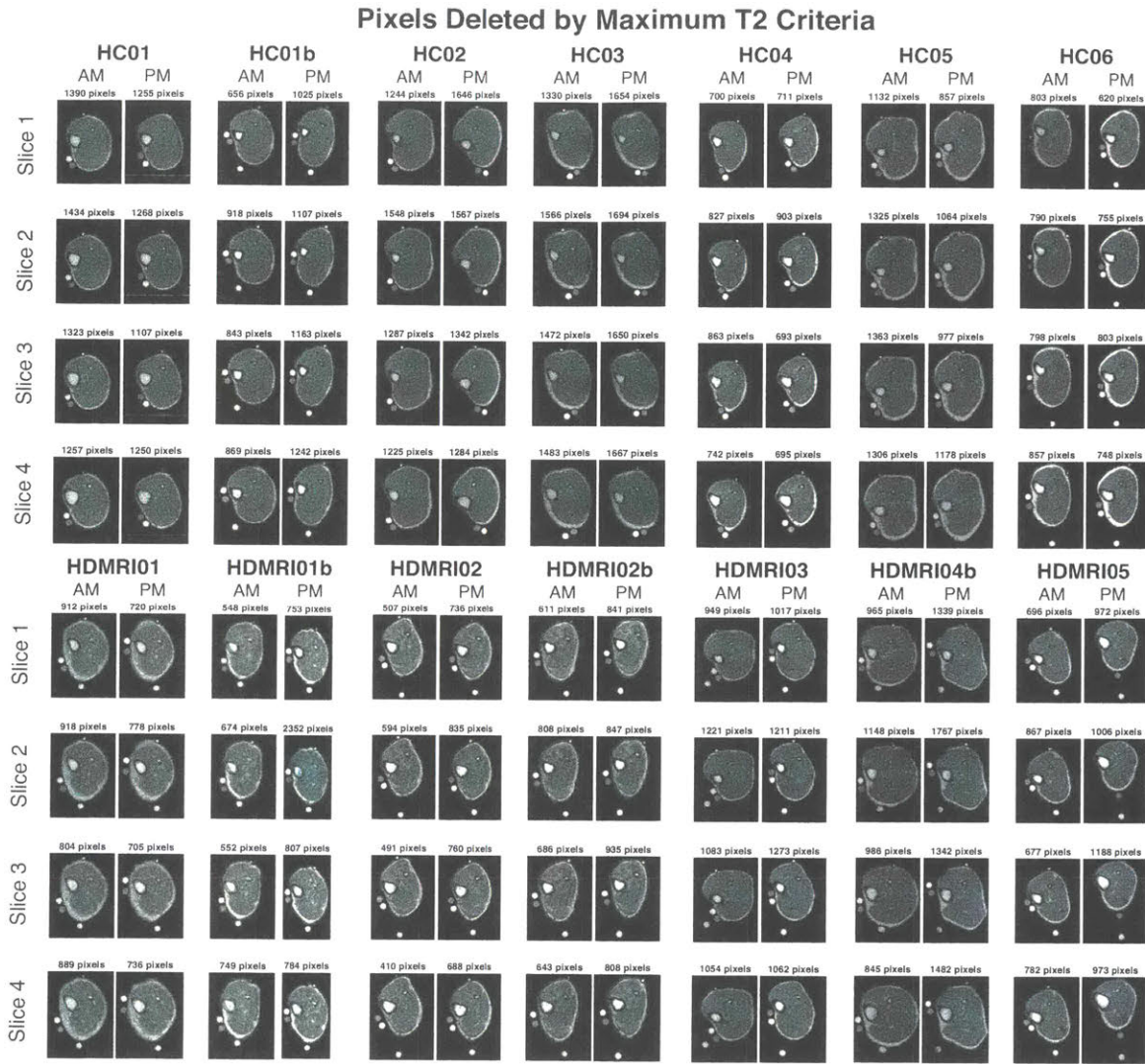


Figure 4-10: Bi-Exponential Fittings: Pixels (highlighted in blue) on each scan that were deleted by the maximum  $T_2$  criteria. The maximum  $T_2$  that can be measured with less than 5% error depended on the pixel's SNR and could be calculated by the empirically-derived formula:  $Max.T_2 = 25.63 * SNR + 197.6$ . The maximum  $T_2$  cutoff was calculated for each pixel based on that pixel's SNR. The pixels deleted by this criterion tended to be spread out throughout the leg and background. This criterion was responsible for deleting the greatest number of pixels from the dataset.

where  $v$  is the degrees of freedom of the fit,  $v = n - m$  with  $n$  being the number of data points (31 for our MRI data) and  $m$  the number of fitted coefficients (in the case of a bi-exponential is 4). The smaller the RMSE value, the more accurately that the fit represents the data.

We calculated the 99th percentile of the RMSE distributions for each subject and deleted pixels whose RMSE values were in the top 1% for that subject. The cumulative distribution functions (CDFs) of the RMSE distributions for each subject are show in Figure 4-11. This criterion deleted pixels in the bone, the background around the leg, and in the arterial pulsation artifacts.

We initially experimented with having a single RMSE cutoff for all patients. We used the 99% of the RMSE distribution of *all* scans analyzed together as the cutoff. The problem with this approach is that the 99th percentile of RMSE was almost entirely determined by the HDMRI01b PM scan, which had the largest errors. Implementing this single cutoff value caused nearly all pixels from HDMRI01b PM to be deleted and barely any pixels from the other scans to be deleted. This did not achieve our intended consequence and so, instead, we implemented the approach of calculating the 99% cutoff for each scan independently.

### 3. **Criteria 3: 95% Confidence Interval is NaN**

The non-linear least squares fit that was performed on each pixel assigned a 95% confidence interval to each parameter. If the fitting gave one or more of the parameters a NaN for its confidence interval, then that pixel was deleted from the dataset. Pixels that were deleted by this criterion tended to be located in the bone and background.

### 4. **Criteria 4: Relaxation Times Less Than 10ms Apart**

There is a limit to how close a bi-exponential curve's two decay rates can be to each other and still be resolved as separate decays. A few pixels had bi-exponential fits with two nearly identical relaxation times and these fits were associated with large 95% confidence intervals. We deleted any pixels that had two relaxation times less than 10ms apart from each other. Few pixels were deleted by this criterion and they tended to be located in blood vessels or perifascial fluid accumulations. Pixels that were deleted by this criterion are shown in Figure 4-12.

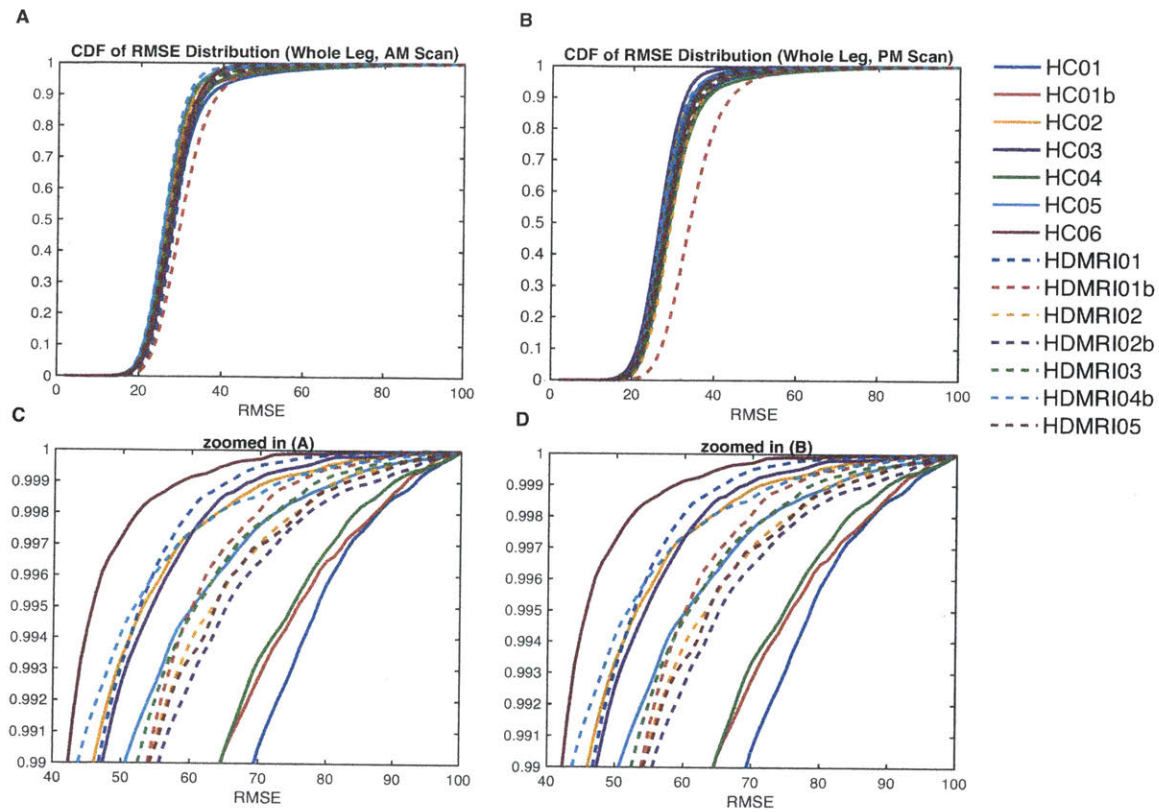


Figure 4-11: Cumulative distribution plots of RMSE distributions for each subject in the (A) AM and (B) PM. The top row (A)-(B) shows the complete CDF and the bottom row (C)-(D) shows the CDF zoomed into the 99th percentile. Subject HDMRI01b scans had the largest RMSE errors, especially in the PM. The RMSE errors are fairly consistent across all other scans.

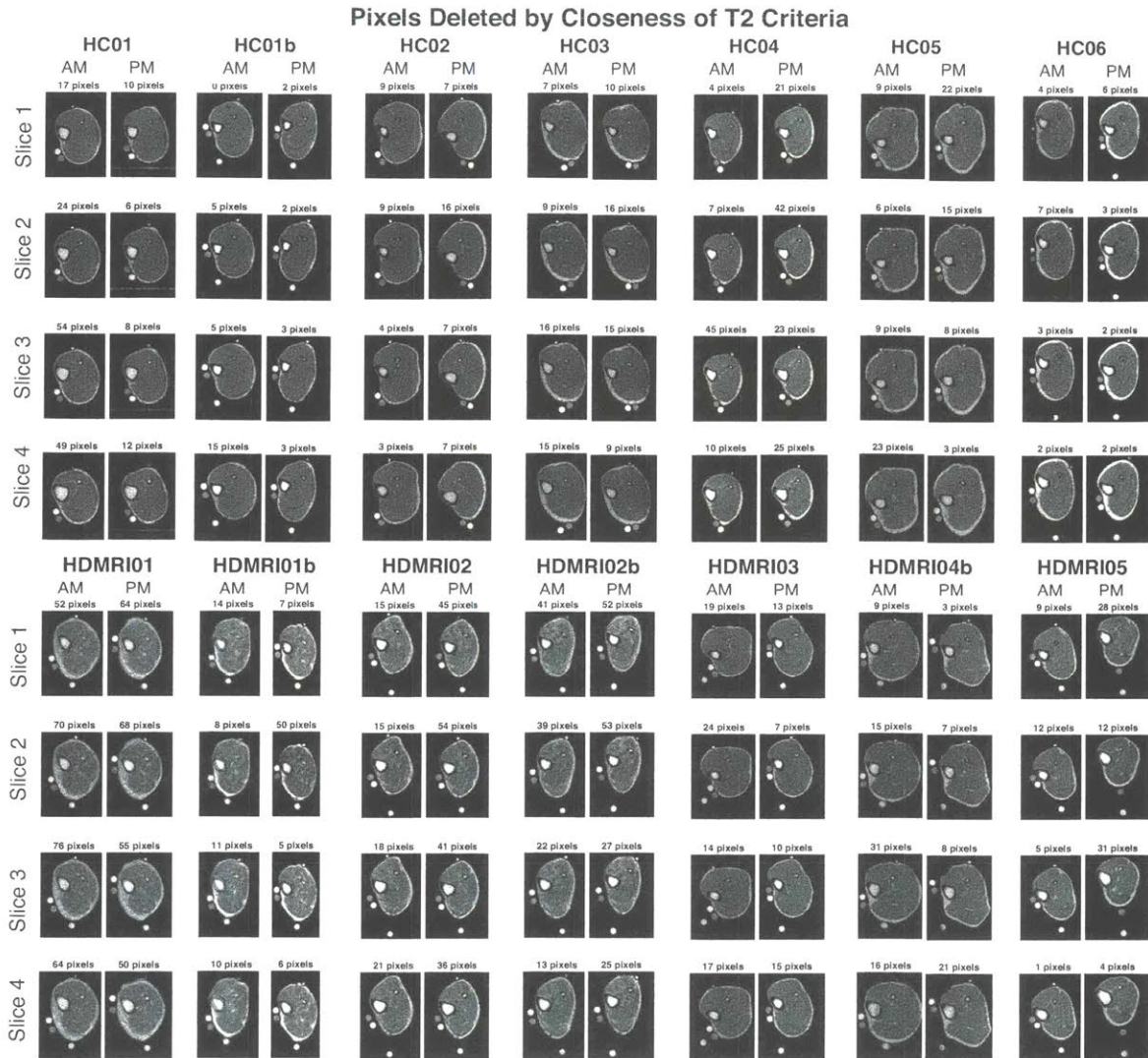


Figure 4-12: Bi-Exponential Fittings: Pixels (highlighted in blue) on each scan that were deleted by the closeness of  $T_2$  relaxation times criterion. Each pixel was fit with a bi-exponential decay and if the two resulting decay times were less than 10ms apart, the fit was deleted. There were few pixels deleted by this criterion and they tended to be located within blood vessels, or in the perifascial fluid accumulations of HDMRI01.

## Summary of Criteria

To summarize, the following criteria were applied to the pixel-by-pixel fit results of MRI data:

1. RMSE > 99th RMSE percentile for that scan
2. Any Relaxation Time < 0.5TE
3. Any Relaxation Time > 5% Relative Error (calculated by  $5\% \text{ Relative Error} = 25.63 * \text{SNR} + 197.6$ )
4. 95% Confidence Interval of any parameter = NaN
5. Relaxation Time 1 - Relaxation Time 2 < 10ms (for bi-exponential fits only)

Figure 4-13 shows *all* of the pixels that were deleted by these combined criteria.

## Implementation Notes

The scripts to generate these figures and simulations are located in the project's Github folder: `syntheticDecays_explore_T2limits_for_TE_SNR.m`, `analyze_pixel_by_pixel_results.m`, `checkfits.m`.

### 4.2.3 Methods: Calculating Pixel SNR

The maximum measurable  $T_2$  criterion used for discarding pixels was based on each individual pixel's SNR. It was therefore important to come up with a robust method for calculating SNR. The methods we utilized to calculate SNR are described in this section. We will first begin with a short introduction on the origins of noise in MRI, then proceed to discussing how to calculate noise and SNR, and finally discuss the limitations of our assumptions.

#### Origins of Noise in MRI

MRI images can be corrupted by many types of noise including thermal noise, physiological noise, quantization noise, and others<sup>92</sup>. Thermal noise - either from the patient or electronics - is the primary source of noise for most MRI images<sup>19,93</sup>.

Thermal noise (or Johnson-Nyquist Noise) is random noise due to the Brownian motion of electrons within a conductor<sup>19,93-96</sup>. The movement of these electrons (or any charge carrier, for

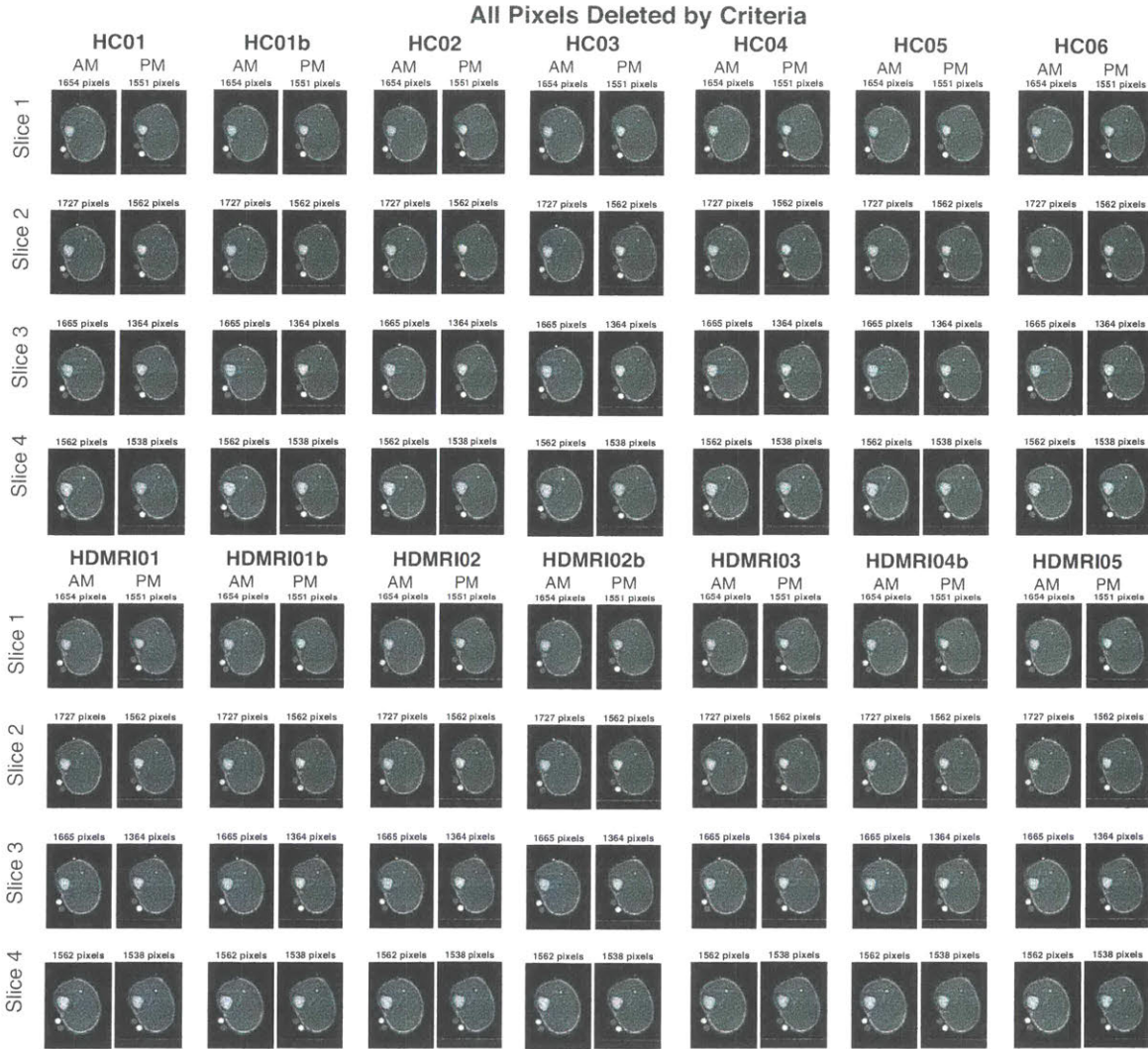


Figure 4-13: Bi-Exponential Fittings: Pixels (highlighted in blue) on each scan that were deleted by all of the criteria imposed together. The greatest number of pixels were deleted by the maximum  $T_2$  criterion. Deleted pixels tended to be spread throughout the leg, with a heavy concentration of deletions in the background (which is desirable) and the vascular pulsation artifacts (seen as horizontal lines of blue pixels across the images).

example, Na<sup>2+</sup> or K<sup>+</sup> in the human body) induce voltages in the receive coil that are picked up as noise<sup>92,93</sup>. Thermal noise can be modeled by the equation:

$$V_{noise(rms)} = \sqrt{4 * k * T * R * BW} \quad (4.13)$$

where V is the standard deviation of the voltage, k is Boltzmann's constant (J/K), T is the temperature of the system (K), R is the effective resistance of the sample (patient plus coils; Ohms) and BW is the bandwidth of the measuring equipment<sup>19,92,94,96,97</sup>.

In high-field imaging (approximately 1T and above), thermal noise from the patient dominates, whereas at low-field, thermal noise from the coils tend to dominate<sup>19,97</sup>. Amplitude distribution of thermal noise is Gaussian<sup>92</sup>.

### Calculating Noise from Magnitude Images

The general method for calculating noise in an MRI image is to take the standard deviation of the background. The standard deviation of magnitude images must be corrected before their standard deviation value is used, however. Magnitude images are formed by combining the real and imaginary signals.

$$Magnitude = \sqrt{Real^2 + Imaginary^2} \quad (4.14)$$

This non-linear mapping results in the noise not following a Gaussian distribution. By taking the magnitude, the following occur to the result: (1) negative numbers are made positive, (2) the mean becomes greater than zero, and (3) the standard deviation is made smaller. The noise distribution in magnitude MRI images is governed by a Rayleigh distribution:

$$f(x; \sigma) = \frac{x}{\sigma^2} e^{-x^2/(2\sigma^2)} \quad (4.15)$$

where  $\sigma$  is the noise. The Rayleigh distribution is a specific case of the more general Rician distribution when the signal amplitude  $A$  is zero,  $Rayleigh(x; \sigma) = Rician(x; A = 0; \sigma)$ <sup>71</sup>. Examples of a Rayleigh distribution can be seen in Figure 4-14.

The Rayleigh noise in our MRI images was calculated by drawing a background ROI devoid of any signal or artifacts and calculating the standard deviation of the pixels intensities in that ROI.

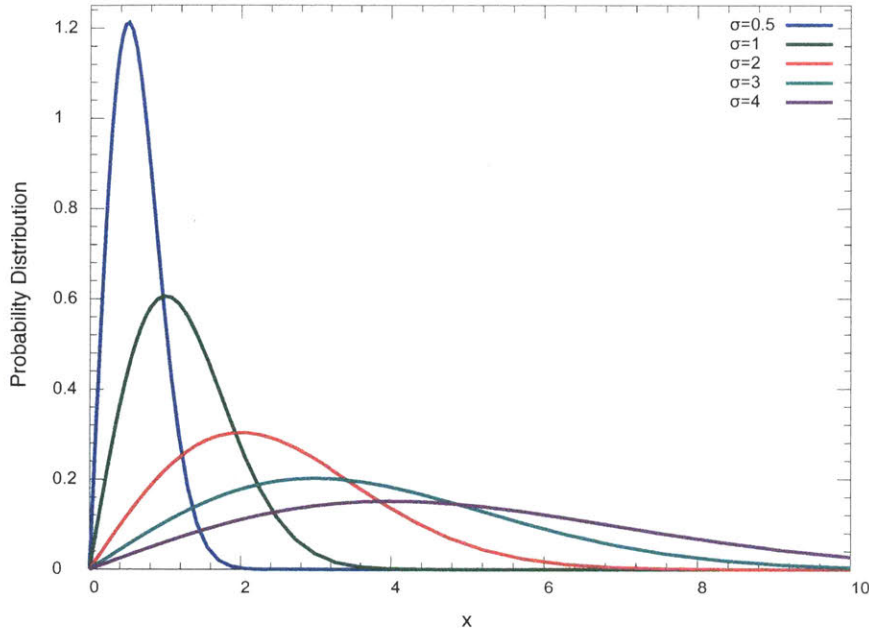


Figure 4-14: Example of Rayleigh probability distributions with different noise,  $\sigma$ , values. Source of image: Wikipedia, "Rayleigh Distribution".

This Rayleigh noise was then converted to Gaussian noise by the following relationship:

$$\sigma_{Rayleigh} = stdev(\text{Background ROI}) \tag{4.16}$$

$$\sigma_{Gaussian} = \frac{\sigma_{Rayleigh}}{\sqrt{2 - \frac{\pi}{2}}} \tag{4.17}$$

Finally, the SNR of each pixel was calculated by dividing the maximum pixel intensity (which generally occurred at TE=16ms) by  $\sigma_{Gaussian}$ .

$$SNR = \frac{max(\text{Signal})}{\sigma_{Gaussian}} \tag{4.18}$$

### SNR Distributions in MRI Images

The distribution of pixel SNRs found in our MRI scans are shown in Figure 4-15. The CDF plots of those SNR distributions in Figure 4-16 shows that less than 10% of all pixels have an SNR below 35. The overlaid SNR CDFs of all subjects' in Figure 4-17 shows that subjects have comparable SNR distributions, though dialysis patients tended to have higher SNRs than healthy controls.

Figure 4-18 shows that the pixels with SNR below 35 are generally located in the bone, blood

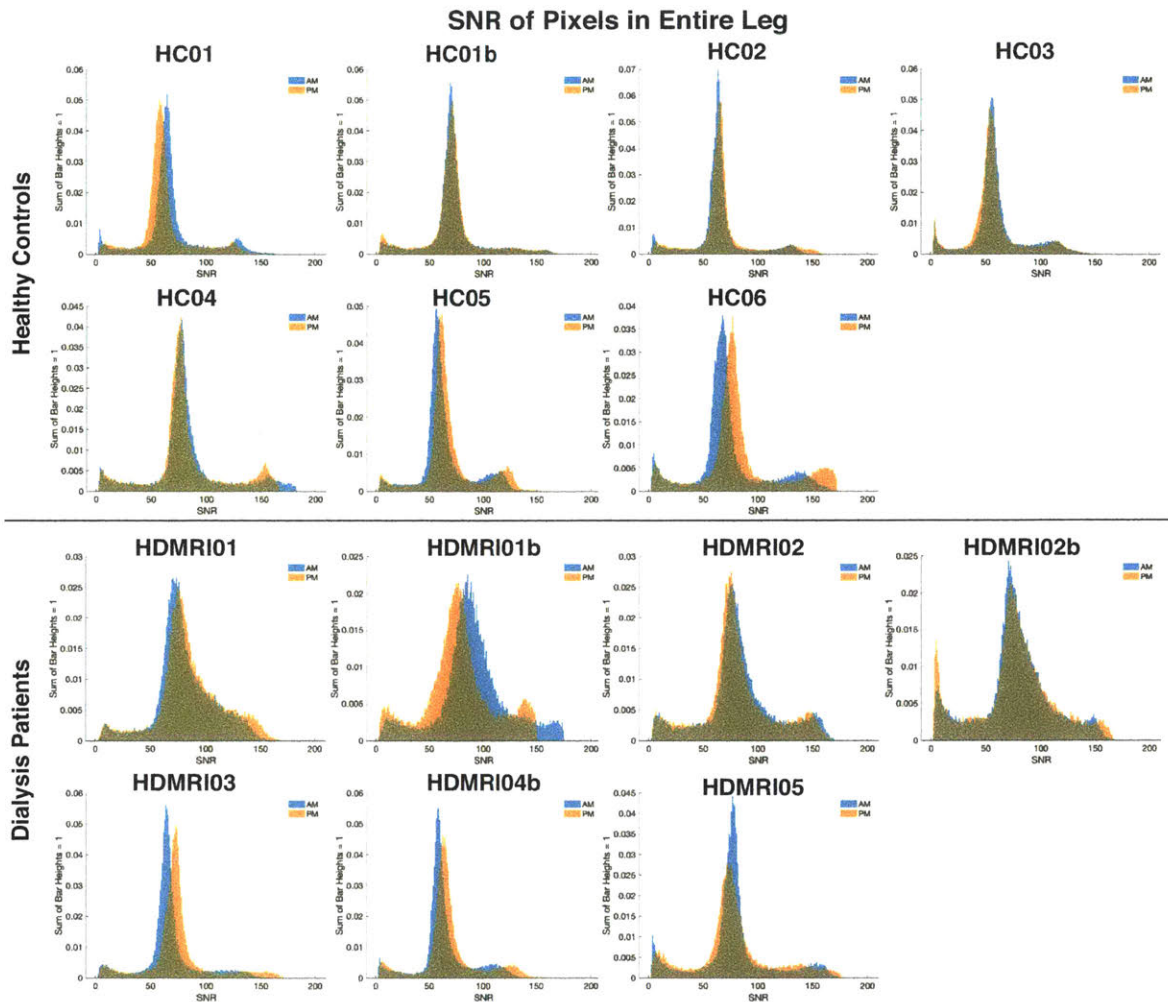


Figure 4-15: Histogram of SNR distributions for each subject with AM (blue) and PM (orange) values shown in different colors. Most pixels had an SNR between 50-100.

vessels, fascia, or background area outside of the leg. We therefore know that the tissues of which we are interested in measuring the  $T_2$  values (i.e. muscular and subcutaneous tissues) have SNRs greater than 35 and mostly greater than 50.

## Limitations

Assuming stationarity of the noise and using a single noise value for the entire MRI image is a popular assumption in the MRI world, but it is not without its limitations. A single noise value  $\sigma$  characterizing the entire MRI volume may be the case in single-coil acquisitions but is certainly not the case for multiple-coil acquisitions<sup>93</sup>. Different methods exist for accurately estimating noise in multi-coil acquisitions but since accurate SNR estimation was not at the core of this work, the

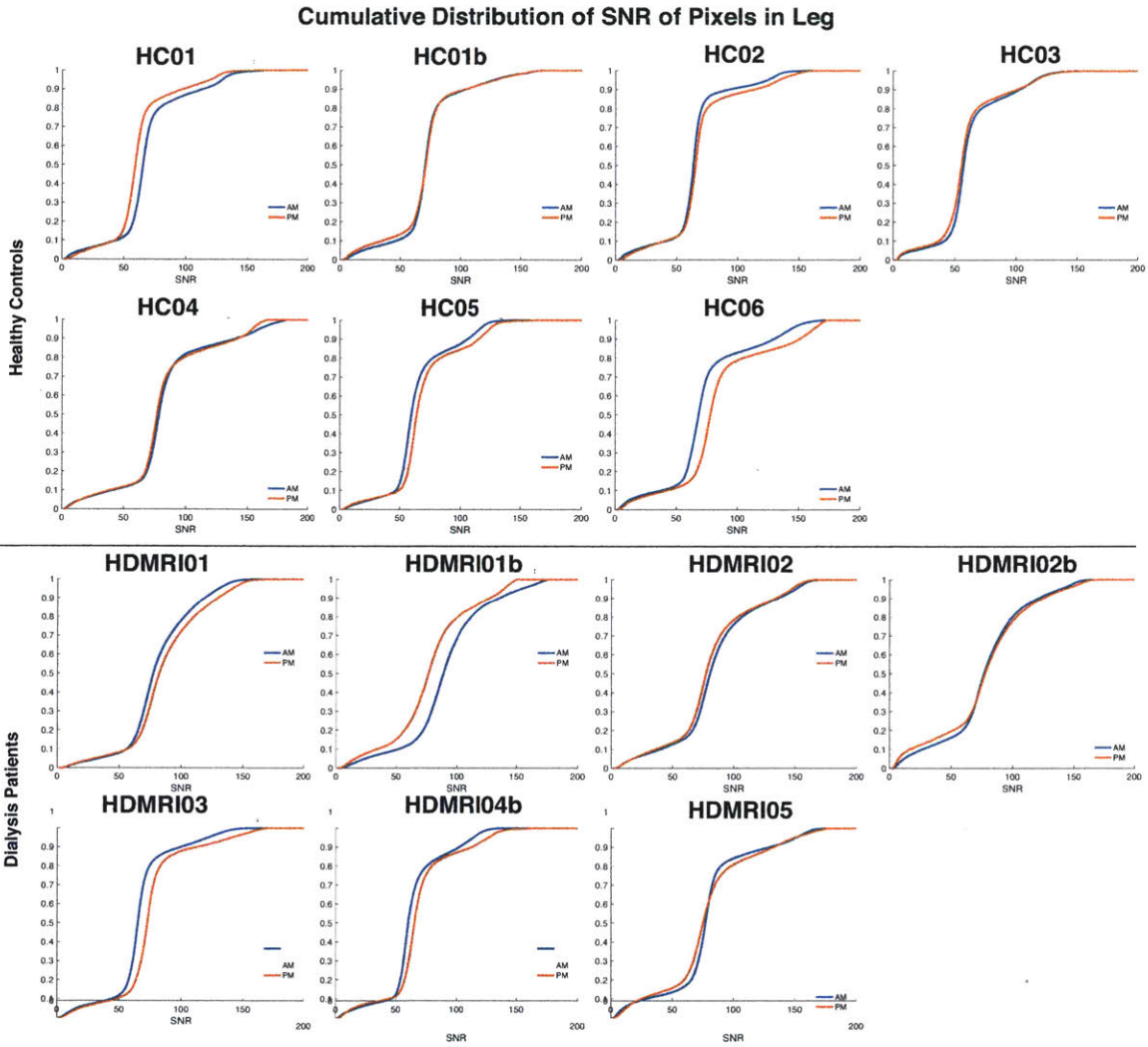


Figure 4-16: CDF plots of pixel SNR distributions for each subject with AM (blue) and PM (orange) values shown in different colors. For each scan, less than 10% of all pixels in that scan have an SNR below 35.

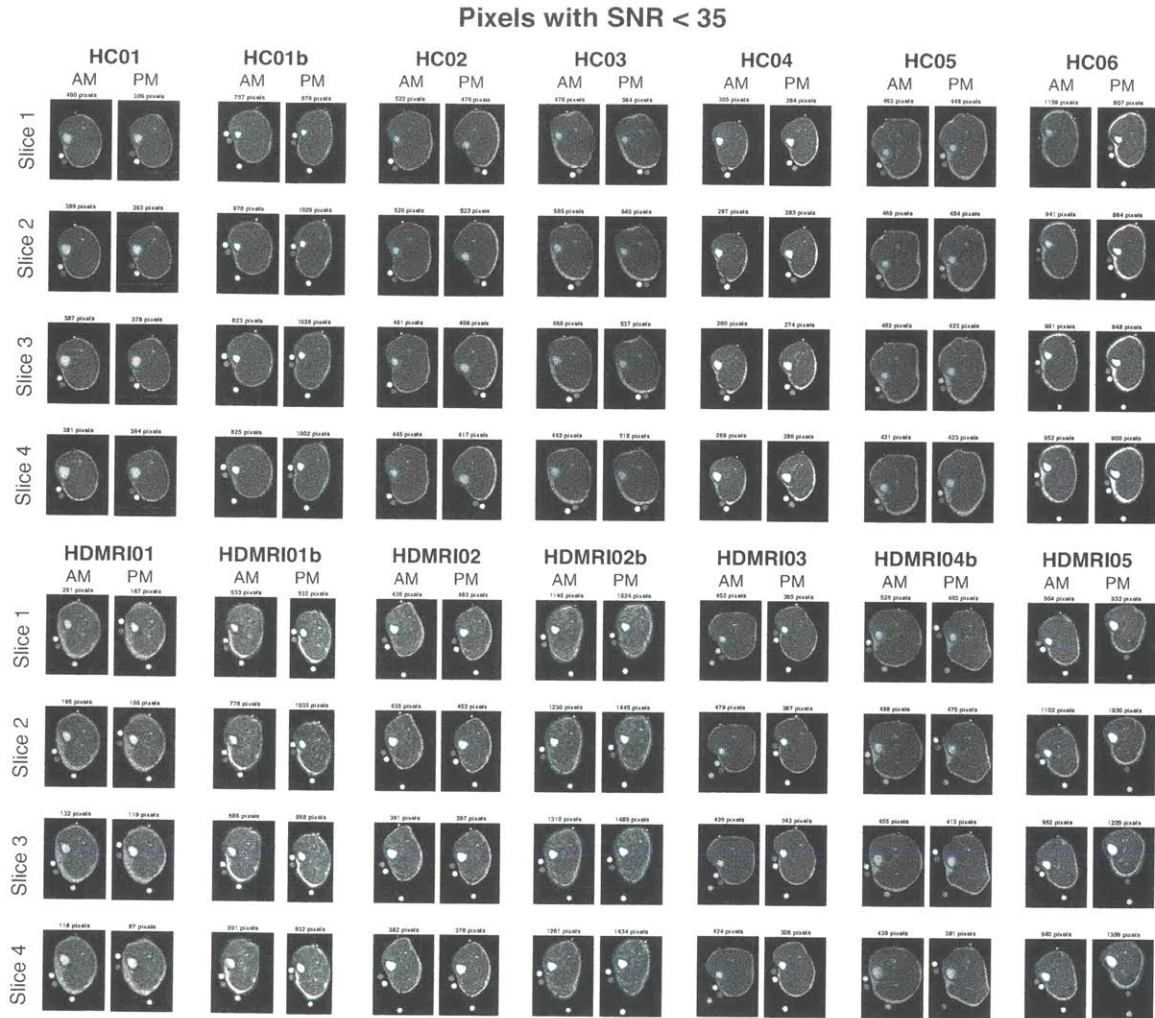


Figure 4-17: Overlaid CDF plots of SNR distributions for all subjects with (A) AM values on the left, and (B) PM values on the right. Dialysis patients typically have higher SNRs in their scans than healthy controls.

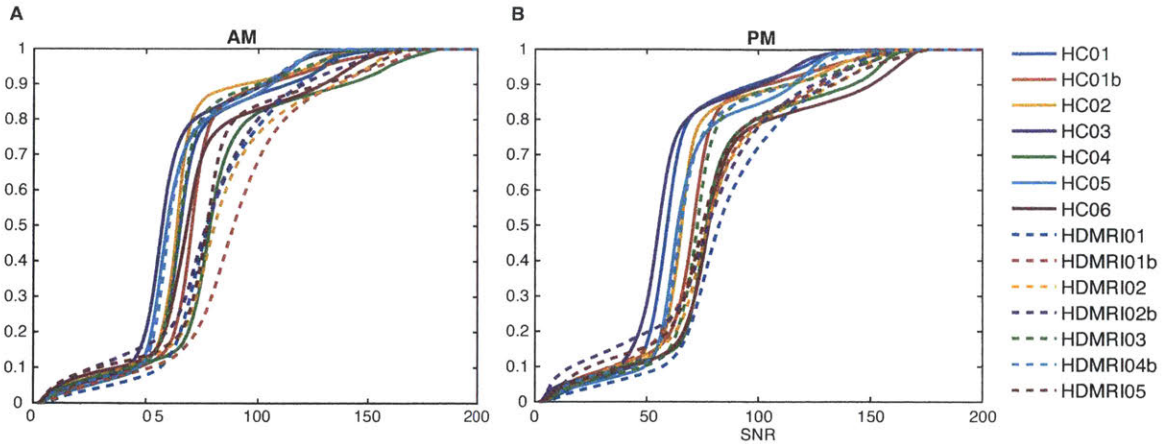


Figure 4-18: Pixels (highlighted in blue) for each scan that have an SNR < 35. Less than 10% of pixels on each scan have an SNR below 35 and they are typically located in the bone, blood vessels, fascia, or background area outside of the leg.

assumption of noise stationarity was used. Future work could involve using alternate methods of calculating noise to obtain more accurate estimates of pixel SNR.

### Implementation Notes

The scripts used to calculate noise and generate SNR plots are located in this project’s Github: `process_noise.m`, `merge_results_with_masks_snr.m`, `analyze_pixel_by_pixel_results.m`.

### 4.2.4 Physiologic Meaning of Bi-exponential Fits

The origin of multi-exponentiality in MR measurements generally arises from the movement of a molecule from one environment to another, such as from the inside to the outside of a cell. Each molecular environment has a different relaxation time. When multiple environments are measured together, the resulting  $T_2$  decay is multi-exponential.

Biological systems are often described as a spectrum of  $T_2$  relaxation times, given the complexity and constantly moving nature of protons in living systems. There are several benefits, however, of reducing a complex biological system to a multi-exponential model including reproducibility and ease of comparing across time points and between subjects. When analyzing biological data with a multi-exponential model, we call on the aphorism:

“All models are wrong, but some are useful.” - George  $B_0x$

There is definite utility in simplifying biological systems to multi-exponential models with a finite

number of components. The question is then: what do the various components correspond to physiologically?

Several researchers have done dedicated experiments to explore this question. It is agreed upon that the short component arises from intracellular fluid, and the longer component extracellular fluid. There is some lack of consensus around whether the interstitial fluid contributes to the short or long component<sup>62,77,98,99</sup>.

Therefore, when we analyze our bi-exponential results, the first component (relaxation time 1 and amplitude 1) is related to intracellular fluid, whereas the second component (relaxation time 2 and amplitude 2) is related to extracellular fluid.

### **Future Work**

Future work could involve experimentally determining the physiological correspondence of the components in our MR data, rather than relying on literature.

The computational manner of doing this is to apply the Bloch-McConnell equations to our data and determine reasonable proton residence time values that still model our data accurately. This method can point towards which exponentials correspond to which fluid compartments in the body: intracellular, interstitial, and vascular. We recommend reading the paper by Araujo, et. al. to understand the methods for doing so<sup>77</sup>.

The experimental manner of figuring out the physiological correspondence of the two exponentials involves administering contrast agents. Gadolinium is designed to equilibrate in both the interstitial and vascular spaces, whereas albumin-based contrast agents will stay solely in the vascular space. Since these contrast agents are also  $T_2$ -shortening agents, we can administer them to a subject, see which relaxation time is shortened as a result, and deduce which component corresponds to which physiological space(s).

## **4.2.5 Results**

Figures 4-19 and 4-20 show heatmaps of relaxation time 1, relaxation time 2, and relative amplitude 2 for each subject.

### **Relaxation Times**

#### **Muscular Tissue**

Figure 4-21 shows AM and PM histograms of relaxation times for each subject. There are not large relaxation time shifts observed in any of the patients. The greatest shifts between AM and PM histograms occurred between 70-170ms in dialysis subjects. Healthy controls did not have the same magnitude of shifts between AM and PM histograms, with the exception of HC02 and HC06.

These two healthy controls proved to be an exception in nearly every analysis type we did; they behaved more like dialysis patients than healthy controls. We believe that these two subjects became dehydrated between their AM and PM MRI scans. Their dehydration (fluid loss) looks similar in MR data to the fluid loss of dialysis patients. This hypothesis is expanded upon in the discussion and conclusions section (Section 4.2.5).

Table 4.3 summarizes the results of a t-test to compare the distribution percentiles of healthy controls compared to dialysis patients. The 15-65% percentiles in the AM were very statistically different between the two populations. In the PM scan, only percentiles 40-85% were statistically different and much less so than in the AM.

#### **Subcutaneous Tissue**

There were no systematic changes in the histogram of relaxation times of the subcutaneous tissue (Figure 4-22). The first relaxation time of both subcutaneous and muscular tissues overlap at approximately 40ms, while their second relaxation times are at distinct locations (~70-170ms for muscular tissue, ~200-250ms for subcu) as seen in Figure 4-23.

### **Relative Amplitude 2**

#### **Muscular Tissue**

Overlaid AM and PM histograms of relative amplitude 2 (from here on called simply 'amp2') in the muscular tissue of HD subjects shows that the amplitude distribution shifted downward after dialysis (Figure 4-24). Healthy control subjects did not have a downward shift in their amp2 distributions, except for HC02 and HC06 for reasons hypothesized above.

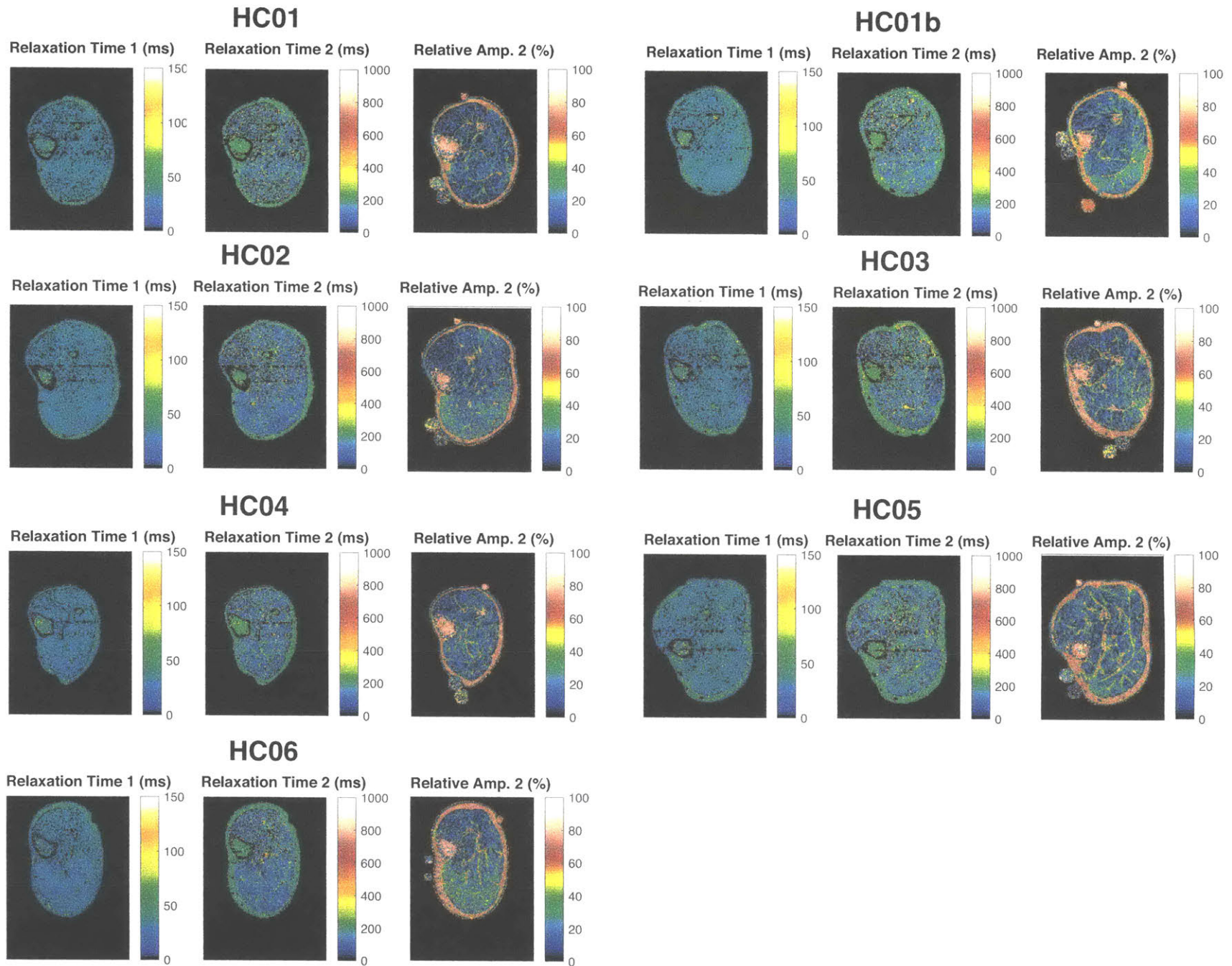


Figure 4-19: Heatmaps of relaxation times and relative amplitude for healthy controls. Heatmaps are from pixel-by-pixel bi-exponential fit results with no pixels deleted yet. Images are of AM scan and slice 1.

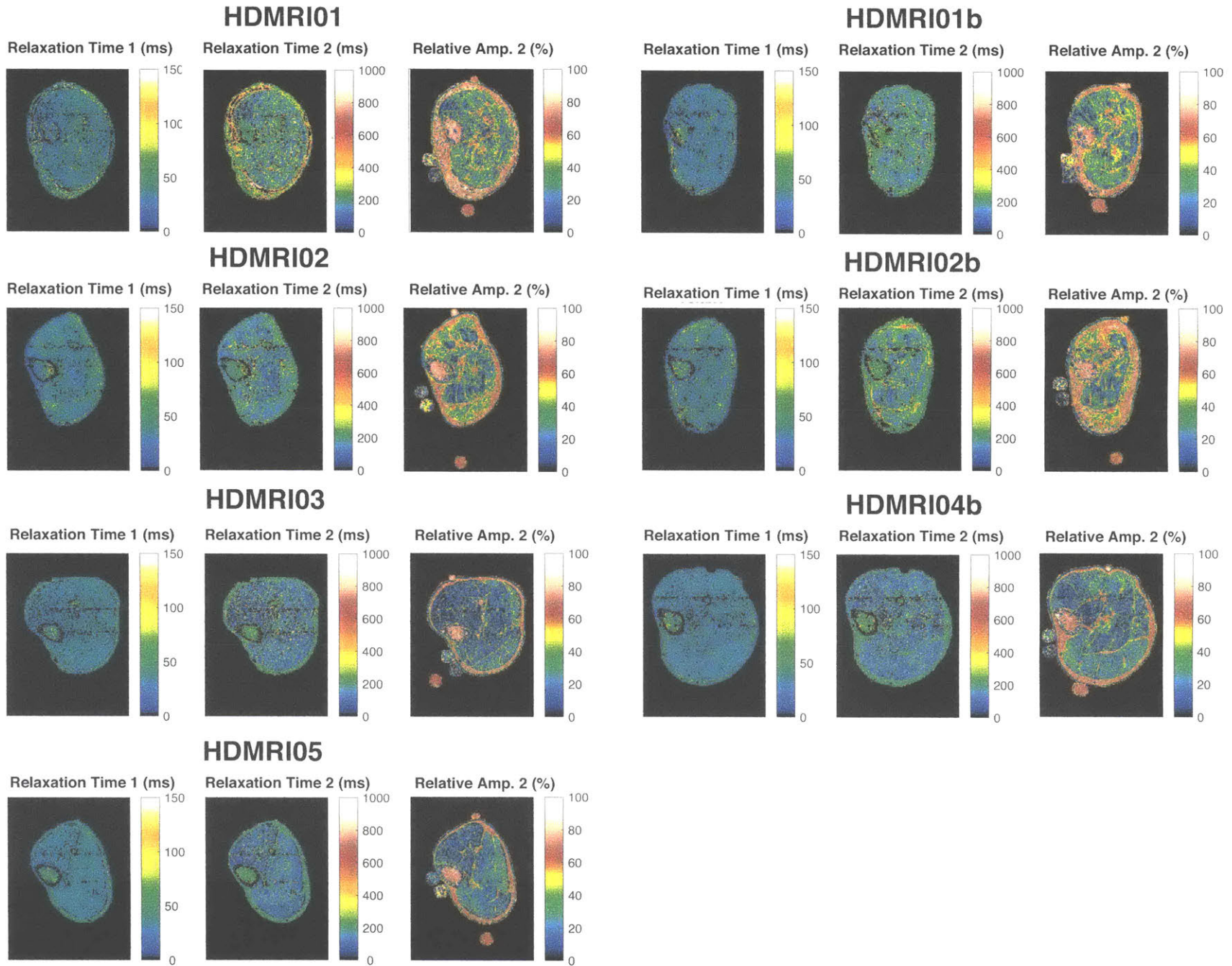


Figure 4-20: Heatmaps of relaxation times and relative amplitude for dialysis patients. Heatmaps are from pixel-by-pixel bi-exponential fit results with no pixels deleted yet. Images are of AM scan and slice 1.

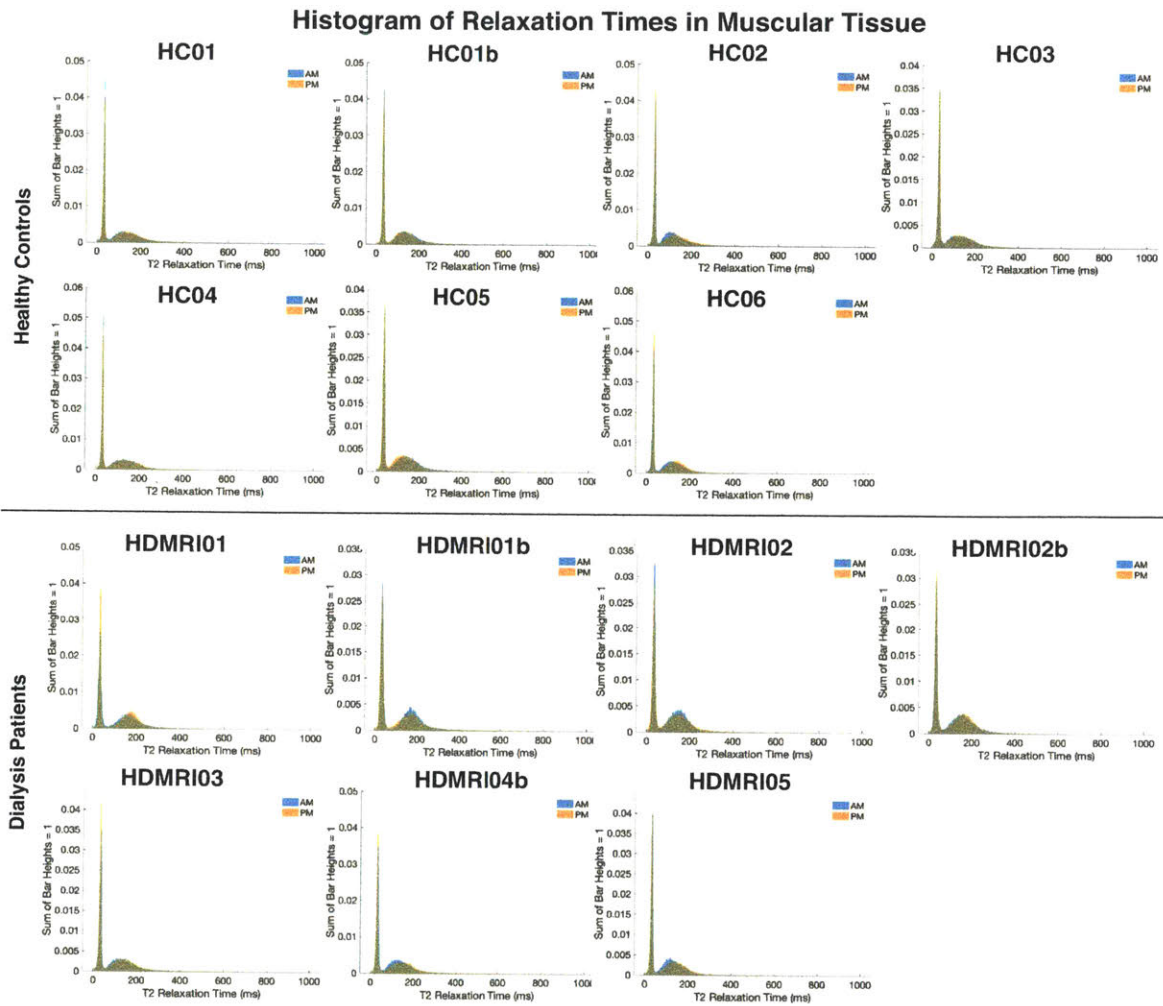


Figure 4-21: Histogram of relaxation times 1 and 2 in the muscular tissue for each subject. AM values (blue) and PM values (orange) are overlaid. Dialysis patients tended to have PM values that shifted, especially in the 70-170ms range. Healthy controls did not have PM values that shifted, except for HC02 and HC06.

Tissue	Parameter		Percentile																		
			5%	10%	15%	20%	25%	30%	35%	40%	45%	50%	55%	60%	65%	70%	75%	80%	85%	90%	95%
Muscular Tissue	Relative Amp 2	AM	0.0041	0.0028	0.0025	0.0021	0.0020	0.0019	0.0019	0.0018	0.0019	0.0019	0.0018	0.0019	0.0020	0.0021	0.0023	0.0027	0.0028	0.0032	0.0035
Muscular Tissue	Relative Amp 2	PM	0.0274	0.0297	0.0281	0.0290	0.0271	0.0263	0.0251	0.0245	0.0246	0.0244	0.0242	0.0239	0.0231	0.0235	0.0237	0.0229	0.0223	0.0222	0.0229
Muscular Tissue	$T_2$ Relax. Times	AM	0.3639	0.2411	0.0379	0.0036	0.0002	0.0000	0.0000	0.0001	0.0002	0.0041	0.0271	0.0359	0.0476	0.0671	0.1027	0.1697	0.3177	0.8314	0.2505
Muscular Tissue	$T_2$ Relax. Times	PM	0.9491	0.9409	0.6391	0.3102	0.1619	0.0956	0.0646	0.0461	0.0307	0.0091	0.0076	0.0038	0.0028	0.0020	0.0017	0.0032	0.0162	0.2013	0.8139
Subcutaneous Tissue	Relative Amp 2	AM	0.2957	0.1925	0.1694	0.1710	0.1771	0.2112	0.2481	0.2607	0.2876	0.3232	0.3318	0.3421	0.3858	0.4843	0.5671	0.7223	0.9329	0.8172	0.5160
Subcutaneous Tissue	Relative Amp 2	PM	0.1919	0.1629	0.1629	0.1598	0.1623	0.1720	0.1731	0.1812	0.1884	0.2040	0.2152	0.2221	0.2596	0.2886	0.3330	0.4269	0.4970	0.8091	0.7998
Subcutaneous Tissue	$T_2$ Relax. Times	AM	0.8645	0.7241	0.7904	0.9269	0.9073	0.7091	0.5269	0.3996	0.2444	0.9869	0.4133	0.9736	0.6800	0.5331	0.4532	0.4019	0.3599	0.3220	0.2842
Subcutaneous Tissue	$T_2$ Relax. Times	PM	0.5744	0.4593	0.4558	0.4692	0.5130	0.6216	0.7743	0.9608	0.8239	0.3056	0.4533	0.9198	0.5509	0.4085	0.3323	0.3062	0.2802	0.2544	0.2259
Whole Leg	Relative Amp 2	AM	0.0044	0.0033	0.0029	0.0029	0.0028	0.0028	0.0031	0.0033	0.0037	0.0043	0.0053	0.0070	0.0112	0.0218	0.0625	0.2123	0.4822	0.6839	0.6490
Whole Leg	Relative Amp 2	PM	0.0269	0.0264	0.0259	0.0242	0.0231	0.0227	0.0220	0.0217	0.0214	0.0214	0.0215	0.0249	0.0336	0.0710	0.1616	0.3733	0.6496	0.7986	0.7839
Whole Leg	$T_2$ Relax. Times	AM	0.6428	0.5165	0.0714	0.0017	0.0002	0.0002	0.0005	0.0022	0.0166	0.0215	0.0358	0.0514	0.0806	0.1428	0.2661	0.3662	0.3683	0.3913	0.6238
Whole Leg	$T_2$ Relax. Times	PM	0.8125	0.7027	0.9850	0.5174	0.2261	0.1003	0.0608	0.0440	0.0685	0.0448	0.0094	0.0057	0.0049	0.0065	0.0164	0.0392	0.0729	0.1280	0.2482

Table 4.3: Summary of p-values from comparing healthy controls' versus dialysis patients' percentile values for various parameters and tissues. Values in blue are statistically significant to the  $p < 0.05$ . The relative amplitude 2 of muscular tissue in the AM were the most statistically significant metric to compare HC vs HD subjects. The relative amplitude 2 values of muscular tissue in the PM were still statistically significant but not as much as in the AM. There were no parameters that were statistically significant for the subcutaneous tissue.

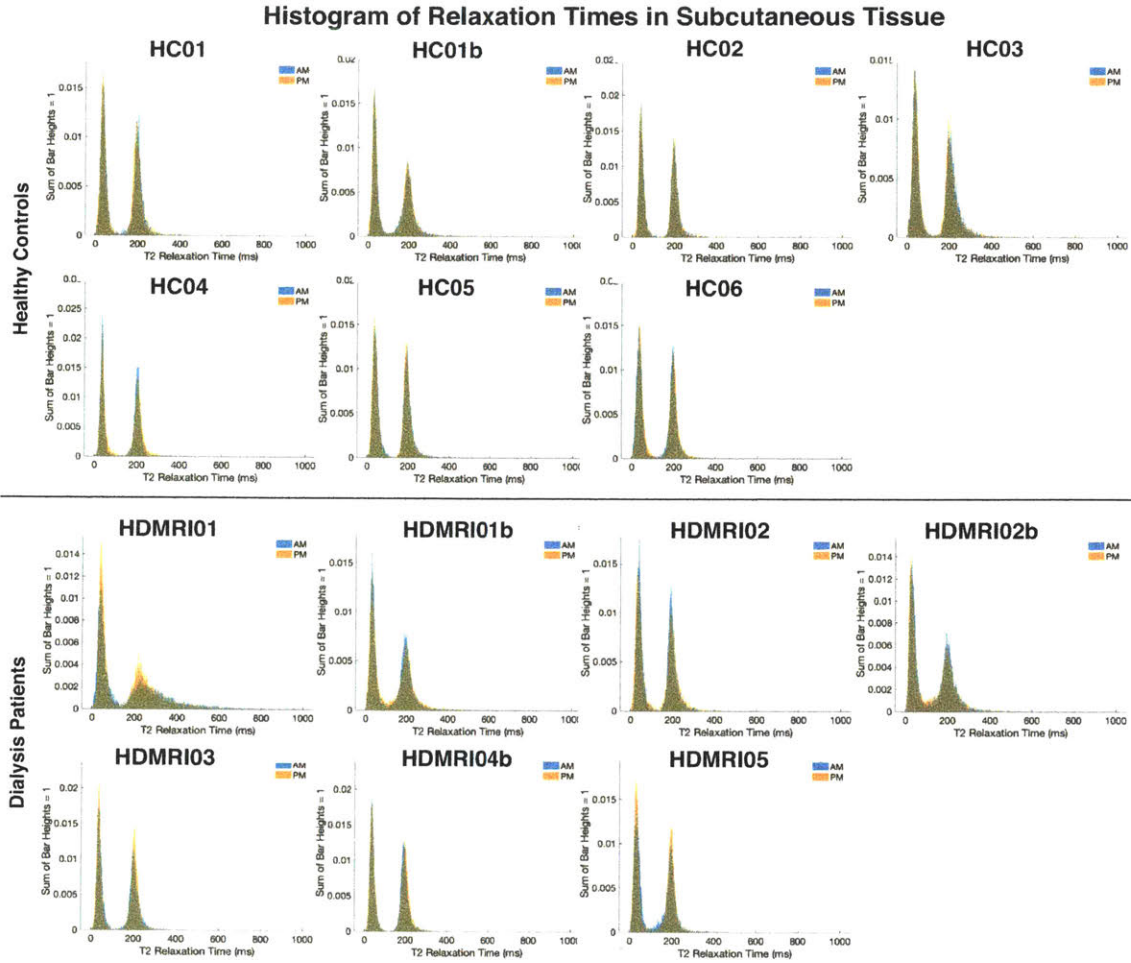


Figure 4-22: Histogram of relaxation times 1 and 2 in the subcutaneous tissue for each subject. AM values (blue) and PM values (orange) are overlaid. There were no systematic changes between the AM and PM distributions for either healthy controls or dialysis patients.

### Histogram of Relaxation Time Values in Subcutaneous vs Muscular Tissues

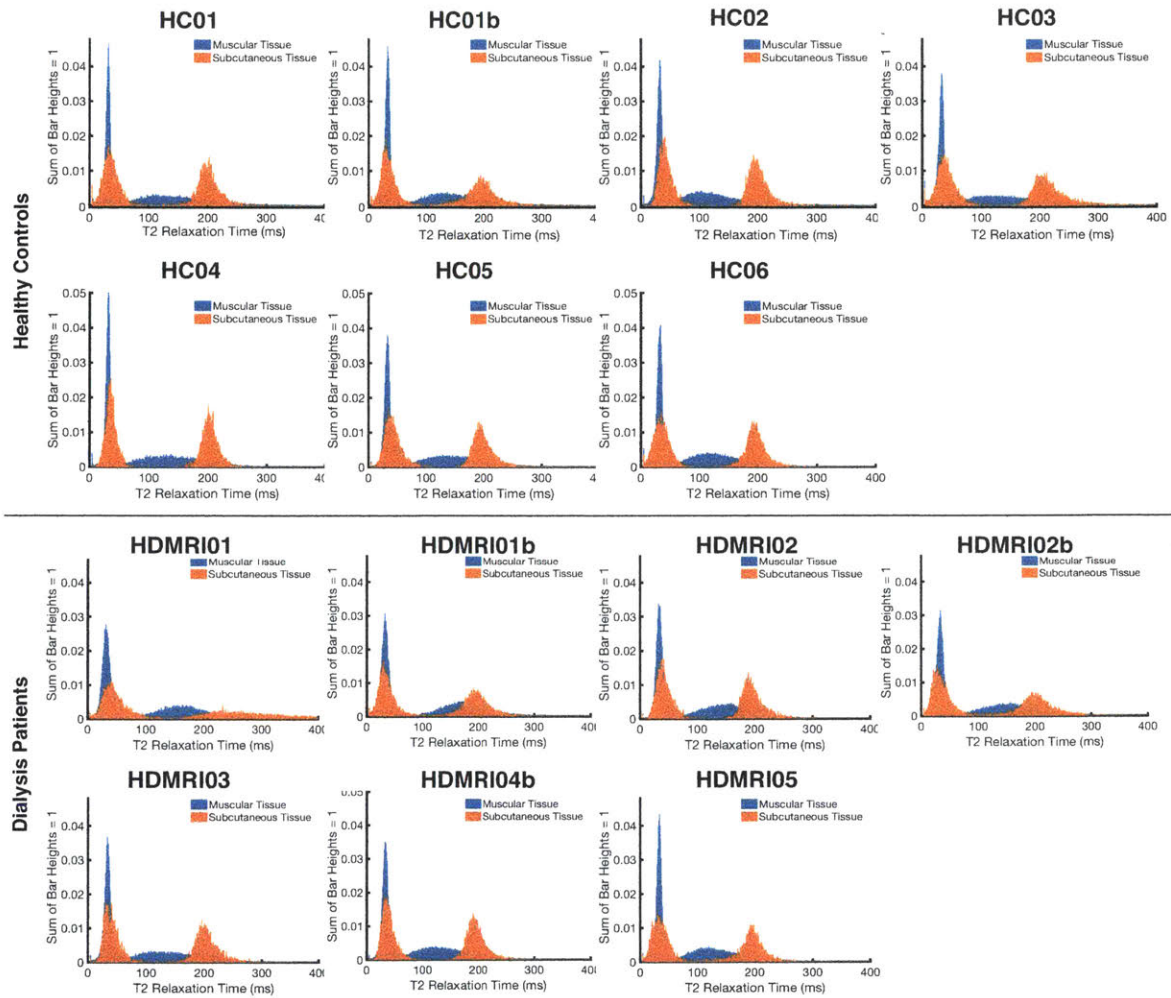


Figure 4-23: Overlaid histogram of relaxation times in the muscular tissue (blue) and subcutaneous tissue (orange). The first relaxation time in each the two tissue types are equal, but the second relaxation times are in distinct locations. The second relaxation time is located at approximately 120ms for the muscular tissue and approximately 200ms for the subcutaneous tissue.

The AM cumulative distribution function (CDF) of the amp2 distributions for HC and HD subjects shows that HD subjects initially had higher amp2's compared to HCs (Figure 4-25). The CDF of dialysis patients shifted downward to be closer to that of healthy controls after dialysis (Figure 4-25). The elevation of amp2 values in HDs was statistically significant from the 5th to the 95th percentile. The 50th percentile was most significant: the average 50th percentile for HCs was 17.5% and HDs was 28.4% ( $p=0.0019$ ). The p-values for comparing HCs versus HDs at each percentile are summarized in Table 4.3.

The area between the AM and PM histograms for each subject was calculated by plotting the AM and PM CDF (Figure 4-26), calculating the difference between the two curves (Figure 4-27), and then integrating across the difference curve (Figure 4-28). A two-sided t-test was performed on the final integral value of HC and HD subjects. The difference in area between HC and HD subjects was statistically significant with  $p=0.0042$ .

### **Subcutaneous Tissue**

Overlaid AM and PM histograms of amp2 in the subcutaneous tissue shows no systematic changes between the AM and PM values for either healthy controls or dialysis patients (see Figure 4-29).

## **Discussion and Conclusions**

### **Fluid Overload**

Through pixel-by-pixel multi-exponential fitting, we have identified the MR parameter in the lower leg (relative amplitude 2) and tissue type (muscle) that is most sensitive to fluid loss after dialysis.

Before the study began, we hypothesized that fluid overloaded subjects would have elevated relaxation times and that fluid removal would lead to a decrease in relaxation times. This hypothesis turned out to be true with some caveats. The most edematous patients – dialysis patients 1, 1b, and 2b – had elevated relaxation times in their muscular tissue compared to all other subjects and their relaxation times shifted downward after dialysis. These more edematous patients – dialysis patients 1 and 2 – are particularly interesting because they both came back to repeat the study 6 months to 1 year later.

During his first visit, dialysis patient 1 had perifascial fluid deposits in his lower leg, as confirmed by an MSK radiologist who looked at his MRI scans, and corresponding elevated relaxation times. When he came back 1 year later, dialysis patient 1 (now referred to as 1b) had had his dry weight

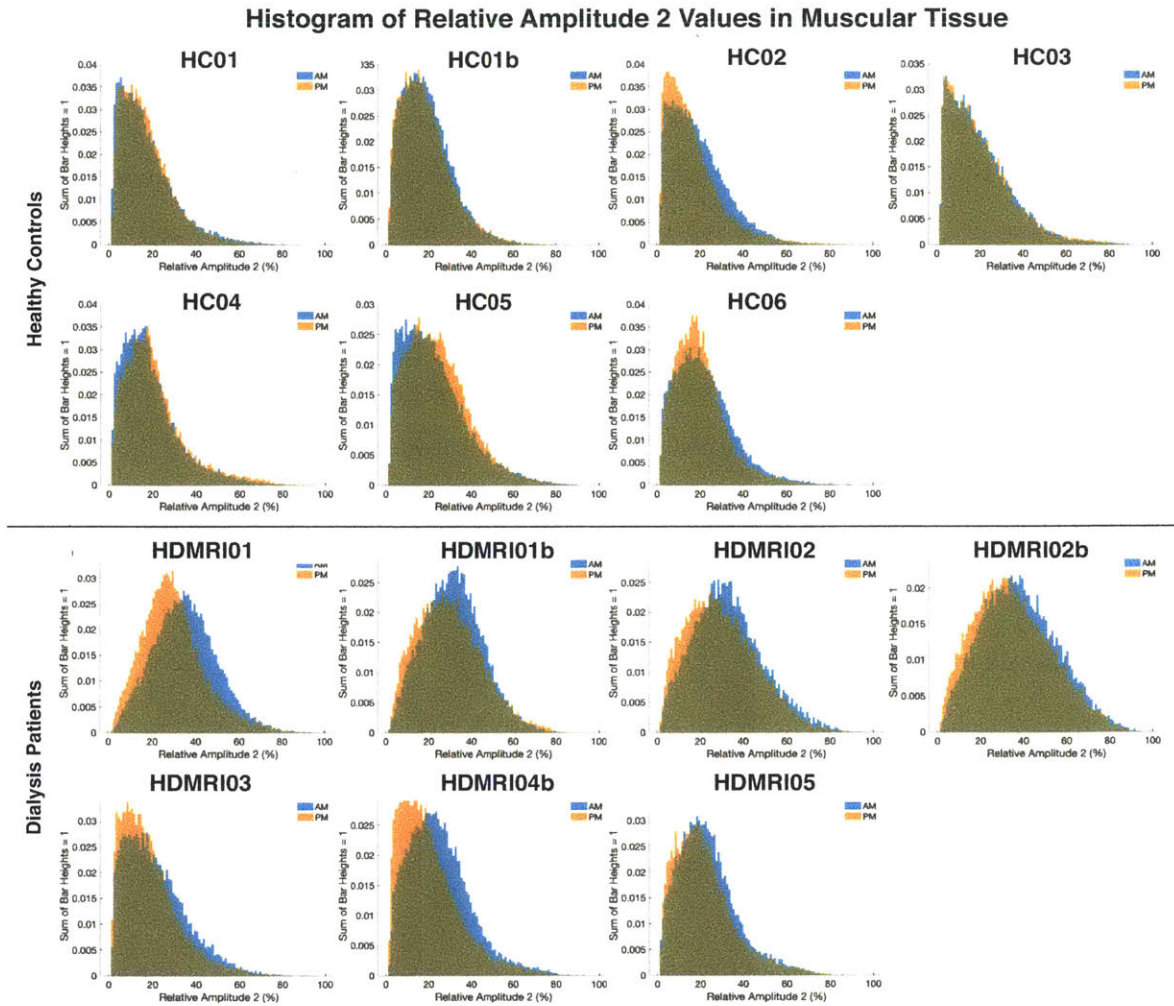


Figure 4-24: Histograms of relative amplitude 2 values for all subjects with AM (blue) and PM (orange) histograms overlaid on top of each other. Dialysis patients had large downward shifts in their histograms after dialysis (PM) compared to before (AM). Healthy controls stayed largely the same, except for HC02 and HC06, who also shifted downwards in the PM scan.

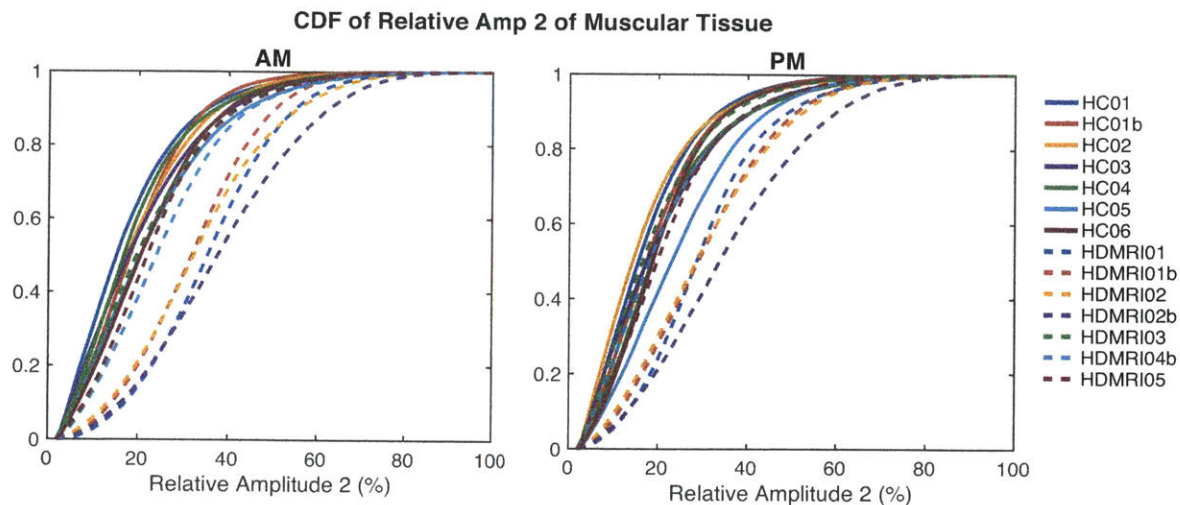


Figure 4-25: The cumulative distribution plots of relative amplitude 2 values for all subjects overlaid on top of each other, with AM values on the left and PM values on the right. Dialysis patients (dotted lines) have tend to have larger relative amplitude 2 values than healthy controls, especially in the AM. Dialysis patients' relative amplitude 2 values shifts downward after dialysis to be closer to that of healthy controls.

lowered by his nephrologist over the course of those 12 months. He had much less perifascial fluid as well as lower relaxation times in his leg.

During dialysis patient 2's first study visit, his relaxation times looked similar to those of a healthy control. When he came back 6 months later, dialysis patient 2 (now referred to as 2b) had elevated relaxation times in his lower leg. During this second visit, dialysis patient 2b had elevated blood pressure throughout his dialysis run, which served as a clinical confirmation that he was more fluid overloaded than normal.

It is important to note that neither of these two patients in any of their visits had signs of lower extremity edema detectable on physical exam, either by the nephrologist, dialysis nurse, or Lina. Our findings of elevated relaxation times in these patients show that relaxation times increase in patients with fluid overload above a certain threshold. Importantly, the relaxation time elevation in the muscular tissue precedes signs of lower extremity edema detectable on physical exam.

Many dialysis patients, however, did not have significantly elevated relaxation times. These other patients had elevated relative amplitude 2 values, however. Relative amplitude 2 of the muscular tissue was the parameter with the greatest sensitivity to changes due to dialysis. All dialysis patients had elevated amplitude 2 values and this amplitude decreased after dialysis to be closer to the values seen in healthy controls. Healthy controls, on the other hand, did not experience significant changes in their relative amplitude 2 values in the morning versus afternoon

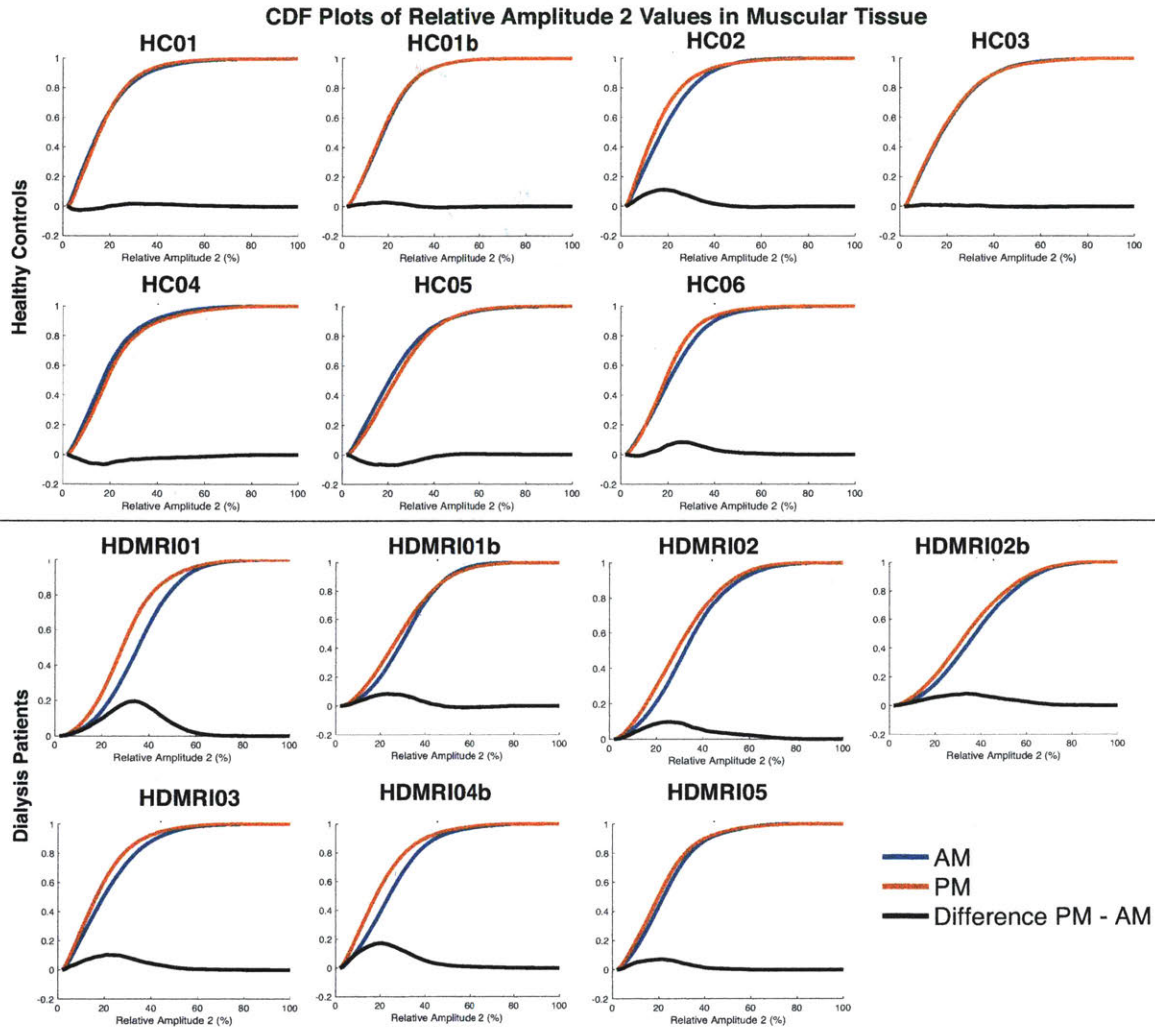


Figure 4-26: Cumulative distribution plots of relative amplitude 2 values for all subjects with AM (blue) and PM (orange) CDFs overlaid on top of each other and the difference between them shown in black. Positive values in the difference curve mean that the PM values decreased. Negative difference values mean that the PM values increased compared to the AM values.

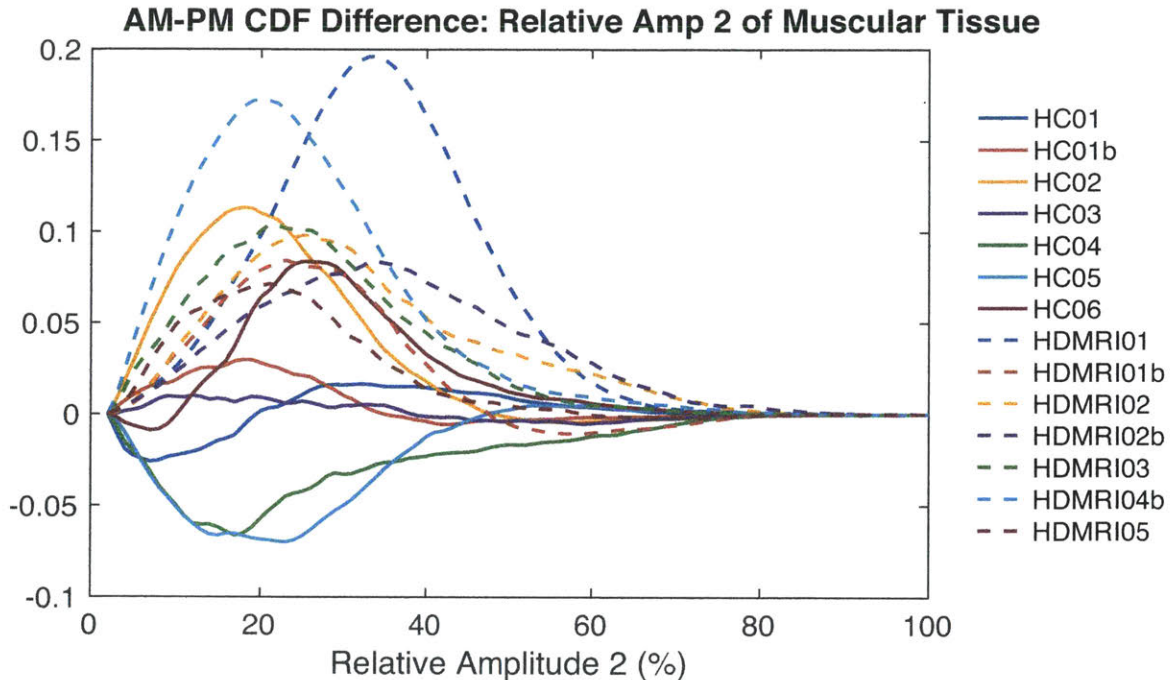


Figure 4-27: The difference between the AM and PM CDFs of relative amplitude 2 values for all subjects overlaid on top of each other. Positive values mean that the PM values decreased, and negative values mean that they increased compared to the AM values.

measurement.

Relative amplitude 2 corresponds to the relative quantity of protons in the extracellular space of the tissue, which are the protons in more mobile (fluid) environments and therefore have longer  $T_2$  relaxation times. An elevation in relative amplitude 2 values indicates that the relative amount of extracellular fluid is increased in the tissue, and vice versa for a decrease. There is literature evidence showing that fluid overloaded patients do, indeed, accumulate fluid in the extracellular space<sup>12,100,101</sup>.

The subcutaneous tissue did not have any consistent AM to PM changes in either the relaxation times or the relative amplitude.

Putting these MRI results together, we learned that the muscular tissue - which includes muscle, connective tissue, and blood vessels - is the location where changes in response to ultrafiltration at dialysis are occurring. The first MR sign of fluid overload is an increase in the relative amplitude of the muscular tissue. After a certain threshold of fluid accumulation has been reached, the relaxation time of the muscular tissue starts to increase. Both relative amplitude and relaxation time (if the subject has reached a yet undefined fluid accumulation threshold) decrease in response to fluid removal during dialysis. Any future MR sensor design should be optimized to measure the muscular

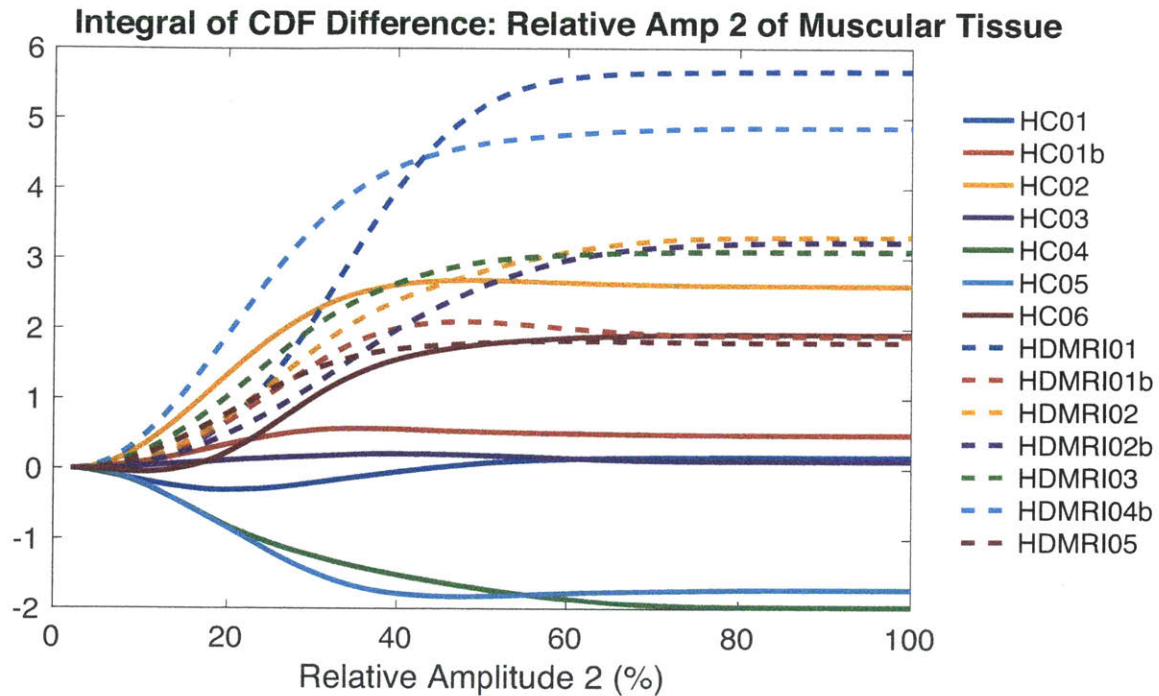


Figure 4-28: The area between AM and PM relative amplitude 2 histograms (in other words, the integral of the curves in Figure 4-27). The value corresponding to 100% on the x-axis indicates the total area between the two histograms. Positive values indicate that the PM amplitude values shifted downwards. Negative values indicate that the PM amplitude values shifted upwards relative to the AM values. Large absolute values indicate large changes between AM and PM histograms. Dialysis patients all had positive integrals. Most healthy controls had negligible or positive integral values. HC02 and HC06 are the exception of two healthy controls who also had positive integrals indicating a decrease in relative amplitude 2 values in the PM scan. The p-value between the dialysis and healthy controls is 0.0026.

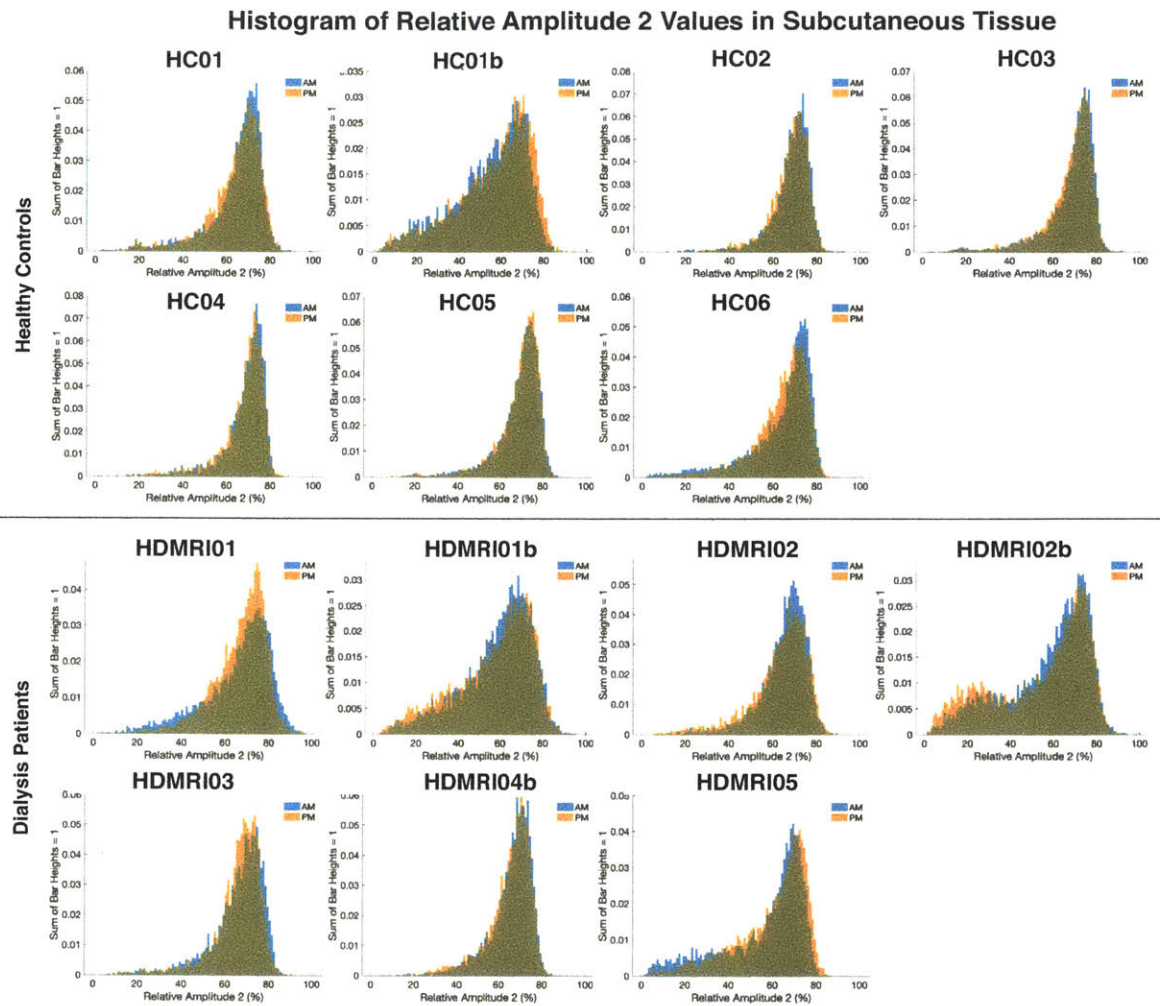


Figure 4-29: Histogram of relative amplitude 2 values in the subcutaneous tissue. There were no systematic changes between the AM and PM distributions for either healthy controls or dialysis patients.

tissue of the lower leg.

### **Dehydration**

The MRI results for healthy controls stayed relatively constant between AM and PM scans with the exception of HC02 and HC06. These two subjects experienced MR changes similar to those of dialysis patients. We hypothesize that both HC02 and HC06 became dehydrated (experienced fluid loss) between the two measurements and therefore their MR signal looked similar to those of dialysis patients who experience fluid losses as well.

HC02 was dehydrated at the start of the study based on serum osmolality and sodium levels (Osm = 302 mOsm/kg, Na = 144 mmol/L) on arrival and became more dehydrated throughout the study since he was not permitted to eat or drink for 4 hours. HC02's AM relative amplitude 2 value was lower than that of all other healthy controls and dropped lower in the PM measurement.

HC06 was remarkable because he did not eat or drink much after the 4-hour portion of the study at MGH Main Campus before returning for the second PM MRI scan. His blood levels (Osm = 294 mOsm/kg, Na = 142 mmol/L) were on the edge of normal, tending toward dehydration, at the start of the study. We hypothesize that he became dehydrated over the course of the study, did not replenish his fluid loss before the second MRI, and was dehydrated for the second scan.

Our study was not specifically designed to assess MR's ability to detect dehydration, but these are promising incidental findings that suggest dehydration may show up in MR measurements through depressed relative amplitude values. A future study specifically designed to assess dehydration should be undertaken to test this hypothesis. Careful tracking of fluid and food intake should continue in any future experiments.

A diagram summarizing our MR findings in the spectrum of hydration states is show in Figure 4-30.

### **Limitations**

Some limitations of MRI for quantitative  $T_2$  measurements include the scanner's limits on echo time and echo train length.

The Siemens 1.5T scanner with extremity coil used in this study had a lower echo time limit of 8ms. By comparison, the MR sensor had a lower echo time limit of 80us. This meant that  $T_2$  values below 4ms could not be measured in the MRI.

Furthermore, Siemens scanners have a hard-limit of 32 echoes in their CPMG sequence (se2d32) and sequence programming experts at the Martinos Center said there was no way around this limit. By comparison, the single-voxel MR sensor can measure 8000 echoes. A  $T_2$  decay curve with only

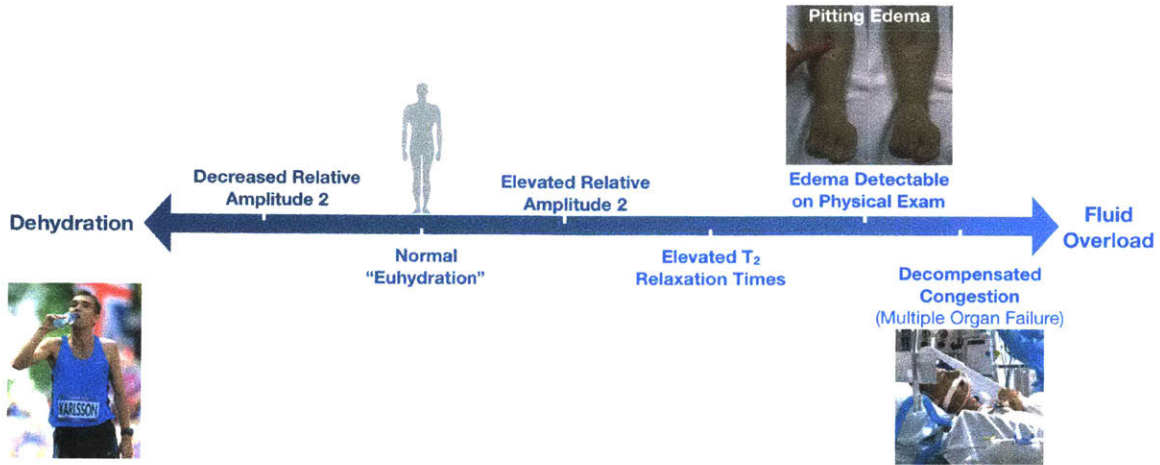


Figure 4-30: The fluid balance continuum and the MR findings at various points along the scale.

32 points has several disadvantages. First, depending on the tissue, the curve does not decay fully, which means that the accuracy of measuring longer relaxation times is compromised. The potential compromise of longer relaxation times is an issue for our study since we hypothesized, and, in fact, observed that fluid overloaded patients have longer relaxation times. Second, there is a limit on the number of exponentials that a decay with so few points can be fit to. Our MRI data can be fit with a maximum of 2 exponentials, whereas the exact same decay data with 200 points instead of 32 may be fit by 3 or more exponentials. More exponentials are not necessarily better. What is better is having the option of increasing the number of exponentials for a potentially improved fit and more granular look into human physiology.

Despite the MRI scanner's limitations, we can apply the insights garnered through this pixel-by-pixel MRI analysis to the data from our single-voxel MR sensors, which do not have these limitations.

## 4.3 ROI Bi-Exponential Analysis

### 4.3.1 Methods

Instead of performing pixel-by-pixel fits like in the previous section, in this section, entire regions were averaged together and analyzed at once. The average 32-pixel decay across all pixels in a particular region (i.e. muscular tissue) was generated and fit with a bi-exponential curve. The first point was ignored, as is standard practice to do, due to the absence of stimulated echo effects on that point.

### 4.3.2 Results and Discussion

The bi-exponential fit results for are discussed separately for each ROI.

#### **Muscular Tissue**

The bi-exponential fit results for muscular tissue are show in Figure 4-31 and the amplitude results summarized in Table 4.4.

The AM relaxation time 1 (relax1) values were statistically different between HC and HD subjects ( $p=1.67e-4$ ). The PM relax1 values were not statistically different between HC and HD subjects ( $p=0.1363$ ). The relax1 values of muscular tissue for HD patients was initially higher than that of HCs and then shifted downward to be closer to that of healthy controls. The HC patients mostly shifted downward as well, though a few of them increased. Although relax1 seems like a good indicator based on these data, the challenge of using relax1 as the core indicator is that the absolute magnitude of the change is small. The entire range of relax1 values was just 3ms with the difference between healthy and dialysis patients just 1.5ms. It is preferable to have an indicator with a larger dynamic range because we do not want the difference between 1L and 2L of fluid overload to be within the noise of the measurement. It remains to be seen whether all healthy controls are as tightly clustered around 31.5-33ms as the ones in this cohort.

Relaxation time 2 (relax2) values for HCs and HDs were interspersed both at the start and end of the study. Relax2 values for both HCs and HDs tended to increase between the AM and PM measurements. The more edematous subjects - HD01, HD01b, HD02b - had higher relax2 values and were separated from the rest of the subjects. This aligned with our hypothesis that patients with more fluid have higher relaxation times.

The relative amplitude 2 (amp2) values of the muscular tissue of HDs was higher than that of HCs before dialysis (AM) and shifted down to be closer to that of HCs after dialysis (PM). The AM amp2 values were statistically different between HC and HD subjects ( $p=0.0021$ ) and became less statistically different after dialysis ( $p=0.0209$ ). The AM to PM change in amp2 values was highly statistically significant when comparing HC to HD subjects ( $p=7.74e-4$ ).

This analysis was able to separate HD from HC subjects with a single time point. One hypothesis is that perhaps there is a reference range of amp2 values signify euvoemia. Based on these data, the ‘normal range’ of amp2 values is between 12-20%. When a person has amp2 values above 20%, they are congested. On the flip side, when a congested patient reaches 12-20%, they are at their dry weight (i.e. euvoemia). Additional data will have to be gathered, especially on individuals of differing races, to corroborate this hypothesis. Both HD03 and HC02 were Asian and are on the low-end of amp2 values, which leads to the hypothesis that there may be different amp2 reference ranges for different races.

The fact that HD03 and HD05 started out in the “normal range” might indicate that they do not accumulate much fluid in their legs, but rather in another body part (i.e. lungs, etc.).

### **Muscular Tissue Sub-Regions**

The results of a bi-exponential fit for muscle subgroups are shown in Figures 4-32-4-36 and the p-values from comparing the relative amplitude 2 values of HC versus HD subjects are summarized in Table 4.5. The short relaxation times (relax1) of most muscle groups have statistically significant differences between AM values and AM-to-PM change values. However, relax1 as an indicator of fluid levels suffers from the same pitfalls as discussed in the previous whole muscular tissue section: the dynamic range of relax1 values is small and an ideal indicator is one with a large working range.

For the relative amplitude 2 values (see Table 4.5), all muscle sub-groups had statistically significant AM differences between HC and HD subjects. Most muscle sub-groups, except for the gastrocnemius and soleus, had a statistically significant AM-to-PM change between HC and HD subjects.

The deep posterior muscle group was the only one with a statistically significant PM difference between HC and HD subjects ( $p=0.0427$ ). The deep posterior muscle group is flanked by major arteries, veins, and nerves. Although we attempted to exclude these anatomical structures from the ROI, it was not always possible to do so. We expect that signal from deep posterior muscle group might be the one most contaminated by blood signal.

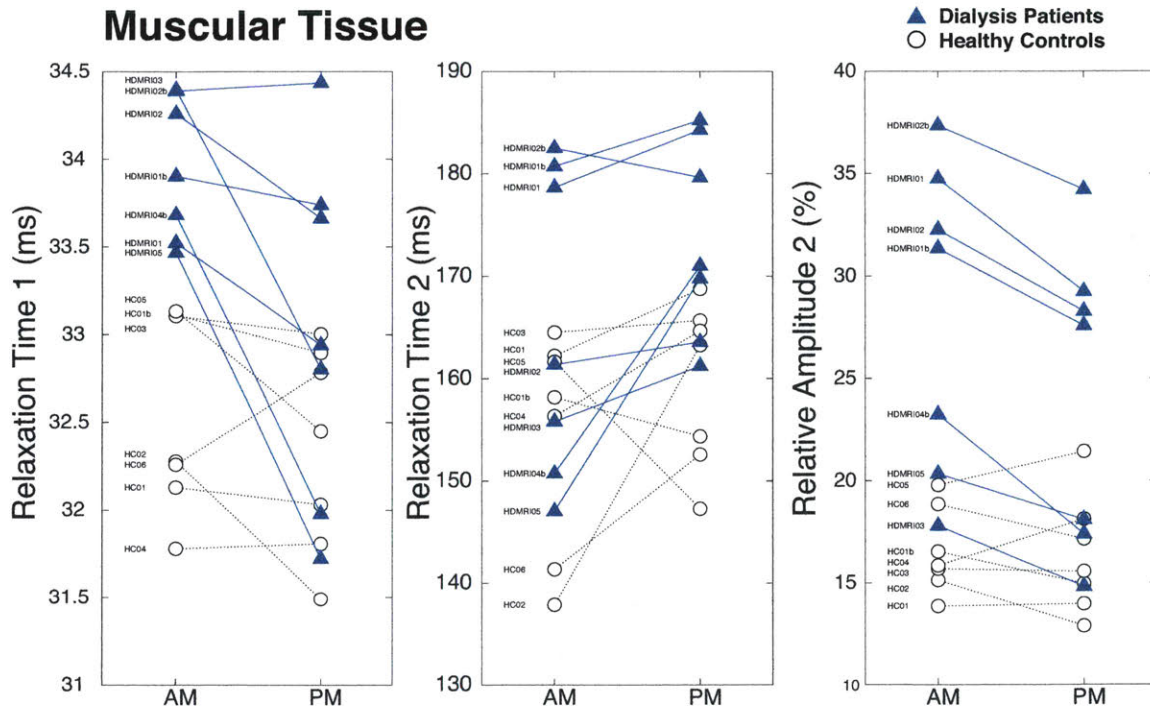


Figure 4-31: The MRI results of the bi-exponential fits for the muscular tissue ROI. The three panels plot AM and PM values of relaxation time 1, relaxation time 2, and relative amplitude 2 from left to right. Both relax 1 and relative amplitude 2 are significantly different between healthy controls and dialysis patients in the AM scan. Dialysis patients' values shift downward to be closer to that of the healthy controls after dialysis.

<b>MRI Muscular Tissue: Relative Amplitude 2</b>			
<b>Subject</b>	<b>AM Amp 2 (%)</b>	<b>PM Amp 2 (%)</b>	<b>Change in Amp 2 (%)</b>
HC01	13.8	14.0	0.1
HC01b	16.5	15.0	-1.6
HC02	15.1	12.9	-2.3
HC03	15.7	15.6	-0.1
HC04	15.9	18.1	2.3
HC05	19.8	21.4	1.6
HC06	18.9	17.1	-1.7
HDMRI01	34.7	29.2	-5.5
HDMRI01b	31.3	27.6	-3.8
HDMRI02	32.3	28.3	-4.0
HDMRI02b	37.3	34.2	-3.1
HDMRI03	17.8	14.8	-3.0
HDMRI04b	23.2	17.4	-5.9
HDMRI05	20.3	18.1	-2.2
<b>HC VS HD t-test, p-value</b>	<b>0.0021*</b>	<b>0.0209*</b>	<b>7.7248e-4*</b>

Table 4.4: Summary of MRI relative amplitude 2 results of the muscular tissue ROI. The AM values of dialysis patients versus healthy controls were statistically different. The PM values were less statistically different. The AM-to-PM change in relative amplitude 2 values between the two groups was highly statistically different.

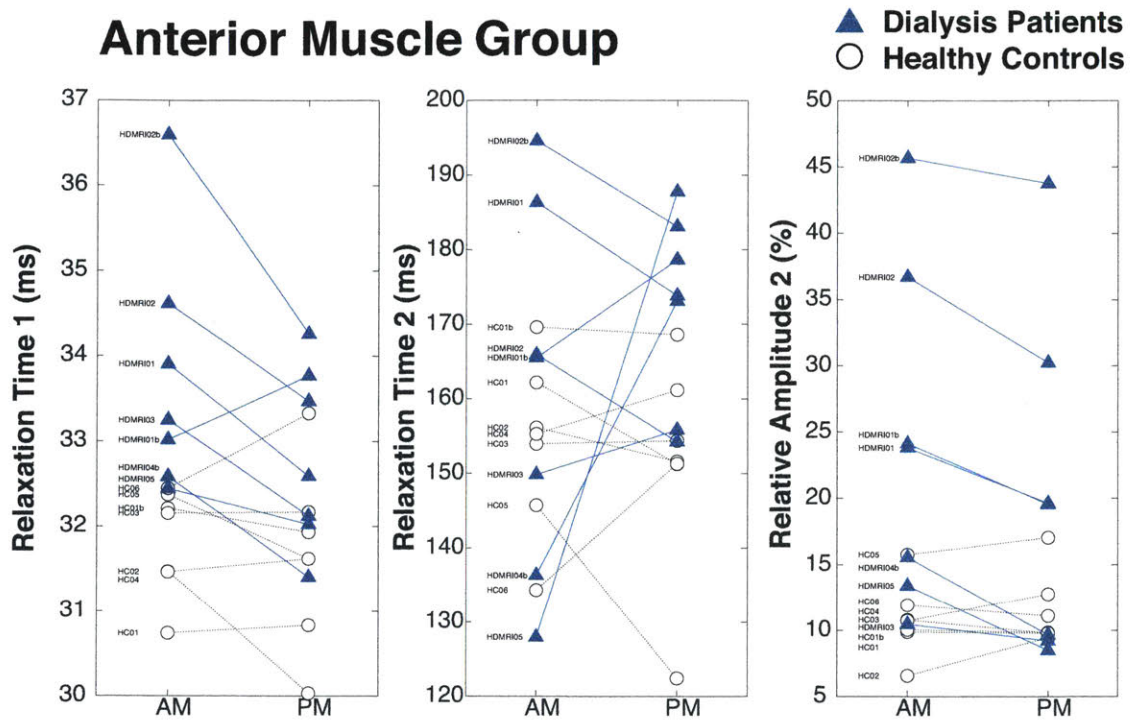


Figure 4-32: The results of a MRI bi-exponential fit for anterior muscle sub-group. The anterior muscles are one of the most promising measurement regions for detecting differences between dialysis patients and healthy controls.

The lateral muscle group had the second best significant difference between HC and HD AM values ( $p=0.00919$ ) but less so on the AM-to-PM change ( $p=0.0191$ ). The anterior muscle group had the most significant difference between AM-to-PM change ( $p=0.000247$ ) and was still significant on the AM value comparison ( $p=0.0195$ ) between HC and HD subjects. In addition to achieving the largest statistical significance of all muscle groups, the lateral and anterior muscle groups are promising ones for further investigation because they are also superficial and therefore easier to measure with a single-sided MR sensor.

### Subcutaneous Tissue

There were no clear HC versus HD separations or AM-to-PM changes for relaxation time 1 (relax1) values of the subcutaneous tissue, except that HD01's – one of the edematous patient's - relax1 value was much higher than that of all other subjects (Figure 4-37). The same was true for relaxation time 2 (relax2). The high relaxation values of HD01 suggest that edematous patients can be identified based on the high  $T_2$  relaxation time of their subcutaneous tissue. This finding has been reported in literature<sup>20,23</sup>. Studies in literature tended to analyze patients that were more

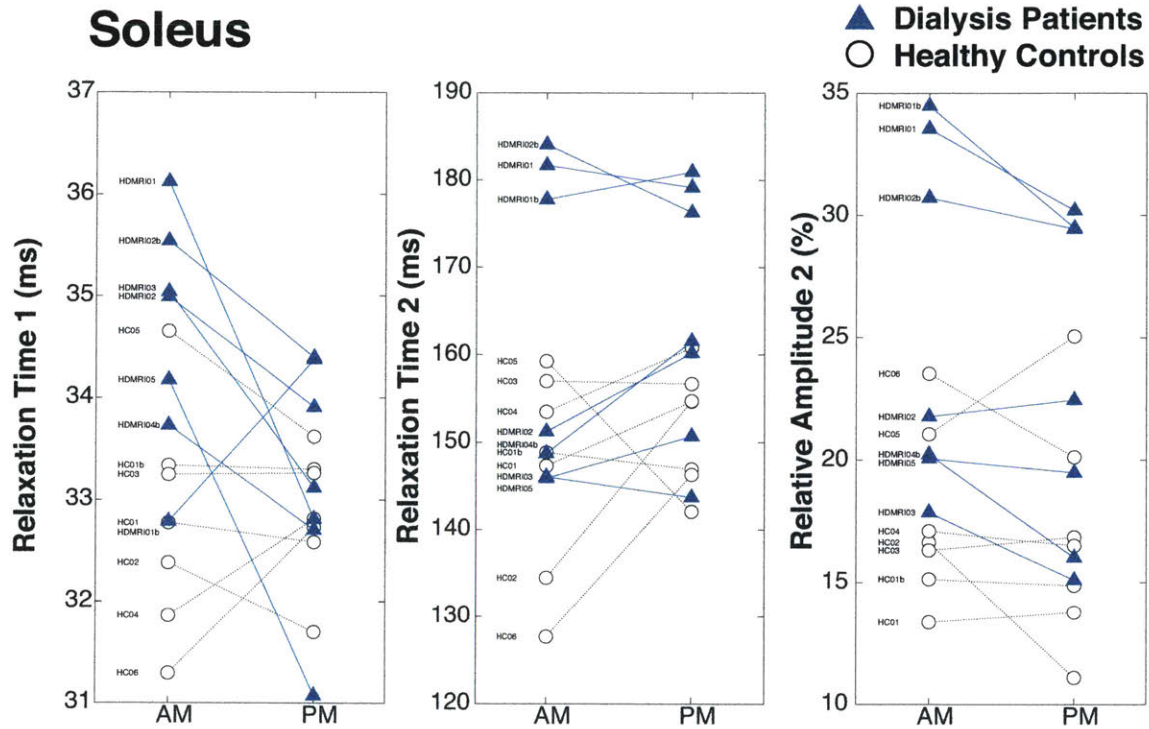


Figure 4-33: The results of a MRI bi-exponential fit for the soleus muscle sub-group.

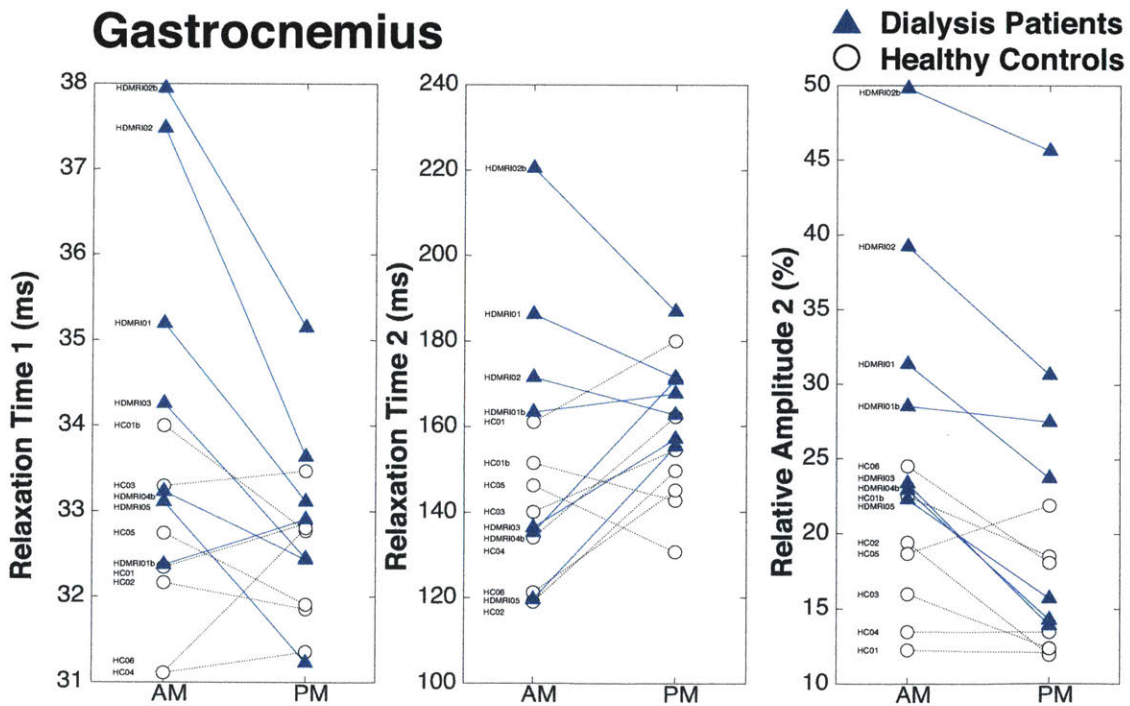


Figure 4-34: The results of a MRI bi-exponential fit for the gastrocnemius muscle sub-group.

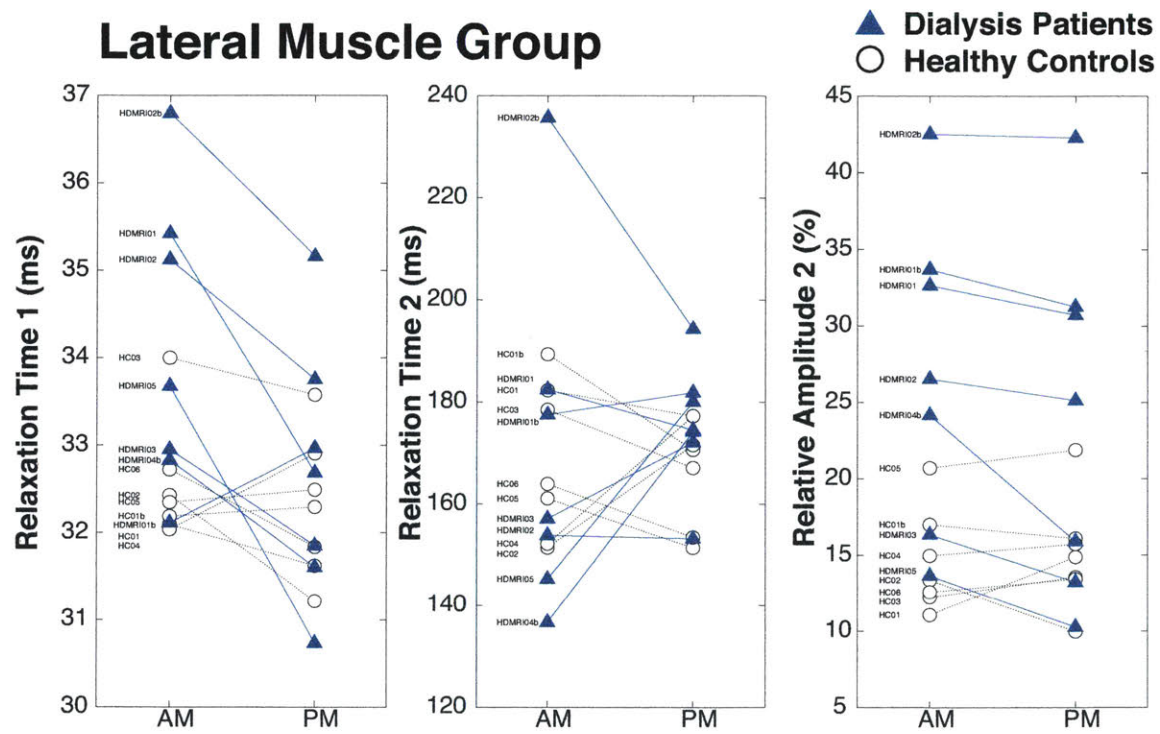


Figure 4-35: The results of a MRI bi-exponential fit for the lateral muscle sub-group. The lateral muscles are one of the most promising measurement regions for detecting differences between dialysis patients and healthy controls.

### MRI Muscular Tissue Sub-ROIs

<b>Relaxation Time 1 (ms)</b>			
	AM (ms)	PM (ms)	Change (%)
Muscle All	0.000167**	0.136	0.0523
Muscle Anterior	0.00723**	0.0598	0.1116
Muscle Deep Posterior	0.00199***	0.2371	0.0488*
Muscle gastrocnemius	0.0228*	0.3206	0.0137*
Muscle Lateral	0.04*	0.538	0.0498*
Muscle Soleus	0.0098**	0.512	0.0542

<b>Relaxation Time 2 (ms)</b>			
	AM (ms)	PM (ms)	Change (%)
Muscle All	0.151	0.0121*	0.582
Muscle Anterior	0.504	0.0144*	0.256
Muscle Deep Posterior	0.265	0.815	0.469
Muscle Gastrocnemius	0.139	0.0544	0.551
Muscle Lateral	0.921	0.179	0.552
Muscle Soleus	0.0826	0.0545	0.671

<b>Relative Amplitude 2 (%)</b>			
	AM (%)	PM (%)	Change (%)
Muscle All	0.00212**	0.0209*	0.000774**
Muscle Anterior	0.0195*	0.111	0.000247***
Muscle Deep Posterior	0.00894*	0.0427*	0.00502*
Muscle Gastrocnemius	0.00979*	0.0732	0.0543
Muscle Lateral	0.00919*	0.0723	0.0191*
Muscle Soleus	0.0211*	0.0600	0.2564

Table 4.5: Summary of bi-exponential fits for muscle sub-ROIs. The p-values from t-tests comparing values of healthy controls versus dialysis patients are summarized for relaxation time 1, relaxation time 2, and relative amplitude 2. \* p<0.05. \*\* p<0.001, \*\*\* p<0.0001.

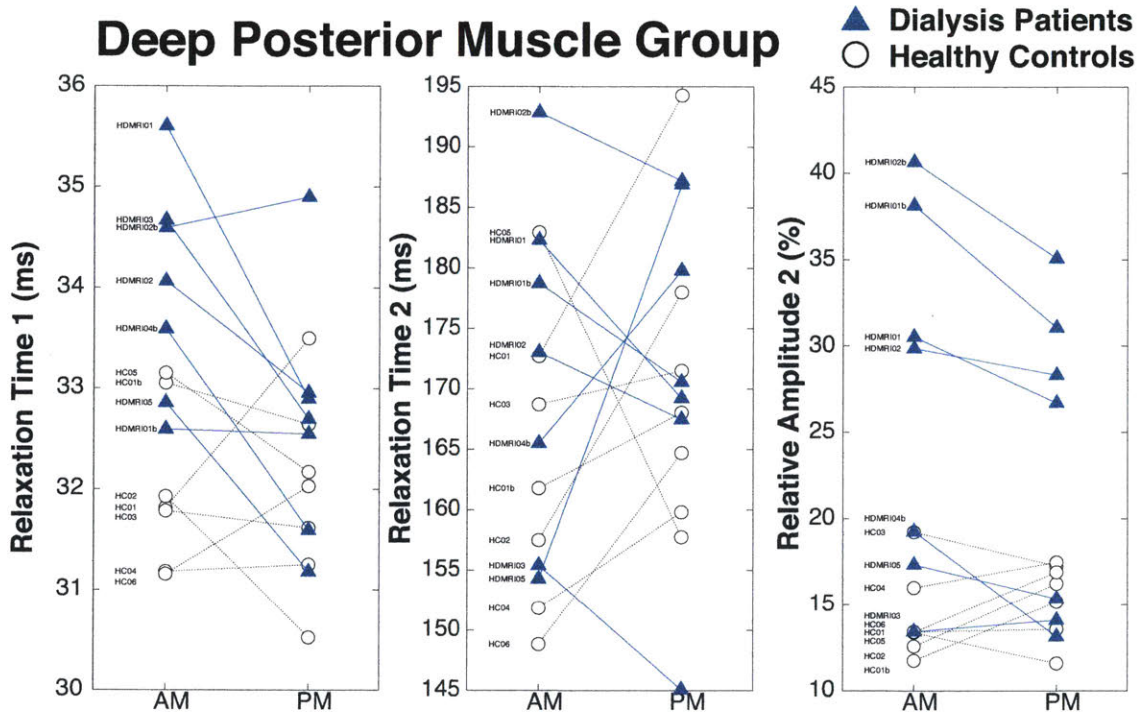


Figure 4-36: The results of a MRI bi-exponential fit for the deep posterior muscle sub-group.

fluid overloaded than our dialysis patient cohort. Note that our subcutaneous tissue ROIs include perifascial fluid deposits when they are present.

Relative amplitude 2 (amp2) values of HCs tended to be higher than that of HDs, with the exception of HC01b, which had the lowest amp2 values of all subjects. Amp 2 values for subcutaneous tissue were  $\sim 70\%$  and tended to decrease very slightly between the AM and PM for all subjects. There were no statistically significant changes for HC versus HD values in the subcutaneous tissue.

### Whole Leg

The 2-exponential fit results for the whole leg are show in Figure 4-38 and the amplitude results are summarized in Table 4.6.

The results for the whole leg were very similar to that of the muscular tissue. Relaxation time 1 (relax1) values of HD subjects were initially higher than that of HCs ( $p=0.0018$ ). Relax1 values decreased such that the HD's PM values were no longer statistically different that those of HDs ( $p=0.2001$ ). HCs also tended to have a decrease in their relax1 values. The AM-to-PM change in relax1 was not statistically significant between HC and HD subjects ( $p=0.0551$ ).

Relax2 values for all the subjects were interspersed and had no consistent AM-to-PM changes.

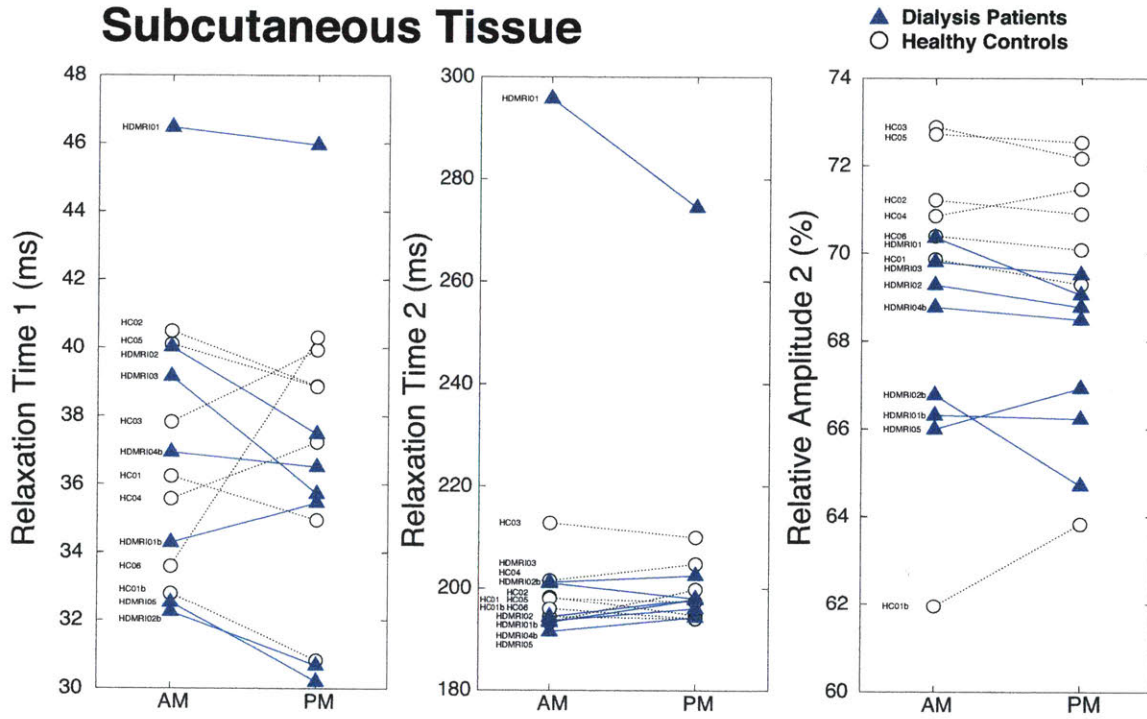


Figure 4-37: The results of a bi-exponential fit for the subcutaneous tissue. There were no clear HC versus HD separations or AM-to-PM changes. HD01, the most edematous of all patients, had higher relaxation times than all other subjects.

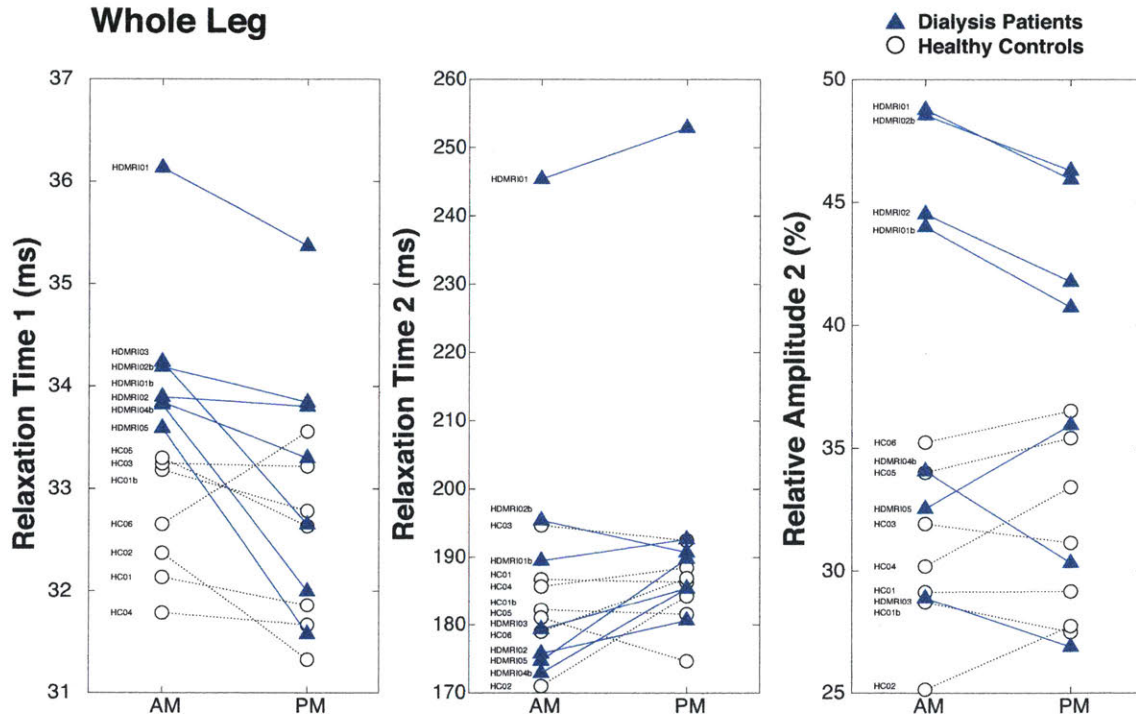


Figure 4-38: The results of the bi-exponential fits for the whole leg. The three panels plot AM and PM values of relaxation time 1, relaxation time 2, and relative amplitude 2 from left to right. Both relax 1 and relative amplitude 2 are significantly different between dialysis patients and healthy controls.

HD01, the most edematous patient, was the exception because he had a much longer relax2 value than all other subjects.

The amp2 of the whole leg of HD subjects was slightly higher than that of HCs in the AM scan and tended to shift downward after dialysis. The AM amp2 values were statistically different between HC and HD subjects ( $p=0.0168$ ) but the PM values were not ( $p=0.0746$ ). The AM to PM change in amp2 values was statistically significant between HC versus HD subjects ( $p=0.0203$ ).

### 4.3.3 Conclusions

Relative amplitude 2 and relaxation time 1 of the muscular tissue had the best ability to differentiate between dialysis patients and healthy controls at the initial time point as well as to detect fluid losses during dialysis. The results support our hypothesis that fluid overloaded patients have longer relaxation times than healthy controls – though we had expected this to be true in both of the relaxation times, not just the first one. Furthermore, the decreased relative amplitude 2 values support our hypothesis that the number of protons in a more free-fluid environment decreases after

<b>MRI Whole Leg: Relative Amplitude 2</b>			
<b>Subject</b>	<b>AM Amp 2 (%)</b>	<b>PM Amp 2 (%)</b>	<b>Change in Amp 2 (%)</b>
HC01	29.0	28.7	-0.337
HC01b	28.7	27.5	-1.211
HC02	24.8	27.3	2.430
HC03	31.4	30.7	-0.660
HC04	30.0	33.1	3.085
HC05	33.8	35.3	1.501
HC06	35.2	36.5	1.296
HDMRI01	49.1	45.9	-3.234
HDMRI01b	44.0	40.8	-3.249
HDMRI02	44.3	41.5	-2.826
HDMRI02b	48.6	46.3	-2.246
HDMRI03	28.1	25.0	-3.025
HDMRI04b	33.6	29.7	-3.882
HDMRI05	32.5	36.0	3.416
<b>HC VS HD t-test, p-value</b>	<b>0.0168*</b>	<b>0.0746</b>	<b>0.0203*</b>

Table 4.6: Summary of relative amplitude 2 results of the whole leg. The AM values of dialysis patients versus healthy controls were statistically different as was the AM-to-PM change in relative amplitude 2 values.

fluid is pulled from the body.

In interpreting the decreases in relative amplitude, it is important to keep in mind that when there is a decrease in relative amplitude 2, it could be due to a true decrease in amplitude 2, a true increase in amplitude 1, or a combination of both. Since the amplitude is relative, it is not possible to know which scenario it is. It generally does not make sense to look at absolute amplitude values in MR because slight variations in noise can cause the amplitude values to change dramatically from one scan to another, making comparison between scans impossible. Analyzing relative amplitude values is preferable to analyzing absolute amplitudes. The relative amplitude 2 decrease suggests that the ECF space is becoming smaller relative to the intracellular fluid space.

The muscular tissue's relative amplitude 2 represents a single measurement that could be performed to tell if a patient is fluid overloaded or not. In our limited population, there appears to be a "normal range" of relative amplitude 2 values between ~15-20%. Subjects who have higher amplitudes are volume overloaded. More data would have to be collected on both healthy and fluid overloaded individuals to corroborate this hypothesis.

We found no evidence of relaxometry changes occurring in the subcutaneous tissue after dialysis. Most of the fluid changes occurred in the muscular tissue. The muscle is more vascular than the surrounding subcutaneous tissue and therefore has more opportunity to respond to changes in the vascular space due to dialysis.

Relax 1 and relative amplitude 2 for the whole leg had the second-best detection and differentiation ability between healthy controls and dialysis patients. The results on the whole leg are similar to that of the muscular tissue, except less statistically significant because the whole leg data is an average of all tissues - muscle, subcutaneous tissue, bone, marrow, etc – in the leg. These other tissues were not found to display significant changes in a single dialysis treatment.

The whole leg bi-exponential fit is analysis that could be done with a single voxel sensor. Data from a single-voxel sensor with shorter echo times and more points in the echo train would likely achieve better results than those from the MRI. The MRI data (from a Siemens' scanner) has a 32-point echo train length limit. This limit did not allow the data to be fit by more than two exponentials. From the pixel-by-pixel analyses we know that the leg is composed of at least three main exponentials. Performing the same whole leg measurement with more points in the decay would enable us to separate out 3+ exponentials in the leg and likely isolate the muscle signal better.

HD01 was the most edematous patient in this study as seen on the MRI scan. He had perifascial

fluid deposits in his legs (visible in the MRI scans), though they were not yet detectable on physical exam. He had elevated  $T_2$  relaxation times and significantly elevated relative amplitude 2 values. This is an encouraging finding: perhaps identifying more hypervolemic patients will be easier than it was in the dialysis population of this study. Future work should aim to take measurements on more volume-overloaded individuals.

Contrary to our expectations, the dialysis patients in this study did not present with much fluid accumulation in their legs – certainly no one with pitting edema. It is possible that our dialysis patients accumulated fluid elsewhere in their bodies – lungs, venous system, peritoneum, etc. – before their legs. Future work should aim at measuring other locations in the body.

## 4.4 ROI ILT Analysis

The following section on analyzing the MRI ROI data with an ILT contains the following sub-sections:

- ILT Background
- L-Curve Criterion
- Methodology
- Results and Discussion

### 4.4.1 Methods: The Inverse Laplace Transform (ILT)

The **Inverse Laplace Transform (ILT)** or **non-negative least squares (NNLS) fitting** - the terms are used interchangeably - refers to a method of decomposing a multi-exponential decay into its constituent exponentials<sup>39,102-104</sup>. When we perform an ILT on a dataset, we obtain a distribution of relaxation times (called a **relaxogram**) that exist within the data. Unlike a multi-exponential analysis where we have to specify a fixed number of exponentials in a model, the ILT method does not require any a priori knowledge or assumptions about the data to be made. In biological systems where there are many complex structures and continuous water movement between these structures, it is thought that a spectrum of relaxation times is a more accurate way of describing the system than a model with a fixed number of exponentials.

The difficulty with inverting a multi-exponential signal is that the problem is inherently ill-posed and ill-conditioned<sup>105,106</sup>; the solution is not unique and noise in the signal can cause the solution to change. There are many distinct relaxograms that will fit the data with an acceptable level of accuracy. The question is how to pick one solution.

Regularization is a way to come up with a stable solution to an ill-posed problem<sup>107</sup>. There are many regularization methods and they all provide different ways of determining a "trade-off" between the complexity and the quality of the fit.

Tikhonov regularization is one of the most commonly used regularization methods for ill-posed problems<sup>103,104,108</sup>. Tikhonov regularization adds a "tuning parameter" to the least squares optimization that penalizes the solution for being complex. Complexity in Tikhonov regularization is measured by the norm of the solution, which is a strictly positive measurement of length of the solution vector.

For example, a regular least squares optimization seeks to minimize the sum of the squared

residuals

$$\| Ax - b \|_2^2 \tag{4.19}$$

where  $\| \cdot \|_2$  is the L2 norm. The L2 norm is defined as  $\| x \|_2 = \sqrt{\sum_{i=1}^n x_i^2}$  for a vector  $x = [x_1, x_2, \dots, x_n]$ .

With Tikhonov regularization, we now seek to minimize the expression

$$\| Ax - b \|_2^2 - \| \alpha Ix \|_2^2 \tag{4.20}$$

where  $I$  is the identity matrix and  $\alpha$  is the regularization parameter. Note that  $\alpha^2 = \lambda$ .  $\lambda$  will be used from here on when referring to the regularization parameter.

The "complexity" of the solution is measured by the L2 norm  $\| x \|_2$ , while the accuracy of the fit is measured by the L2 norm of the residuals  $\| Ax - b \|_2^2$ . The goal is to minimize both of these quantities.

#### 4.4.2 Methods: L-Curve Criterion

There are many methods for picking an optimal regularization parameter  $\lambda$  including cross validation, the L-curve method, restricted maximum likelihood and many more. We utilized the L-curve criterion to find an optimal  $\lambda$ <sup>109</sup>.

The L-curve criterion plots the two quantities we are trying to minimize against each other. A sample L-curve and regularization solutions are shown in 4-39.

The L-curve is plotted on log-log axes with the norm of the residual on the x-axis and the norm of the solution. The L-curve is a "trade-off curve" between two quantities that we want to control.

The optimal  $\lambda$  is the one at the corner of the L-curve.

The solutions at the top of the vertical line of the "L" have very low regularization parameters and large solution norms. Visually, a large solution norm means many "spikey" peaks in the relaxogram. These solutions are over-fit. Although they have low residual error, they are not stable and are dominated by contributions from noise.

On the other extreme, the solutions at the right-most, horizontal line of the "L" have very high regularization parameters. These solutions are under-fit and over-smoothed. Although their solution norm is low and they are not significantly impacted by noise in the data, these solutions have high residual norms and do not fit the data well.

The solution at the "corner" of the L-curve has the best of both worlds. The noisier a dataset, the larger the optimal regularization parameter will be. The larger the regularization parameter, the broader the relaxogram peaks will be. The width of the peaks is both dependent on the SNR of the data as well as the true width of the underlying phenomenon<sup>39</sup>. The L-curve method is known to come up with larger optimal regularization parameters than some other methods.

### SVD Approach to Determining the Optimal Regularization Parameter

The naive method of finding the "corner" of the L-curve is to perform the ILT at many different regularization parameter ( $\lambda$ ) values and calculate the residual norm and solution norm for each resulting relaxogram. Generating a full L-curve in this manner, however, can be extremely time consuming and require a lot of computing power. This is especially true for noisy data since noisy data has a larger optimal regularization parameter, which requires more computing power.

Rather than this brute-force (though effective) approach to generating the L-curve, there are faster and more elegant methods as well. We utilized a singular value decomposition (SVD) approach described by Hansen, et. al<sup>109</sup>. We will describe it here because *we found an error - a  $\lambda^2$  where it should have been a  $\lambda^4$  in Hansen's paper and code.* The method does not work with the equation in Hansen's paper.

Hansen's approach involves performing SVD of the matrix  $A$ , which for an  $m \times n$  matrix with  $m \geq n$  is

$$A = \sum_{i=1}^n u_i \sigma_i v_i^T \quad (4.21)$$

where the left and right singular vectors  $u_i$  and  $v_i$  are orthonormal, and the singular values  $\sigma_i$  are nonnegative.

Hansen's paper<sup>109</sup> goes through his SVD method in detail so we will pick up in the last step where his derivation goes wrong. Readers can reference his paper<sup>109</sup> to understand the full method derivation.

Let us begin at Hansen's<sup>109</sup> equation 14:

$$\kappa = 2 \frac{\hat{\rho}' \hat{\eta}'' - \hat{\rho}'' \hat{\eta}'}{((\hat{\rho}')^2 + (\hat{\eta}')^2)^{(3/2)}} \quad \text{Hansen eq.14} \quad (4.22)$$

Our goal is to turn the equation for  $\kappa$  - which represents the curvature of the L-curve - into terms containing the solution norm, the residual norm, and the regularization parameter  $\lambda$ .

First, here are the definitions of these parameters:

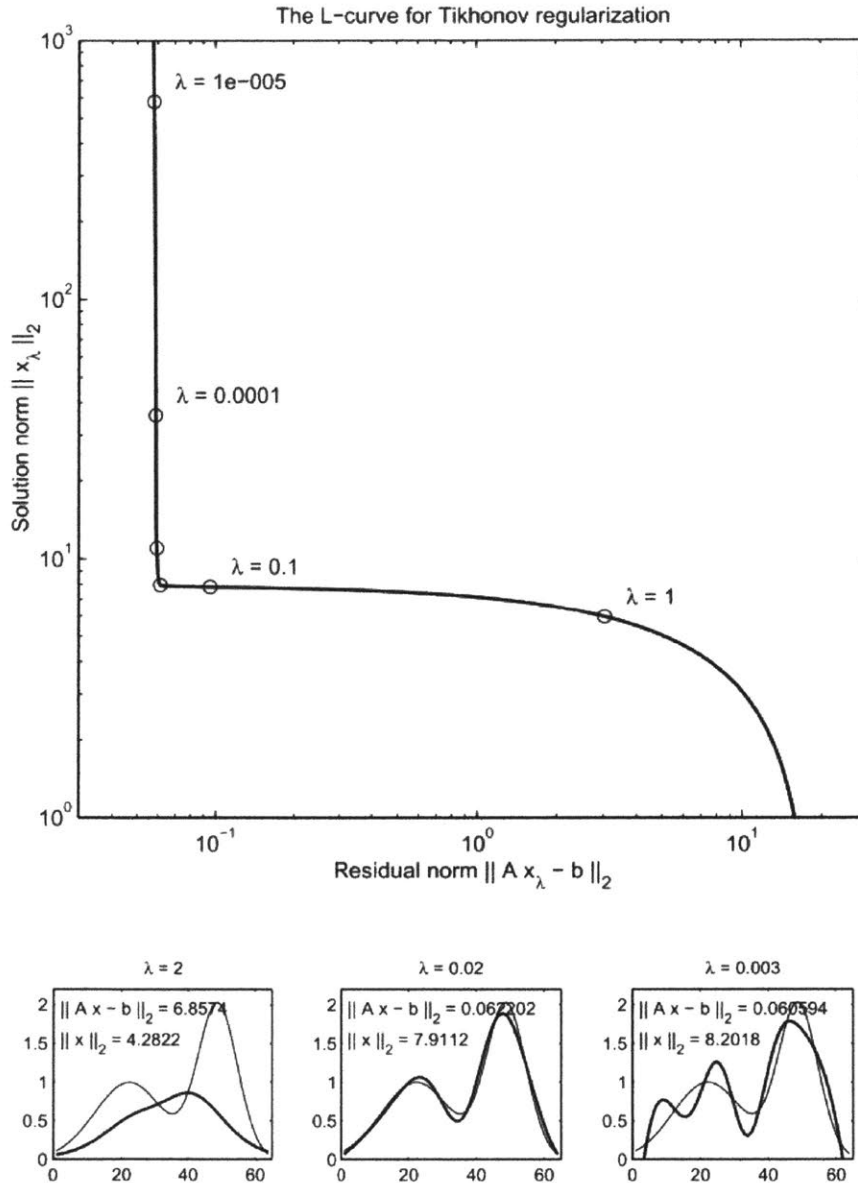


Figure 4-39: L-curve on top with with sample relaxograms of the same data inverted with different regularization parameters,  $\lambda$ , on the bottom, corresponding to over-smoothing, appropriate smoothing, and under-smoothing. The exact inversion solution is shown by a thin line and the experimental relaxograms are shown in thick lines. The larger the regularization parameter, the smoother the solution and larger the error. The smaller the regularization parameter, the "spikier" the solution and the larger the complexity of the solution. [Source of figures is P. C. Hansen, 2000<sup>109</sup>.]

$$\eta = \|x\|_2^2 = \text{solution norm (Hansen eq.12)}$$

$$\rho = \|Ax - b\|_2^2 = \text{residual norm (Hansen eq.12)}$$

$$\hat{\eta} = \log(\eta) \text{ and } \hat{\rho} = \log(\rho)$$

$\hat{\eta}'$ ,  $\hat{\rho}'$ ,  $\hat{\eta}''$ , and  $\hat{\rho}''$  are the first and second derivatives of  $\hat{\eta}$  and  $\hat{\rho}$  with respect to  $\lambda$ .

Second, here are the relationships that we will need in order to simplify equation 4.22:

$$\hat{\eta}' = \frac{\eta'}{\eta} \text{ and } \hat{\rho}' = \frac{\rho'}{\rho} \text{ Hansen unnamed equations btw eq.14-15} \quad (4.23)$$

$$\hat{\eta}'' = \frac{d}{d\lambda} \frac{\eta'}{\eta} = \frac{\eta''\eta - (\eta')^2}{\eta^2} \text{ and } \hat{\rho}'' = \frac{d}{d\lambda} \frac{\rho'}{\rho} = \frac{\rho''\rho - (\rho')^2}{\rho^2} \text{ Hansen unnamed equations btw eq.16-17} \quad (4.24)$$

$$\rho' = -\lambda^2 \eta' \text{ Hansen eq.16} \quad (4.25)$$

$$\rho'' = \frac{d}{d\lambda} (-\lambda^2 \eta') = -2\lambda \eta' - \lambda^2 \eta'' \text{ Hansen eq.17} \quad (4.26)$$

We will consider the numerator and denominator of equation 4.22 separately and then put them

together at the end. Here is the derivation for the numerator:

$$\begin{aligned}
\kappa_{\text{numerator}} &= 2(\hat{\rho}'\hat{\eta}'' - \hat{\rho}''\hat{\eta}') \\
&\text{substitute equations 4.24 and 4.23} \\
&= 2\frac{\rho'}{\rho}\frac{\eta''\eta - \eta'^2}{\eta^2} - \frac{\rho''\rho - \rho'^2}{\rho^2}\frac{\eta'}{\eta} \\
&\text{simplify} \\
&= 2\frac{\rho\rho'\eta\eta'' - \rho\rho'\eta'^2}{\rho^2\eta^2} - \frac{\rho\rho''\eta\eta' - \rho'^2\eta\eta'}{\rho^2\eta^2} \\
&\text{substitute 4.25} \\
&= 2\frac{-\rho\lambda^2\eta'\eta\eta'' + \lambda^2\rho\eta'^3 - \rho\rho''\eta\eta' + (-\lambda^2\eta')^2\eta\eta'}{\rho^2\eta^2} \\
&\text{substitute 4.26} \\
&= 2\frac{-\rho\lambda^2\eta\eta'\eta'' + \lambda^2\rho\eta'^3 - \rho(-2\lambda\eta' - \lambda^2\eta'')\eta\eta' + \lambda^4\eta\eta'^3}{\rho^2\eta^2} \\
&\text{simplify} \\
&= 2\frac{\eta'^2}{\rho^2\eta^2}(\lambda^2\rho\eta' + 2\lambda\rho\eta + \lambda^4\eta\eta')
\end{aligned} \tag{4.27}$$

Derivation for the denominator of the curvature equation:

$$\begin{aligned}
\kappa_{\text{denominator}} &= ((\hat{\rho}')^2 + (\hat{\eta}')^2)^{3/2} \\
&\text{substitute equations 4.23} \\
&= \left[\left(\frac{\rho'}{\rho}\right)^2 + \left(\frac{\eta'}{\eta}\right)^2\right]^{3/2} \\
&\text{substitute equation 4.25} \\
&= \left[\left(\frac{-\lambda^2\eta'}{\rho}\right)^2 + \left(\frac{\eta'}{\eta}\right)^2\right]^{3/2} \\
&\text{simplify} \\
&= \left(\frac{\lambda^4\eta^2\eta'^2 + \rho^2\eta'^2}{\eta^2\rho^2}\right)^{3/2}
\end{aligned} \tag{4.28}$$

Putting the numerator (equation 4.27) and denominator (equation 4.28) together we get:

$$\begin{aligned}
\kappa &= \frac{2\frac{\eta'^2}{\rho^2\eta^2}(\lambda^2\rho\eta' + 2\lambda\rho\eta + \lambda^4\eta\eta')}{\left(\frac{\lambda^4\eta^2\eta'^2 + \rho^2\eta'^2}{\eta^2\rho^2}\right)^{3/2}} \\
&\text{Simplify} \\
&= \frac{2\eta'^2(\eta^2\rho^2)^{3/2}(\lambda^2\rho\eta' + 2\lambda\rho\eta + \lambda^4\eta\eta')}{(\rho^2\eta^2)(\lambda^4\eta^2\eta'^2 + \rho^2\eta'^2)^{3/2}} \\
&= 2\frac{\eta\rho}{\eta'}\frac{(\lambda^2\rho\eta' + 2\lambda\rho\eta + \lambda^4\eta\eta')}{(\lambda^4\eta^2 + \rho^2)^{3/2}}
\end{aligned} \tag{4.29}$$

Therefore the final equation for calculating  $\kappa$  - the curvature of the L-curve - according to our calculations is

$$\kappa_{Our\ Calculation} = 2\frac{\eta\rho}{\eta'}\frac{(\lambda^2\rho\eta' + 2\lambda\rho\eta + \lambda^4\eta\eta')}{(\lambda^4\eta^2 + \rho^2)^{3/2}} \tag{4.30}$$

whereas Hansen's equation 18 has a  $\lambda^2$  in the denominator instead

$$\kappa_{Hansen} = 2\frac{\eta\rho}{\eta'}\frac{(\lambda^2\rho\eta' + 2\lambda\rho\eta + \lambda^4\eta\eta')}{(\lambda^2\eta^2 + \rho^2)^{3/2}} \tag{4.31}$$

Figure 4-40 shows the L-curve and its corresponding curvature plot. The maximum of the curvature plot corresponds to the corner of the L-curve, which is the optimal regularization parameter value as determined by the L-curve criterion. If we use Hansen's curvature equation (equation 18 in his paper<sup>109</sup>), the curvature plot looks like an exponential decay and there is no maximum (except the initial point).

## Implementation Notes

The scripts to implement an ILT and the L-curve criterion and visualize the results can be found in the Github folder: `process_ilt.m`, `visualize_ilt_Lcurve.m`, `visualize_ilt_lambdaSweep.m`.

Subfunctions for performing ILT on a single  $T_2$  decay: `ilt.m`, `ilt_multiplelambdas.m`, `lcurvecriterion.m`.

### 4.4.3 Methods: Applying the ILT and Post-Processing

Pixels from entire regions were averaged together to produce a single average  $T_2$  decay for that ROI (the same averaging that was done in Section 4.3). The ILT was applied to those average  $T_2$  decays for each subject and tissue type.

Two types of ILT analyses were performed on each individual subject: (1) an ILT was performed

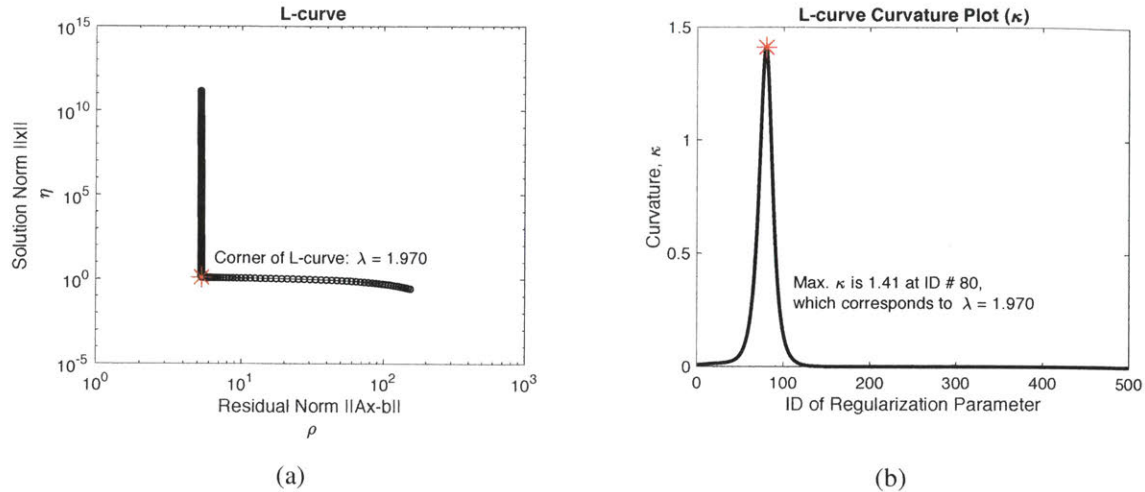


Figure 4-40: (a) L-curve on log-log axes with the residual norm  $\rho$  plotted on x-axis and the solution norm  $\eta$  plotted on the y-axis, (b) The corresponding curvature ( $\kappa$ ) plot of the L-curve. The maximum of the curvature plot corresponds to the corner of the L-curve.

using the regularization parameter found by the L-curve criterion, and (2) many ILT inversions were performed by sweeping the regularization parameter from  $1e-5$  to 2. The results of the ILT sweep were summarized by extracting the peak position and peak area under the curve (AUC) of each relaxogram and plotting them against the regularization parameter. Additional analysis was done with the ILT sweep data by (1) subtracting the AM-to-PM difference of the extracted parameters across all regularization values and (2) summing those differences. This approach allowed us to quantify AM-to-PM changes in a manner that was independent of regularization parameter choice. The results of this additional analysis is not shown in this thesis.

Finally, group relaxograms were generated for the following groups: HC AM, HC PM, HD AM, and HD PM. ILTs with both the L-curve criterion and a small regularization parameter were applied to these four average  $T_2$  decays.

After each raw relaxogram was generated (*ySpec\_raw*), it underwent post-processing where peaks were deleted if they did not meet certain criteria. Our peak deletion criteria were: (1) a peak was located at  $<TE/2$  (a criteria that was established in section 4.2.2) (Minimum  $T_2$  Criteria), and/or (2) a peak AUC represented  $<2\%$  of the signal (this was done to avoid too many spurious peaks from appearing in the relaxogram). Once these peaks were deleted, the normalized relaxogram was calculated (*ySpec\_norm*) and parameters (peak positions and peak AUCs) were extracted.

#### 4.4.4 Results and Discussion

##### Individual Subjects: Whole Leg

###### Single Regularization Parameter: L-curve Method

The optimal regularization parameter determined by the L-curve Method for the whole leg ranged from between 0.55 to 0.68. The AM and PM relaxograms for each subject are shown in Figure 4-41. The relaxograms are very smoothed out, with just a single peak and then a long tail peak that extends beyond the x-limit (1000ms) of the relaxogram. We believe this long tail is an artifact of the ILT method as  $T_2$  relaxation times above 1s are not expected to be found in the body, especially those of healthy controls.

The relaxograms for the healthy controls are surprisingly similar between the AM and PM scans, except for HC02 (dehydrated) and HC04. The AM vs PM relaxograms for the dialysis patients shift to varying degrees between AM and PM scans. The dialysis patients tend to have the relaxogram region between 100-300ms shift downward in the PM scan to lower relaxation times. This may reflect a decrease in extracellular fluid volume, since we found in the bi-exponential fits that relaxation times >40ms were associated with extracellular fluid.

###### Regularization Parameter Sweep

Figure 4-42 shows the extracted parameters from the relaxograms for regularization parameters ranging from  $1e-5$  to 2. The peak positions and peak areas under the curve (AUCs) are relatively stable from  $1e-5$  to about  $1e-2$ , after which the values can vary considerably from one regularization parameter to the next. It is impressive that the ILT is able to extract two parameters from the whole leg  $T_2$  decay that closely match the peaks seen in the pixel-by-pixel histogram. The first peak occurs at approximately 40ms and contributes to approximately 30% of the signal. The second peak occurs around 225ms and contributes to approximately 70% of the area in healthy controls. The AUC associated with the longer relaxation time (the  $\sim 225$ ms peak) had a larger variability in dialysis patients (from 64-84%) than in healthy controls, whose second AUC was fairly stable at 70%. The exception to this was HC02, who had a low second AUC – 65.5% - in the AM measurement and an even lower one – 64% - in the PM measurement.

HC02 and HD03 were the two Asian subjects in this study, and HD03 had a relatively low second area - 63% - as well. Perhaps there is variability within races that needs to be taken into account. More measurements on a cohort with greater racial diversity should be done in the future.

The HC relaxation times were unchanged or decreased slightly between AM and PM scans.

Whole Leg: Relaxogram with Regularization Parameter chosen by L-Curve Method

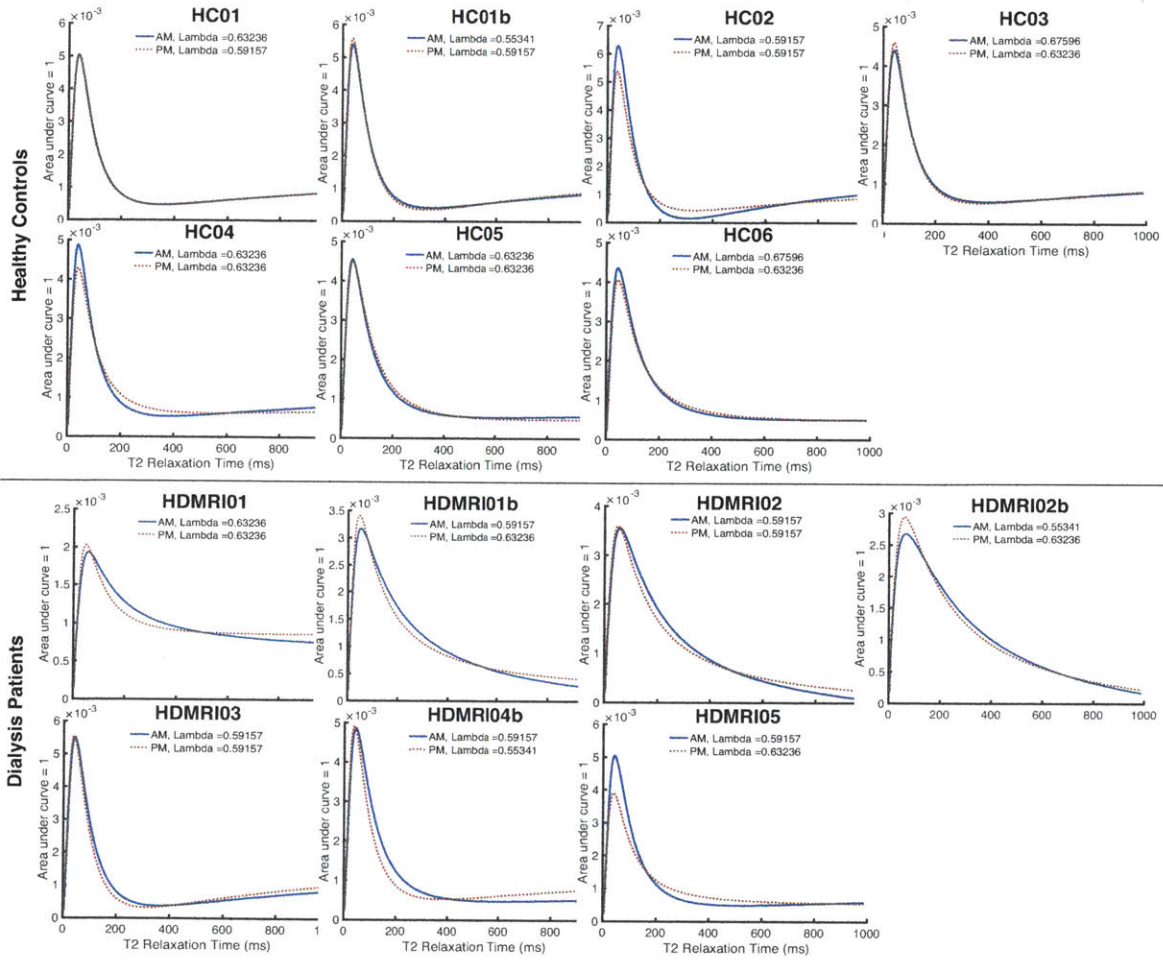


Figure 4-41: Whole Leg ILT with L-curve Method: The resulting relaxograms from performing an ILT on each signal with the regularization parameter determined to be optimal based on the L-curve criterion. The AM (solid line) and PM (dotted line) relaxograms for each subject are overlaid.

The HC amplitudes were either unchanged between AM and PM scans or increased slightly. The subjects whose amplitudes increased (HC02, HC04, and HC06) had elevated serum osmolality values, indicative of dehydration, at the start of the study. It is not possible to know what the expected change in amplitude values for a healthy control should be due to the small sample size (n=7). Future studies specifically dedicated to characterizing healthy controls and looking at dehydration should be done.

The HD amplitudes were relatively unchanged between AM and PM scans, but tended to increase slightly. This goes against what we hypothesize and what we saw in the multi-exponential analysis.

The HD relaxation times tended to increase slightly between AM and PM scans. This was counter to what we had hypothesized. Upon further reading of the literature, we discovered that urea is a  $T_2$  shortening agent and it can effectively cross cell walls<sup>110,111</sup>. Patients with ESRD accumulate urea and other toxins as a consequence of reduced or absent filtering by the kidneys. The pixel-by-pixel bi-exponential analysis also saw an increase in the longer relaxation time after dialysis. We did not, however, see any consistent relaxation time patterns in the whole ROI bi-exponential analyses.

We are therefore unsure how to interpret the behavior of relaxation time in response to dialysis. The second relaxation time seems to clearly increase in the ILT regularization parameter sweep analysis. However, we know that the relaxograms at low regularization parameters are overfit. When we look at the AM vs PM relaxograms from the L-curve method, we do not see an increase in relaxation times. Our current hypothesis is that the relaxation time increase seen in this analysis is an artifact of undersmoothed ILTs.

## **Individual Subjects: Muscular Tissue**

### **Single Regularization Parameter: L-curve Method**

The optimal regularization parameter determined by the L-curve criterion for the muscular tissue ranged from between 0.55 to 0.64. The AM and PM relaxograms for each subject are shown in Figure 4-43. The relaxograms are very smoothed out, with just a single peak and then an unfinished second peak that begins around 500ms and is still rising at the end of the x-axis (1000ms). We believe this long tail is an artifact of the ILT method as explained above. The relaxograms for the healthy controls are surprisingly similar between the AM and PM scans. The AM vs PM relaxograms for the dialysis patients shift to varying degrees between AM and PM scans. The PM

### Whole Leg: Relaxogram with Sweep of Regularization Parameters

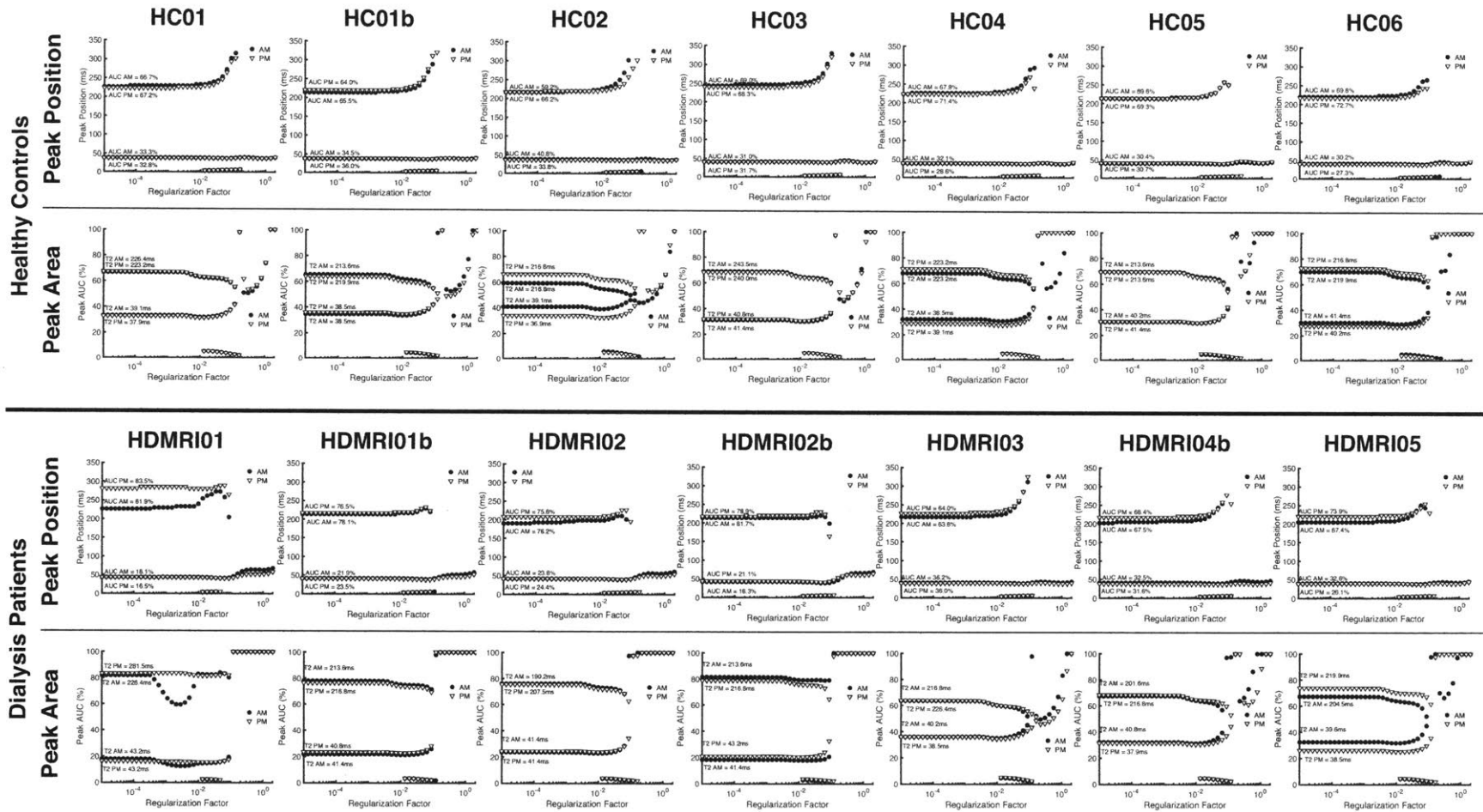


Figure 4-42: Whole Leg ILT Sweep: The extracted parameters - peak position and peak AUC - from relaxograms obtained in a regularization parameter sweep. The AM (shaded circle) and PM (open triangle) parameters are shown overlaid for each subject.

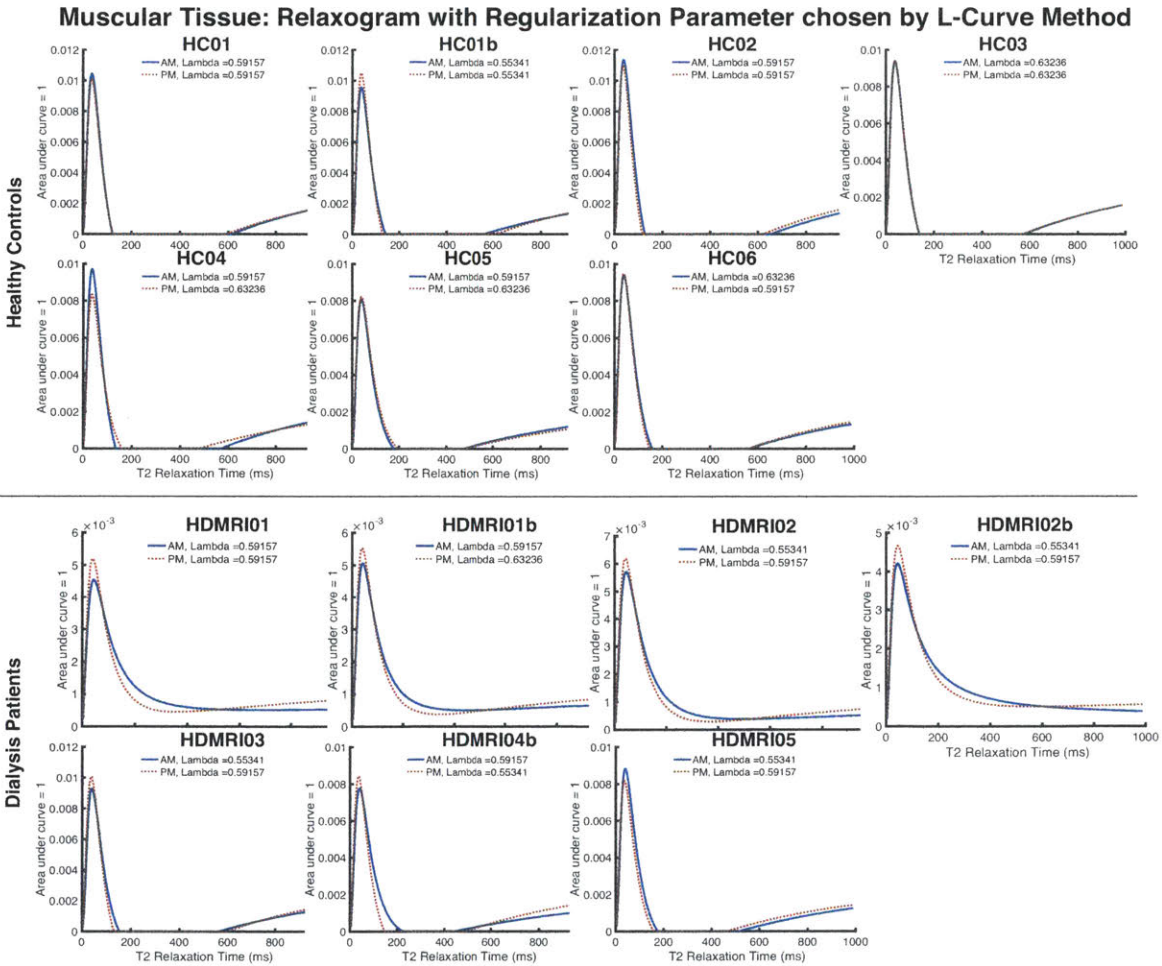


Figure 4-43: Muscular Tissue ILT with L-curve Method: The resulting relaxograms from performing an ILT on each signal with the regularization parameter determined to be optimal based on the L-curve criterion. The AM (solid line) and PM (dotted line) relaxograms for each subject are overlaid.

relaxograms for dialysis patients generally have a left-ward shift towards lower relaxation times, which is what we expect to happen when free fluid is removed from the body.

### Regularization Parameter Sweep

Figure 4-44 shows the extracted parameters from the relaxograms for regularization parameters ranging from  $1e-5$  to 2. The peak positions and peak areas under the curve (AUCs) are relatively stable from  $1e-5$  to about  $1e-3$ , after which the values can vary considerably from one regularization parameter to the next. The extracted peak locations match those found in the previous bi-exponential analyses for the first peak – 40ms – but not for the second peak, which occurs between 200-250ms in this ILT sweep but around 140-180ms in the previous bi-exponential analyses.

The resulting ILT relaxograms of the muscular tissue has two peaks, the first around 40ms and

representing  $\sim 55\%$  of the signal, the second peak  $\sim 250\text{ms}$  and  $\sim 45\%$  of the signal. Occasionally another peak appeared at  $\sim 10\text{ms}$  for a few smoothing factors and then disappeared again.

For several dialysis patients, the larger signal AUC corresponded to the longer relaxation time (200-250ms) instead of the shorter relaxation times (40ms) as was the case for healthy controls. This means that the percent of the signal coming from the extracellular fluid is larger in dialysis (fluid overload) patients than in healthy controls, which is what we expect.

A few healthy controls – HC04, HC05 - and dialysis patients – HD04b, HD05 – had nearly 50-50% AUC splits between the two peaks, which we are unsure how to interpret.

The AUC associated with the longer relaxation time (extracellular fluid) decreased in all dialysis patients. This result is consistent with what we saw in both of the previous bi-exponential analyses. A decrease in the AUC associated with extracellular fluid signifies that the relative volume of the extracellular space is getting smaller as fluid is removed from the body.

Similar to what we saw in the whole leg ILT sweep, the longer relaxation time of the dialysis patients increases after dialysis. For the same reasons hypothesized previously, we believe this is an artifact of the ILT algorithm at low smoothing factors. There are no clear patterns to describe the AM to PM shifts in healthy controls for either relaxation times or AUCs.

## **Individual Subjects: Subcutaneous Tissue**

### **Single Regularization Parameter: L-curve Method**

The optimal regularization parameter determined by the L-curve method for the subcutaneous tissue ranged from between 0.51 to 0.64. The AM and PM relaxograms for each subject are shown in Figure 4-45. The relaxograms are very smoothed out, with just a single peak, whose tail ends around 800ms for all subjects except for HD01. HD01 is the subject with very visible perifascial fluid deposits - essentially free fluid collections in the body - which were included in the subcutaneous tissue ROI and show up here as extremely long relaxation times.

The relaxograms for both healthy controls and dialysis patients are surprisingly similar between the AM and PM scans, with the exception of HD01. There does not seem to be much MR signal change occurring in the subcutaneous tissue. This is consistent with what we saw in the previous bi-exponential analyses.

### **Regularization Parameter Sweep**

Figure 4-46 shows the extracted parameters from the relaxograms for regularization parameters ranging from  $1e-5$  to 2. The peak positions and peak areas under the curve (AUCs) are relatively

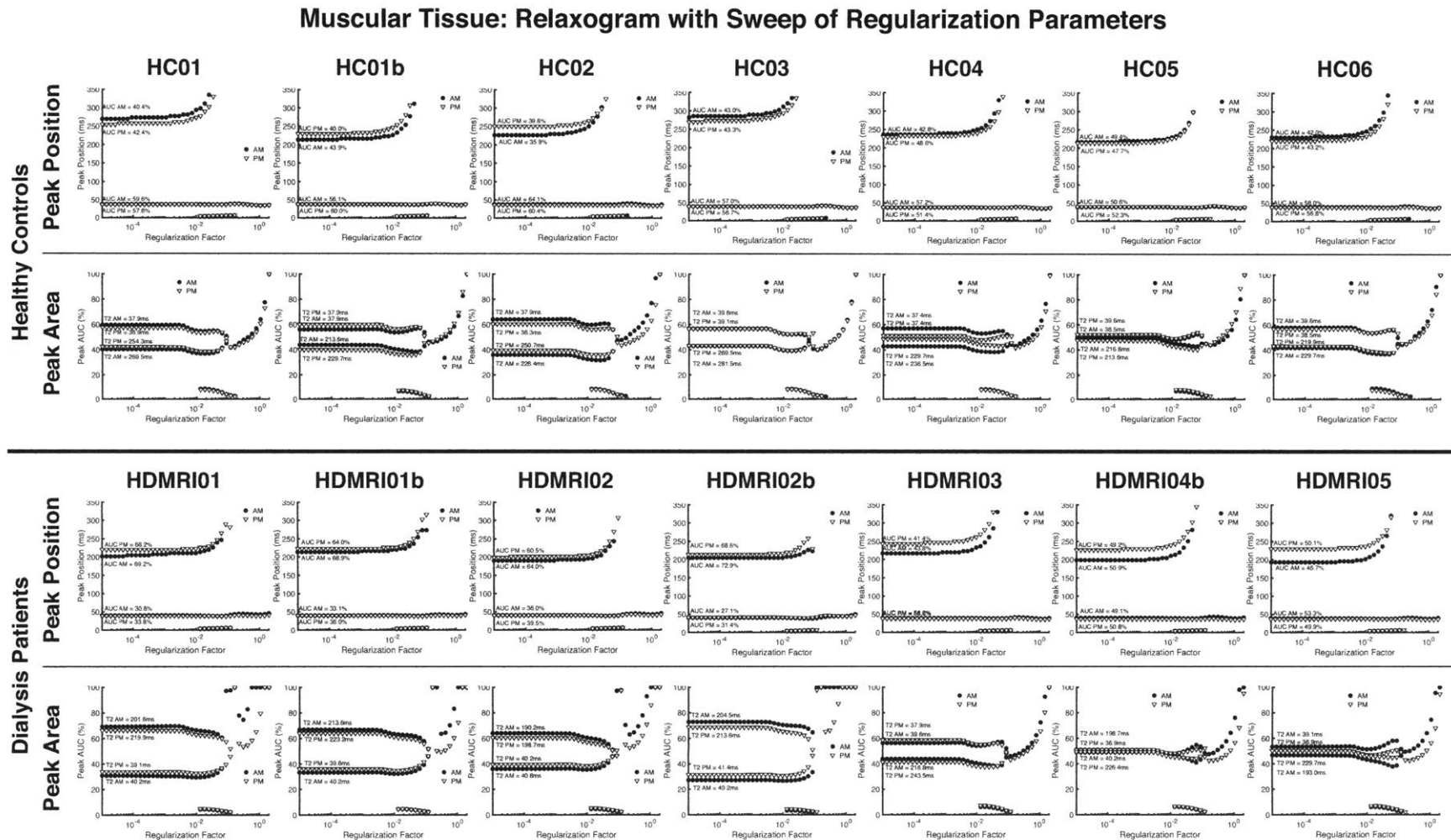


Figure 4-44: Muscular Tissue ILT Sweep: The extracted parameters - peak position and peak AUC - from relaxograms obtained in a regularization parameter sweep. The AM (shaded circle) and PM (open triangle) parameters are shown overlaid for each subject.

### Subcutaneous Tissue: Relaxogram with Regularization Parameter chosen by L-Curve Method

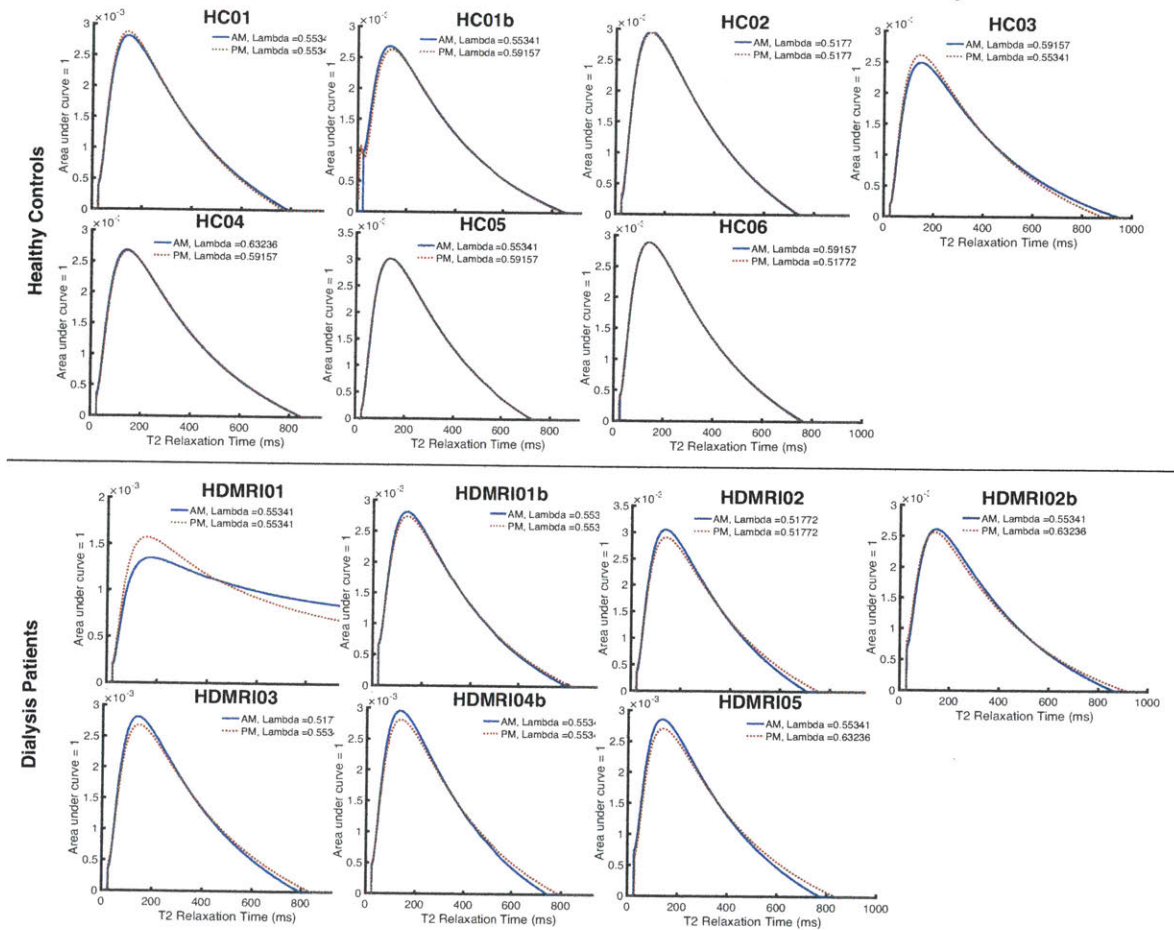


Figure 4-45: Subcutaneous Tissue ILT with L-curve Method: The resulting relaxograms from performing an ILT on each signal with the regularization parameter determined to be optimal based on the L-curve criterion. The AM (solid line) and PM (dotted line) relaxograms for each subject are overlaid.

stable from  $1e-5$  to about  $1e-2$ , after which the values can vary considerably from one regularization parameter to the next. The extracted peak locations match those found in the previous bi-exponential analyses.

The resulting ILT relaxograms of the subcutaneous tissue had two peaks, the first around 40ms and representing  $\sim 10\%$  of the signal, the second peak  $\sim 225$ ms and  $\sim 90\%$  of the signal. Occasionally another peak appeared at  $\sim 10$ ms for a few smoothing factors and then disappeared again.

There are not many AM-to-PM shifts nor HC versus HD differences in the subcutaneous tissue ILTs. The largest shift occurs in HD01, whose AUC associated with the longer relaxation time decreased from 90% to 88.6% after dialysis. This decrease can either be due to the true reduction in free fluid or due to a slightly different subcutaneous tissue ROI selection in the AM and PM scans. It is challenging to tell where the perifascial fluid deposits are located on a normal grey, magnitude MRI image and it is therefore possible that we selected less perifascial fluid on the PM scan than in the AM one.

The overall conclusion of this ILT analysis on the subcutaneous tissue is that there are not many changes that occur in the subcutaneous tissue in response to dialysis.

## **Group Averages**

### **AM vs PM**

The relaxogram results of the grouped healthy controls and grouped dialysis patients are shown in Figure 4-47 (ILT with L-curve method) and Figure 4-48 (ILT with a small regularization parameter). In both the L-curve relaxograms and small regularization parameter relaxogram, there are no significant AM to PM changes in any tissue type in healthy controls.

In the relaxograms with a small regularization parameter, dialysis patients have a slight relaxation time increase in all tissue types. Dialysis patients have a decrease in amplitude associated with the longer relaxation time in muscular tissue, as seen by the shorter peak height in Figure 4-48.

In the relaxograms with a regularization parameter picked via the L-curve method, we see that the whole leg and muscular tissue relaxograms have a slight left-ward shift towards lower relaxation times in the PM. This is what we hypothesized would happen when free fluid is removed from the body. The subcutaneous tissue AM and PM relaxograms are nearly identical, indicating that few changes occur in the subcutaneous tissue in response to dialysis.

In conclusion, the largest AM to PM change in the lower leg in response to dialysis occurs in the muscular tissue. The amplitude associated with extracellular fluid decreases in the muscular tissue,

### Subcutaneous Tissue: Relaxogram with Sweep of Regularization Parameters

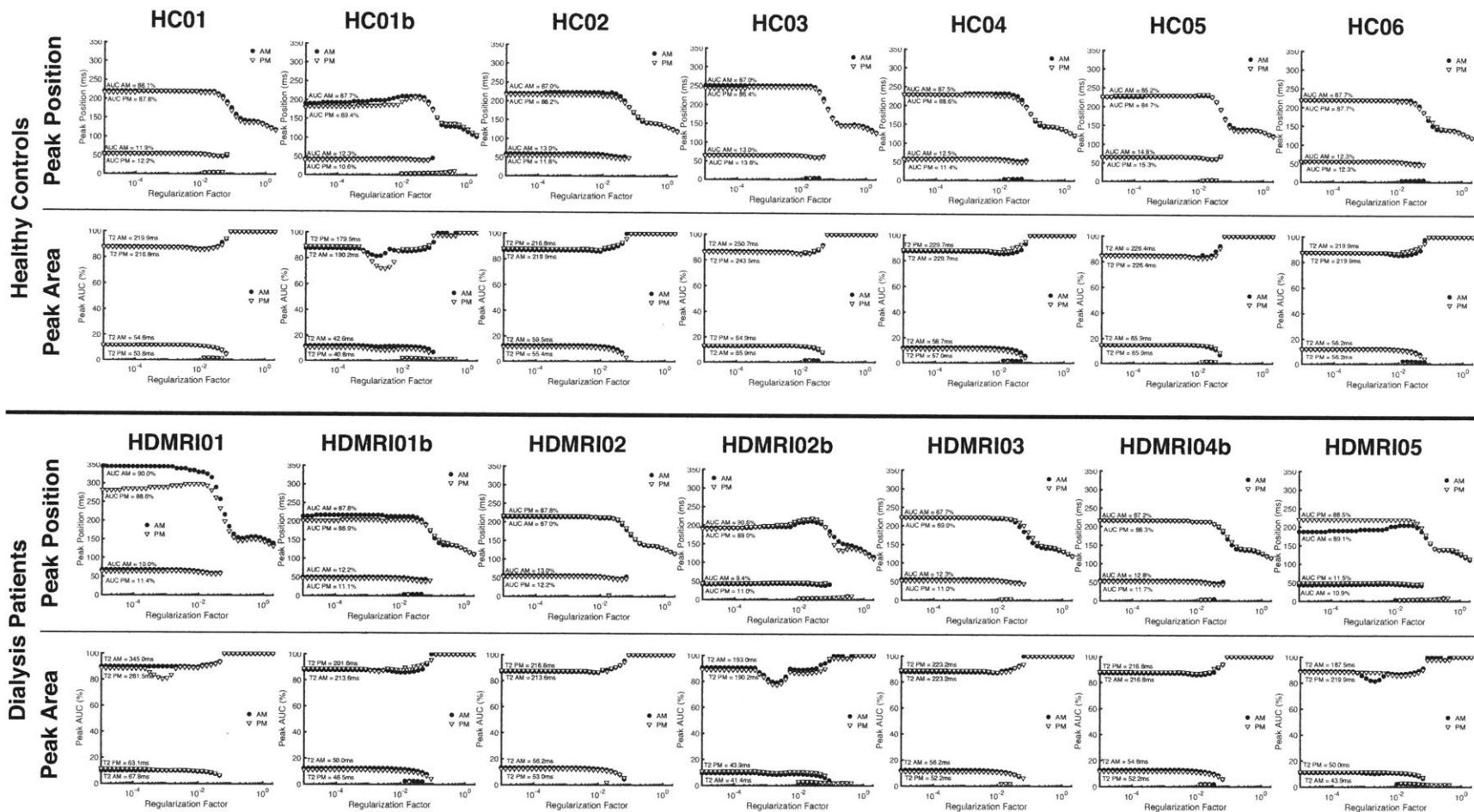


Figure 4-46: Subcutaneous Tissue ILT Sweep: The extracted parameters - peak position and peak AUC - from relaxograms obtained in a regularization parameter sweep. The AM (shaded circle) and PM (open triangle) parameters are shown overlaid for each subject.

### AM vs PM: Relaxograms with Regularization Parameter chosen by L-Curve Method

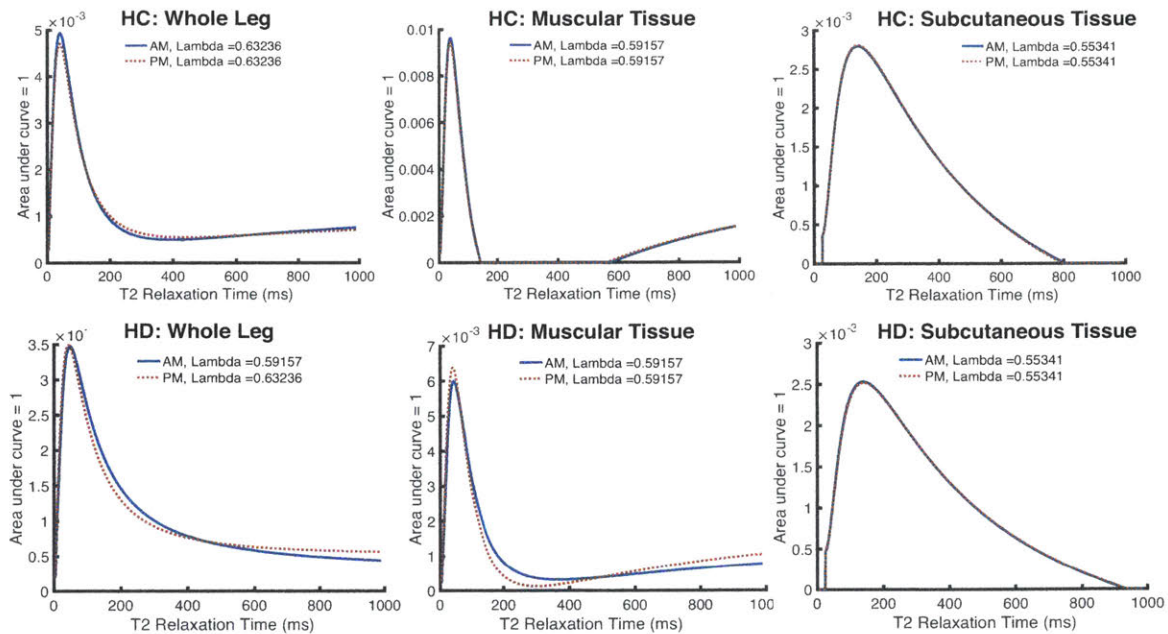


Figure 4-47: Average relaxograms of healthy controls and dialysis patients for each tissue type. Relaxograms were obtained with the regularization parameter determined to be optimal based on the L-curve criterion. AM and PM relaxograms for each group and tissue type are overlaid for easy comparison.

which is what we expect in response to fluid removal and is consistent with our findings in the previous bi-exponential analyses. The relaxograms of healthy controls look very similar between AM and PM, indicating that healthy controls are stable between the two measurements.

#### Healthy Controls versus Dialysis Patients

The relaxogram results of the grouped healthy controls and dialysis patients are shown in Figure 4-49 (ILT with L-curve method) and Figure 4-50 (ILT with a small regularization parameter) with healthy and dialysis relaxograms aggregated on the same plot for easy comparison.

On the relaxograms with a small regularization parameter, the healthy controls and dialysis patients look nearly identical across AM and PM measurements for both the whole leg and subcutaneous tissue ROIs. The dialysis patients have a lower relaxation time and higher amplitude compared to healthy controls in the peak associated with extracellular fluid. The difference becomes smaller in the PM measurement.

On the relaxograms with a regularization parameter chosen by the L-curve method, the healthy controls and dialysis patients look very different. The dialysis patients have longer right “tails” across all tissues. Dialysis patients have relaxograms that have shifted slightly closer to those of

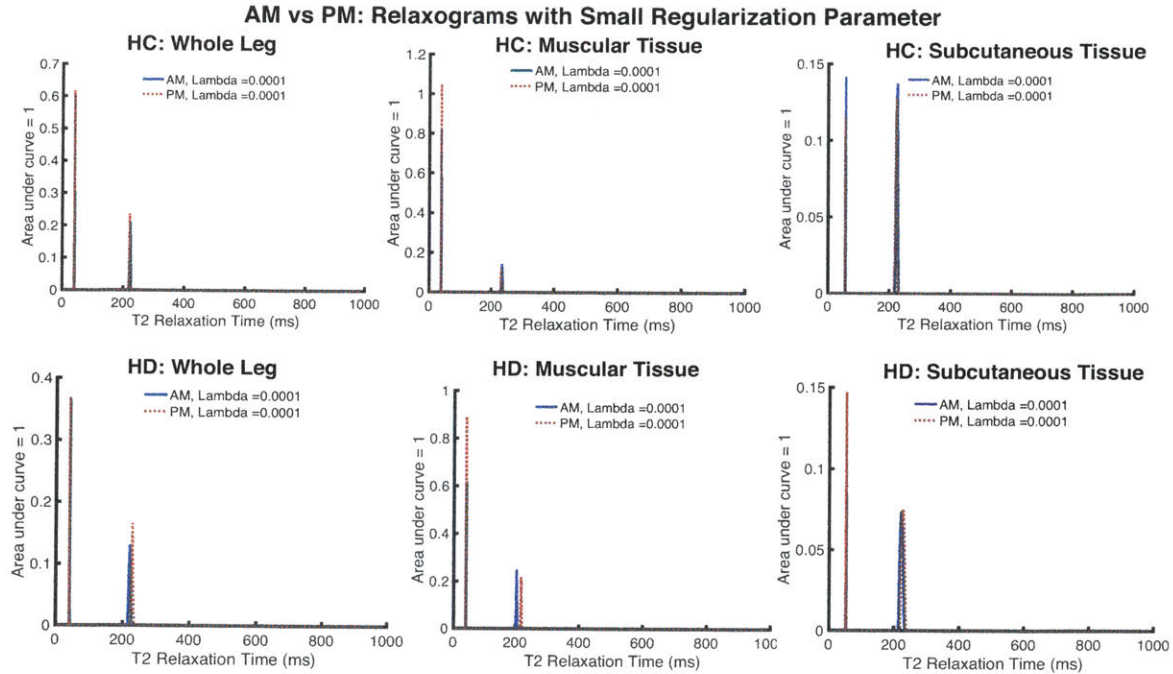


Figure 4-48: Average relaxograms of healthy controls and dialysis patients for each tissue type. Relaxograms were obtained with a very small regularization parameter to facilitate comparison of the peaks. AM and PM relaxograms for each group and tissue type are overlaid for easy comparison.

healthy controls in the PM measurements.

In conclusion, the largest differences between healthy controls and dialysis patients are seen in the muscular tissue. The muscular tissue relaxogram of dialysis patients looks more like that of healthy controls after dialysis.

**HC vs HD: Relaxograms with Regularization Parameter chosen by L-Curve Method**

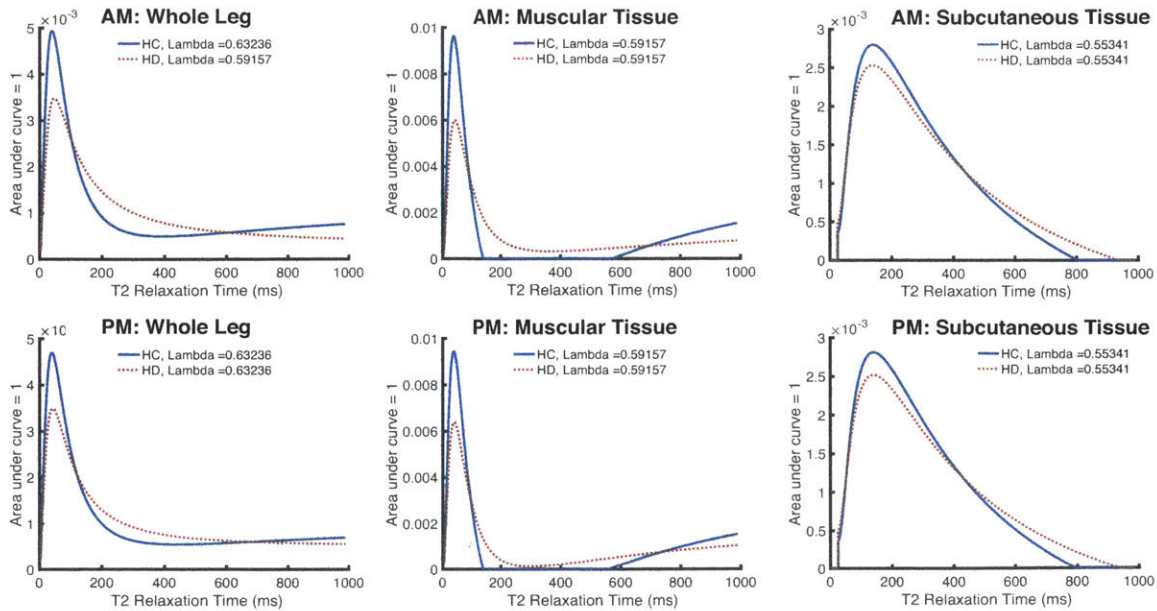


Figure 4-49: Average relaxograms of healthy controls and dialysis patients for each tissue type. Relaxograms were obtained with the regularization parameter determined to be optimal based on the L-curve criterion. HC and HD relaxograms for each tissue type are overlaid for easy comparison.

**HC vs HD: Relaxograms with Small Regularization Parameter**

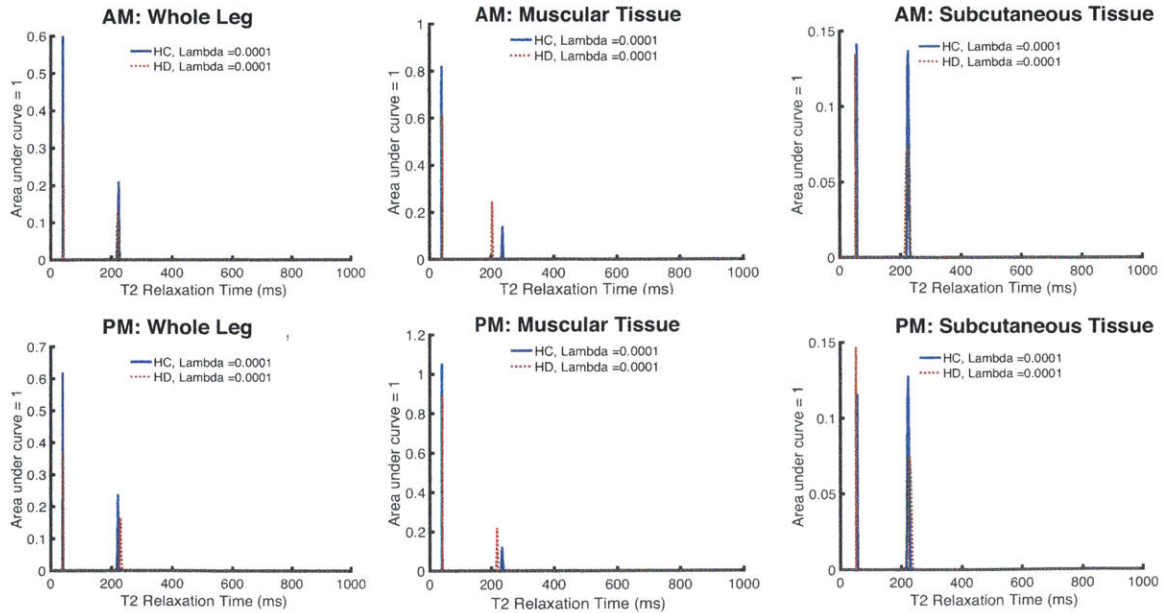


Figure 4-50: Average relaxograms of healthy controls and dialysis patients for each tissue type. Relaxograms were obtained with a very small regularization parameter to facilitate comparison of the peaks. HC and HD relaxograms for each tissue type are overlaid for easy comparison.

## **Chapter 5**

# **Phantom Studies**

The goal in this chapter was to understand how to translate relaxometry results between an MRI and MR sensor. We measured phantom and ex-vivo tissue samples on both a traditional MRI and our custom MR sensor. We tested various analysis methods – ILTs and multi-exponential fits – and compared how the results of each method matched up between the two sensors.

## 5.1 Methods

### 5.1.1 Phantoms and Ex-Vivo Tissues Experiment

We measured four phantoms - two agar phantoms (agar short and agar long), a vegetable oil phantom, and a copper sulfate ( $\text{CuSO}_4$ ) phantom. We took quantitative  $T_2$  MRI scans with the same Siemens 1.5T scanner, extremity coil, and  $T_2$  mapping pulse sequence used in human measurements (see details in section 4.1).

We also measured three ex-vivo tissue samples - muscle (bovine), fat (porcine), and skin (porcine) - from Whole Foods Market. The tissues were kept in a sealed petri dish to avoid dehydration over time as much as possible.

We took  $T_2$  measurements (approximately 10 averages) of the phantoms and tissues with the MR sensor.

We analyzed the MRI data with (1) a pixel-by-pixel mono- and bi-exponential fit, (2) a whole ROI mono- and bi-exponential fit, and (3) a whole ROI ILT. We analyzed the MR sensor data with an ILT, mono-, and bi-exponential fits.

### 5.1.2 Agar Phantoms Experiment

We made 8 different agar-based phantoms with a variety of  $T_2$  relaxation times. The exact protocol used to make the phantoms is detailed in a paper by Hattori, et. al.<sup>112</sup>. Note that we used 5% w/w Listerine instead of sodium azide in this particular batch of phantoms as the anti-microbial agent. The  $T_2$  relaxation times of the agar phantoms were measured on both the MRI as well as on our MR sensor. We analyzed the MRI data with a ROI mono-exponential fit and the MR sensor data with a mono-exponential fit as well.

### 5.1.3 Results and Discussion

Figure 5-1 shows the  $T_2$  decays of each sample on both the MRI and MR sensor.

#### ILT

The top row of Figure 5-2 shows the relaxogram of each sample with the regularization parameter chosen by the L-curve criterion. The MRI and MR sensor relaxograms are incredibly similar across all samples, except for the agar long and  $\text{CuSO}_4$  phantoms where the MRI relaxogram has higher

# MRI vs MR Sensor T2 Decays

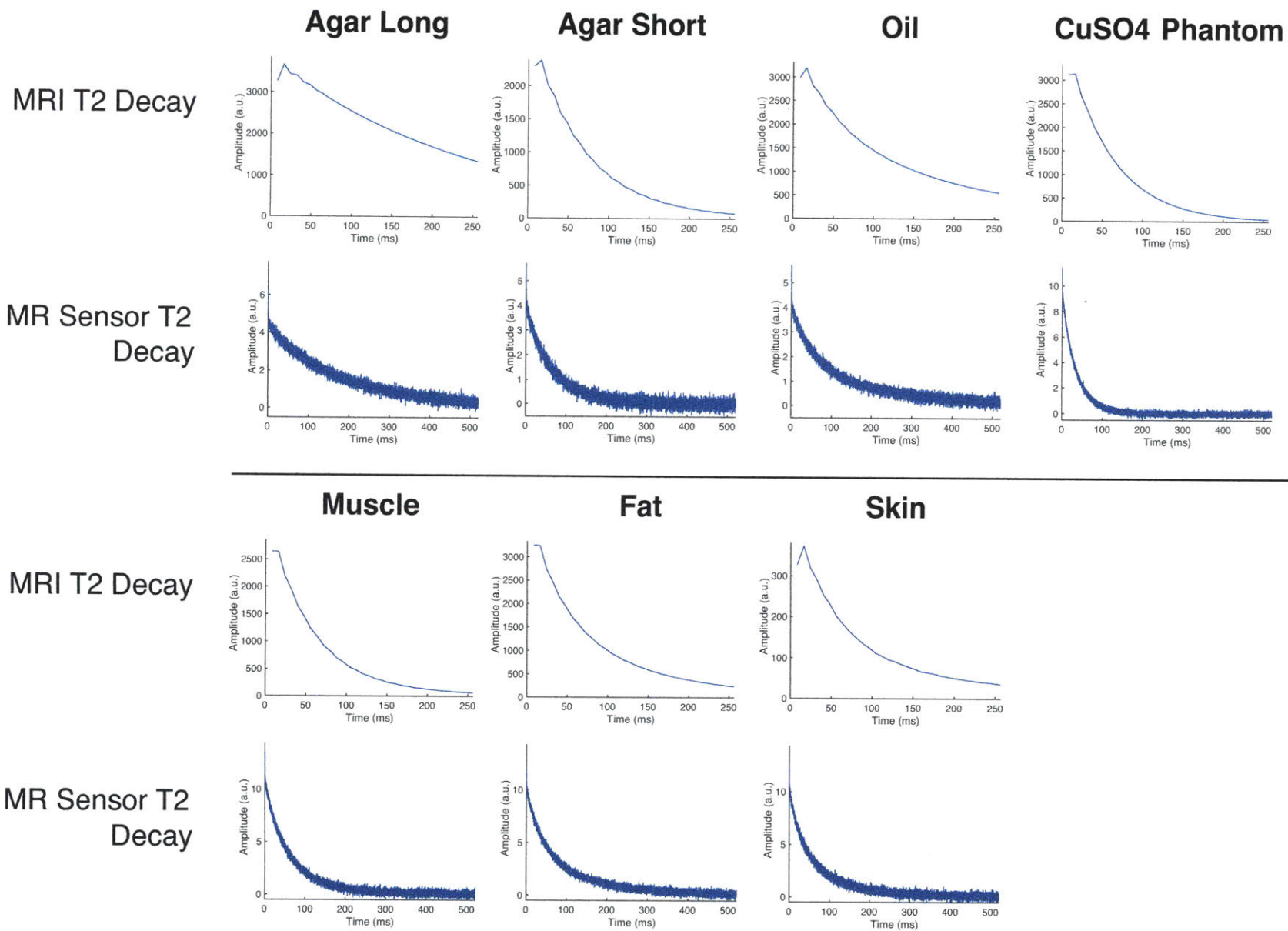


Figure 5-1: The  $T_2$  relaxation decay of each sample for both MRI and our MR Sensor.

relaxation times. The optimal regularization parameter for the MR sensor and MRI data are very different – usually  $\sim 2$  for the MR sensor data versus  $\sim 0.5$  for the MRI data. It is both surprising and encouraging that the L-curve method was able to select optimal regularization parameters that, despite being so different, make the two relaxograms similar to each other.

The bottom two rows of Figure 5-2 shows the extracted parameters – peak position and peak AUC – of the ILT regularization parameter sweep for each sample. One of the overall trends is that more peaks are identified in the MR sensor data than the MRI data.

The biggest discrepancies in number of peaks identified occurs in the tissues – muscle, fat, and skin. The MR sensor relaxograms of the phantoms sometimes have one additional peak than the MRI relaxograms, but the extra peak usually has a small contribution to the signal (AUC < 15%).

We know that data from the MR sensor can encode more discrete exponentials because of the increased number of points on the curve and the fact that the points are closer together than in the MRI data. What is unknown is whether the increased number of peaks in the MR sensor relaxograms reflects an underlying reality of more compartmentation in the tissue or whether the peaks are simply an artifact of noisy data.

The flat region of these extracted parameter plots (i.e. where the greatest number of peaks occurs) represents under-smoothed and overfit relaxograms. We know that the peaks of these relaxograms are heavily impacted by noise in the signal and may not reflect true behavior of the measured protons. The fact that the tissues have a larger discrepancy in peaks than the phantoms suggests that perhaps the additional peaks do reflect the compartmentalization of the protons being measured.

## **Multi-Exponential**

Figure 5-3 shows the mono-exponential fit results and Figure 5-4 shows the bi-exponential fit results for the MRI pixel-by-pixel, the MRI whole ROI signal, and the MR sensor. Table 5.1 summarizes the results of the MRI ROI versus MR sensor mono-exponential fits.

For the mono-exponential fits, the MR sensor relaxation time was within 10ms (and usually within 5ms) of the MRI results for all samples, except for the agar long and CuSO<sub>4</sub> phantoms (the same two phantoms we noted were different in the ILT analysis). Skin also had a large error (18.0ms) between MRI mono-exponential and MR sensor mono-exponential results (see Table 5.1), but the error between MRI pixel-by-pixel and the MR sensor was minimal (<5ms) (see Figure 5-3). It was surprising that skin had a different MRI pixel-by-pixel and MRI ROI result.

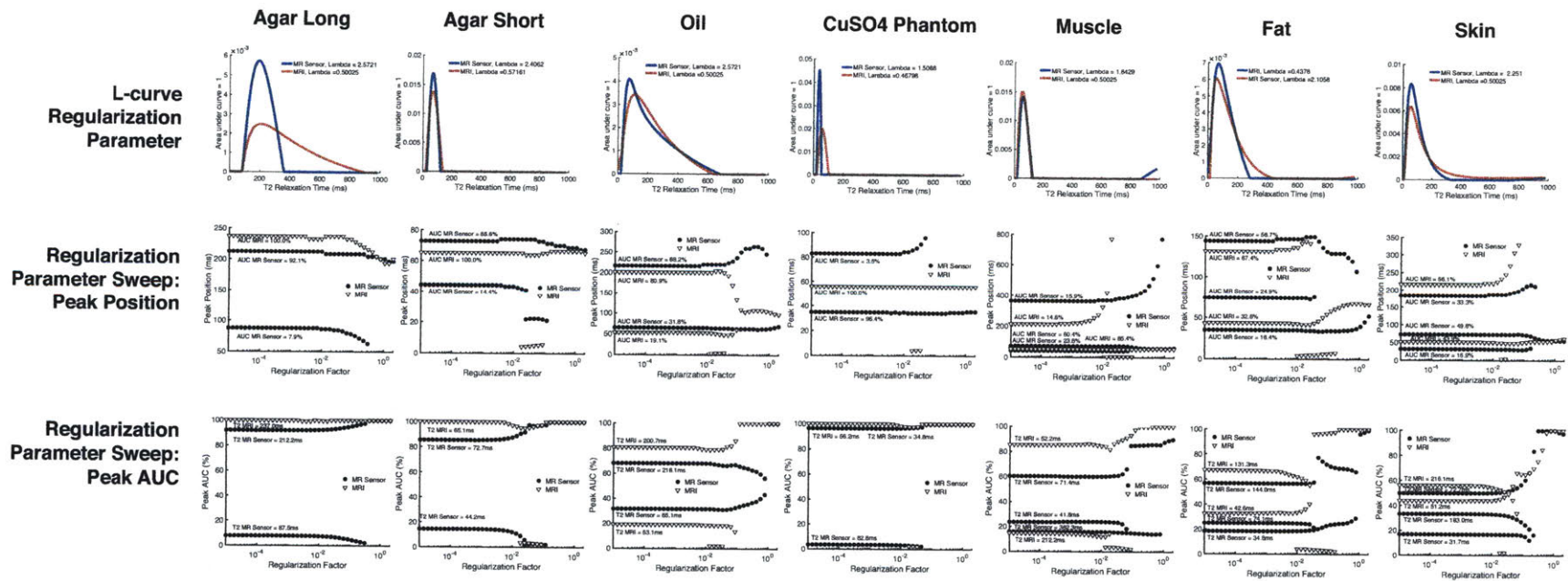


Figure 5-2: The relaxograms of each sample for both MRI and MR Sensor (overlaid in a single graph). The top row shows relaxograms where the ILT was performed with the regularization parameter chosen by the L-curve criterion. The relaxograms are impressively similar between MRI and MR sensor across all samples, except for the agar long and CuSO4 phantoms. The bottom two rows show the extracted parameters of ILTs performed with a regularization parameter sweep. The MR Sensor ILTs tend to have more peaks than the MRI ILTs.

Sample	MR Sensor			MRI			$T_2$ Difference (ms)
	$T_2$ (ms)	95% CI (ms)	$r^2$	$T_2$ (ms)	95% CI (ms)	$r^2$	
Agar Long	186.9	0.8	0.976	242.2	2.5	0.999	-55.3
Agar Short	64.7	0.4	0.970	66.6	1.2	0.999	-1.9
CuSO4 Phantom	34.4	0.1	0.994	55.7	0.4	1.000	-21.3
Oil	124.3	0.8	0.960	128.8	6.3	0.987	-4.5
Fat	84.6	0.5	0.976	80.2	4.0	0.990	4.4
Muscle	63.0	0.3	0.987	56.7	1.3	0.998	6.3
Skin	66.7	0.4	0.974	84.7	5.0	0.985	-18.0

Table 5.1: Summary of the mono-exponential results of the MR Sensor and MRI.

We analyzed the inherently multi-exponential samples with a bi-exponential fit (Figure 5-4) and the results were equally as promising. The MR sensor results match closely to the MRI pixel-by-pixel histogram. The MR sensor results match better with the pixel-by-pixel MRI histogram than the MRI average ROI results do. We hypothesize that the reason the MRI pixel-by-pixel and MRI ROI results do not always match well is that averaging many pixels together may lead to unwanted signal accumulation that would otherwise not exist when each pixel is analyzed separately.

## Conclusions, Limitations, and Future Work

There was excellent correspondence between MRI and MR sensor measurements across all samples and all analysis methods, except for the agar long and CuSO4 phantoms. We hypothesize that this is because these two are the most liquid phantoms and therefore have the highest diffusion coefficients. The diffusion contribution is discussed in further detail in section 5.3.

We noted that the relaxation times were more similar between MRI and MR sensor than the AUCs. This might suggest that we should do EPG-based correction of our MRI signal and/or MR sensor signal. EPG-based corrections of stimulated echoes have been done on MRI data to improve accuracy of AUC estimations<sup>89</sup>. To our knowledge, no one has done stimulated echo correction of single-voxel MR data.

Another layer of analysis that may have to be added to further improve the correspondence between MRI and MR sensor data is amplitude-weighting. Our MR sensor has a rapid drop-off in amplitude of its signal. Therefore, the data we measure is weighted by this amplitude profile. Contributions from tissue closer to coil are more heavily weighted in the signal than contributions from tissue further away. MRI data, on the other hand, does not have this weighting profile. To make MRI data correspond better to the MR sensor data, it may be necessary to apply an amplitude

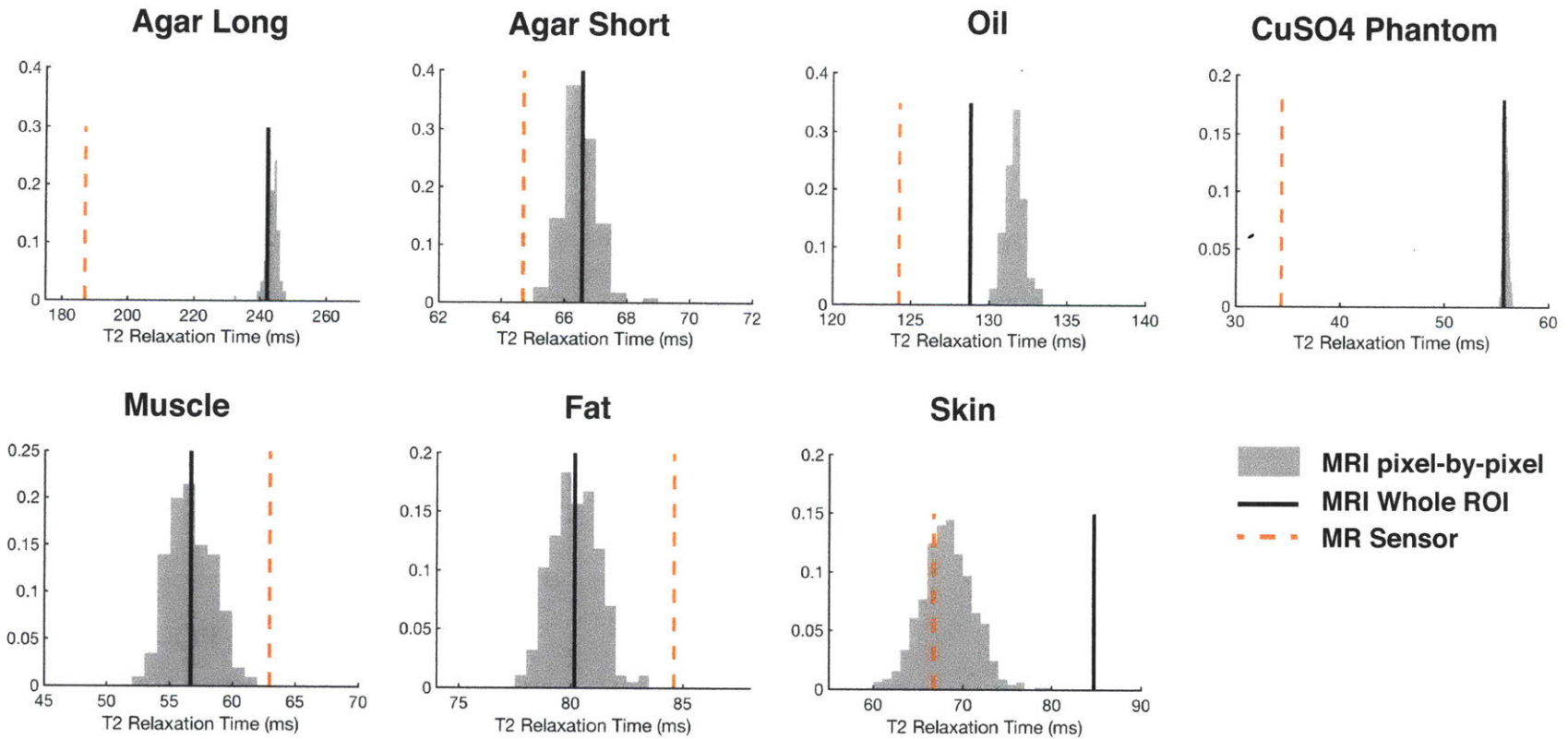


Figure 5-3: The mono-exponential results of each sample for both MRI and MR sensor (overlaid in a single graph). The histogram shows the MRI pixel-by-pixel result, the black vertical line is the MRI ROI result, and the orange dotted line is the MR Sensor result.

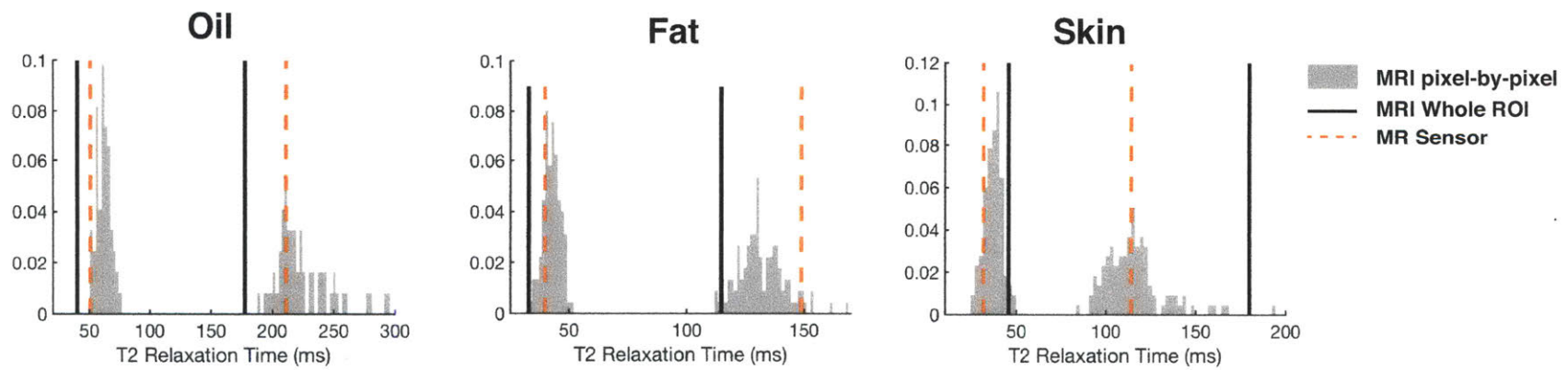


Figure 5-4: The bi-exponential results of samples that are inherently multi-exponential for both MRI and MR sensor (overlaid in a single graph). The histogram shows the MRI pixel-by-pixel result, the black vertical line is the MRI ROI result, and the orange dotted line is the MR Sensor result.

weighting to pixels based on how far away they are from an imaginary coil (as if the sample were being placed on the MR sensor).

## 5.2 Agar Experiment

Figure 5-5 shows the  $T_2$  relaxation times of the 8 agar phantoms on the MRI and MR sensor. There is a high correlation between the two values ( $r^2=0.988$ ) which means that we can directly map  $T_2$  values from the MRI to the MR sensor.

The MRI  $T_2$  relaxation time values tended to be longer than those measured with the MR sensor. We note, however, that for the shorter agar phantoms (30-50ms), the relaxation times between MRI and MR sensor are nearly identical. This finding corroborates our hypothesis from the previous section that the reason the agar long and CuSO<sub>4</sub> phantoms were not equal between the MRI and MR sensor is that they have higher diffusivities than the other samples. The diffusivity - or diffusion coefficient - of a material characterizes the mobility of its molecules. Solids have a lower diffusivity than liquids.

In this agar experiment, the higher the relaxation time of the agar phantom, the more the phantom tended towards a liquid state. The agar phantom with the highest relaxation time was barely a solid and nearly dissolved when it was touched. The more liquid the phantom, the higher its diffusivity.

When a sample with a large diffusivity coefficient is measured with a CPMG sequence within a field gradient, the measured  $T_2$  relaxation time is reduced due to diffusion effects<sup>26,27</sup>. The MR sensor has a field gradient and, as expected, the  $T_2$  relaxation times measured on the MR sensor are shorter than those measured in the much more homogeneous MRI. Let us now explore the diffusion contribution to the  $T_2$  signal as well as other contaminations.

## 5.3 Contamination of T2 Measurement

### Pure $T_2$ Relaxation Time

A pure  $T_2$  (or spin-spin) relaxation time measurement is a measure of how quickly the transverse component of the magnetization vector decays. The measurement captures the interaction of protons with one another in the system being measured. More mobile (liquid) protons have longer  $T_2$  relaxation times, whereas less mobile (i.e. bound hydrogen) protons have short  $T_2$  relaxation times.

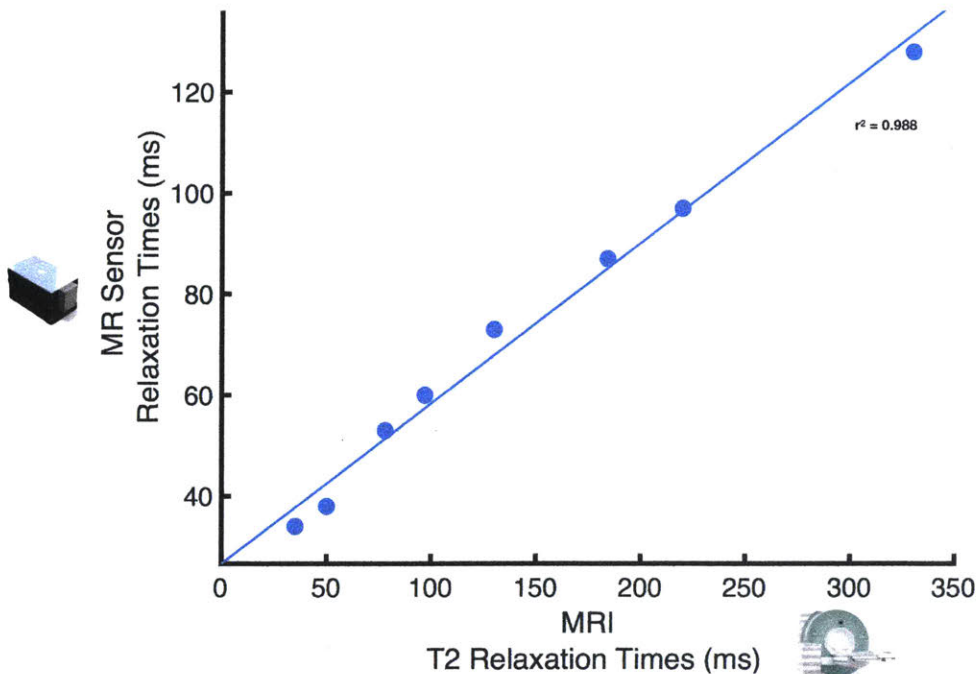


Figure 5-5: The  $T_2$  relaxation times of agar phantoms measured with MRI (x-axis) and the MR sensor (y-axis). The data were fit with a mono-exponential decay. There is a strong correlation between the MRI and MR sensor values ( $r^2=0.988$ ) indicating that the results can be translated between the two sensors.

Pure  $T_2$  measurement, unlike  $T_1$ , is largely field independent<sup>113–115</sup>. It is extremely difficult to obtain a pure  $T_2$  measurement, however. None of our MRI nor MR sensor measurements are expected to be a pure  $T_2$  measurement. They are corrupted by both diffusion and stimulated echoes – which depend on  $T_1$ ,  $T_2$  and flip angle.

### Factors Contaminating Our $T_2$ Measurement

The traditional gold-standard method for obtaining a  $T_2$  relaxation measurement is a spin echo (SE) experiment performed in a homogenous magnetic field. A 90-degree pulse is applied, followed by a delay (TE), and then a 180-degree pulse and readout. This experiment obtains a single point on the  $T_2$  decay curve. The experiment is then repeated as many times as desired with a different TE each time. It is necessary to wait for the longitudinal magnetization ( $T_1$ ) to recover fully in between each experiment, which is time consuming and the reason that this method is rarely used.

Instead, a CPMG sequence is the more practical method for obtaining a  $T_2$  relaxation measurement. In a CPMG sequence, the initial 90-degree pulse is followed by a train of 180-degree pulses with varying phases (called phase cycling). Signal is acquired after each 180-degree pulse and each

acquisition forms a point on the  $T_2$ -decay curve. The whole  $T_2$  decay curve can be measured in a single experiment using a CPMG pulse sequence. Benefits of the CPMG sequence include both speed and reduction in diffusion effects in the signal because it utilizes shorter TE than in SE measurements. The problem is that a CPMG measurement also contaminates the signal with contributions - called stimulated echoes - from additional parameters.

### Stimulated Echoes

Any time there are three or more pulses, stimulated echoes are created. A stimulated echo is signal arising from spins that were previously in the z-plane and were flipped back to the transverse plane by a later pulse.

Since a CPMG sequence contains many sequential pulses, stimulated echoes are created. Stimulated echoes give the MR signal a boost that is often desirable in qualitative MRI imaging. Stimulated echoes create a problem, however, for quantitative applications because they are dependent on not just the  $T_2$  relaxation time, but also on  $T_1$  relaxation time and the  $B_1$  flip angle. Since  $T_1$  is field dependent, the effective  $T_2$  measurement is contaminated by some  $T_1$  signal, it is often reported that  $T_2$  is field dependent.

Several researchers have developed extended phase graph (EPG)-methods of modeling these contributions to the CPMG signal<sup>83,87,89,90,116,117</sup> and they are summarized by the following equation:

$$\begin{bmatrix} M_1 \\ M_2 \\ \vdots \\ M_n \end{bmatrix} = M_0 \cdot \sin\alpha_{excitation} \cdot PD \cdot EPT(n, TE, T_1, T_2, \alpha_{1,2,\dots,n}) \quad (5.1)$$

where  $M_0$  is the longitudinal magnetization immediately after the excitation pulse  $\alpha_{excitation}$ , PD is the proton density, n is the number of echoes in the CPMG echo train, and TE is the inter-echo spacing. The vector M is the resulting decay.

Note that these stimulated echoes, and, particularly, the contribution from imperfect refocusing pulses, are also responsible for the alternating odd-even echo height behavior often seen in CPMG decay data<sup>83</sup>.

### Diffusion

The  $T_2$  relaxation time that is measured through a CPMG sequence is actually a summation of multiple different relaxation mechanisms:

- **Bulk fluid relaxation** (affects both  $T_1$  and  $T_2$ ) – this is the intrinsic relaxation property of the fluid
- **Diffusion in the presence of magnetic field gradients** (affects only  $T_2$ ) – molecular diffusion through a field gradient leads to additional dephasing and an accompanying increase in the  $T_2$  relaxation (i.e.  $T_2$  relaxation times gets shorter).
- **Surface relaxation** (affects both  $T_1$  and  $T_2$ ) –occurs at fluid-solid interfaces. Surface relaxation does not play much of a role in biological data. Instead, biological data has compartmentalization of fluids in semi-permeable compartments (i.e. cells) leading to multi-exponential measurements. The Bloch-McConnell equations are one well-accepted model for describing this relaxation behavior<sup>77</sup>.

These mechanisms can be summarized by the following relation, which is described in the NMR petrophysics literature<sup>26,27</sup>.

$$\frac{1}{T_2} = \frac{1}{T_{2bulk}} + \frac{1}{T_{2surface}} + \frac{1}{T_{2diffusion}} \quad (5.2)$$

When the fluid is in a non-uniform magnetic field, the CPMG measurement is affected by field gradient, inter-echo spacing, and the fluid's diffusivity. The larger any of these parameters, the greater the reduction on the measured  $T_2$  relaxation time. As a molecule diffuses within a field gradient, it moves into zones where the magnetic field is different and therefore the precession rate is different. This accelerates the existing dephasing processes occurring due to intrinsic  $T_2$  relaxation.

The diffusion-induced  $T_2$  relaxation time ( $T_{2,diffusion}$ ) is given by:

$$\frac{1}{T_{2,diffusion}} = \frac{D(\gamma GTE)^2}{12} \quad (5.3)$$

where  $D$  is the molecular diffusion coefficient,  $\gamma$  is the gyromagnetic ratio of a proton,  $G$  is the field-strength gradient (G/cm), and  $TE$  is the inter-echo spacing of the CPMG sequence.

We can encode diffusion information in our  $T_2$  measurements by repeating multiple CPMG measurements with varying echo times. The diffusion constant of the sample can be estimated through the relationship in Figure 5-6.

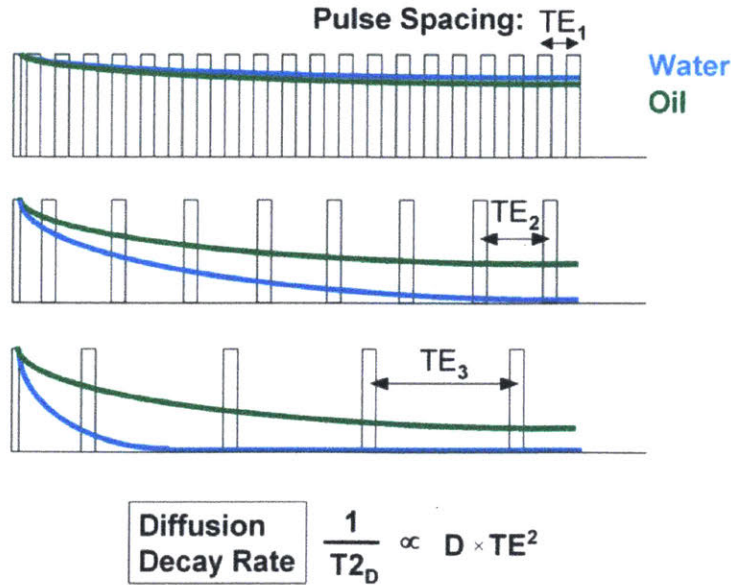


Figure 5-6: Schematic illustrating that diffusion information can be encoded in a CPMG measurement by varying the pulse spacing (TE). The diffusion-induced decay is proportional to both the square of TE and the diffusion constant (D) of the sample. [Source: Freedman, et. al., 2004<sup>27</sup>]

## 5.4 Conclusions

In conclusion, in this section we showed that it is possible to translate results between MRI and our MR sensor using a variety of analysis techniques. The most promising way to translate results between the two sensors is to analyze the MRI data with a pixel-by-pixel fitting and the MR sensor data with a multi-exponential fitting. We showed that the direct translation of  $T_2$  relaxation times between MRI and our MR sensor breaks down for samples with a high diffusivity coefficient. This is because the MR sensor has a field gradient and molecules diffusing through a magnetic gradient experience additional dephasing. The measured relaxation time in these situations is a combination of both bulk relaxation and diffusion-induced relaxation, and the result is a faster  $T_2$  relaxation time than would otherwise be measured in a homogeneous field.

## Future Work

Future work could involve full modeling of both the stimulated echo effects and diffusion-weighting in our  $T_2$  measurements across both MRI and MR sensor. We have not yet seen the EPG-based stimulated echo correction methods applied to data from a single-voxel MR sensor.

## **Implementation Notes**

The code to analyze the phantom data can be found on this project's Github:

`phantoms_tidyData_MRIsMRsensorExperiment.m`,

`phantoms_analysis_MRIsMRsensorExperiment.m`, `phantoms_tidyData_MRIPixelbyPixel.m`,

`phantoms_visualize_MRIsMRsensorExperiment.m`

## **Chapter 6**

# **Dialysis Study: MR Sensor**

This chapter presents the MR sensor portion of the dialysis study. The sensor hardware, measurement pulse sequences, and clinical set up are introduced. Specific methods for taking MR sensor measurements and analyzing the MR sensor data that were not already demonstrated in the MRI chapter are discussed here. MR sensor results are compared to bioimpedance and MRI values. Finally, a computational exploration to inform future MR sensor design specifications is performed.

## 6.1 MR Sensor Methodology

### 6.1.1 MR Sensor Hardware

The Cima Lab developed a custom single-sided MR sensor that can be placed against any part of the anatomy (Figure 6-1)<sup>118</sup>. The magnet has a 0.27T main magnetic field ( $B_0$ ) created by a unilateral Halbach design<sup>119</sup>. 150 cuboidal neodymium iron boron (NdFeB, N52 grade) magnets (Viona Magnetics, New York, USA) were positioned across 5 slabs in a 5x6 grid within each slab. The magnets were anisotropic and magnetized in a particular orientation direction. The magnets were placed in the 5x6 grids with their magnetization orientations pointing in a different direction based on which slab they were in, as shown in Figures 6-2 and 6-3. The sensor measures approximately 3.5x3.5x6" and weighs approximately 12 pounds.

This arrangement of magnet orientations as well as the depressed position of the central slab created what is called a "sweet spot" region, a volume that has a uniform  $B_0$  field strength that is parallel to the magnet surface<sup>119</sup>. Our magnet's "sweet spot" region has a saddle shape and is approximately  $0.73\text{cm}^3$  in volume at 0.27T field strength. The coil is a simple circular solenoid coil approximately 1cm in diameter tuned to 11.61MHz. More about the sensor design can be read in Matthew Li's doctoral thesis and paper<sup>118,120</sup>.

### 6.1.2 MR Sensor Pulse Sequence

The  $T_2$  relaxation time of the person's upper calf was measured using a CPMG sequence. We connected the custom magnet to a Kea spectrometer and utilized Prospa software to run various pulse sequences (Magritek, Ltd.). The  $T_2$  measurements were taken with a CPMG sequence with 8000 echoes, 65us echo time, 3 dummy echoes, 12us pulse length, 16 points per echo, 0.5us dwell time, 2000 kHz bandwidth, 800-3500ms inter-experimental delay, auto-phasing, 8 averages per measurement, and 11.61Mz  $B_1$  frequency. Hard 90- and 180-degree pulses were used and the following phase cycling was performed:

$$\text{Phase Cycling} = \begin{bmatrix} -x & +x & -x & +x : 90\text{-degree phase} \\ -y & +y & -y & +y : 180\text{-degree phase} \\ -x & +x & -x & +x : \text{Acquire phase} \end{bmatrix} \quad (6.1)$$

8 averages were taken per measurement, and 3-10 measurements per time point that were then averaged together in the post-processing analysis.

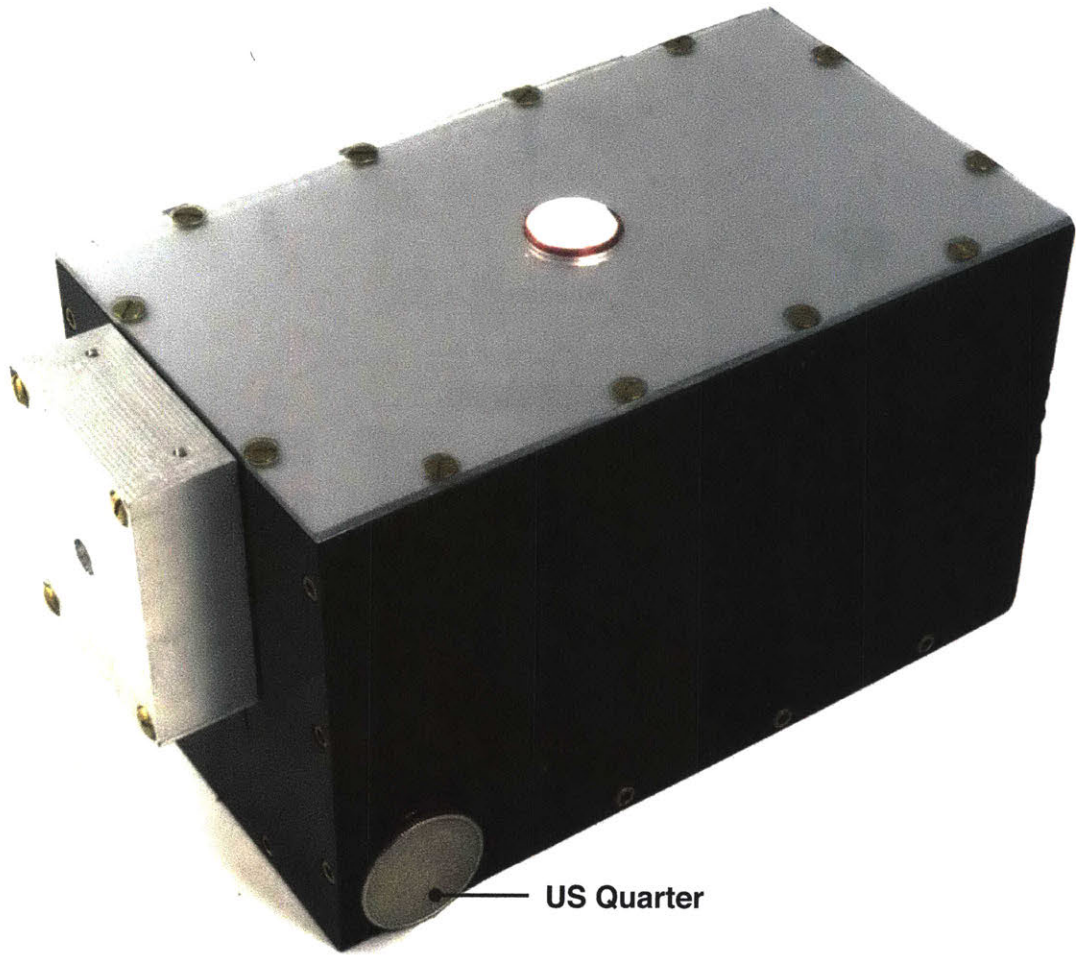


Figure 6-1: A photo of the Cima Lab's custom MR sensor with a US Quarter for scale.

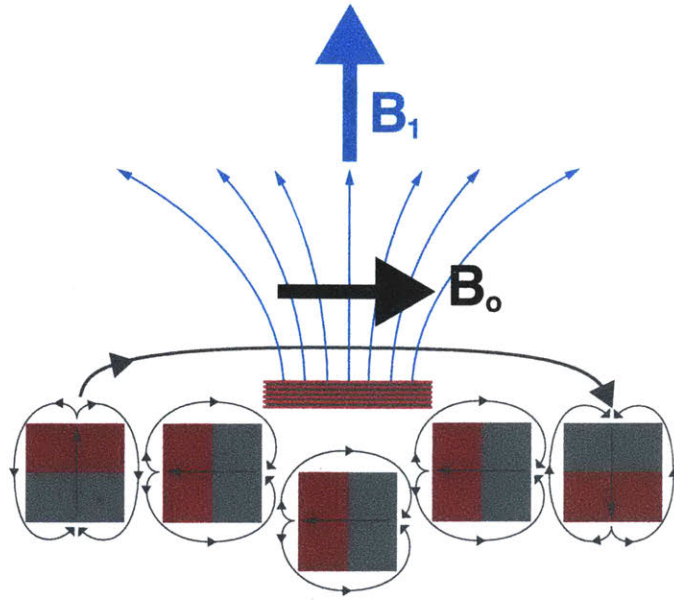


Figure 6-2: A schematic of the linear Halbach magnet arrangement used in our MR sensor. The 5 magnets create a net  $B_0$  magnetic field that is parallel to the surface of the magnet. The solenoid coil creates a  $B_1$  field that is perpendicular to the surface of the magnet.

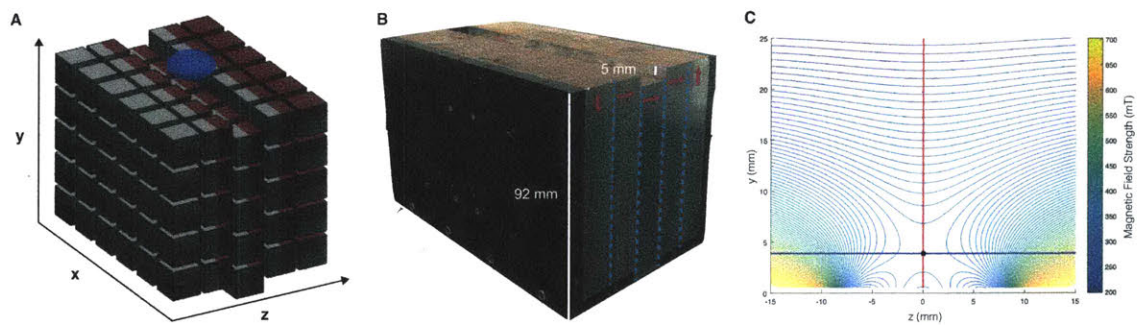


Figure 6-3: (A) A computer model of the cuboidal magnet arrangements and their respective orientations in the sensor. (B) A photo of our MR sensor with the 5 inner slabs visible and their magnetization direction shown by arrows. (C) A simulation of our sensor's field map. [Figures courtesy Matt Li]

### 6.1.3 MR Sensor Set-up in the Hospital

The single-sided MR sensor was mounted on an extendable platform of a custom aluminum-frame cart. The platform could extend onto the hospital bed's surface to make it more comfortable for the subject (see Figure 6-4). We aimed to put the sensor's coil at the same position as the MRI localizer capsule so that the same location could be measured on both the MRI and MR sensor. The sensor measured approximately 4-6mm into the leg. We used aluminum plates underneath a subject's leg to raise their leg if their leg was small so that the right portion of the calf reached the coil.

It was important to get good contact between the subject's leg and the metal platform to which all electronics were grounded. Lack of grounding caused noise levels to increase dramatically. The hospital rooms often had higher noise levels than the MIT laboratory. Strategies that helped reduce noise levels included plugging the electronics into a different outlet or unplugging telemetry equipment (blood pressure, EKG, etc.) that was attached to the patient for the duration of the sensor measurement.

### 6.1.4 MR Sensor Data Analysis

The  $T_2$  decays from each time point were averaged together using a straight-averaging technique. The first point was deleted from the averaged decay. The decay signal was fit to a three-exponential decay based on what was learned through the MRI pixel-by-pixel results. The MR sensor's signal contains mostly subcutaneous tissue and some muscular tissue. The MRI results found that the subcutaneous tissue and muscular tissue, when analyzed together, have 3 distinct peaks (see Figure 6-5). The first peak ( $\sim 40$ ms) contains signal from both the muscular and subcutaneous tissue. The second peak ( $\sim 70$ - $170$ ms) contains signal almost exclusively from the muscular tissue. The third peak ( $\sim 200$ - $250$ ms) contains signal almost exclusively from the subcutaneous tissue.

The phantom studies showed that the pixel-by-pixel MRI results line up well with multi-exponential MR sensor results. We therefore forced the MR sensor data to fit to a 3-exponential decay where the first exponential was fixed at 40ms, the third exponential was fixed at 250ms and all other parameters were allowed to float:

$$\text{3-Exponential Model} = Amp_1 e^{-\frac{time}{40ms}} + Amp_2 e^{-\frac{time}{T_2 \text{ Relaxation Time}_2}} + Amp_3 e^{-\frac{time}{250ms}} \quad (6.2)$$

The starting values used for the fit were [9, 5, 7, 100] for each of the amplitudes and relaxation



Figure 6-4: Photos of the MR sensor and custom cart in use at the MGH Dialysis Clinic.

times, respectively. The lower and upper limits for the fittings were set to 0 and infinity, respectively, for the amplitudes, and 40 and 250 for relaxation time 2. We used a non-linear least squares fitting method with a Trust-Region algorithm to perform the fits using the Matlab 2017a software (Mathworks, Inc., Natick, MA).

The relative amplitudes were calculated by dividing the absolute amplitude values by the sum of all amplitude values.

$$\text{Relative Amplitude 2} = \frac{Amp_2}{Amp_1 + Amp_2 + Amp_3} \times 100\% \quad (6.3)$$

The second type of analysis we performed on the MR sensor data involved performing an ILT. We performed an ILT sweep with a range of regularization parameters from 1e-5 to 2. We also performed an ILT with the regularization parameter chosen by the L-curve criterion.

## 6.2 Results and Discussion

### 6.2.1 3-Exponential Analysis

The free-floating relaxation time 2 was fit to values between 80-130ms, which is in the 70-170ms that we expected based on the MRI data.

The relative amplitude 2 values are shown in Figure 6-7 for AM and PM time points. The values and the changes between AM and PM values are summarized in Table 6.1.

Relative amplitude 2 decreases in dialysis patients after fluid is removed. Relative amplitude 2 does not change significantly in healthy controls. The change in relative amplitude 2 between healthy controls and dialysis patients is statistically significant ( $p=0.0196$ ). We hypothesize that relative amplitude 2 corresponds to the amount of extracellular fluid in the muscular tissue based on reported literature values (see Section 4.2.4). The relative amount of extracellular fluid decreases after dialysis in MRI data and the same decrease occurs in our MR sensor data.

The AM relative amplitude 2 values are not statistically significant between healthy controls and dialysis patients. They are statistically different in the *MRI* bi-exponential whole leg and *MRI* bi-exponential muscular tissue results. We hypothesize the reason that the AM MR sensor results are not statistically different has to do with the limitations of looking at relative amplitudes. The sum of relative amplitudes 1, 2 and 3 must equal 100%. When relative amplitude 2 decreases, we do not know if that is due to (1) a true decrease in the number of protons within that environment,

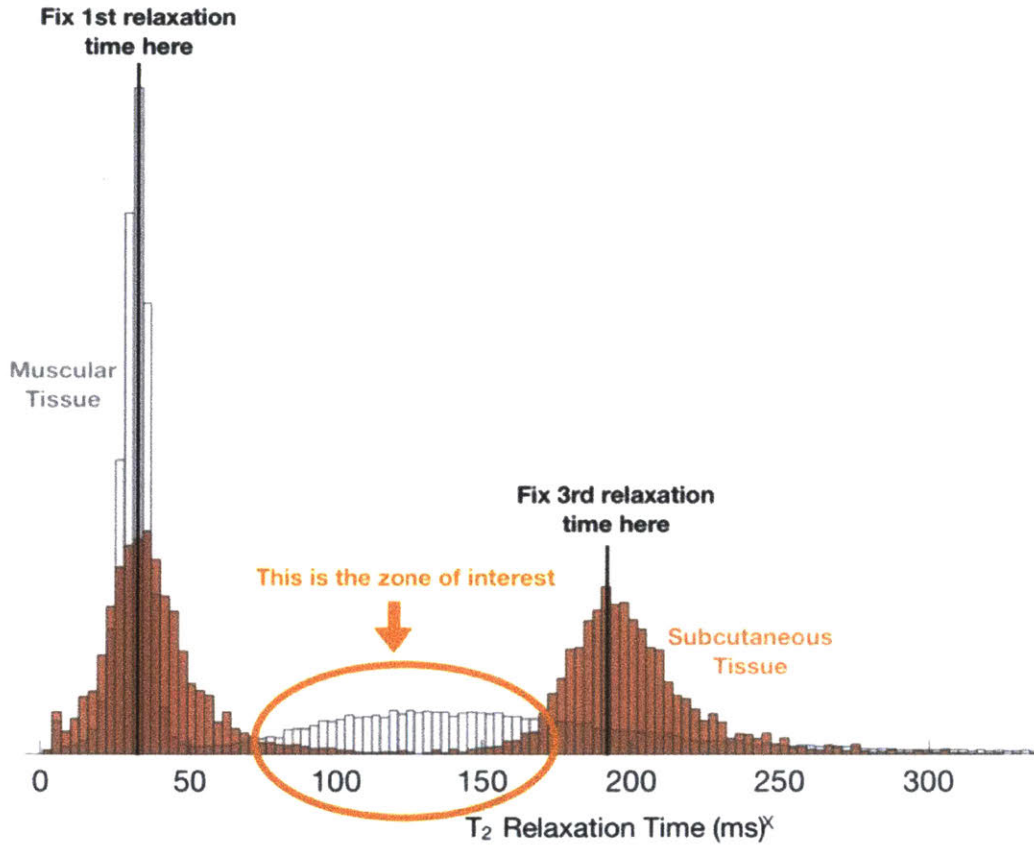


Figure 6-5: MRI pixel-by-pixel 2-exponential fit results for subcutaneous and muscular tissue. There are 3 distinct humps when these two tissues are analyzed together. We applied a 3-exponential decay model to the MR sensor data where the first and third relaxation times were fixed at the values identified in the MRI data. All other components of the 3-exponential fit were allowed to float. We learned from our phantom studies that the pixel-by-pixel MRI results lined up well with multi-exponential MR sensor results.

(2) an increase in amplitudes 1 or 3, or (3) a combination of those effects.

We expect that component 3 is associated with the subcutaneous tissue. Indeed, Figure 6-6 shows that there is a positive correlation between relative amplitude 3 and skin-subcutaneous tissue thickness ( $r^2=0.67$ ).

Ideally, component 1 would take all the compensation necessary such that component 3 would be purely related to the subcutaneous tissue and component 2 would be purely related to the muscular tissue. We know that this is not how non-linear least squares works, however. Our non-linear least squares fits 6 possible parameters, and it is not always clear how it chooses to compensate for changes in one parameter across all the others. A relationship between tissue thickness in relative amplitude 3 also affects relative amplitude 2 values since the sum of all relative amplitudes must equal 100%.

Despite the limitations of looking at relative amplitude values, it is still preferable to looking at absolute amplitude values. The SNR of scans can vary drastically from one measurement to another, which means that a decrease in amplitude could be due to either a true decrease in proton volume or simply a higher noise level. Unless noise values are tightly controlled, relative amplitude is the best way to analyze amplitude data.

Figure 6-8 shows the relationship between changes in relative amplitude 2 and changes in the calf bioimpedance's Ro values. Ro is thought to represent fluid in the extracellular space. There is a positive correlation between the two values ( $r^2=0.53$ ). This corroborates our hypothesis that relative amplitude 2 represents fluid in the extracellular space.

Figure 6-9 shows the relationship between the MR sensor's change in relative amplitude 2 values and those of the MRI muscular tissue. There is a positive correlation between the two values ( $r^2=0.405$ ). Figure 6-10 shows the relationship between the MR sensor's change in relative amplitude 2 and those of the MRI for a  $0.5\text{cm}^3$  voxel in the lateral muscle group. The lateral muscle group is the location where MR sensor measurements are made.

### **6.3 Necessary ROI Size to Separate Fluid Overload Patients from Healthy Controls**

Our current MR sensor was able to distinguish healthy controls from dialysis patients based on the AM-to-PM changes in their leg measurements. It was not, however, able to distinguish the two populations from each other with a single time point measurement. Our goal is ultimately to take

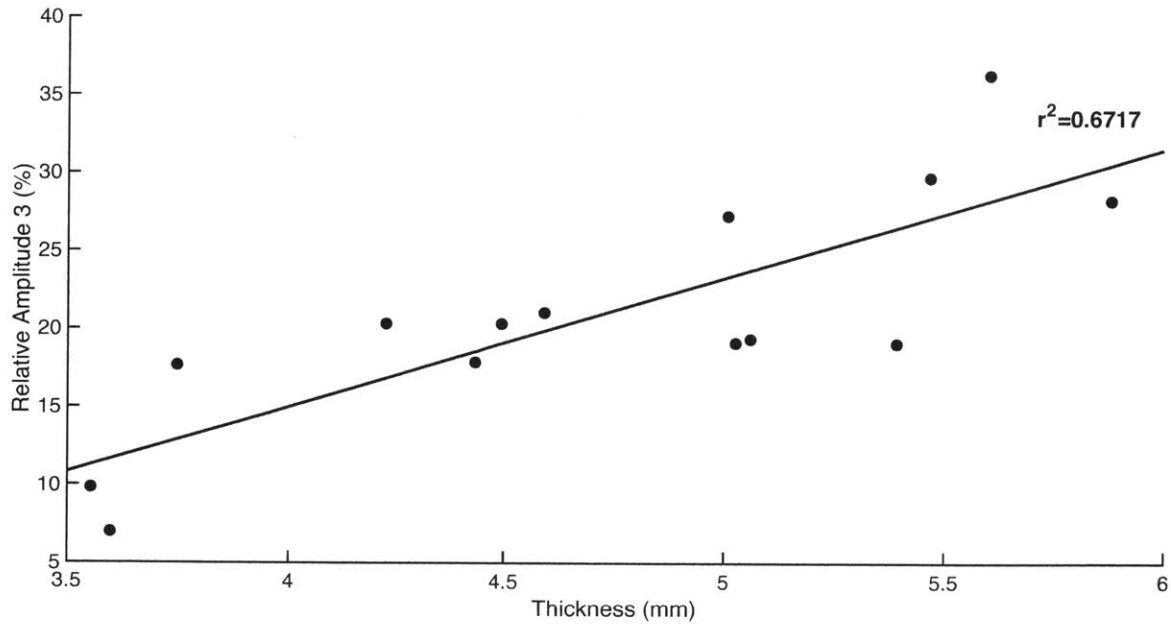


Figure 6-6: Relative Amplitude 3 of the AM MRI scan versus total thickness of skin and subcutaneous tissue for each subject. There is a positive correlation ( $r^2=0.672$ ) between relative amplitude 3 of the MR sensor data and the skin-subcutaneous tissue thickness of the subject. Variable subcutaneous thickness might be one of the reasons why the MR sensor's AM values are not statistically different between healthy controls and dialysis patients like they were in the MRI data.

**MR Sensor: Relative Amplitude 2 (%)**

Subject	AM Amp 2 (%)	PM Amp 2 (%)	Change in Amp 2 (%)
HC01	36.0	33.9	-2.1
HC01b	34.7	35.7	1.0
HC02	32.2	32.2	0
HC03	36.3	37.6	1.3
HC04	29.5	30.2	0.7
HC05	35.6	33.9	-1.7
HC06	32.0	34.3	2.3
HDMRI01	41.3	43.1	1.8
HDMRI01b	45.1	40.3	-4.8
HDMRI02	33.1	27.9	-5.1
HDMRI02b	30.9	30.7	-0.3
HDMRI03	35.9	29.0	-7.0
HDMRI04b	21.0	13.0	-8.1
HDMRI05	25.1	22.3	-2.8
<b>HC VS HD t-test, p-value</b>	<b>0.8772</b>	<b>0.2804</b>	<b>0.0196*</b>

Table 6.1: Summary of relative amplitude 2 values and AM-to-PM changes of the MR sensor. Negative change values indicate that the PM value decreased compared to the AM value. Positive change values indicate that the PM value increased compared to the AM value. Dialysis patients' relative amplitudes decreased, whereas those of healthy controls did not do so consistently. \* indicates p-value < 0.05.

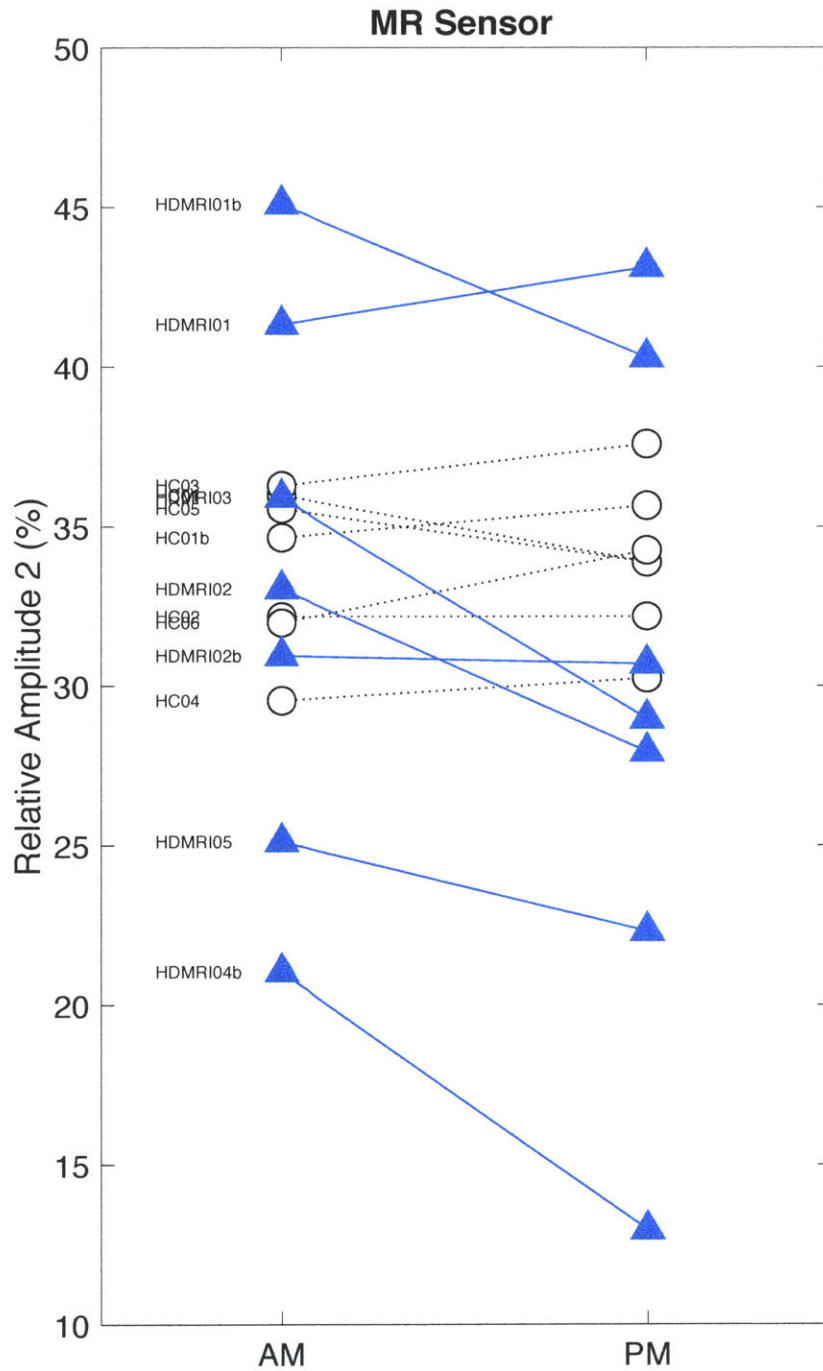


Figure 6-7: MR Sensor Relative Amplitude 2 Results. The relative amplitude 2 values of healthy controls (empty circles) and dialysis patients (shaded triangles) in the AM and PM with the MR sensor data. Dialysis patients had a decrease in relative amplitude 2 after dialysis, whereas healthy controls stayed approximately the same. The AM-to-PM change when comparing HCs and HDs is statistically significant ( $p=0.0196$ ).

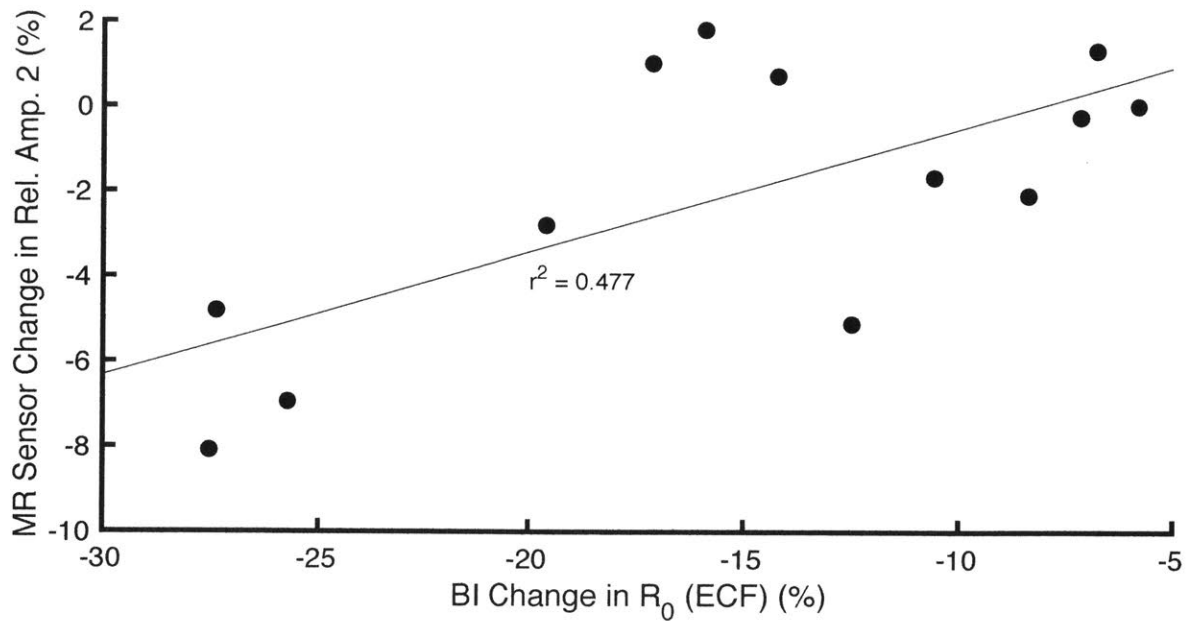


Figure 6-8: MR sensor versus calf bioimpedance results. There is a positive correlation between changes in the MR sensor's relative amplitude 2 and changes in the leg bioimpedance's  $R_0$  values.  $R_0$  represents fluid in the extracellular space, which corroborates the hypothesis that fluid is pulled from the extracellular muscular tissue space during dialysis.

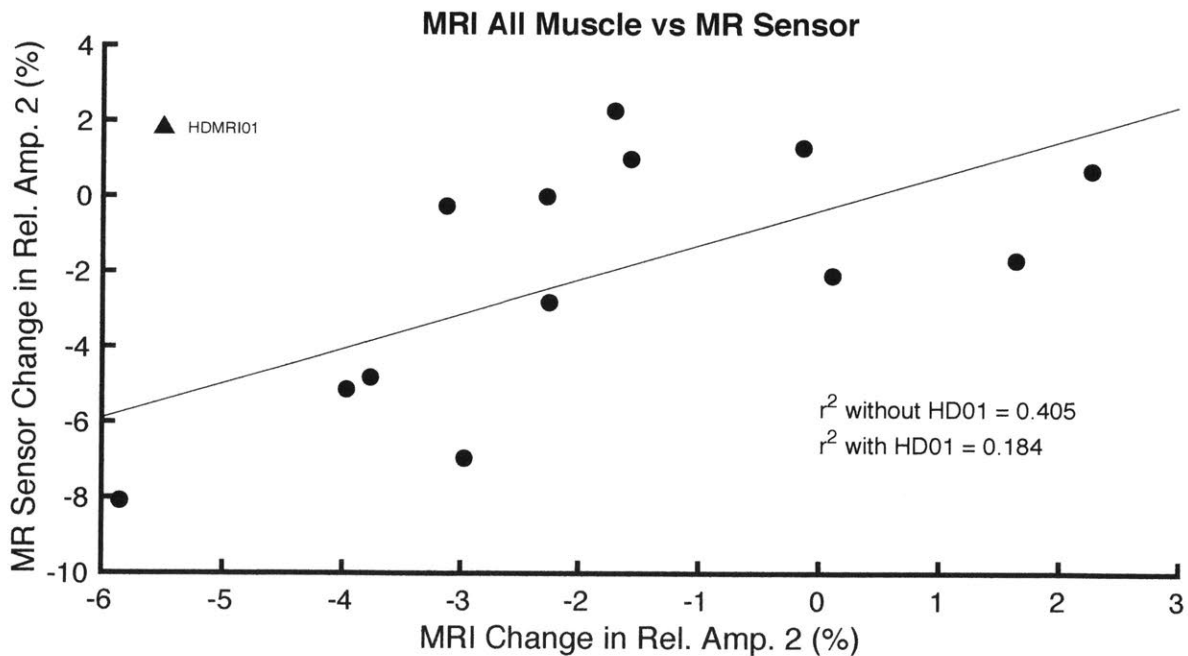


Figure 6-9: MRI All Muscle vs MR Sensor Results. There is a positive correlation between relative amplitude 2 changes in the MRI data of muscular tissue and MR sensor data ( $r^2 = 0.4053$ ). HD01 does not fit into the correlation well ( $r^2=0.1842$  when HD01 is included). This may be because the MR sensor was not able to measure deep enough to get signal from the muscular tissue since this patient had both thick subcutaneous tissue and perifascial fluid deposits between the subcutaneous and muscular tissue.

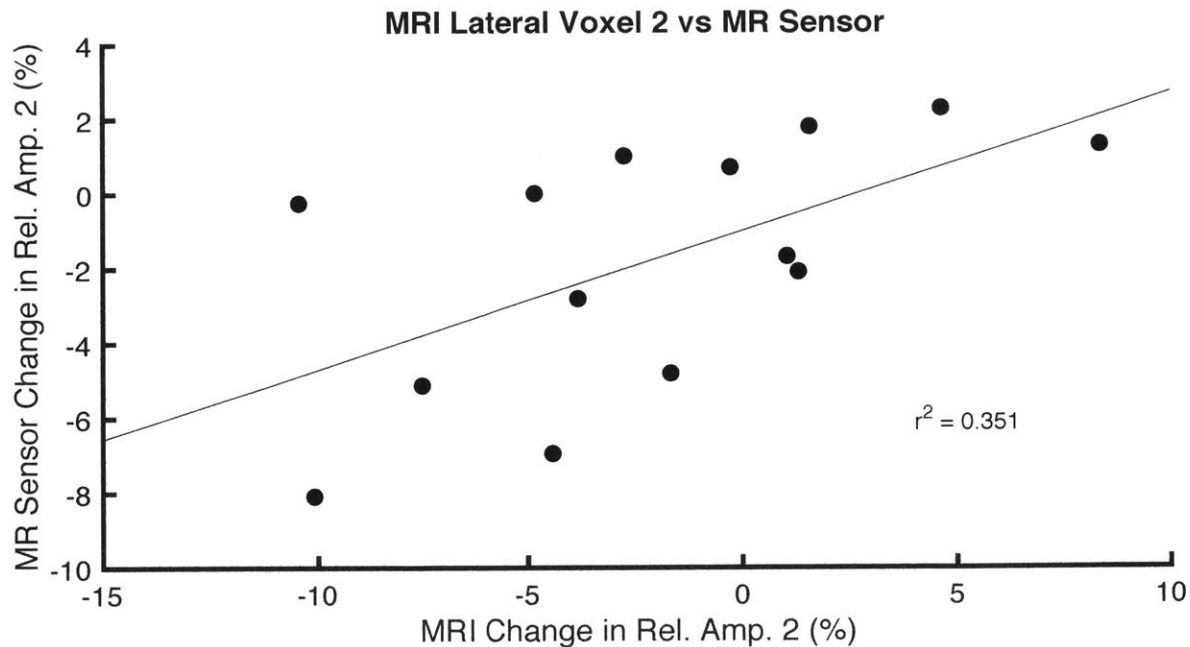


Figure 6-10: MRI Lateral Voxel 2 vs MR Sensor Results. There is a positive correlation between relative amplitude 2 changes in the MRI data of a voxel in the lateral muscle group and MR sensor data ( $r^2=0.351$ ). The lateral muscle group is the location where the MR sensor measurements were made.

a single measurement to quantify a patient’s fluid overload. Our MRI measurements were able to do this. We hypothesize that the reason our MR sensor was not able to do so is that it does not measure enough muscular tissue. In this section, we explore the minimum size that the MR sensor’s measurement region ultimately needs to be to distinguish healthy from volume overloaded patients with a single measurement.

From the sub-muscle group results of Section 4.3.2, we knew that the lateral and anterior muscle groups were the most sensitive regions for our measurement. We therefore drew small ROIs within these anatomical regions to see how small we could make the measurement region and still reach the same conclusions.

## Methods

We drew the following ROIs (10x10x5mm square regions unless otherwise specified) on the first slice of each MRI scan:

- **Voxel Lateral 1:** ROI from the surface of the skin inward into the lateral muscle group (includes subcutaneous and muscular tissue)
- **Voxel Lateral 2:** ROI purely in the muscular region of the lateral muscle group (as close to

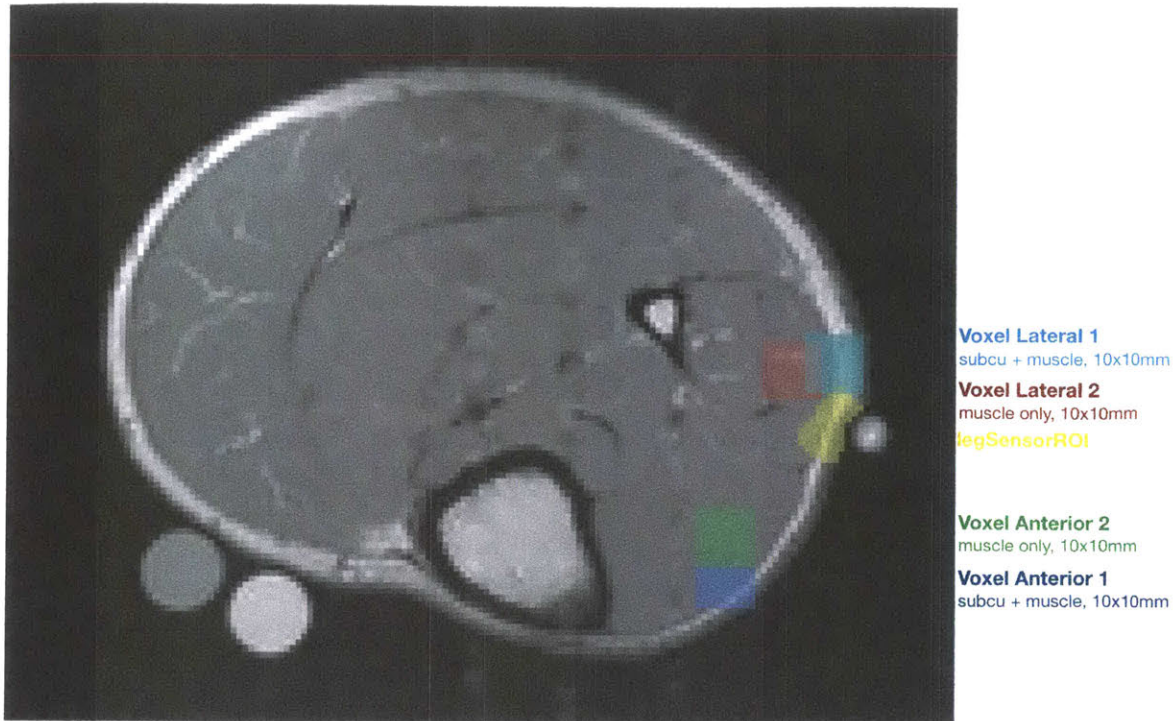


Figure 6-11: Visualization of the smaller ROIs that were drawn in order to explore the minimum necessary voxel size of a future sensor design.

the skin as possible)

- **Voxel Anterior 1:** ROI from the surface of the skin inward into the anterior muscle group (includes subcutaneous and muscular tissue)
- **Voxel Anterior 2:** ROI purely in the muscular region of the anterior muscle group (as close to skin as possible)
- **Leg Sensor ROI:** ROI located at the localizing marker, approximately 10x6x5mm in size on all four slices of the scan. Usually located within the lateral muscle group, but occasionally the marker was placed low in the soleus muscle or high at the border between the lateral and anterior muscle groups. This ROI is slightly larger than the true MR sensor measurement voxel.

The ROIs are shown in Figure 6-11. We analyzed the  $T_2$  decay of the average signal from each of these ROIs with a bi-exponential fit.

## Results

The results for each ROI are summarized in Table 6.2.

The results of the ROI corresponding to the region that our MR sensor measures are not statistically

significant across any measurement parameter when comparing healthy and dialysis patients.

The relative amplitudes 2 of the lateral voxels are not statistically significant for either the AM values or AM-to-PM change between HC and HD subjects when the voxel includes both subcutaneous and muscular tissue (lateral 1). The lateral voxel is statistically different for both AM and AM-to-PM measurements when it is a voxel of pure muscular tissue (lateral 2).

The anterior voxels have a similar pattern but both anterior 1 (subcutaneous and muscular tissue) and anterior 2 (purely muscular tissue) have statistically different AM-to-PM changes between HC and HD subjects. Only the pure muscular tissue voxel (anterior 2) has statistically significant differences in the AM value.

## **Discussion and Conclusion**

We drew small ROIs on our MRI images to explore the necessary voxel size a future sensor would need to have in order to distinguish between healthy versus dialysis patients with a single time point measurement.

It was reassuring that the MRI data is also not able to separate healthy versus dialysis patients with a single measurement if the small ROI contains both subcutaneous and muscular tissue.

A  $0.5\text{cm}^3$  pure muscle voxel in both the anterior and lateral muscle groups is enough to distinguish healthy versus dialysis patients in the AM time point. This is encouraging because the anterior and lateral muscle groups are also two of the easiest to access. The subcutaneous tissue in the anterior region is typically the thinnest of anywhere in the leg, which allows easier access to the muscle.

This experiment illustrates that our current MR sensor's voxel size is acceptable and does not have to be larger. It simply needs to measure deeper into the leg so that the voxel contains more muscle and less subcutaneous tissue contribution.

A **future sensor design** should be designed to measure a sensitive region further away from the RF coil so that more muscle is measured. It may be possible to achieve this with the current sensor design by tuning the RF coil off-resonance so that it excites protons that are further away from the coil. The number of excited protons will be smaller with the off-resonance tuning, but sweeping through several off-resonance frequencies and aggregating the measurements may allow a sufficient amount of signal from the muscle to be captured.

## Limitations

One of the limitations of doing this small voxel analysis on the MRI data is that the MRI data cannot be fit by more than 2 exponentials. Yet we know that there are at least three exponentials when there is both subcutaneous and muscular tissue in a voxel. This may be the reason that nearly all of the MRI voxels that contained both muscle and subcutaneous tissue in this section failed to produce statistically significant results: we were fitting a decay that contained 3-exponentials to a bi-exponential model.

We expect to achieve better results if the same measurement is taken with a greater number of points and analyzed with a 3-exponential model. That is the case when we compare our MR sensor results (8,000 points and 3-exponential fit: the change in amplitude 2 is statistically significant when comparing healthy and dialysis patients) to the MRI leg sensor ROI results (32 points and bi-exponential fit: none of the parameters are statistically significant when comparing healthy and dialysis patients).

Nevertheless, performing this MRI ROI analysis is still a useful benchmark to inform future sensor design.

## 6.4 ILT Analysis

### 6.4.1 Individual Subjects

The AM and PM relaxograms for each subject with a small regularization parameter are shown in Figure 6-13 and with the regularization parameter determined by the L-curve criterion in Figure 6-12.

In the small regularization parameter relaxograms, there are between 3 and 4 peaks in a single subject. It can be hard to match which AM peak corresponds to which PM peak, particularly when there are not the same number of peaks in the morning and afternoon measurements. For example, in HDMRI05's plot in Figure 6-13, there are three peaks in the AM relaxogram and four peaks in the PM one. Depending on how one matches those up and chooses to ignore either the first or last PM peak, the peak locations either increase or decrease after dialysis.

In the L-curve criterion relaxograms on Figure 6-12, there is generally one peak, though occasionally a second one is visible. There does not seem to be patterns in these L-curve method relaxograms.

The results of the regularization parameter sweep are shown in Figure 6-14. The peak positions

### MRI Small ROI Exploration

<b>Relaxation Time 1 (ms)</b>			
	AM (ms)	PM (ms)	Change (%)
Voxel Lateral 1	0.190	0.267	0.284
Voxel Lateral 2	0.137	0.543	0.0541
Voxel Anterior 1	0.112	0.994	0.230
Voxel Anterior 2	0.0021*	0.016*	0.0542
Leg Sensor ROI	0.325	0.271	0.727
<b>Relaxation Time 2 (ms)</b>			
	AM (ms)	PM (ms)	Change (%)
Voxel Lateral 1	0.807	0.371	0.860
Voxel Lateral 2	0.571	0.487	0.678
Voxel Anterior 1	0.648	0.326	0.959
Voxel Anterior 2	0.0770	0.00692*	0.332
Leg Sensor ROI	0.341	0.391	0.333
<b>Relative Amplitude 2 (%)</b>			
	AM (%)	PM (%)	Change (%)
Voxel Lateral 1	0.310	0.130	0.125
Voxel Lateral 2	0.02*	0.104	0.021*
Voxel Anterior 1	0.082	0.498	0.0308*
Voxel Anterior 2	0.027*	0.191	0.0239*
Leg Sensor ROI	0.277	0.458	0.434

Table 6.2: Exploration of size and location for future MR sensor design. Several small ROIs were drawn in the lateral and anterior muscle groups of the MRI calf scans to determine the optimal measurement location for a future MR sensor. The p-values from t-tests comparing values of healthy controls versus dialysis patients are summarized for relaxation time 1, relaxation time 2, and relative amplitude 2. \* signifies a p-value < 0.05.

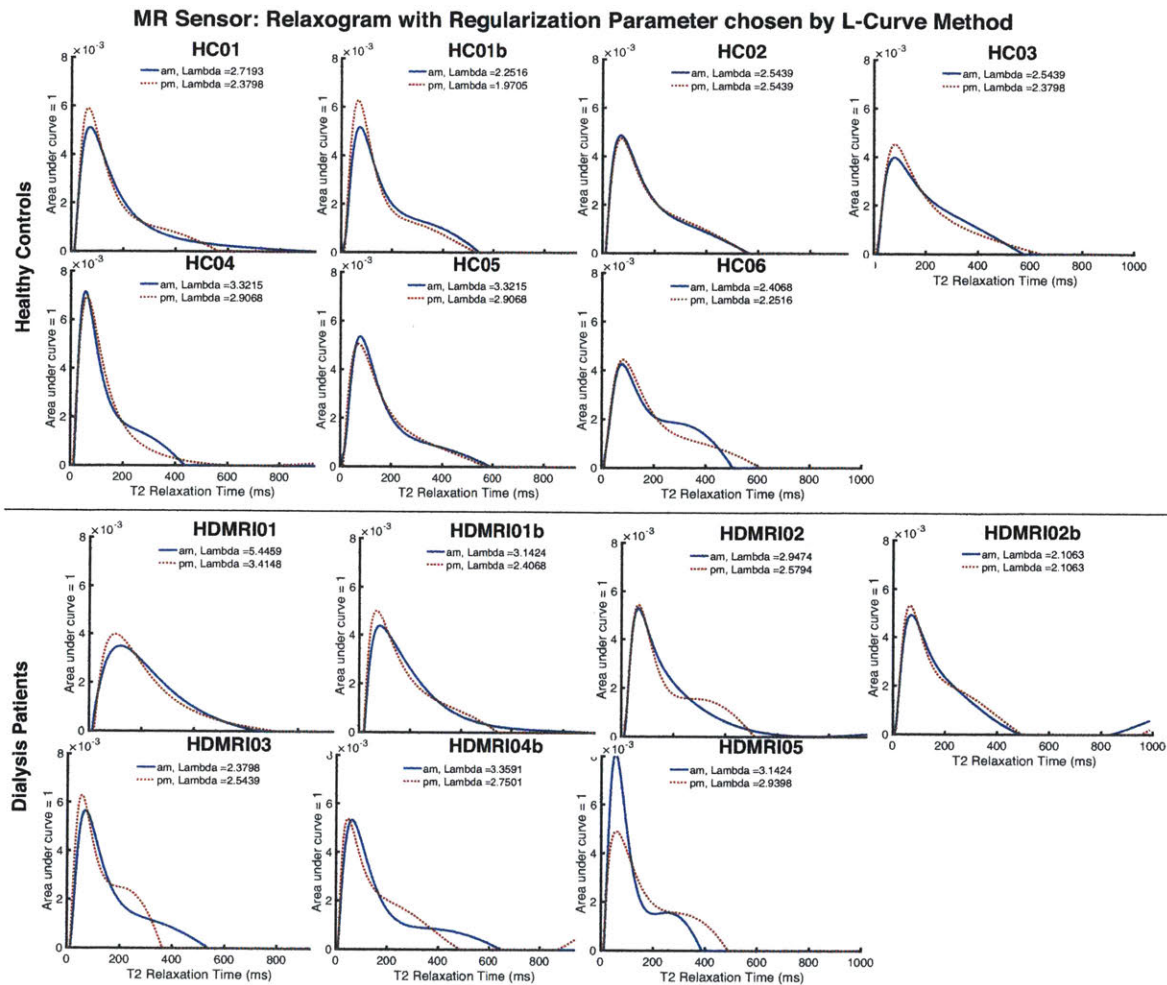


Figure 6-12: The L-curve method relaxogram results for each subject. The AM and PM relaxograms for each subject are overlaid on a single plot.

and peak AUCs vary considerably. There does not seem to be a pattern that all healthy controls fit.

There seems to be a tradeoff between the longest relaxation time decreasing, and the associated AUC decreasing, and vice versa. Several of the dialysis patients have relaxograms that shift leftward toward lower relaxation times after dialysis, but not all of the patients do.

There are no clear patterns that emerge from either the L-curve criterion plots, the small regularization parameter plots, or the regularization parameter sweep. In **conclusion**, the ILT algorithm was not a good method for analyzing the MR sensor data of *individual* subjects. The ILT results highlight the need for understanding the underlying model in our biological data. We know that overfit, undersmoothed (small regularization parameters) relaxograms are dominated by the effects of noise in the data and that seems to be happening in our MR sensor results.

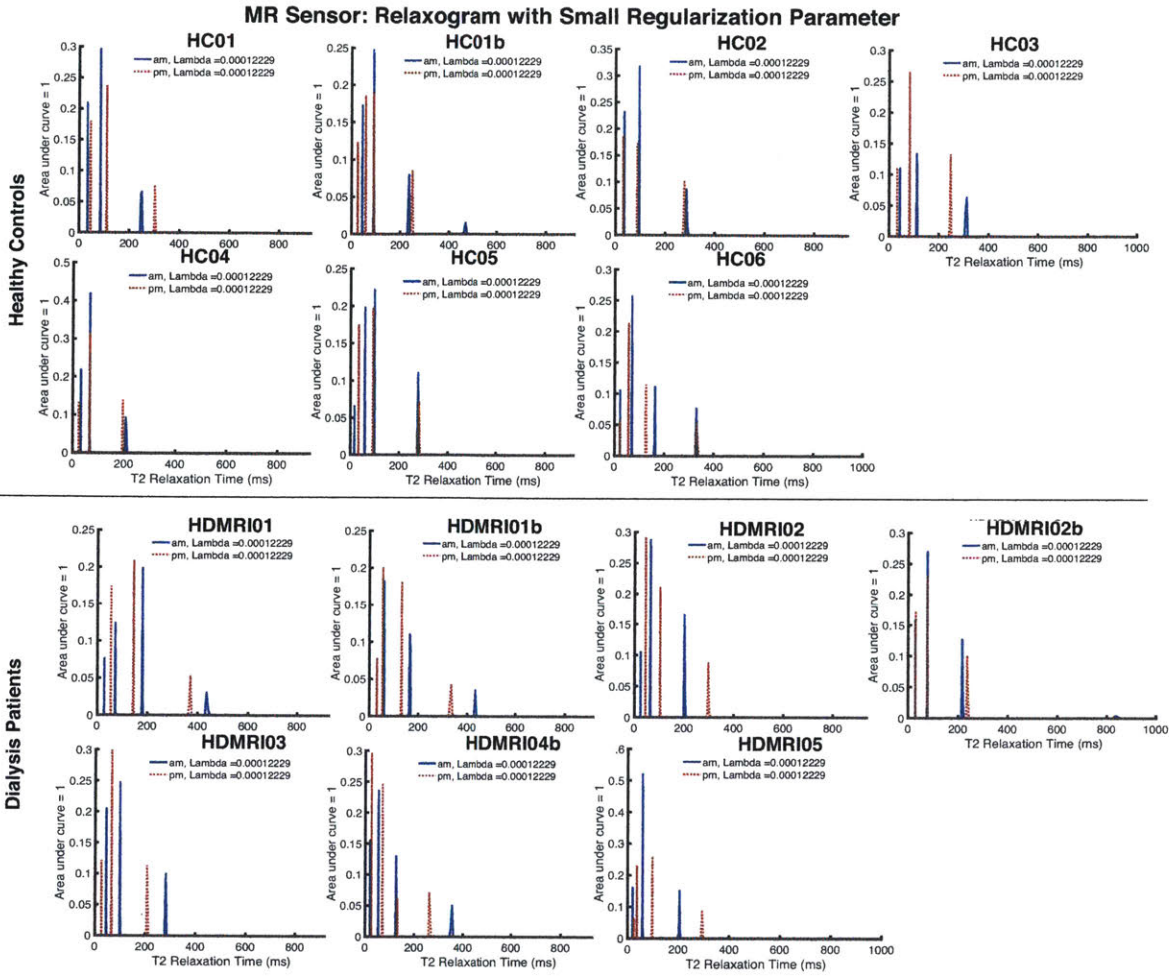


Figure 6-13: The relaxogram results for each subject with the ILT performed using a very small regularization parameter. The AM and PM relaxograms for each subject are overlaid on a single plot.

### MR Sensor: Relaxogram with Sweep of Regularization Parameters

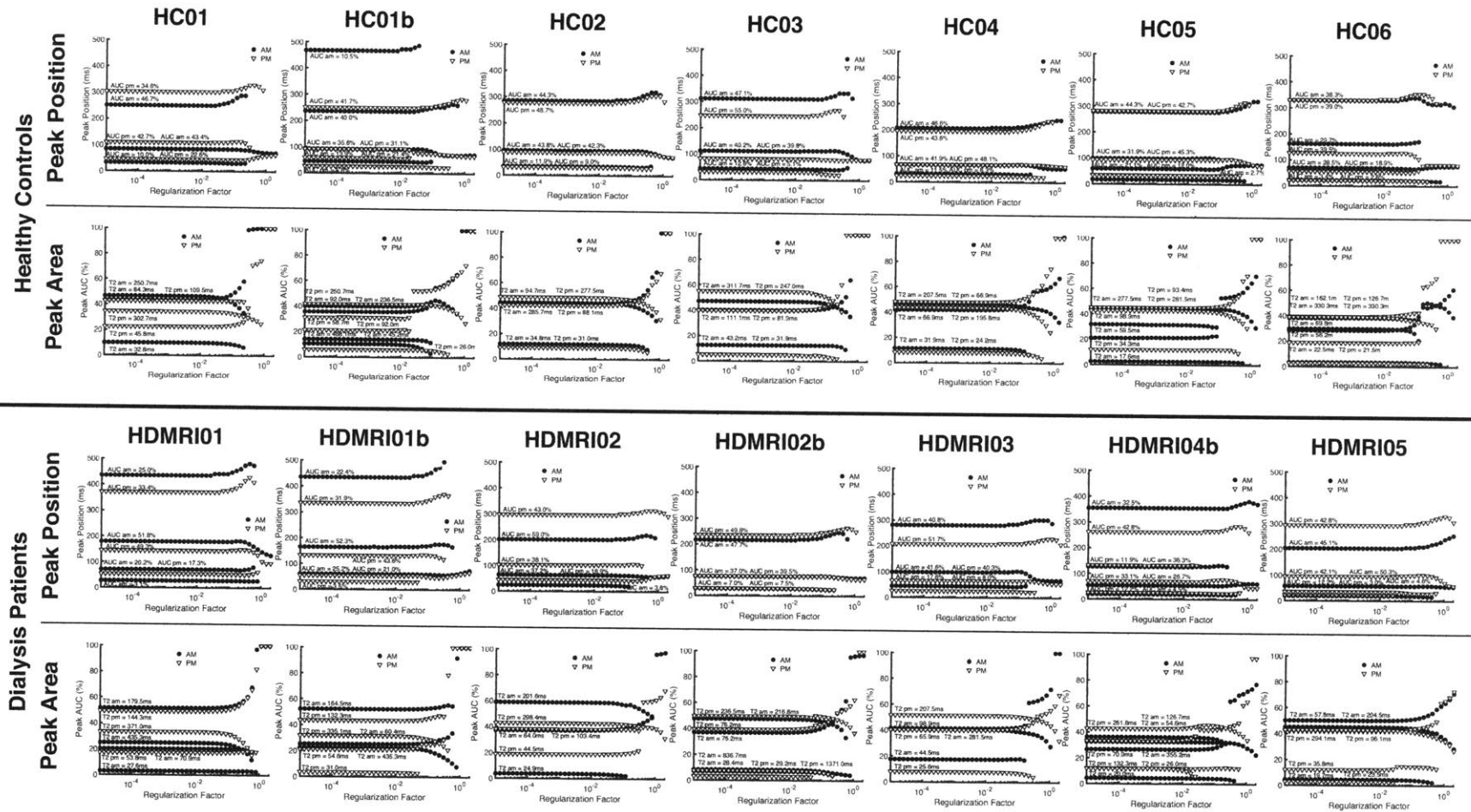


Figure 6-14: The extracted relaxogram parameters (peak position and peak AUC) for each subject resulting from performing an ILT sweep with regularization parameters ranging from 1e-5 to 2. The AM parameters are shown as a filled in circle and the PM parameters are shown by an empty triangle.

## 6.4.2 Group Averages

The ILT analysis of the average healthy control and average dialysis patient groups were a more fruitful analysis than that of individual subjects. The relaxograms of the average healthy control and dialysis patient populations are shown in Figures 6-15 and 6-16. Figure 6-15 plots the AM and PM values together on a single plot and Figure 6-16 plots HC and HD values together on a single plot for easy comparison.

Healthy controls have three peaks whereas dialysis patients have four in their relaxogram. The three longer out of four total peaks in dialysis patients' relaxogram match up to the three peaks of healthy controls. It is the initial (shortest, 10-20ms) peak of dialysis patients that does not have a healthy control counterpart.

### AM versus PM

From Figure 6-15 A and B we see that both healthy controls and dialysis patients have a leftward shift in the position of the last (longest,  $\sim 300$ ms) peak between AM and PM scans. Dialysis patients have both a larger leftward shift and also a leftward shift in the third peak ( $\sim 100$ ms). The L-curve criterion relaxograms (Figure 6-15 C and D) look similar between AM and PM time points, except that dialysis patients have a long tail that extends past the healthy controls' relaxogram on the right. The relaxogram of dialysis patients is a single hump with a long tail, whereas the relaxogram of healthy controls has two distinguishable humps. After dialysis, that right tail disappears and the relaxogram of healthy control and dialysis patients looks nearly identical. They both end at a similar right boundary and both have two humps.

These results are consistent with our hypotheses that fluid overloaded subjects have longer relaxation times and that free fluid removal during dialysis would cause a decrease in the longer  $T_2$  relaxation times.

### Healthy Controls versus Dialysis Patients

From Figure 6-16 we see that all peaks of dialysis patients are longer than those of healthy controls in the AM scan. After dialysis, dialysis patients look almost identical to healthy controls both in the relaxogram with the small regularization parameter and the one with L-curve regularization parameter.

### Regularization Parameter Sweep

Figure 6-17 shows the extracted parameters of the ILTs resulting from a regularization parameter sweep (from  $1e-5$  to 2). We see that the extracted parameters are stable across all regularization

### MR Sensor: Relaxograms of AM vs PM Group Averages

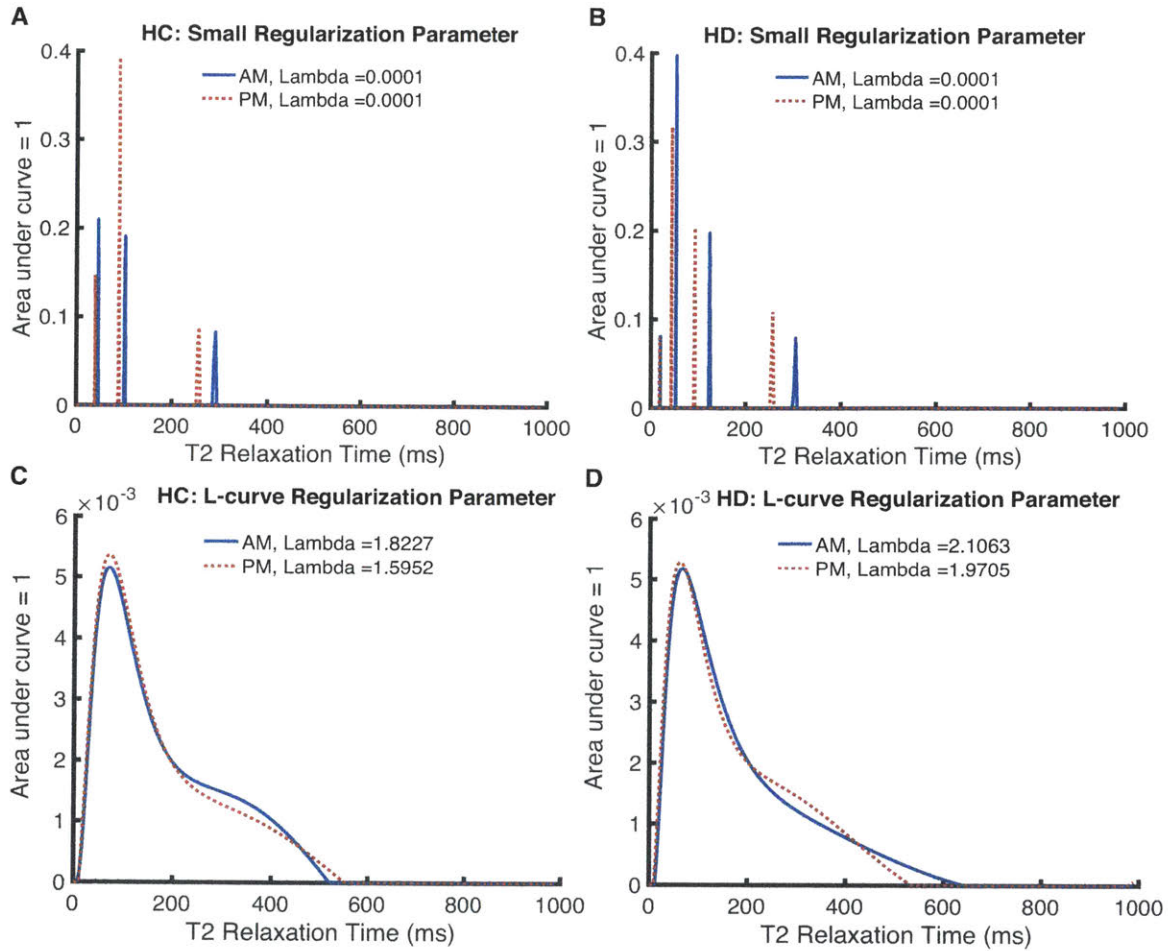


Figure 6-15: The relaxogram results for the HC and HD groups. The AM and PM relaxograms for each group are overlaid on a single plot. Subplots (A)-(B) show relaxograms with a small regularization parameter and subplots (C)-(D) show relaxograms with the regularization parameter chosen by the L-curve criterion.

**MR Sensor: Relaxograms of Healthy Controls' vs Dialysis Patients' Group Averages**

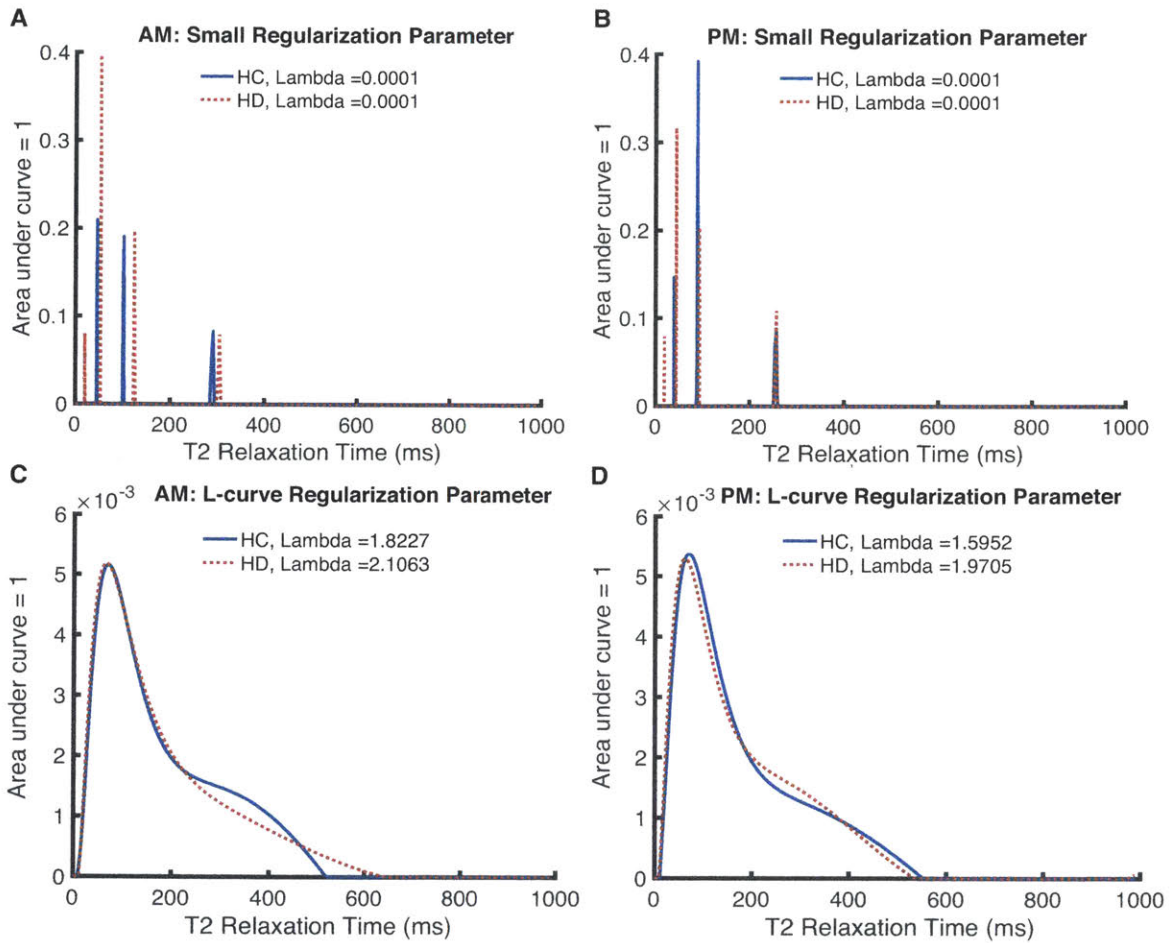


Figure 6-16: The relaxogram results for the HC and HD groups. The HC and HD relaxograms are overlaid on a single plot so that the values of these two groups can be easily compared. Subplots (A)-(B) show relaxograms with a small regularization parameter and subplots (C)-(D) show relaxograms with the regularization parameter chosen by the L-curve criterion.

parameters from  $1e-5$  to 0.1, after which certain peaks disappear and the peak locations and peak AUCs vary. Healthy controls have three peaks until the regularization parameter becomes 0.1, after which they only have two, and then eventually one peak. Dialysis patients have four peaks until the regularization parameter becomes 0.1, after which they only have two, and then eventually one peak. The fourth peak that exists for dialysis patients is a short ( $\sim 20$ ms) peak that represents only 2% of the signal.

We see that across all regularization parameters, all peak positions for healthy controls decrease in the PM measurement compared to AM. The peak AUCs of the two longer ( $\sim 100$ ms and  $\sim 275$ ms) peaks increases slightly (about 2%) and the peak AUC of the shortest ( $\sim 40$ ms) peak decreases (about 4%). The AUCs of all peaks must sum to 100%, so whatever happens in two peaks must be accounted for in the AUC of the final peak.

For dialysis patients, the peak position of the two longer peaks ( $\sim 100$ ms and  $\sim 275$ ms) across all regularization parameters decreases after dialysis. The peak position decreases in dialysis patients are larger than the decreases seen in healthy controls. The peak AUC of longest peak ( $\sim 275$ ms) increases after dialysis by approximately 10%. The peak AUC of the remaining peaks decreases.

### **Conclusion**

In conclusion, these group average relaxogram results support our hypothesis that dialysis (fluid overloaded) patients have a higher relaxation times than healthy controls and that the relaxation times decrease in response to fluid removal during dialysis. Furthermore, one of the benefits of the ILT approach is that it does not require us to specify a pre-determined model to apply to the data. We saw in the regularization parameter sweep that our conclusions hold independently of our choice of regularization parameter. However, the ILT results for peak AUC go counter to what we observed in the multi-exponential analyses and what we expect to happen. We expected the AUC associated with longer relaxation times to decrease in response to dialysis. While most of the dialysis patients' peak AUCs did decrease, the AUC associated with the longest peak ( $\sim 275$ ms) increased considerably. It is also confusing that the peak AUCs of the healthy controls increased. We **conclude** that while the ILT holds promise as an analysis method, it must be further optimized and tuned for our application before its results can be utilized.

### MR Sensor: Relaxogram Sweep of Group Averages

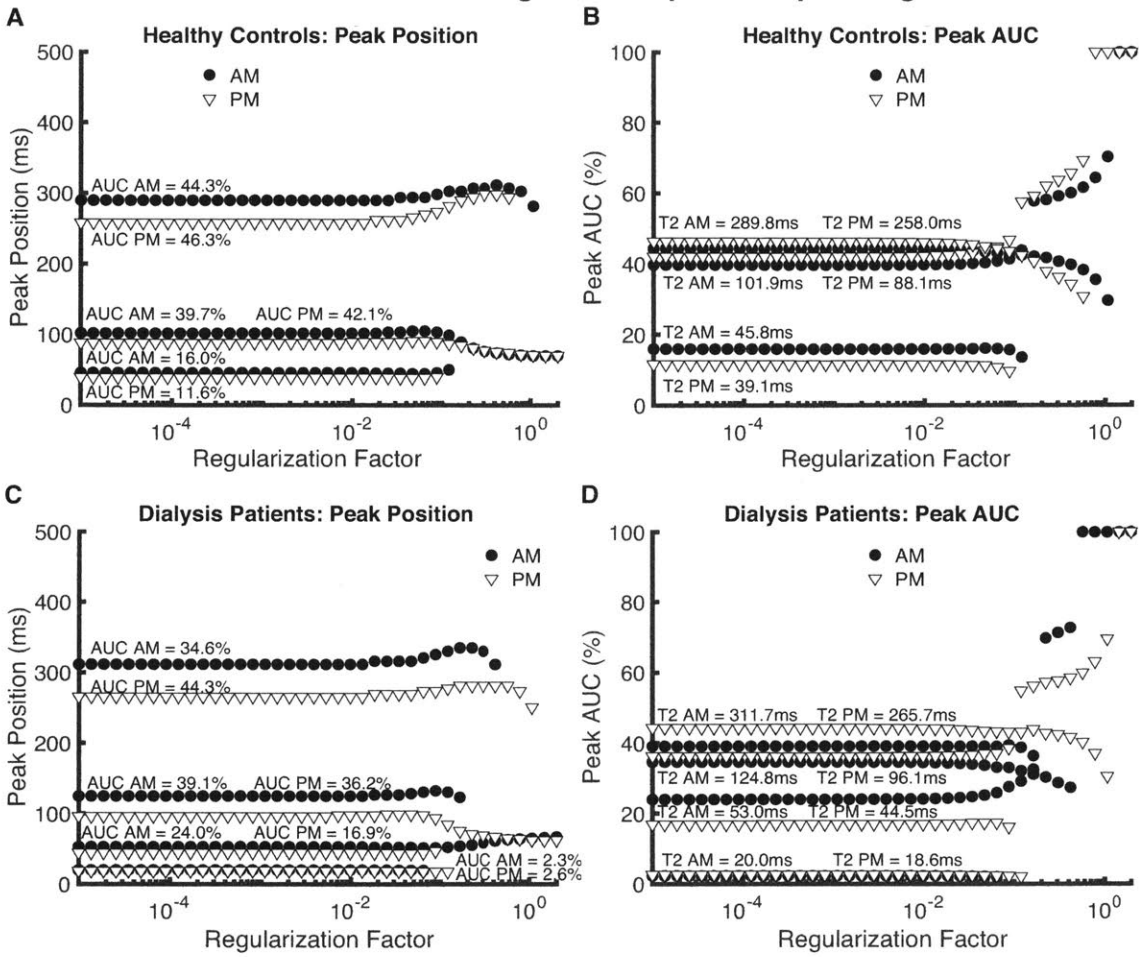


Figure 6-17: The extracted relaxogram parameters (peak position and peak AUC) for the HC and HD groups resulting from performing an ILT sweep with regularization parameters ranging from 1e-5 to 2. The AM parameters are shown as a filled in circle and the PM parameters are shown by an empty triangle.

## Chapter 7

# Conclusions

The goal of this doctoral work was to harness the diagnostic potential of quantitative MRI using portable MR sensors. Specifically, we explored the ability of bedside MR sensors to quantify fluid overload. Here is a summary of the conclusions from this work.

### **Dialysis Study: Overview**

We conducted a clinical study with 7 dialysis patients ( $n=7$ ,  $n=5$  unique individuals, mean age  $55.1 \pm 10.3$  years) and 7 age-matched healthy controls ( $n=6$  unique individuals, mean age  $54.2 \pm 4.9$  years). Subjects had quantitative  $T_2$  measurements taken of their upper calves with both an MRI as well as the Cima Lab's custom MR sensor both before and after dialysis (or before and after 4 hours of bedrest in the case of healthy controls). We chose to work with ESRD patients treated with hemodialysis (HD) because they experienced large fluid losses in a short period of time, which enabled us to take measurements in the same day of the same person at two different fluid states.

### **Dialysis Study: MRI Results**

We learned a lot about how fluid physiology shows up in MR signal through the MRI portion of the Dialysis Study. We analyzed the quantitative  $T_2$  MRI data with a bi-exponential fit of each individual pixel, with a bi-exponential fit of entire regions of interest (ROIs), and with an inverse Laplace transform (ILT) of entire ROIs. Across all these analysis methods, we learned that the parameter in the lower leg that is most sensitive to changes occurring during dialysis is component 2 of the muscular tissue. Component 2 (relaxation time 2 and amplitude 2) correspond to the extracellular fluid. There are almost no changes in subcutaneous tissue in response to a single

dialysis treatment.

In the pixel-by-pixel bi-exponential fit results, **all dialysis patients** had elevated relative amplitudes of the extracellular fluid component of the muscular tissue. This means that the relative volume of extracellular fluid was larger in HD patients compared to healthy controls ( $p=0.0019$ ). The relative volume of extracellular fluid decreased after dialysis, such that HD patients' relative amplitude values were closer to those of healthy controls (HC vs HD relative volume shift,  $p=0.0026$ ). The **most fluid-overloaded** HD patients had elevated  $T_2$  relaxation times in their muscular tissue. There were two healthy controls who seemed to become dehydrated between their AM and PM MRI measurements. These **dehydrated and hypovolemic** patients had decreased relative amplitude values. This incidental finding suggests that dehydrated patients lose extracellular fluid volume, though our study was not specifically designed to detect dehydration.

From these results, we conclude that the first sign of fluid overload is increased relative amplitude of the long component (corresponds to expansion of the extracellular fluid space). After a certain amount of fluid accumulates, the relaxation time of the long component starts to increase as well (molecular environment of the extracellular fluid space becomes closer in mobility to free-fluid). Importantly, both of these MR findings occur *before any signs of lower extremity edema is detectable on physical exam*.

Since the pixel-by-pixel fitting is a type of analysis that is not possible to do with a single-voxel sensor, the next step was to analyze the MRI data in a manner more similar to what would be done with MR sensor data. We **averaged pixels from entire ROIs** together and applied bi-exponential fits to the entire averaged signal. We first did this on signal from the muscular tissue since that was the tissue with the greatest sensitivity to changes due to dialysis in the pixel-by-pixel results.

The muscular tissue's relative amplitude 2 values were significantly higher in HDs than in HCs before dialysis ( $p=0.0021$ ). The relative amplitude values became less significantly different between HD and HC subjects after dialysis ( $p=0.0209$ ). The AM-to-PM change in relative amplitude 2 was very significantly different between HD and HC subjects ( $p=7.7e-4$ ). These results, again, suggest that the relative volume of extracellular fluid in the muscle is expanded in dialysis patients and then decreases after dialysis.

Specifically, the lateral and anterior muscle groups had the **greatest sensitivity** to detecting HD versus HC subjects out of all the muscle groups. This finding was fortuitous since the lateral and anterior muscle groups are also two of the most superficial muscles, making them easier to measure with a single-sided sensor.

Next, having seen that we could reach the same conclusions by averaging all muscle pixels together as by analyzing each of them separately, we performed a bi-exponential fit on the average of all pixels in the leg. The results of the whole leg were similar to those of just the muscular tissue. The relative amplitude values were significantly higher in HD patients than HCs at the AM measurement ( $p=0.0168$ ) and then decreased such that they were no longer statistically different after dialysis ( $p=0.0746$ ). The AM-to-PM change in relative amplitude 2 was statistically difference between HC and HD subjects ( $p=0.0203$ ). The results of the whole-leg ROI analysis are important because this is a type of analysis that can be done with a single-voxel sensor.

## **Phantom Studies**

We performed experiments on multiple phantoms and ex-vivo tissue samples to learn how to translate relaxometry results from MRI to an MR sensor. We found that there was good correspondence between MRI and MR sensor results across all samples, except for phantoms with a large diffusivity coefficient. The phantoms with large diffusivities had relaxation times that were lower in the MR sensor than in the MRI. Since the MR sensor has a magnetic field gradient, the  $T_2$  measurements taken with a CPMG sequence will have accelerated dephasing due to diffusion in the presence of a gradient.

The L-curve method relaxograms for MRI and the MR sensor were impressively similar despite the L-curve method selecting very different regularization parameters for the MRI versus MR sensor data. There was also very good correspondence between MRI pixel-by-pixel multi-exponential results and MR sensor multi-exponential results. We utilized this conclusion to develop a model with which to analyze the MR sensor data based on our learnings from the MRI pixel-by-pixel results.

## **Dialysis Study: MR Results**

We used the results from the MRI pixel-by-pixel analysis to develop a 3-exponential model with which to analyze our MR sensor data. Both muscular and subcutaneous tissues have two peaks – the first of which corresponded to intracellular fluid and overlaps between the two tissue types. The second muscular tissue peak occurs around 70-170ms and the second subcutaneous tissue peak occurs around 200-250ms.

A voxel containing both muscular and subcutaneous tissue has three peaks (40ms, 70-170ms, 200-250ms). We therefore fit the MR sensor data – which measured through the subcutaneous tissue

to get to the muscle – with a forced 3-exponential decay. The relaxation time of the first exponential was fixed at 40ms, the third exponential was fixed at 250ms, and all the other parameters were allowed to float. The middle free-floating relaxation time (associated with extracellular fluid in the muscular tissue) was fit to values between 80-130ms, which is what we expected, and provided confirmation that our model was working as expected.

The change in the relative amplitude 2 (relative fraction of extracellular fluid of the muscular tissue) from AM to PM measurements was statistically different between HC and HD subjects ( $p=0.0196$ ). This shows that our MR sensor is capable of detecting fluid changes related to dialysis.

There was a correlation between relative amplitude 2 changes and extracellular fluid changes measured by leg bioimpedance ( $r^2=0.53$ ). This strengthens our hypothesis that amplitude 2 is related to extracellular fluid volume.

The AM relative amplitude 2 value was not statistically different between HC and HD subjects like we had seen in the MRI results. This shows that our MR sensor is not yet capable of identifying HC versus HD patients with a measurement at a single time point. This capability is our ultimate goal.

We hypothesize that the reason for the lack of statistical significance has to do with the limitations of looking at relative amplitude. The sum of relative amplitudes 1, 2 and 3 must equal 100%. When relative amplitude 2 decreases, we do not know if that is due to (1) a true decrease in the number of protons within that environment, (2) an increase in amplitudes 1 or 3, or (3) a combination of those effects. There is a correlation between relative amplitude 3 (associated with subcutaneous tissue) and the subcutaneous tissue thickness ( $r^2=0.67$ ). The thicker the subcutaneous tissue, the larger relative amplitude 3. When there is a correlation in one parameter, it is not clear how the NLLS algorithm compensates across the other parameters. Since relative amplitude 3 is correlated to the subcutaneous tissue thickness, we expect that relative amplitude 2 is also affected by subcutaneous tissue due to compensations made by the algorithm. Measuring more muscle tissue with the MR sensor we expect will fix the lack of significance issue.

We did a study to see how large our MR sensor measurement region would have to be to be able to identify HC versus HD patients with a single measurement. We determined that a sensor that can measure  $0.5\text{cm}^3$  of muscle in either the lateral or anterior muscle groups would be sufficient to do so. This result can inform future sensor design specifications.

We analyzed our MR sensor data with an ILT, but this analysis method was not very effective. We believe the ILT could hold promise if more work is done to tune it for our application. Nevertheless,

our ILT analyses were fruitful in the sense that we developed an analysis method that enables us to draw conclusions about changes in relaxograms that are independent of the choice of regularization parameter.

### **Putting It All Together**

The results illustrate that it is possible to translate relaxometry insights from an MRI to a portable, bedside MR sensor for both phantom and human data. We also discovered how various fluid balance states (dehydration, slight fluid overload, more extreme fluid overload) appear in MR data. Importantly, we were able to detect fluid overload using MR before any signs of lower-extremity edema were detectable on physical exam.

The MRI is a multi-million-dollar piece of equipment, requires bringing the patient to a special RF-shielded room, and takes at least 15 minutes to acquire the data. Our MR sensor costs a few thousand dollars, can be brought to the patient bedside, and takes about 2 minutes to acquire data. The MR sensor can be used like a bedside x-ray or EKG equipment that can be wheeled next to the patient when needed. We are hopeful that in the future, hydration measurements will be as easy and ubiquitous as taking a blood oxygenation measurement with a pulse ox.

Furthermore, as MRF studies continue and more discoveries about the diagnostic use-cases of relaxometry parameters are made, we would like the MR community to keep in mind that many of those diagnostic insights can be translated to a portable MR sensor. Portable MR sensors open the doors to taking relaxometry measurements in cases where the measurements are useful for patient care but may not make financial sense to do with a traditional MRI.

In conclusion, single-voxel MR sensors have a promising future in the toolbox of the 21st century physician.

## Chapter 8

# Recommended Next Steps

We learned a tremendous amount about how fluid physiology shows up in MR measurements and how to translate results from a traditional MRI to a portable MR sensor. The journey to get to these insights led to dozens of additional questions to explore and experiment ideas to try. Here is a discussion of the following 5 experiments that we would recommend doing next and why:

### 8.1 Analyze Additional Dialysis Study Data

We collected much more data in the dialysis study than was analyzed in this thesis. The additional data we collected includes: (1) MRI  $T_1$  maps, (2) MRI Diffusion maps (on all HD and 2 HC subjects), (3) Crit-line data on some HD patients, (4) MRI  $T_2$  maps on the fingers, (5) MR sensor  $T_2$  measurements on the finger, and (6) bioimpedance data for both the whole body and calf-only at hourly time points.

There is nearly another doctoral thesis worth of work involved in analyzing these additional datasets.

We believe it will especially promising to analyze the MRI leg  $T_1$  and diffusion scans. These are additional relaxometry parameters that will provide additional views of human fluid physiology. We expect that diffusion will be an especially sensitive biomarker to fluid overload, since more samples that are more mobile (like free fluid) have larger apparent diffusion coefficients. Analyzing and describing these results will be a novel contribution to the field.

## 8.2 Low Field Scanner Measurements

Matt Rosen has a custom low-field electromagnet scanner in his lab at the Martinos Center. It has a 5mT  $B_0$  field strength, is big enough for a human to walk into (one of the original applications for the scanner was to image the lungs in an upright position), does not have the seemingly illogical limitations of the Siemens scanners (like a 32-echo limit on a CPMG sequence), and is very easy to program.

We recommend repeating our study (and the many more measurements described in this section) on the LF scanner. First, doing so will allow us to see if our results are repeatable at 5mT. If they are, one can start to imagine a wearable, electromagnet form-factor for the sensor. Second, and most importantly, the LF scanner is an ideal sandbox in which to learn more about human fluid physiology in MR.

One of the biggest learnings from this thesis research is that we need to separate the discovery from the engineering. It is nearly impossible (and, at best, wildly ineffective) to both miniaturize and discover something new about physiology at the same time. The miniaturization goals should only exist once the discovery has been made.

Hydration monitoring with MRI is not a well-established field. We therefore need to do the scientific work to discover the relevant parameters and anatomical locations to measure. Once we do that, the engineering work becomes much easier. MRI data provides invaluable help with developing the right model with which to analyze the MR sensor data.

We do not believe we have even scratched the surface of what is possible to do with fluid detection and MR. One need only look at the oil industry, airport security equipment, and food quality control industry to realize the incredible potential of single-voxel MR relaxometry measurements. We believe MR has the potential to be the non-invasive gold standard of hydration monitoring, nearly equivalent to and much more convenient than isotope dilutions.

We need to assess our ability to measure fluid accumulation in different areas of the anatomy (like the abdominal cavity and lungs). We saw that many of our dialysis patients did not have signs of lower extremity edema detectable on physical exam, yet they had many liters of fluid pulled from them. Where did the fluid accumulate?

Let us use the LF scanner to measure the lungs and peritoneal space to see if we can detect fluid removal from these regions of the body. Quantifying accumulation of fluid in the lungs is even more critical to physicians than quantifying it in the lower legs. Exploring where fluid deposits in

te body of ESRD patients will be a novel contribution to the field.

It will also be a novel contribution to the literature to explore where fluid deposits in the body of ESRD patients in between dialysis treatments.

Rather than having to spend months/years and thousands of dollars developing new portable MR sensors for each different part of the anatomy, let us first discover the optimal anatomical regions we should be measuring and then focus on miniaturization. This thesis work has already established that it is possible to translate insights from one MR sensor to another.

### **8.3 Healthy Human Study**

One of the key takeaways from this thesis work is that we need a better understanding of what healthy controls behave like. Similar to the rationale for Google's (Verily) Baseline study<sup>121</sup>, we cannot understand disease until we understand what normal looks like. Our healthy controls in the Dialysis Study displayed a range of values across various parameters. We need to understand what a normal reference range is across these parameters. We also need to measure women and people representing greater race and age diversity.

### **8.4 2-D Relaxometry Measurements**

#### **Background**

2-dimensional relaxometry measurements are measurements that contain information from two different relaxation parameters encoded in them at the same time. For example,  $T_1$ - $T_2$  and  $T_2$ -Diffusion are two common 2-D measurements. By applying a 2-D ILT on these 2-D measurements, one obtains a 2-D relaxogram where, for example, the projection on the x-axis would be a regular  $T_2$  ILT and the projection on the y-axis would be a pure  $T_1$  ILT.

The benefit of taking 2D measurements is that they allow us to take a deeper look into the physiology and potentially pull out more information about the body's fluid compartments.

We took  $T_1$ - $T_2$  measurements on phantoms to illustrate the power of 2D measurements. We measured four phantoms in the Bruker Minispec mq7.5: A, B, B', C. Phantoms A, B, and C all had distinct  $T_2$  relaxation times. Applying an ILT on just phantoms A, B, C yields a 3-peak relaxogram where the area under each hump is approximately 1/3 of the signal (see Figure 8-1).

Phantom B' has the same  $T_2$  relaxation time as phantom B but a different  $T_1$  relaxation time.

If we take a pure  $T_2$  measurement of these four tubes, we get a 3-peak relaxogram where the area under second hump (B and B') is over twice as large as that under the first (A) and third (C) humps individually. From this relaxogram, we do not know whether we have three unequal phantoms or something else (see Figure 8-2). By taking a 2D ILT of these 4 phantoms we are able to clearly identify the 4 tubes that we measured (see Figure 8-3). The  $T_1$  axis gives additional information with which to pick apart the various compartments of the sample.

In our human data, we saw that both subcutaneous and muscular tissue have two relaxation times, the first of which overlaps for both tissues ( $\sim 40$ ms). Perhaps doing 2D relaxometry measurements will allow us to pick apart those overlapping values into two distinct compartments with distinct  $T_1$  or diffusion values.

We took a couple of 2D  $T_1$ - $T_2$  measurements on a whole mouse as well as its ex-vivo tissues to illustrate the potential of this method for helping distinguish between various tissue types in the body (see Figure 8-4).

## Rationale

These 2D measurements have not yet to our knowledge been done on humans. Matt Rosen's scanner enables easy programming of these pulse sequences, making it the ideal place to test them. We hypothesize that diffusion will be a very sensitive parameter to fluid levels in the body, and that fluid overloaded patients will have larger diffusion coefficients than healthy controls. Taking 2D measurements will enable new depths of exploration into the human physiology.

## 8.5 Apply EPG-correction Methods to CPMG data

### Background

Due to  $B_1$  inhomogeneities, stimulated echoes corrupt the pure exponential decay signal in a  $T_2$  relaxation measurement. The  $T_2$  signal is actually a function not only of  $T_2$  but also of  $T_1$  and the refocusing flip angle. The assumption (made by us and most MRI researchers) that the  $T_2$  signal is well modeled by sums of exponential decays is not completely valid and can result in inaccurate  $T_2$  parameter estimations.

Our methods in this hydration-monitoring work are similar to those of multiple sclerosis (MS) researchers in measuring myelin water fraction (MWF). There are EPG-approaches to accounting for the non-primary echo contributions to the data and obtaining more accurate  $T_2$  estimates. When

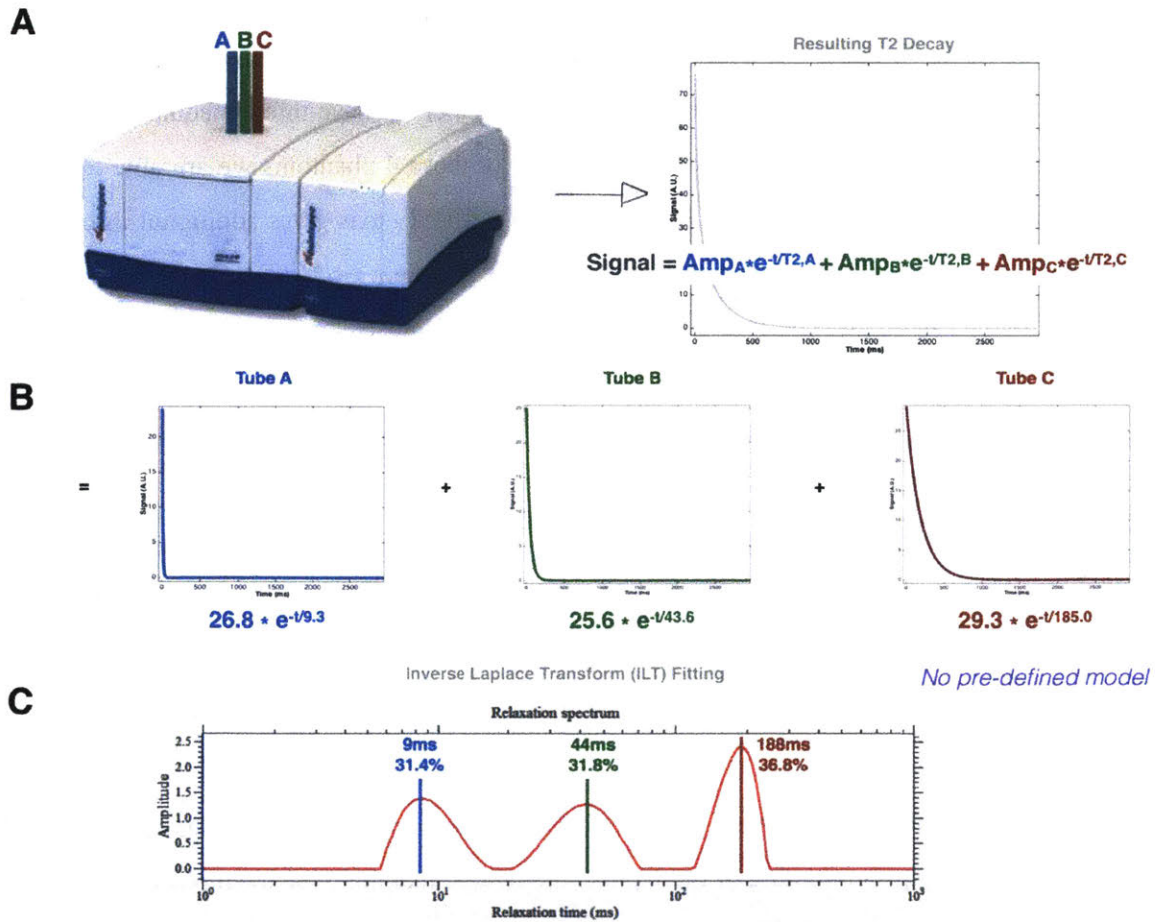


Figure 8-1: (A) Schematic illustrating the three liquid copper sulfate phantoms that were measured with the Bruker MR sensor and the resulting  $T_2$  relaxation decay signal, (B) The three individual compartments resulting from fitting the  $T_2$  decay signal with a 3-exponential decay. Each component contributes approximately 1/3 of the signal, (C) A relaxogram from applying an ILT to the  $T_2$  decay. Three peaks are identified, each of which contributes to approximately 1/3 of the signal. We did not need to specify a model or make any a priori assumptions to obtain this result.

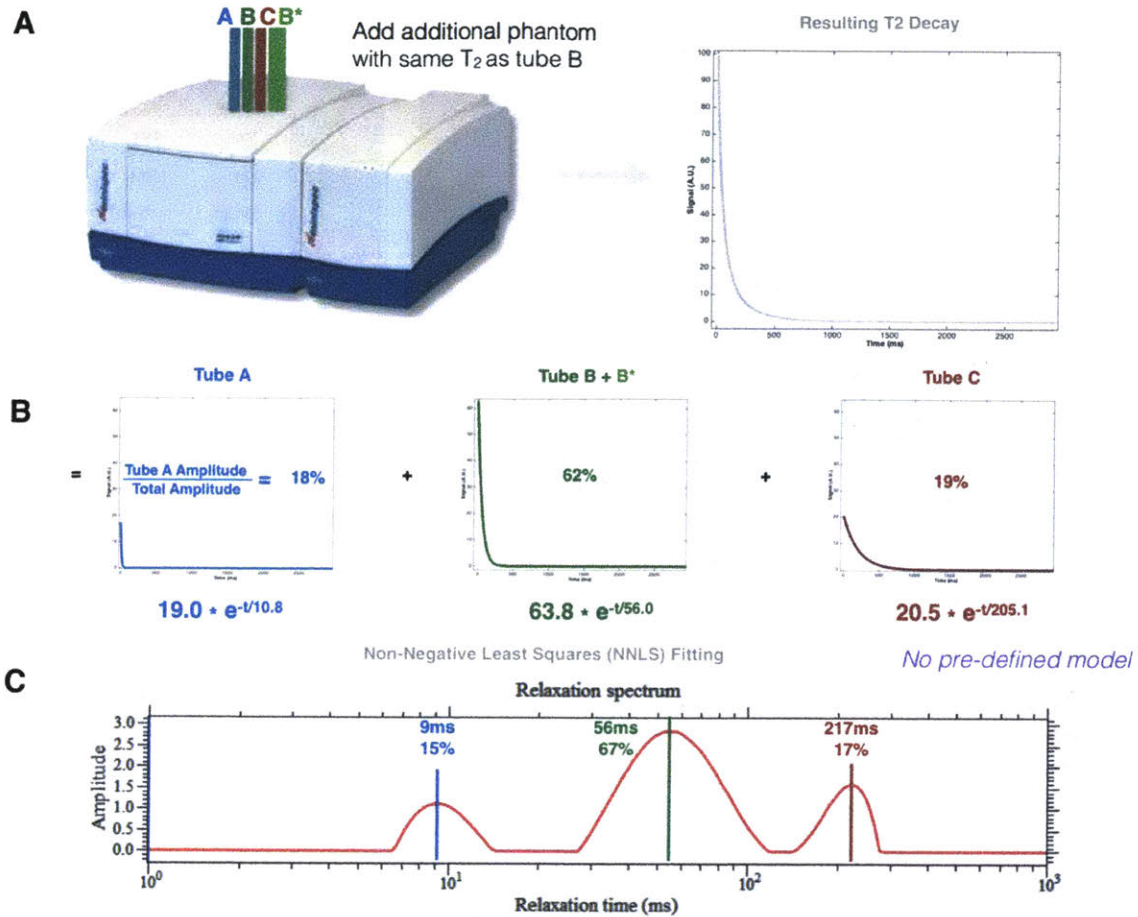


Figure 8-2: (A) Schematic illustrating the 3 liquid copper sulfate and 1 agar phantoms that were measured with the Bruker MR sensor and the resulting  $T_2$  relaxation decay signal. The agar phantom has the same  $T_2$  relaxation time as one of the copper sulfate phantoms. (B) The result from applying a three-exponential decay model to the data. The signal coming from the second compartment (associated with the two agar and copper sulfates phantoms with the same  $T_2$  relaxation time) is more than twice as large as the signal from other other components. (C) The ILT also finds that the second component is more than twice as large as the other components. We do not know if this is because there are three samples where the second sample is large, or if there are four samples where two-samples have the same relaxation time.

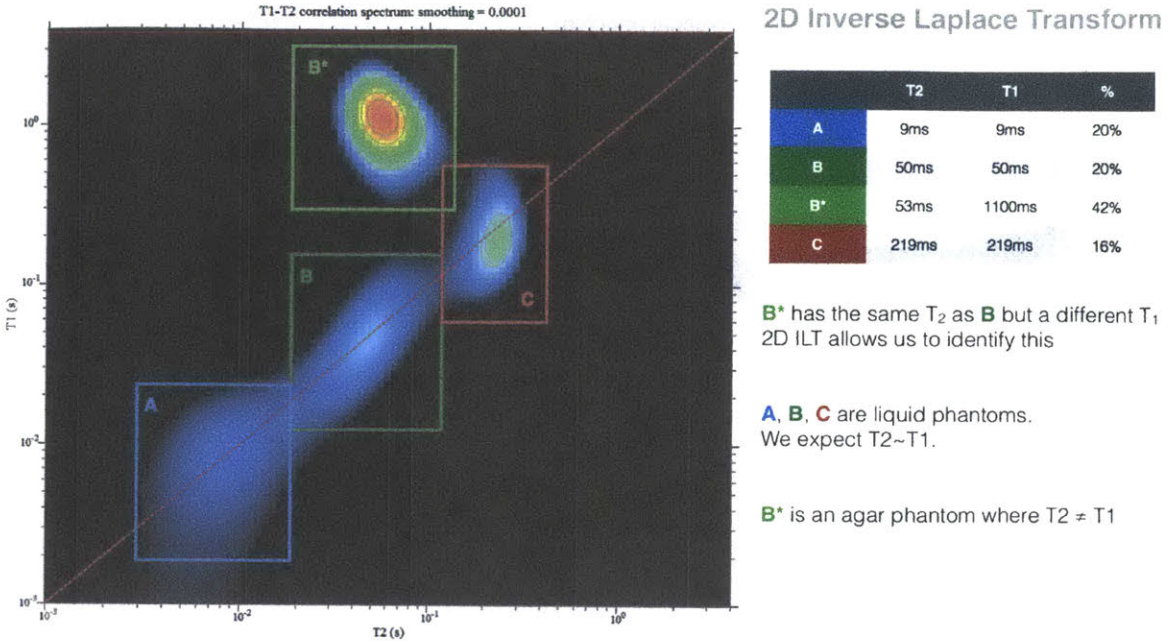


Figure 8-3: Results of a 2D ILT on  $T_1$ - $T_2$  data on 3 liquid copper sulfate and 1 agar phantoms. The agar phantom has the same  $T_2$  relaxation time as one of the copper sulfate phantoms. With a 2D ILT we can clearly distinguish 4 different samples that were measured despite the fact that two of them have the same  $T_2$  relaxation time.

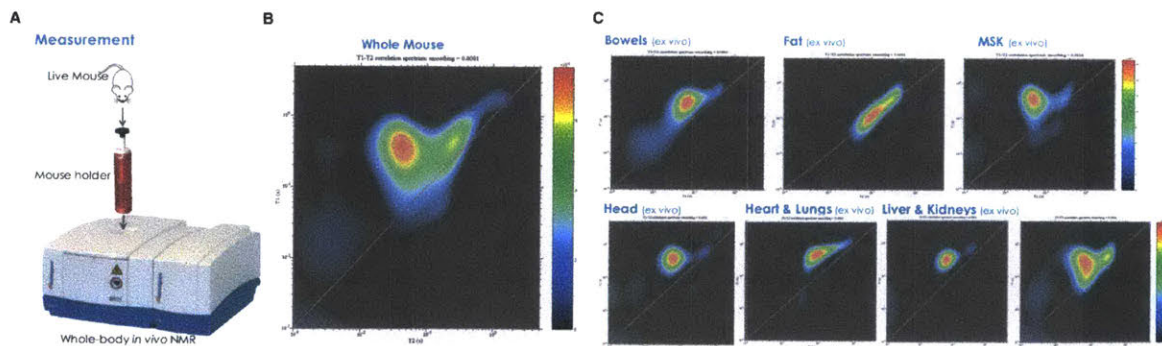


Figure 8-4: Results of a 2D ILT on a whole mouse and ex-vivo tissues. 2D relaxometry measurements enable a greater level of detail when probing the physiology.

these EPG corrections were applied to MWF work, researchers found that the MWF had previously been drastically underestimated. It is likely that our MRI results will also change once the EPG correction is performed on our data. We should perform EPG-based correction on both our MRI data and MR sensor data.

## **Rationale**

As we continue to translate insights from an MRI to a portable MR sensor, it is important to understand the true  $T_2$  values as well as the other parameters that contaminate the signal. Both MRI and our MR sensor data have different factors that corrupt their signals (i.e.  $B_0$  inhomogeneities, imperfect flip angles, etc.). It is important to understand what those factors are and be able to account for them. As far as we are aware, no one has yet performed EPG-correction on quantitative musculoskeletal MRI scans nor on single-voxel MR sensor data - doing so would be a novel contribution to the field.

## **Appendix A**

### **Analysis Workflow**

All scripts for data wrangling, processing, analysis, and visualization related to this project can be found in the project's Github repository: <https://github.com/lcolucci>.

All raw and processed data files related to this project are located in the Cima Lab's server.

Details of the analysis workflow (protocols and video tutorials), video of the thesis defense presentation, and many other multi-media materials related to this doctoral work can be found at: [www.linacolucci.com/PhD](http://www.linacolucci.com/PhD).

# Bibliography

- [1] Ian R. Young. Significant Events in the Development of MRI. *Journal of Magnetic Resonance Imaging*, 20:183–186, 2004.
- [2] Larry Wald and Kawin Setsompop. HST.584/22.561 Magnetic Resonance, 2014.
- [3] F. Bloch, W. W. Hansen, and M. Packard. The Nuclear Induction Experiment. *Physical Review*, 70(7-8):474–485, 1946.
- [4] E. M. Purcell, H. C. Torrey, and R. V. Pound. Resonance Absorption by Nuclear Magnetic Moments in a Solid. *Physical Review*, 69:37–38, 1946.
- [5] F. Bloch. Nuclear Induction. *Physical Review*, 70(7-8):460–474, 1946. URL <https://sites.fas.harvard.edu/~phys191r/References/c4/bloch1946.pdf>.
- [6] Dan Ma, Vikas Gulani, Nicole Seiberlich, Kecheng Liu, Jeffrey L. Sunshine, Jeffrey L. Duerk, and Mark A. Griswold. Magnetic Resonance Fingerprinting. *Nature*, 495(7440): 187–192, 2013. doi: 10.1038/nature11971.Magnetic.
- [7] Hai Ling Margaret Cheng, Nikola Stikov, Nilesh R. Ghugre, and Graham A. Wright. Practical medical applications of quantitative MR relaxometry. *Journal of Magnetic Resonance Imaging*, 36(4):805–824, 2012. ISSN 10531807. doi: 10.1002/jmri.23718.
- [8] Thomas. Yankeelov, David R. Pickens, and Ronald R. Price. *Quantitative MRI in cancer*. CRC Press, 2012. ISBN 1439820589. URL [https://books.google.com/books?id=8FLRBQAAQBAJ{%&}dq=mri+rician+t2+distribution{%&}source=gbs{%}\\_navlinks{%}\\_s](https://books.google.com/books?id=8FLRBQAAQBAJ{%&}dq=mri+rician+t2+distribution{%&}source=gbs{%}_navlinks{%}_s).
- [9] John C. Wood, Cathleen Enriquez, Nilesh Ghugre, J. Michael Tyzka, Susan Carson, Marvin D. Nelson, and Thomas D. Coates. MRI R2 and R2\* mapping accurately estimates hepatic iron concentration in transfusion-dependent thalassemia and sickle cell disease patients. *Blood*, 106(4):1460–1465, 2005. ISSN 00064971. doi: 10.1182/blood-2004-10-3982.
- [10] Mariell Jessup and Susan Brozena. Heart Failure. *The New England Journal of Medicine*, 348(20):2007–18, may 2003. ISSN 1533-4406. doi: 10.1056/NEJMra021498. URL <http://www.ncbi.nlm.nih.gov/pubmed/18063155>.
- [11] Rajiv Agarwal and Matthew R Weir. Dry-weight: a concept revisited in an effort to avoid medication-directed approaches for blood pressure control in hemodialysis patients. *Clinical Journal of the American Society of Nephrology (CJASN)*, 5(7):1255–60, jul 2010. ISSN 1555-905X. doi: 10.2215/CJN.

01760210. URL <http://www.pubmedcentral.nih.gov/articlerender.fcgi?artid=2893058&tool=pmcentrez&rendertype=abstract>.

- [12] Shuta Ishibe and Aldo J. Peixoto. Methods of Assessment of Volume Status and Intercompartmental Fluid Shifts in Hemodialysis Patients: Implications in Clinical Practice. *Seminars in Dialysis*, 17(1):37–43, jan 2004. ISSN 08940959. doi: 10.1111/j.1525-139X.2004.17112.x. URL <http://doi.wiley.com/10.1111/j.1525-139X.2004.17112.x>.
- [13] Helen Hogan, Frances Healey, Graham Neale, Richard Thomson, Charles Vincent, and Nick Black. Preventable deaths due to problems in care in English acute hospitals: a retrospective case record review study. *BMJ Quality & Safety*, 22(2):182–182, 2013. ISSN 2044-5415. doi: 10.1136/bmjqs-2012-001159. URL <http://qualitysafety.bmj.com/lookup/doi/10.1136/bmjqs-2012-001159>.
- [14] David R. Thomas, Syed H. Tariq, Sohail Makhdomm, Rami Haddad, and Asif Moinuddin. Physician misdiagnosis of dehydration in older adults. *Journal of the American Medical Directors Association*, 4(5):251–254, 2003. ISSN 15258610. doi: 10.1016/S1525-8610(04)70368-0.
- [15] Hong Xiao, Janet Barber, and Ellen S Campbell. Economic burden of dehydration among hospitalized elderly patients. *American journal of health-system pharmacy : AJHP : official journal of the American Society of Health-System Pharmacists*, 61(23):2534–40, dec 2004. ISSN 1079-2082. URL <http://www.ncbi.nlm.nih.gov/pubmed/15595228>.
- [16] J Xuan, P T Duong, P A Russo, M J Lacey, and B Wong. The economic burden of congestive heart failure in a managed care population. *The American Journal of Managed Care*, 6(6):693–700, jun 2000. ISSN 1088-0224. URL <http://www.ncbi.nlm.nih.gov/pubmed/10977478>.
- [17] S. Kim. Preventable Hospitalizations of Dehydration: Implications of Inadequate Primary Health Care in the United States. *Annals of Epidemiology*, 17(9):736, sep 2007. ISSN 10472797. doi: 10.1016/j.annepidem.2007.07.043. URL [http://www.annalsofepidemiology.org/article/S1047-2797\(07\)00308-0/abstract](http://www.annalsofepidemiology.org/article/S1047-2797(07)00308-0/abstract).
- [18] G Salvatori, F Ronco, M Bonello, and M Bottero. Management of fluid overload in congestive heart failure: learning from a case report. *The International Journal of Artificial Organs*, 29(2):187–96, feb 2006. ISSN 0391-3988. URL <http://www.ncbi.nlm.nih.gov/pubmed/16552666>.
- [19] Donald W. McRobbie, Elizabeth A. Moore, Martin J. Graves, and Martin R. Prince. *MRI From Picture to Proton*. Cambridge University Press, 2nd edition, 2006. ISBN 9780521865272.
- [20] Jin-Zhao Wang, Reuben S. Mezrich, and John B. Kostis. The Use of Magnetic Resonance Imaging in the Study of Edema. *Angiology*, pages 358–365, 1991.
- [21] S Dhamija, T Major, and S Liachenko. Quantification of Acute Peripheral Muscle Edema in Rats using MRI. *Proc. Intl. Soc. Mag. Reson. Med.* 14, 14:3621, 2006.

- [22] K W Sievers, E Lohr, and T Bauermann. MR Relaxometry: Estimating Overhydration in Renal Failure. *Computerized Medical Imaging and Graphics*, 19(2):219–226, 1995.
- [23] J. D. Meler, M. A. Solomon, J. R. Steele, C. W. Yancy, R. W. Parkey, and J. L. Fleckenstein. The MR appearance of volume overload in the lower extremities. *Journal of Computer Assisted Tomography*, 21(6):969–73, 1997. ISSN 0363-8715. URL <http://www.ncbi.nlm.nih.gov/pubmed/9386292>.
- [24] B. Blümich, J. Perlo, and F. Casanova. Mobile Single-Sided NMR. *Progress in Nuclear Magnetic Resonance Spectroscopy*, 52(4):197–269, may 2008. ISSN 00796565. doi: 10.1016/j.pnmrs.2007.10.002. URL <http://linkinghub.elsevier.com/retrieve/pii/S007965650700091X>.
- [25] Federico Casanova, Juan Perlo, and Bernhard Blümich. *Single-Sided NMR*. 2011. ISBN 9783642163067. doi: 10.1007/978-3-642-16307-4\_1. URL <http://www.springer.com/materials/characterization+{&}+evaluation/book/978-3-642-16306-7>.
- [26] George R. Coates, Lizhi Xiao, and Manfred G. Prammer. NMR Logging: Principles and Applications. Technical report, Halliburton Energy Services, Houston, 1999.
- [27] R. Freedman and N. Heaton. Fluid Characterization Using Nuclear Magnetic Resonance Logging. *Petrophysics*, 45(3):241–250, 2004. ISSN 15299074 (ISSN). URL [https://class.stanford.edu/c4x/HumanitiesSciences/CHEM291/asset/Freedman\\_{\\_}2004.pdf](https://class.stanford.edu/c4x/HumanitiesSciences/CHEM291/asset/Freedman_{_}2004.pdf).
- [28] D Allen, S Crary, and B Freedman. How to use borehole nuclear magnetic resonance. *Oilfield Review*, Summer:34–57, 1997. ISSN 09231730. URL <http://yadda.icm.edu.pl/yadda/element/bwmeta1.element.elsevier-7b53984b-4aa3-35ae-9c75-918f82def9c9>.
- [29] H Nate Bachman, Jack Lavigne, Rob Leveridge, Nick Heaton, Martin D Hürlimann, Wim J Looyestijn, and Jim White. Nuclear Magnetic Resonance Comes Out of Its Shell. *Oilfield Review*, 20(4):4–23, 2009.
- [30] Bill Kenyon, Robert Kleinberg, Straley Christian, Greg Gubelin, and Chris Morriss. Nuclear Magnetic Resonance Imaging — Technology for the 21st Century. *Oilfield Review*, Autumn: 19–33, 1995.
- [31] H Todt, G Guthausen, W Burk, D Schmalbein, and a Kamlowski. Water/moisture and fat analysis by time-domain NMR. *Food Chemistry*, 96(3):436–440, jun 2006. ISSN 03088146. doi: 10.1016/j.foodchem.2005.04.032. URL <http://linkinghub.elsevier.com/retrieve/pii/S0308814605004541>.
- [32] C.M. Andersen and Å. Rinnan. Distribution of Water in Fresh Cod. *LWT - Food Science and Technology*, 35(8):687–696, dec 2002. ISSN 00236438. doi: 10.1006/fstl.2002.0924. URL <http://linkinghub.elsevier.com/retrieve/pii/S0023643802909242>.
- [33] Ida Grong Aursand. *Low-field NMR and MRI studies of fish muscle: Effects of raw material quality and processing*. Doctoral thesis, Norwegian University of Science and Technology (NTNU), 2009.

- [34] Bulat Rameev, Georgy Mozzhukhin, and Bekir Aktaş. Magnetic Resonance Detection of Explosives and Illicit Materials. *Applied Magnetic Resonance*, 43(4):463–467, 2012. ISSN 0937-9347. doi: 10.1007/s00723-012-0423-9. URL <http://link.springer.com/10.1007/s00723-012-0423-9>.
- [35] L. J. Burnett and M. A. Fineman. Evaluation of One-Sided Nucleare Magnetic Resonance for Remote Detection of Explosives. Technical report, Naval Ocean Systems Center, US Navy, San Diego State University, 1987.
- [36] David A Reiter, Ping-Chang Lin, Kenneth W Fishbein, and Richard G Spencer. Multicomponent T2 relaxation analysis in cartilage. *Magnetic Resonance in Medicine*, 61(4):803–9, apr 2009. ISSN 1522-2594. doi: 10.1002/mrm.21926. URL <http://www.pubmedcentral.nih.gov/articlerender.fcgi?artid=2711212{&}tool=pmcentrez{&}rendertype=abstract>.
- [37] Morten Bruvold, John Georg Seland, Heidi Brurok, and Per Jynge. Dynamic water changes in excised rat myocardium assessed by continuous distribution of T1 and T2. *Magnetic resonance in medicine : official journal of the Society of Magnetic Resonance in Medicine / Society of Magnetic Resonance in Medicine*, 58(3):442–7, sep 2007. ISSN 0740-3194. doi: 10.1002/mrm.21340. URL <http://www.ncbi.nlm.nih.gov/pubmed/17763343>.
- [38] Michael Prange and Yi Qiao Song. Quantifying uncertainty in NMR T2 spectra using Monte Carlo inversion. *Journal of Magnetic Resonance*, 196(1):54–60, 2009. ISSN 10907807. doi: 10.1016/j.jmr.2008.10.008. URL <http://dx.doi.org/10.1016/j.jmr.2008.10.008>.
- [39] Yi Qiao Song. Resolution and uncertainty of Laplace inversion spectrum. *Magnetic Resonance Imaging*, 25(4):445–448, 2007. ISSN 0730725X. doi: 10.1016/j.mri.2006.11.023.
- [40] Shanshan Chen, Hongzhi Wang, and Xuelong Zhang. Study on Multi-Exponential Inversion Method for NMR Relaxation Signals with Tikhonov Segularization. 2013(October):32–37, 2013.
- [41] PC Hansen. The L-curve and its use in the numerical treatment of inverse problems. pages 1–24, 1999. URL <http://www.sintef.no/upload/IKT/9011/SimOslo/vskoler/2005/notes/Lcurve.pdf>.
- [42] J.B Miller and a.N Garroway. NMR imaging of solids with a surface coil. *Journal of Magnetic Resonance (1969)*, 77(1):187–191, mar 1988. ISSN 00222364. doi: 10.1016/0022-2364(88)90046-7. URL <http://linkinghub.elsevier.com/retrieve/pii/0022236488900467>.
- [43] B. Manz, A. Coy, R. Dykstra, C. D. Eccles, M. W. Hunter, B. J. Parkinson, and P. T. Callaghan. A mobile one-sided NMR sensor with a homogeneous magnetic field: The NMR-MOLE. *Journal of Magnetic Resonance*, 183(1):25–31, 2006.
- [44] Dr. Supriyo Ghosh. Bruker Time-Domain (TD) NMR Benchtop Systems. Technical report, Bruker. URL <https://www.bruker.com/products/mr/td-nmr.html>.
- [45] Meghan E. Halse. Magritek Terranova: Student Guide. Technical report, Magritek Limited, 2006. URL <http://www.magritek.com/products/terranova/>.

- [46] G. Eidmann, R. Savelsberg, P. Blümmler, and B. Blümich. The NMR MOUSE, a Mobile Universal Surface Explorer. *Journal of Magnetic Resonance, Series A*, 122(1):104–109, sep 1996. ISSN 10641858. doi: 10.1006/jmra.1996.0185. URL <http://linkinghub.elsevier.com/retrieve/pii/S1064185896901850>.
- [47] Lawrence E Armstrong. Assessing hydration status: the elusive gold standard. *Journal of the American College of Nutrition*, 26(5 Suppl):575S–584S, oct 2007. ISSN 0731-5724. URL <http://www.ncbi.nlm.nih.gov/pubmed/17921468>.
- [48] Lawrence E. Armstrong. Hydration Assessment Techniques. *Nutrition Reviews*, 63(6):40–54, jun 2005. ISSN 00296643. doi: 10.1301/nr.2005.jun.S40-S54. URL <http://doi.wiley.com/10.1301/nr.2005.jun.S40-S54>.
- [49] Alex Leeper. AKI Report: A review of the care of patients who died in hospital with a primary diagnosis of acute kidney injury. Technical report, 2009.
- [50] Ross Breckenridge. Heart failure and mouse models. *Disease models & mechanisms*, 3(3-4): 138–43, 2010. ISSN 1754-8411. doi: 10.1242/dmm.005017. URL <http://www.ncbi.nlm.nih.gov/pubmed/20212081>.
- [51] Mariell Jessup and Susan Brozena. Heart failure. *The New England Journal of Medicine*, 348(20):2007–18, may 2003. ISSN 1533-4406. doi: 10.1056/NEJMra021498. URL <http://www.ncbi.nlm.nih.gov/pubmed/18063155>.
- [52] William C Stanley, Fabio A Recchia, and Gary D Lopaschuk. Myocardial Substrate Metabolism in the Normal and Failing Heart. *Physiol Rev*, 85:1093–1129, 2005. doi: 10.1152/physrev.00006.2004.
- [53] Leonard S. Lilly, editor. *Pathophysiology of Heart Disease*. Lippincott Williams & Wilkins, 5th edition, 2011. ISBN 9780080439242. doi: 10.1016/B978-008043924-2/50055-9.
- [54] Jorge P. Navas and Manuel Martinez-Maldonado. Pathophysiology of Edema in Congestive Heart Failure. *Heart Disease and Stroke*, 2(4):325–329, 1993.
- [55] J J McMurray and S Stewart. Epidemiology, aetiology, and prognosis of heart failure. *Heart (British Cardiac Society)*, 83(5):596–602, may 2000. ISSN 1468-201X. URL <http://www.pubmedcentral.nih.gov/articlerender.fcgi?artid=1760825&tool=pmcentrez&rendertype=abstract>.
- [56] Zaid Abassi, Ilia Goltsman, Tony Karram, Joseph Winaver, and Aaron Hoffman. Aorticaval fistula in rat: a unique model of volume-overload congestive heart failure and cardiac hypertrophy. *Journal of Biomedicine & Biotechnology*, 2011:729497, jan 2011. ISSN 1110-7251. doi: 10.1155/2011/729497. URL <http://www.pubmedcentral.nih.gov/articlerender.fcgi?artid=3025398&tool=pmcentrez&rendertype=abstract>.
- [57] Catherine Fallick, Paul A. Sobotka, and Mark E. Dunlap. Sympathetically mediated changes in capacitance: redistribution of the venous reservoir as a cause of decompensation. *Circulation. Heart failure*, 4(5):669–75, sep 2011. ISSN 1941-3297. doi: 10.1161/CIRCHEARTFAILURE.111.961789. URL <http://www.ncbi.nlm.nih.gov/pubmed/21934091>.

- [58] Robert W. Schrier and Michel Niederberger. Conferences and Reviews Paradoxes of Body Fluid Volume Regulation in Health and Disease A Unifying Hypothesis. *West J Med*, 161: 393–408, 1994.
- [59] Leonardo De Luca, William T. Abraham, Gregg C. Fonarow, Mihai Gheorghide, and Leonardo De Luca. Congestion in Acute Heart Failure Syndromes: Importance of Early Recognition and Treatment. *Reviews in cardiovascular medicine*, 7(2):69–74, jan 2006. ISSN 1530-6550. URL <http://www.ncbi.nlm.nih.gov/pubmed/16915125>.
- [60] CMS Medicare Readmission Reduction Program. Technical report, CMS: Affordable Care Act (Section 3025), aug 2013. URL <http://www.cms.gov/Medicare/Medicare-Fee-for-Service-Payment/AcuteInpatientPPS/Readmissions-Reduction-Program.html>.
- [61] Anuradha Sawant, Andrew a. House, Bert M. Chesworth, Joseph Gati, Robert Lindsay, Denise M. Connelly, Robert Bartha, and Tom J. Overend. Reliability of Calf Bioelectrical Impedance Spectroscopy and Magnetic-Resonance-Imaging-Acquired Skeletal Muscle Hydration Measures in Healthy People. *Physiology Journal*, 2013:1–12, 2013. ISSN 2314-4300. doi: 10.1155/2013/563494. URL <http://www.hindawi.com/journals/physiology/2013/563494/>.
- [62] Reuben H. Fan and Mark D. Does. Compartmental Relaxation and DTI Measurements In Vivo in  $\lambda$ - Carrageenan Induced Edema in Rat Skeletal Muscle. *NMR Biomed.*, 21(6):566–573, 2008. doi: 10.1002/nbm.1226.Compartmental.
- [63] J. T. Skinner and M. D. Does. Compartmental Relaxation Measurements in a Graded Muscle Edema Model 1. *Proc. Intl. Soc. Mag. Reson. Med.* 17, 17:1918, 2009.
- [64] Chun S. Zuo, Rosemond A. Villafuerte, Michael E. Henry, Robert L. Dobbins, Chunnin Lee, Younghoon Sung, Charlotte Haws, Michelle Butman, Sam Miller, Alan Manos, Barbara S. Orban, Andrew P. Brown, Rebecca Hodge, Derek J. Nunez, and Perry F. Renshaw. MRI assessment of drug-induced fluid accumulation in humans: validation of the technology. *Magnetic Resonance Imaging*, 26(5):629–637, 2008. ISSN 0730725X. doi: 10.1016/j.mri.2008.01.003.
- [65] K W Sievers, J Gauger, T Bauermann, and E Löhr. Changes of soft-tissue water examined with magnetic resonance and electrical impedance tomography: an in vivo experiment. *Angiology*, 44:889–895, 1993. ISSN 0003-3197. doi: 10.1177/000331979304401107.
- [66] Chun S. Zuo, Rosemond A. Villafuerte, Michael E. Henry, Michelle Butman, Robert L. Dobbins, Yiwu He, Barbara S. Orban, Kenroy Cayetano, Liqun Wang, Andrew P. Brown, Derek J. Nunez, John Brown, and Perry F. Renshaw. Proton and sodium MRI assessment of fluid level in calf tissue. *Journal of Magnetic Resonance Imaging*, 24(1):191–195, 2006. ISSN 10531807. doi: 10.1002/jmri.20624.
- [67] Maulik D. Majmudar, Lina Avancini Colucci, and Adam B. Landman. The quantified patient of the future: Opportunities and challenges. *Healthcare*, 3(3):153–156, 2015. ISSN 22130772. doi: 10.1016/j.hjdsi.2015.02.001.
- [68] S J Graham, M J Bronskill, J W Byng, M J Yaffe, and N F Boyd. Quantitative correlation of breast tissue parameters using magnetic resonance and X-ray mammography. *British Journal of Cancer*, 73(2):162–168, 1996. ISSN 0007-0920.

- [69] S. M. Maillard. Quantitative assessment of MRI T2 relaxation time of thigh muscles in juvenile dermatomyositis. *Rheumatology*, 43(5):603–608, 2004. ISSN 1460-2172. doi: 10.1093/rheumatology/keh130. URL <http://www.rheumatology.oupjournals.org/cgi/doi/10.1093/rheumatology/keh130>.
- [70] GraphPad Software Inc. GraphPad Curve Fitting Guide. *GraphPad*, 2014. URL <http://www.graphpad.com/guides/prism/6/curve-fitting/index.htm?reg{ }the{ }difference{ }between{ }linea.htm>.
- [71] Hakon Gudbjartsson and Samuel Patz. The Rician Distribution of Noisy MRI Data. *Magn Reson Med.*, 34(6):910–914, 1995.
- [72] Ruiliang Bai, Cheng Guan Koay, Elizabeth Hutchinson, and Peter J Bassler. A framework for accurate determination of the T2 distribution from multiple echo magnitude MRI images. *Journal of Magnetic Resonance*, 244:53–63, 2014. ISSN 1096-0856. doi: 10.1016/j.jmr.2014.04.016. URL <http://www.sciencedirect.com/science/article/pii/S1090780714001232>.
- [73] Thorarin a Bjarnason and J Ross Mitchell. AnalyzeNNLS: magnetic resonance multiexponential decay image analysis. *Journal of Magnetic Resonance*, 206(2):200–4, oct 2010. ISSN 1096-0856. doi: 10.1016/j.jmr.2010.07.008. URL <http://www.ncbi.nlm.nih.gov/pubmed/20688549>.
- [74] Andrew Melbourne, Nicolas Toussaint, David Owen, Ivor Simpson, Thanasis Anthopoulos, Enrico De Vita, David Atkinson, and Sebastien Ourselin. NiftyFit: a Software Package for Multi-parametric Model-Fitting of 4D Magnetic Resonance Imaging Data. *Neuroinformatics*, 14(3):319–337, 2016. ISSN 15392791. doi: 10.1007/s12021-016-9297-6. URL <http://dx.doi.org/10.1007/s12021-016-9297-6>.
- [75] Frank J. Vergeldt, Alena Prusova, Farzad Fereidouni, Herbert Van Amerongen, Henk Van As, Tom W.J. Scheenen, and Arjen N. Bader. Multi-component quantitative magnetic resonance imaging by phasor representation. *Scientific Reports*, 7(1):1–10, 2017. ISSN 20452322. doi: 10.1038/s41598-017-00864-8.
- [76] Dimitris Mitsouras, Robert V. Mulkern, and Stephan E. Maier. Multi-Component T2 Relaxation Studies of the Avian Egg. *Magn Reson Med*, 70(5):2156–2164, 2016. ISSN 1527-5418. doi: 10.1097/OGX.000000000000256.Prenatal.
- [77] Ericky C A Araujo, Yves Fromes, and Pierre G. Carlier. New Insights on human skeletal muscle tissue compartments revealed by in vivo t2 NMR relaxometry. *Biophysical Journal*, 106(10):2267–2274, 2014. ISSN 15420086. doi: 10.1016/j.bpj.2014.04.010. URL <http://dx.doi.org/10.1016/j.bpj.2014.04.010>.
- [78] R Harrison, M J Bronskill, and R M Henkelman. Magnetization transfer and T2 relaxation components in tissue. *Magn Reson Med*, 33(4):490–6, apr 1995. ISSN 0740-3194. URL <http://www.ncbi.nlm.nih.gov/pubmed/7776879>.
- [79] Gary D. Fullerton, Janet L. Potter, and N. Carol Dornbluth. NMR Relaxation of Protons in Tissues and Other Macromolecular Water Solutions. *Magnetic Resonance Imaging*, 1: 209–228, 1982.

- [80] R L Kamman, C J Bakker, P van Dijk, G P Stomp, A P Heiner, and H J Berendsen. Multi-exponential relaxation analysis with MR imaging and NMR spectroscopy using fat-water systems. *Magnetic Resonance Imaging*, 5(5):381–92, jan 1987. ISSN 0730-725X. URL <http://www.ncbi.nlm.nih.gov/pubmed/3695824>.
- [81] Dushyant Kumar, Thanh D. Nguyen, Susan A. Gauthier, and Ashish Raj. Bayesian algorithm using spatial priors for multiexponential T2 relaxometry from multiecho spin echo MRI. *Magnetic Resonance in Medicine*, 68(5):1536–1543, 2012. ISSN 07403194. doi: 10.1002/mrm.24170.
- [82] Jorge Zavala Bojorquez, Stéphanie Bricq, Clement Acquitter, François Brunotte, Paul M. Walker, and Alain Lalande. What are normal relaxation times of tissues at 3 T? *Magnetic Resonance Imaging*, 35:69–80, 2017. ISSN 18735894. doi: 10.1016/j.mri.2016.08.021. URL <http://dx.doi.org/10.1016/j.mri.2016.08.021>.
- [83] David Milford, Nicolas Rosbach, Martin Bendszus, and Sabine Heiland. Mono-exponential fitting in T2-relaxometry: Relevance of offset and first echo. *PLoS ONE*, 10(12):1–13, 2015. ISSN 19326203. doi: 10.1371/journal.pone.0145255.
- [84] Gaby S. Pell, Regula S. Briellmann, Anthony B. Waites, David F. Abbott, David P. Lewis, and Graeme D. Jackson. Optimized clinical T2 relaxometry with a standard CPMG sequence. *Journal of Magnetic Resonance Imaging*, 23(2):248–252, 2006. ISSN 10531807. doi: 10.1002/jmri.20490.
- [85] Yanqiu Feng, Taigang He, Peter D. Gatehouse, Xinzhong Li, Mohammed Harith Alam, Dudley J. Pennell, Wufan Chen, and David N. Firmin. Improved MRI R2\* relaxometry of iron-loaded liver with noise correction. *Magnetic Resonance in Medicine*, 70(6):1765–1774, 2013. ISSN 07403194. doi: 10.1002/mrm.24607.
- [86] Gaby S. Pell, Regula S. Briellmann, Anthony B. Waites, David F. Abbott, and Graeme D. Jackson. Voxel-based relaxometry: A new approach for analysis of T2 relaxometry changes in epilepsy. *NeuroImage*, 21(2):707–713, 2004. ISSN 10538119. doi: 10.1016/j.neuroimage.2003.09.059.
- [87] David Milford, Martin Bendszus, and Sabine Heiland. A novel method for T2 quantification in presence of B1 inhomogeneities. *Zeitschrift für Medizinische Physik*, 28(1):63–72, 2018. ISSN 18764436. doi: 10.1016/j.zemedi.2017.08.002. URL <http://dx.doi.org/10.1016/j.zemedi.2017.08.002>.
- [88] S. Majumdar, S. C. Orphanoudakis, A. Gmitro, M. O’Donnell, and J. C. Gore. Errors in the measurements of T2 using multiple-echo MRI techniques. II. Effects of static field inhomogeneity. *Magnetic Resonance in Medicine*, 3(4):562–574, 1986. ISSN 15222594. doi: 10.1002/mrm.1910030410.
- [89] Thomas Prasloski, Burkhard Mädler, Qing San Xiang, Alex MacKay, and Craig Jones. Applications of stimulated echo correction to multicomponent T2 analysis. *Magnetic Resonance in Medicine*, 67(6):1803–1814, 2012. ISSN 07403194. doi: 10.1002/mrm.23157.
- [90] R. Marc Lebel and Alan H. Wilman. Transverse relaxometry with reduced echo train lengths via stimulated echo compensation. *Magnetic Resonance in Medicine*, 70(5):1340–1346, 2013. ISSN 07403194. doi: 10.1002/mrm.24568.

- [91] C Jones, Q. Xiang, K. Whittall, and A. Mackay. Calculating T2 and B1 from Decay Curves Collected with non-180 degree Refocusing Pulses. *Proceedings of the International Society for Magnetic Resonance in Medicine*, 11:1018, 2003. URL <http://cds.ismrm.org/ismrm-2003/1018.pdf>.
- [92] Thomas Liu. MRI Noise and SNR. URL <http://cfmriweb.ucsd.edu/ttliu/be280a{ }08/BE280A08{ }mri6.pdf>.
- [93] Santiago Aja-Fernández and Gonzalo Vegas-Sánchez-Ferrero. *Statistical Analysis of Noise in MRI*. 2016. ISBN 978-3-319-39933-1. doi: 10.1007/978-3-319-39934-8. URL <http://link.springer.com/10.1007/978-3-319-39934-8>.
- [94] H. Nyquist. Thermal agitation of electric charge in conductors. *Physical Review*, 32(1): 110–113, 1928. ISSN 0031899X. doi: 10.1103/PhysRev.32.110.
- [95] J. B. Johnson. Thermal Agitation of Electricity in Conductors. *Nature*, 119(2984):50–51, 1927.
- [96] J. B. Johnson. Thermal Agitation of Electricity in Conductors. *Physical Review*, 32:97–, 1928.
- [97] Assaf Tal. Lecture 9 - SNR, 2014. URL <https://www.weizmann.ac.il/chemphys/assaf{ }tal/sites/chemphys.assaf{ }tal/files/uploads/MRI{ }2014/lecture{ }9{ }-{}snr.pdf>.
- [98] Giulio Gambarota, Brian E. Ciarns, Charles B. Berde, and Robert V. Mulkern. Osmotic Effects on the T2 Relaxation Decay of In Vivo Muscle. *Magn Reson Med*, (46):592–599, 2001.
- [99] Zaid Ababneh, Helene Beloeil, Charles B Berde, Giulio Gambarota, Stephan E Maier, and Robert V Mulkern. Biexponential parameterization of diffusion and T2 relaxation decay curves in a rat muscle edema model: decay curve components and water compartments. *Magnetic Resonance in Medicine*, 54(3):524–31, sep 2005. ISSN 0740-3194. doi: 10.1002/mrm.20610. URL <http://www.ncbi.nlm.nih.gov/pubmed/16086363>.
- [100] Yanna Dou, Fansan Zhu, and Peter Kotanko. Assessment of extracellular fluid volume and fluid status in hemodialysis patients: current status and technical advances. *Seminars in Dialysis*, 25(4):377–87, jul 2012. ISSN 1525-139X. doi: 10.1111/j.1525-139X.2012.01095.x. URL <http://www.ncbi.nlm.nih.gov/pubmed/22686593>.
- [101] Nancy M. Albert. Fluid Management Strategies Heart Failure. *Critical Care Nurse*, 32(2): 20–33, 2012.
- [102] Stephen W. Provencher. CONTIN: A general purpose constrained regularization program for inverting noisy linear algebraic and integral equations. *Computer Physics Communications*, 27(3):229–242, sep 1982. ISSN 00104655. doi: 10.1016/0010-4655(82)90174-6. URL <http://linkinghub.elsevier.com/retrieve/pii/0010465582901746>.
- [103] Andrei A Istratov and Oleg F Vyvenko. Exponential analysis in physical phenomena. *Review of Scientific Instruments*, 70(2):1233–1257, 1999.

- [104] Paula Berman, Ofer Levi, Yisrael Parmet, Michael Saunders, and Zeev Wiesman. Laplace Inversion of Low-Resolution NMR Relaxometry Data Using Sparse Representation Methods. *Concepts in Magnetic Resonance*, 42A(April 2013):72–88, 2013. doi: 10.1002/cmr.a.
- [105] Editors V Pereyra and G Scherer. *Exponential Data Fitting and its Applications*. Bentham Science Publishers, mar 2012. ISBN 9781608050482. doi: 10.2174/97816080504821100101. URL <http://www.eurekaselect.com/51853/volume/1>.
- [106] Robert L. Parker and Yi Qiao Song. Assigning uncertainties in the inversion of NMR relaxation data. *Journal of Magnetic Resonance*, 174(2):314–324, 2005. ISSN 10907807. doi: 10.1016/j.jmr.2005.03.002.
- [107] Heinrich Voss. Regularization of Least Squares Problems, 2010.
- [108] Per Christian Hansen and Dianne Prost O’Leary. The Use of the L-Curve in the Regularization of Discrete Ill-Posed Problems. *SIAM J. Sci. Comput.*, 14(6):1487–1503, 1993.
- [109] P C Hansen. The L-Curve and its Use in the Numerical Treatment of Inverse Problems. in *Computational Inverse Problems in Electrocardiology*, ed. P. Johnston, *Advances in Computational Bioengineering*, 4:119–142, 2000. doi: 10.1.1.33.6040. URL <http://citeseerx.ist.psu.edu/viewdoc/summary?doi=10.1.1.33.6040>.
- [110] GAutam Bhave and Eric G. Neilson. Volume Depletion versus Dehydration: How Understanding the Difference Can Guide Therapy. *Am J Kidney Dis.*, 58(2):302–309, 2011. ISSN 08966273. doi: 10.1053/j.ajkd.2011.02.395.
- [111] J K Nicholson, P J Foxall, M Spraul, R D Farrant, and J C Lindon. 750 MHz <sup>1</sup>H and <sup>1</sup>H-<sup>13</sup>C NMR spectroscopy of human blood plasma. *Analytical Chemistry*, 67(5):793–811, mar 1995. ISSN 0003-2700. URL <http://www.ncbi.nlm.nih.gov/pubmed/7762816>.
- [112] Kengo Hattori, Yusuke Ikemoto, Wataru Takao, Seiichiro Ohno, Takashi Harimoto, Susumu Kanazawa, Masataka Oita, Koichi Shibuya, Masahiro Kuroda, Hirokazu Kato, and Kengo Hattori. Development of MRI phantom equivalent to human tissues for 3.0-T MRI. *Med Phys*, 032303(2013):0–11, 2013. doi: 10.1118/1.4790023.
- [113] V. Pollak and B. Melton. Proton Spin Relaxation and Mobility of Water in Muscle Tissue. *Zeitschrift fur Naturforschung - Section C Journal of Biosciences*, 28(1-2):59–62, 1973. ISSN 18657125. doi: 10.1515/znc-1973-1-209.
- [114] Greg J Stanisz, Ewa E Odrobina, Joseph Pun, Michael Escaravage, Simon J Graham, Michael J Bronskill, and R Mark Henkelman. *T1, T2 relaxation and magnetization transfer in tissue at 3T*. PhD thesis, sep 2005. URL <http://www.ncbi.nlm.nih.gov/pubmed/16086319>.
- [115] Bruce Rosen and Larry Wald. HST.584J/22.561 Magnetic resonance, 2006. ISSN 0933033X.
- [116] Noam Ben-Eliezer. Rapid and accurate T2 mapping from multi-spin-echo data using bloch-simulation-based reconstruction. *Magnetic Resonance in Medicine*, 0, mar 2014. ISSN 1522-2594. doi: 10.1002/mrm.25156.

- [117] Benjamin Marty, Pierre Yves Baudin, Harmen Reyingoudt, Noura Azzabou, Ericky C A Araujo, Pierre G. Carlier, and Paulo L. de Sousa. Simultaneous muscle water T2 and fat fraction mapping using transverse relaxometry with stimulated echo compensation. *NMR in Biomedicine*, 29(4):431–443, 2016. ISSN 10991492. doi: 10.1002/nbm.3459.
- [118] Ashvin Bashyam, Matthew Li, and Michael J Cima. Design and experimental validation of Unilateral Linear Halbach magnet arrays for single-sided magnetic resonance. *Journal of Magnetic Resonance*, 9(292):36–43, 2018. ISSN 1090-7807. doi: 10.1016/j.jmr.2018.05.004. URL <https://doi.org/10.1016/j.jmr.2018.05.004>.
- [119] Andrew E. Marble, Igor V. Mastikhin, Bruce G. Colpitts, and Bruce J. Balcom. A compact permanent magnet array with a remote homogeneous field. *Journal of Magnetic Resonance*, 186(1):100–104, 2007. ISSN 10907807. doi: 10.1016/j.jmr.2007.01.020.
- [120] Matthew Li. *Methods and Devices for Noninvasive Physiologic Fluid Volume Assessment*. Doctoral thesis, Massachusetts Institute of Technology, 2016.
- [121] Project Baseline - Verily Life Sciences. URL <https://verily.com/projects/precision-medicine/baseline-study/>.